THE HYDROGEN EMBRITTLEMENT OF TITANIUM ALLOYS

A thesis submitted for the degree of Doctor of Philosophy

by

David Louis Arditti, B.Sc., M.Sc.

Department of Materials,
Imperial College of Science,
Technology & Medicine,
London SW7 2BP

October 1993

Acknowledgements

Professor Harvey M. Flower

Technical staff Graham Briers, John Woodall

and Nalin Salpadoru

Postgraduate students and postdoctoral researchers

past and present

"I could hardly imagine a more damning case," I remarked. "If ever circumstantial evidence pointed to a criminal it does so here."

"Circumstantial evidence is a very tricky thing," answered Holmes thoughtfully; "it may seem to point very straight to one thing, but if you shift your own point of view a little, you may find it pointing in an equally uncompromising manner to something entirely different."

Holmes and Watson in "The Boscombe Valley Mystery" by Sir Arthur Conan Doyle

So many distingushed persons have studied this subject that we will soon know nothing about it whatever.

Mark Twain

Abbreviations Used

BEI..... Backscattered electron imaging

SADP..... Selected area diffraction pattern

SEI..... Secondary electron imaging

SEM..... Scanning electron microscope

TEM..... Transmission electron microscope

Abstract

Tensile specimens of commercially-pure titanium, grade 12 titanium (an alloy containing nickel and molybdenum), grade 5 titanium (an alloy containing aluminium and vanadium) and two binary titanium-nickel alloys have been variously heat-treated, then given a standard cathodic hydrogen-charging treatment for various lengths of time and subjected to slow strain rate testing, metallographic and fractographic examination, and X-ray and electron diffraction. The effect of annealing after hydrogen charging has also been studied, the cracking process has been studied in-situ in the high voltage electron microscope, and the effect of stress applied concurrently with the hydrogen charging has been examined.

Measurable hydrogen embrittlement as a result of the treatment has been found only in the alloys containing nickel. Reduction in ductility is greatest in grade 12, but almost as severe in Ti-3.5Ni and Ti-5Ni. In grade 12 there is a strong dependence on microstructure, the reduction in tensile strength being 4 times greater for a basketweave than for an equiaxed microstructure. This has been shown by backscattered electron imaging in the SEM to be due to the effect of the more connected β phase paths in the basketweave material conducting solute hydrogen into the sample to precipitate hydrides in the α phase on the grain boundaries. It is, however, doubted by the author whether fracture in the embrittled alloys can be attributed to crack nucleation by brittle hydrides, since evidence of crack propagation paths does not support this theory, and the embrittlement of the binary titanium-nickel alloys is not accompanied by detectable hydride precipitation. Annealing of the grade 12 above 250°C for 24 hours results in hydride redistribution and a partial recovery of ductility. Annealing of Ti-3.5Ni at 250°C and higher temperatures results in gradually increased impairment of tensile properties, a halving of ductility resulting from an anneal at 450°C for 24 hours. This is associated with fractographic evidence of a diffusional spread of the embrittled layer. Samples which have been strained during hydriding show a more rapid penetration of hydrides, the

difference being greater for the grade 2 than for the grade 12. At a strain rate of 3×10^{-7} /s hydride penetration is still 2-3 times more rapid in the grade 12, however. It is thought most likely that the effect of stress is due to the cracking of the protective oxide layer. The grade 5 has been found to be the alloy least susceptible to the effects of hydrogen under all circumstances. Electron diffraction has shown 4 different orientation relationships between hydrides and the alloys and 3 different habit planes for the hydrides. A theory has been proposed to account for the differing susceptibilities of the alloys to hydrogen embrittlement in terms of the properties of the protective oxide layer.

CONTENTS

LIST OF TABLES

LIST OF FIGURES

1 INTRODUCTION

1.1 Use of Titanium and its Alloys

The salient characteristics of titanium and its alloys are their high strength to weight ratio, good thermal conductivity, and, particularly, their outstanding corrosion resistance (see table 1.1). The first of these characteristics is the primary reason for the use of titanium in the aerospace industry. The second two are responsible for the uses of titanium on land and in the sea in such applications as seawater-cooled heat exchangers in nuclear power stations, components in chemical plants, and parts of oil rigs and ships. Titanium is generally restricted to specialised applications because of the cost of the material: three times that of stainless steel, on a weight basis. But it must be remembered that the low density of titanium means generally that less mass is required. In the construction of heat exchangers, this means that the tube walls will be thinner and the heat transfer more efficient, since the thermal conductivity is on a par with that of stainless steel. In addition, pure titanium (grade 1) used in seawater-cooled heat exchangers has been shown to outlast all other materials by a factor of 4[1], so when the cost of replacement is taken into account, titanium often becomes economical.

1.2 Titanium in the Offshore Oil Industry

This project was prompted chiefly by the use, and projected use, of titanium components on oil rigs. The uses of titanium are being extended from heat exchangers and small components of a non-load bearing variety to, in some cases, much larger sections. Fig. 1.1 shows an ambitious application, a stress joint in an undersea well riser[2]. Titanium was chosen here for its corrosion resistance, particularly at the high temperatures encountered at the well head, and because it gives the slight flexibility required at the lowest joint in the riser because of the drift of the rig owing to wind and currents.

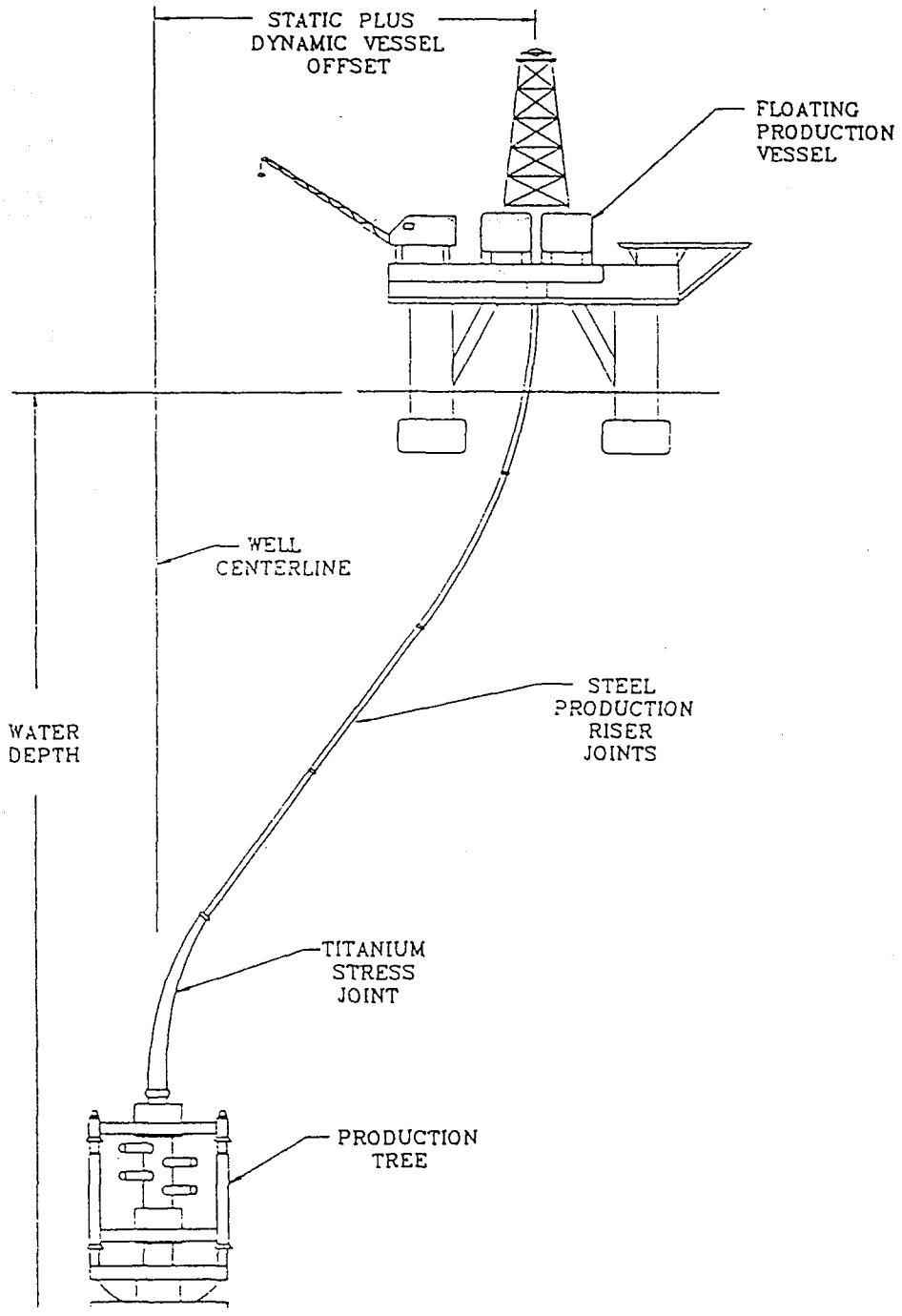

Fig. 1.1 Titanium stress joint in undersea oil well riser, after Fisher and Dziekonski[2]

	Titanium	18-8 stainless steel	Admiralty brass	90-10 cupro-nickel	70-30 cupro-nickel	Aluminium-brass
Density at 20°C (10^3 kg/m^3)	4.5	7.9	8.53	8.94	8.95	8.33
Coeff. thermal exp. 20-300°C (10^{-6}°C)	8.4	17	20.2	17.1	16.2	18.5
Thermal conductivity at 20°C (10^{-3} J/mKs)	9.84	9.36	62.4	26.4	6.8	57.6
Young's modulus (10^3 MPa)	10.4	19.6	11.2	12.6	15.4	11.2
Yield strength (MPa)	34	28	14	14	18	18
Tensile strength (MPa)	44	61	35	36	43	46
Elongation (%)	40	60	65	42	45	59
Flow rate (m/s)*	>20	>20	2	4	2-3	2-3

Table 1.1 Physical properties of some corrosion-resistant materials, after Lunde[19]

*Flow rate is the maximum acceptable water velocty without erosion corrosion.

1.3 Galvanic Corrosion and Cathodic Protection

One problem with titanium in seawater and other corrosive media arises from the fact that at some point it must be bonded to another metal. The position of titanium in the electrochemical series makes it one of the more anodic metals. Its corrosion resistance is thus not due to lack of reactivity with oxygen, but quite the reverse. As in the case of aluminium, a coherent oxide film forms instantly on the surface of the titanium when it first comes into contact with air, which passivates it and makes it immune to further attack. The result of this is that in the electrochemical series of corrosion, titanium is cathodic with respect to all other engineering metals.

When titanium is joined to another metal immersed in an electrolyte a galvanic cell is set up in which titanium becomes the cathode and the metal the anode. Electrons flow through the couple from the metal to the titanium, OH^- ions are produced at the titanium surface and positive metal ions at the metal surface, which subsequently dissolve away. Hence the joining of titanium to another metal accelerates the corrosion of the metal.

The normal counter-measure to this galvanic attack is to apply cathodic protection to the whole structure. The structure is put at -1 to -1.5 v with respect to the sacrificial anode. This is sufficient to stop the dissolution of the metal. Now, however, both metals become prone to attract any H^+ ions present in solution, and the titanium, being most cathodic, will be their preferred destination. On contact with the titanium the H^+ ions are reduced to hydrogen atoms. These are capable of diffusing through the oxide film, and then interstitially through the titanium lattice. If the concentration of hydrogen in the titanium becomes sufficiently high, hydrogen embrittlement occurs. This can lead to cracking and eventually failure of stressed components.

1.4 This Project

Hydrogen embrittlement has been an important factor limiting the increased use of titanium and its alloys in seawater and some other corrosive media, such as hydrogen sulphide (present in North Sea oil). The objectives of this project have been to clarify the nature of the process, to test the relative susceptibilities to embrittlement of titanium with various alloying additions, and to suggest what alloys or treatments should be used to minimise its impact.

The project was a joint venture under the EURAM programme of the Commission of the European Community with 3 other European research institutions. The emphasis in this part of the work was on microstructural characterisation using electron microscopy to study: 1) the mechanism of the embrittlement process, and 2) the influence of the compositions and microstructures of alloys on the process.

2 LITERATURE REVIEW

2.1 General Properties of Titanium

Titanium is non-magnetic and its electrical and thermal conductivities and specific heat capacity are near those of stainless steel[3]. Commercial grades of titanium all exhibit moderately good ductility at temperatures down to 20K. Their elongations at fracture actually increase as the temperature decreases from 300K, passing through broad maxima (40-50%) at about 77K, thereafter descending rapidly. Cold rolling increases the yield and ultimate strengths but at the expense of ductility.

The effects of interstitial elements on plastic properties have been considered by Conrad[4]. Carbon, nitrogen and oxygen, which bond in a covalent manner to the surrounding titanium atoms, considerably increase the strength of otherwise unalloyed titanium, particularly at temperatures below about one half the melting point. Hydrogen as an alloying element, on the other hand, provides very little increase in strength but can seriously impair both the ductility and fracture toughness.

In the many investigations of this effect that have been carried out, the degree of impairment of properties reported varies greatly. This is no doubt due to variations in the purity and microstructural state of the materials used, and particularly to variation in the distribution of hydrogen in the material resulting from the different experimental methods used. For example, a given hydrogen content in a sample may be achieved either by a distribution in solution through the bulk, with no precipitates, or by a concentration in particular areas, for example at the surface or on grain boundaries, with resultant precipitation of hydrides. The resulting mechanical properties may be very different. These issues will be discussed in more detail later.

2.2 Metallurgy of Titanium and its Alloys

Up to 882°C titanium has a hexagonal structure, known as α, while above this temperature it changes to the body-centered cubic form known as β, which is more easily worked. When crystals of β titanium, on cooling, transform to α, a particular crystallographic relationship between the phases (the Burgers relationship) is observed[5]. The process is exactly reversible, and on heating to above the transformation temperature not only the β structure, but also the original grain orientations are restored.

Alloying elements can be classified into two groups:

1) Those which produce little change in the transformation temperature (e.g. tin) (neutral elements) or cause it to increase (e.g. aluminium and oxygen). These are known as α stabilisers. They are generally non-transition elements.

2) Those which decrease the phase transformation temperature (e.g. molybdenum and vanadium, and also hydrogen). These are known as β stabilisers. They are generally transition metals which, like titanium, have unfilled or just-filled d electron shells[6].

In the alloys the single phase α and single phase β regions are not in contact as they are in the pure metal, but are separated by a two-phase α+β region whose width usually increases with increasing solute concentration[7]. Hence titanium alloys can be classified into α, β or α+β, according to their structures at room temperature.

α alloys are characterised by their good strength, toughness, creep resistance and weldability[8]. The absence of a brittle-ductile transformation, a property of the BCC structure, makes them suitable for cryogenic applications. The α-stabilising elements act as solid solution strengtheners in titanium. They can generally be added up to the point at which the field of α stability is terminated by the formation of compounds of the type

Ti_3M, where M is the α-stabiliser, which are also hexagonal in structure[9]. The classic α titanium alloy is Ti-Al. Alloying with aluminium has the advantages of decreasing the density and increasing the resistance to oxidation at elevated temperatures[6].

β alloys are extremely formable, but prone to a ductile-brittle transformation at low temperatures. The β stabilising action of transition metal solutes becomes greater the further they are from titanium in the periodic table[10]. The classic β titanium alloy is Ti-Mo. Room-temperature β alloys do not consist of thermodynamically stable β phase[11]. Rather, the $\beta \rightarrow \alpha + \beta$ reaction kinetics are too slow to allow conversion to α even during slow cooling. Hence the structure of these alloys is metastable β, and the precipitaton of α phase or intermetallic compounds according to the equilibrium diagrams is likely if the alloys are held at elevated temperatures for substantial periods.

Although many β-stabilised alloys in thermodynamic equilibrium are two-phase, practical α+β alloys usually contain mixtures of both α and β stabilisers. These alloys are characterised by good fabricability, high room temperature strength and moderate elevated temperature strength[12]. They may contain between 10 and 50% β phase at room temperature, but if they contain more than 20% they are not weldable. Their properties can be controlled by heat treatments which are used to adjust the microstructural state of the β component. The simplest and best-known of the α+β alloys is Ti-6Al-4V.

Titanium alloys are used in the aerospace industry for compressor blades, discs, castings, engine forgings and bolts and in sheet form to produce airframe components, and in the chemical industry[6].

2.3 Titanium and Alloy Microstructures

Unalloyed titanium transforms martensitically from BCC to HCP during very rapid cooling below its β to α allotropic transformation temperature, 882°C[8]. The behaviour of

titanium alloys when passing through the β to α change is similar to that of steel passing through the γ to α change.

α-stabilised alloys, when cooled rapidly from the β field, change to α by an almost instantaneous reaction which produces a martensitic structure. The α is supersaturated with the alloy addition because of the diffusionless change. Unlike in steel, however, the martensite is not hard because the solute produces a symmetrical distortion of the α titanium lattice, which interacts only weakly with screw dislocations, hence producing little hardening effect.

The addition of β-stabilising elements depresses the martensitic start temperature. If it is depressed below room temperature, martensite will not form during cooling from the β field, and the β will be retained to room temperature[6]. The minimum additions for the complete retention of the β phase at room temperature are 15% V, 6.5% Mn, 4% Fe or 8% Ni. Tempering of retained β at 350-400°C can cause precipitation of a transition phase called ω, which causes excessive brittleness[14]. Further ageing transforms the ω to α phase. At higher ageing temperatures the α forms directly from the β.

If the alloys are cooled slowly from the β field, the α phase nucleates and grows on the grain boundaries, forming a network, within which transcrystalline lamellae of α form[6]. The residual β, present between the lamellae, may be retained or may change to an α+β mixture at lower temperatures or upon subsequent heat treatment.

α+β alloys like Ti-6Al-4V are used after annealing to relieve stresses and to form small rounded islands of β[12]. Heating above the transformation temperature can result in a loss of ductility owing to the formation of a coarse α+β Widmanstatten structure.

2.4 Plastic Deformation of Titanium

2.4.1 Slip

HCP metals generally slip on the basal plane (0001), which is the most densely-packed plane. This is true of those metals which have the ideal c/a ratio for the hexagonal system of 1.633 or greater, such as zinc and cadmium. This results in the 3 slip systems in the 3 $<11\bar{2}0>$ close-packed directions.

Titanium, however, has a c/a ratio lower than the ideal, and the prismatic $\{10\bar{1}0\}$ planes are almost as closely packed as the (0001), and hence slip also occurs on these 3 planes[14]. The slip on these planes is always in the close-packed $<11\bar{2}0>$ directions. Slip may also occur in these directions on the pyramidal $\{10\bar{1}1\}$ planes, and also on these planes in the $<11\bar{2}3>$ directions (fig. 2.1). α titanium thus has a total of 12 slip systems (though not all independent), and as a result is considerably more workable than zinc or cadmium at room temperature.

β titanium, being BCC, has no close-packed planes, but the close-packed direction is <111>, the cube diagonal, and slip is expected to occur in this direction. According to Ling et al.[15], titanium-vanadium β phase alloys in the range 20-40% vanadium exhibit slip on the {110} and {112} planes, resulting in a total of 24 slip systems. To this increased number of slip systems may be attributed the increased ductility of β alloys over α titanium, although for some alloys twinning may also be very significant (see below).

2.4.2 Twinning

α titanium also deforms plastically by twinning, which generally occurs on the $\{10\bar{1}2\}$, {1121} or {1122} planes. Williams and Eppelsheimer[16] have found that the critical shear stresses for slipping and twinning processes are related by

$$C_{s\{0001\}} = 1.1\ C_{s\{10\bar{1}1\}} = 1.02\ C_{s\{10\bar{1}0\}} = C_{t\{10\bar{1}2\}} = C_{t\{11\bar{2}2\}}.$$

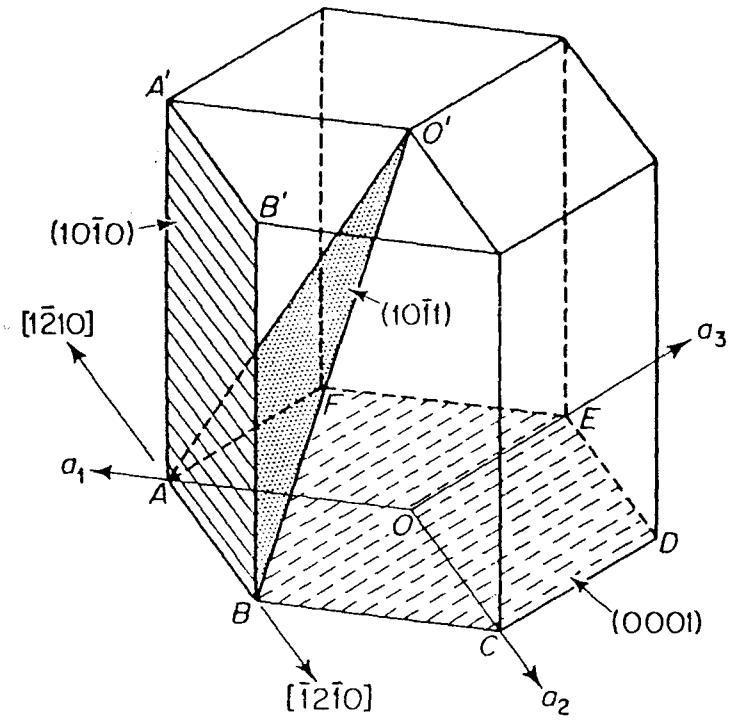

Fig. 2.1 Slip planes and directions in the α titanium lattice, after Polakowski & Ripling[14] (Slip also occurs on the (10$\bar{1}$1) plane in the [1$\bar{2}$13] direction, not shown here.)

Ling et al. have also observed deformation by twinning on {112} planes in β phase titanium-vanadium alloys, and this was found to be the predominant mode of deformation for a 20 weight % vanadium alloy, but when the vanadium content was increased above this level, slip became the dominant mode.

2.4.3 Effect of Impurities

Interstitial atoms such as oxygen and nitrogen are thought to strengthen titanium by interfering with the slip process. These atoms occupy the octahedral positions in the α titanium unit cell at (1/3, 2/3, 1/4) and (1/3, 2/3, 3/4). Erlich[17] has pointed out that these two positions lie between the $(10\bar{1}1)$ layers and the $(10\bar{1}0)$ layers respectively. The strain fields of atoms located in these positions would therefore be expected to affect particularly slip on these planes. The relatively small effect of hydrogen atoms when located in these interstitial positions on the flow stress is presumably due to their small size compared with oxygen and nitrogen atoms.

2.5 Commercial Titanium

Titanium is manufactured in various grades regulated by the ASTM[18] and numbered 1-12. The lower the grade number, the higher is the purity. The chemical specifications of the grades are given in table 2.1.

The normal quality of unalloyed, commercially-pure titanium is grade 2, which is extensively used in corrosive environments, although the more expensive grade 1 is used for lining heat exchanger tube plates[19]. In aerospace applications, higher strength, lower ductility alloyed grades such as 5 (Ti-6Al-4V) are being used. In some environments, such as hot chloride solutions, small amounts of alloying additions of palladium, grade 7, or molybdenum and nickel, grade 12, serve to improve corrosion resistance.

Element	Composition, %									
	Grade									
	1	2	3	4	5	6	7	10	11	12
Nitrogen, max	0.03	0.03	0.05	0.05	0.05	0.05	0.03	0.05	0.03	0.03
Carbon, max	0.10	0.10	0.10	0.10	0.10	0.10	0.10	0.10	0.10	0.08
Hydrogen,[A] max	0.015	0.015†	0.015	0.015	0.015	0.020	0.015	0.020	0.015	0.015
Iron, max	0.20	0.30	0.30	0.50	0.40	0.50	0.30	0.35	0.20	0.30
Oxygen, max	0.18	0.25	0.35	0.40	0.20	0.20	0.25	0.18	0.18	0.25
Aluminum	...	...	...	...	5.5 to 6.75	4.0 to 6.0	...	...	...	...
Vanadium	...	...	...	...	3.5 to 4.5	...	...	...	...	...
Tin	...	...	...	...	...	2.0 to 3.0	...	3.75 to 5.25	...	...
Palladium	...	...	...	...	...	...	0.12 to 0.25	...	0.12 to 0.25	...
Molybdenum	...	...	...	...	...	...	...	10.0 to 13.0	...	0.2 to 0.4
Zirconium	...	...	...	...	...	...	...	4.50 to 7.50	...	...
Nickel	...	...	...	...	...	...	...	...	...	0.6 to 0.9
Residuals[B,C] (each), max	0.1	0.1	0.1	0.1	0.1	0.1	0.1	0.1	0.1	0.1
Residuals[B,C] (total), max	0.4	0.4	0.4	0.4	0.4	0.4	0.4	0.4	0.4	0.4
Titanium[D]	remainder	remainder	remainder	remainder	remainder	remainder	remainder	remainder	remainder	remainder

[A] Lower hydrogen may be obtained by negotiation with the manufacturer.

[B] Need not be reported.

[C] A residual is an element present in a metal or an alloy in small quantities inherent to the manufacturing process but not added intentionally.

[D] The percentage of titanium is determined by difference.

† Editorially corrected.

Table 2.1 ASTM chemical specifications for grades of titanium[18]

2.6 Sources of Hydrogen

The embrittlement of titanium through internal hydrogen present as a result of the manufacturing process was once a problem, but is no longer thanks to improvements in the process which have resulted in hydrogen levels normally below about 50 ppm in the finished product[20]. Thus today all problems of hydrogen embrittlement should be environmental.

Contamination of titanium alloys by hydrogen has been reported in cases where oxide scaling due to hot working has been removed by acid pickling[21]. A similar phenomenon is the ingress of hydrogen that has been reported due to etching in acid solutions[22]. Such etching is often used to remove the oxygen-stabilised α surface layer from α-β alloys that have been hot-worked in air. In these cases the hydrogen is present as H^+ ions in the environment. At the metal surface the hydrogen ions gain an electron. The resulting H atoms may be directly adsorbed on to the surface, or they may combine to form H_2 molecules in solution[23]. In neutral solutions as well, however, hydrogen molecules can be evolved by the process of galvanic corrosion (fig. 2.2). An atmospherically oxidised piece of titanium placed in an electrolyte will already be passivated and essentially will suffer no further corrosion. However, if there is a crack or a flaw in the oxide film a microscopic galvanic cell will be set up with the bare metal as the anode and the oxidised area as the cathode[24]. At the anode the titanium will dissolve by dissociating according to the reaction

$$Ti \rightarrow Ti^{4+} + 4e^-,$$

and at the cathode hydroxide ions will be evolved according to the reaction

$$4H_2O + 4e^- \rightarrow 4OH^- + 2H_2,$$

which then meet the titanium ions in the solution to precipitate as the oxide:

$$4OH^- + Ti^{4+} \rightarrow TiO_2 + 2H_2O,$$

The electrons produced in the anode reaction are conducted through the metal to be consumed in the cathode reaction, and the by-product of the cathode reaction is

molecular hydrogen, which, depending on the concentration of oxygen in the solution may itself be oxidised to water, or it may be adsorbed onto the anode or cathode surface. In order to to be adsorbed by the metal or oxide surface the molecular hydrogen must dissociate into atoms:

$$H_2 \rightarrow 2H \text{ (phase boundary reaction)}^{25}.$$

Because the reaction products form in solution, corrosion in the microscopic galvanic cell is not stopped by passivation.

Hydrogen can also be evolved by a similar process through the corrosion of another less noble metal to which the titanium is galvanically coupled[26] (fig. 2.3). In this case the anodic reaction occurs at the surface of the metal and the cathodic reaction at the titanium oxide/solution interface. This will typically happen in a crevice at the joint between the two metals, and under the reducing (oxygen depleted) conditions in this environment the oxidation of the hydrogen produced in the reaction is less likely, and the oxide film on the titanium may be thinner and less effective at resisting the hydrogen diffusion.

Hydrogen may also be evolved through the application of a constant current in order to protect cathodically a less noble metal. In this case the anodic dissolution reaction is inhibited for both the titanium and the other metal (but encouraged at the sacrificial anode), and the cathodic reaction takes place at the titanium oxide/solution and metal oxide/solution interfaces. If, additionally, the electrolyte is acidic, a further cathodic reaction will take place,

$$2H^+ \text{ (from solution)} + 2e^- \rightarrow H_2,$$

contributing to the hydrogen available at the cathode surface for the phase boundary reaction. The titanium, being more cathodic than the other metal in the first place, will suffer more severely from this. It has been reported that a rapid increase in hydrogen absorption occurs at a voltage more negative than -700 mV relative to a saturated calomel electrode[19]. The absorption also becomes much more rapid at temperatures over 100°C. Hence the problem with cathodic protection in heat exchangers.

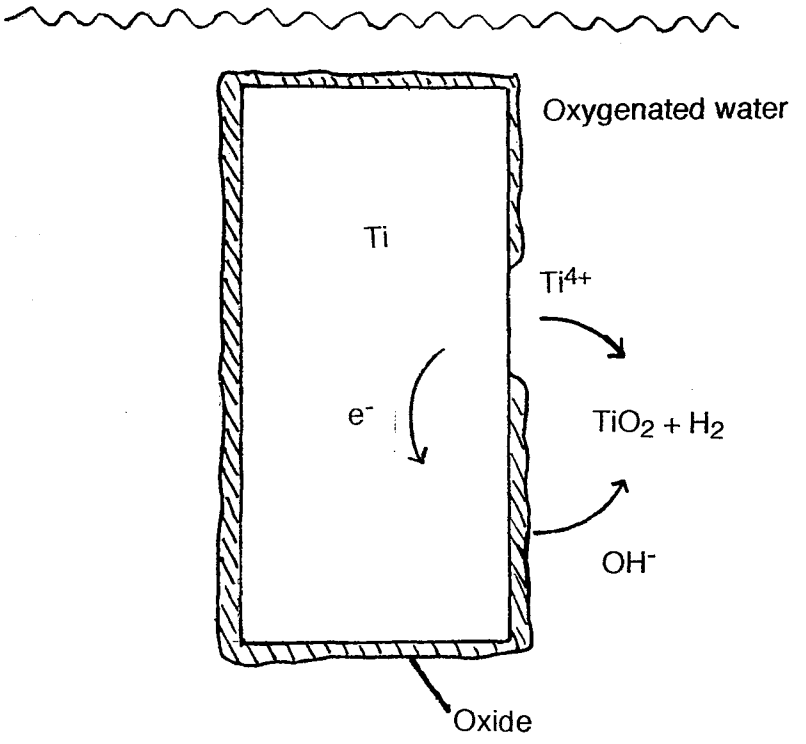

Fig. 2.2 Galvanic corrosion of an oxidised titanium surface

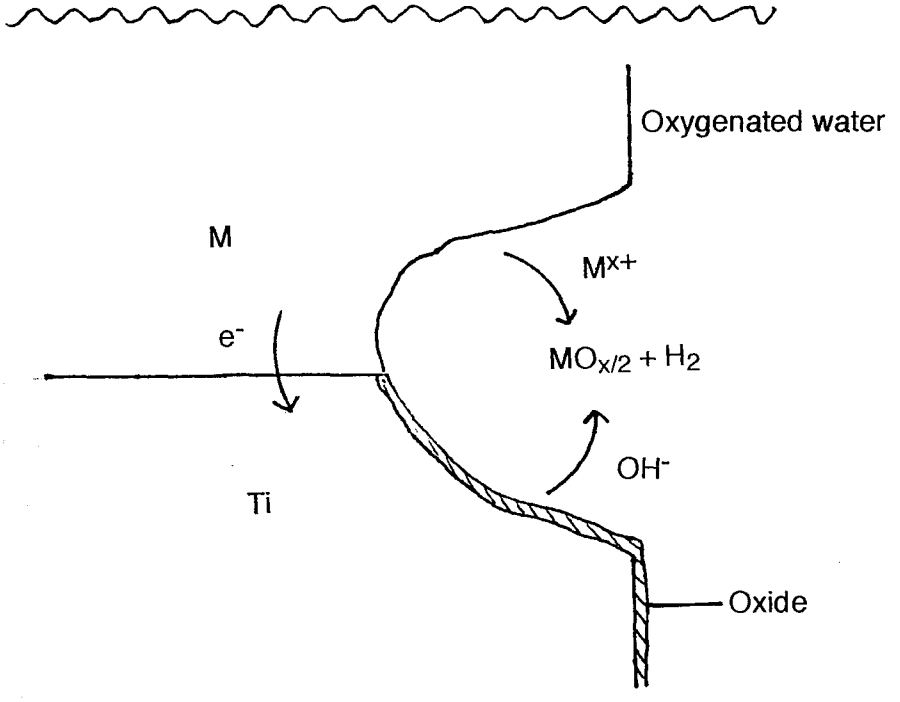

Fig. 2.3 Galvanic corrosion of a titanium-metal couple occurring in a crevice

Hydrogen contamination has also been reported to occur through acidic electropolishing or electrothinning procedures[27, 28], though in this case the acidic environment cannot be to blame because the metal is anodic, and therefore the contamination presumably originates from hydrogen gas evolved at the cathode going into solution. It has also been suggested, however, that in these cases the entry of hydrogen into the material occurs at the earlier stage of mechanical grinding, during which the continual creation of fresh metal surfaces in the presence of water allows the continuation of the reaction

$$Ti + 2H_2O \rightarrow TiO_2 + 2H_2$$[29].

Hydrogen can also be absorbed from the gas phase, but this generally does not seem to have been a problem except at temperatures in excess of 250°C[19], whereas embrittlement due to reactions in solution has often been reported at much lower temperatures. The reason for this might just be that the concentrations of hydrogen at the sample surfaces in cathodic solution reactions correspond to effective hydrogen pressures far higher than those usually encountered in gaseous situations[23], but it is also likely that the protective influence of oxide films is significant in determining the hydrogen uptake in these various situations. In the case of a perfectly clean titanium surface, the rate of absorption is controlled only by the hydrogen pressure and the diffusion rate in the metal. Oxide films, which will be discussed further below, retard the absorption. The region of stability of the oxide film in terms of pH and potential is given in the Pourbaix diagram for titanium (fig. 2.4), after Jaffee[30]. It can be seen that the oxide is removed at lower pH values and more negative potentials, hence under appropriate electrochemical conditions hydrogen absorption is also expected to be facilitated by this means.

2.7 Reaction of Titanium with Oxygen

The principal oxide formed on titanium is TiO_2 (rutile), and it forms a surface layer coherent with α titanium. A high free energy of oxidation produces a chemically stable and almost stoichiometric oxide as is also found in the cases of aluminium, chromium and

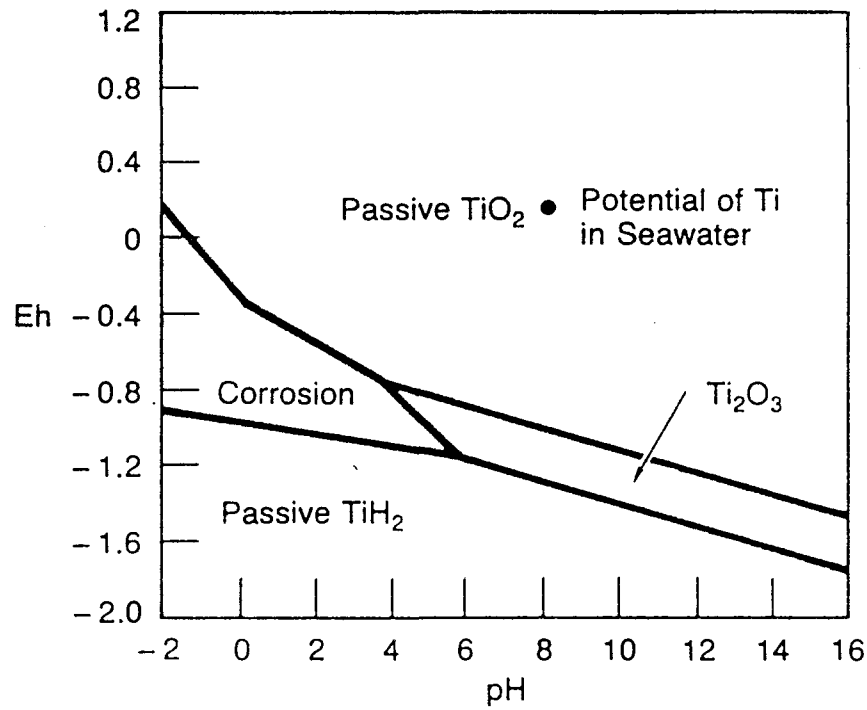

Fig. 2.4 Pourbaix diagram for titanium, after Jaffee[30]

beryllium, and, also in common with these metals, the Pilling-Bedworth criterion is satisfied, meaning that the specific volume of the oxide is slightly greater than that of the metal[26]. Thus the scale that forms is compact and dense, with pores closed up, and it grows downward at the oxide-metal interface by the movement of oxygen ions through the scale[31]. These factors contribute to the tenacity of the oxide layer and the high corrosion resistance of titanium.

The rate of growth of the oxide scale is dependent on temperature, but the kinetics of the oxidation process show different rate laws at different temperatures[32, 33]. Above about 350°C the oxidation rate is limited by the thermal diffusion of oxygen ions through the oxide and the square of the growth rate of the oxide film is inversely proportional to time (parabolic rate law). At lower temperatures the thermal energy of the oxygen ions is insufficient to allow them to overcome the activation energy barrier for diffusion in significant numbers, and the oxidation rate becomes controlled by the electrostatic effect of charge build-up on the oxide surface, the potential due to which can help a proportion of the oxygen ions to overcome the activation energy barrier. Under these circumstances the rate of growth of the film is proportional to the logarithm of the time, because growth of the film rapidly attenuates the effect of the static field, and thus for temperatures in this range there will be a limiting scale thickness that will be achieved after a sufficiently long period. At room temperature this thickness is only of the order of about 4 nm[34].

In both temperature regions the ingress of oxygen is thought to be by the movement of oxygen ions. There must therefore be an electron current outward through the scale in order to maintain the supply of ions at the surface[35]. The oxide growth rate is therefore influenced by the conductivity of rutile. Rutile is thought to be an anion defect conductor, in which conduction depends on vacancies in the oxygen sub-lattice, and therefore replacement of titanium ions with metallic ions of a higher valency would be expected to increase the conductivity of the scale, resulting in faster scale growth and greater ultimate scale thickness[36].

2.8 The Diffusion of Hydrogen in Titanium

Clearly the state of an oxide-free sample of titanium absorbing hydrogen will depend on both the equilibrium solubility of hydrogen and on the diffusion rates through the metal and hydride layer.

Diffusion in one dimension is described by the differential equation

$$\partial C/\partial t = D\partial^2 C/\partial x^2$$

where C is the concentration of the diffusing substance at position x and time t, an D is the diffusion coefficient, given by

$$D = A \exp(-Q/RT).$$

Wasilewski & Kehl[37] found that for the diffusion of hydrogen from the gas phase into α and β titanium respectively,

$$A_\alpha = 1.8 \times 10^{-6}\ m^2/s, \qquad Q_\alpha = 516\ J/kg\ mol,$$

$$A_\beta = 1.95 \times 10^{-7}\ m^2/s, \qquad Q_\beta = 277\ J/kg\ mol.$$

These results were obtained by measurements between 500 and 824 °C. Assuming that they can be extrapolated outside this range, and also assuming that grain boundary diffusion is not significant, we obtain that at 300 K

$$D_\alpha = 1.7 \times 10^{-15}\ m^2/s,$$

$$D_\beta = 2.8 \times 10^{-12} m^2/s.$$

Thus at room temperature the diffusion of hydrogen in β titanium is 1600 times faster than in α titanium.* The difference in diffusion rates and diffusion activation energies between the two structures was attributed by Wasilewski & Kehl to the greater interstitial space available in the BCC β structure as compared HCP α structure, 32% as compared with 26.5% of the total volume of the lattices, and also to the increased number of nearest

* It is interesting that the calculated room temperature diffusivity of hydrogen in the β phase is very similar to the room temperature diffusivity of carbon in α iron[38], another interstitial solute in a BCC metal.

neighbours in going from the tetrahedral interstitial positions in the β lattice to the octahedral interstitial positions in the α lattice.

A knowledge of the diffusion coefficients permits calculation of the rate of absorption of hydrogen from an infinite source provided that the metal remains in a single phase condition. On the appearance of a second phase the reaction rate will be influenced by the rate at which the new phase can grow. Despite this, Wasilewski & Kehl found that when there was a layer of titanium hydride on the surface of the samples, the rate of hydrogen absorption was constant. This they attributed to the fact that the hydride, having a larger specific volume than the metal from which it was formed, cracked on formation and behaved as a porous layer.

2.9 Influence of the Oxide Film on Hydrogen Absorption

In practice it is expected that the diffusion rate of hydrogen in the oxide film as well as the diffusion rate of hydrogen in the metal will affect the hydrogen uptake in titanium. The diffusivity of hydrogen in rutile has been measured by Caskey, who has reported that it varies greatly with direction in the lattice[39]. Rutile has a tetragonal structure with a = 0.459 nm, c = 0.295 nm[40]. The room temperature diffusivity is about 10^{-20} m^2/s parallel to the a axis, and about 10^{-16} m^2/s parallel to the c axis (c. f. about 10^{-15} m^2/s in α titanium). Thus, bearing in mind the epitaxial relationship that exists between the metal and the oxide, a preferred orientation in the metal could have a large influence on the hydrogen absorption rate via the orientation of the oxide.

Cold-rolled titanium sheet shows a strong texture with the basal plane (0001) rotated 40° towards the transverse direction about an axis in the rolling plane, and with the $(10\bar{1}0)$ plane parallel to the rolling direction[36]. Consequently, the oxide film is likely to be preferentially orientated with its a axis at 40° to the perpendicular to the plane of the sheet. A film of this orientation is expected to be less permeable to hydrogen than one based on random metal grain orientations. This has been confirmed by Fukuzawa et al.[41],

who have found that the absorption of hydrogen is faster in annealed samples than in as-rolled ones.

2.10 The Hydrogen-Titanium System

The hydrogen-titanium system is typical of gas-metal systems in that, so long as the temperature is high enough to permit finite reaction rates, alloys between the gas and the metal can only exist in equilibrium with a gaseous hydrogen atmosphere whose pressure is a function of temperature and the hydrogen concentration in the metal. This is the basis of the method that has been used to deduce the phase-diagram. Mc.Quillan[42] and others have measured the quantity of hydrogen absorbed by titanium in equilibrium with an atmosphere as a function of the pressure for a range of different temperatures. Curves of the type shown in fig. 2.5 are obtained. It follows from the phase rule,

$$P + F = C + 2,$$

where P is the number of phases, F is the number of degrees of freedom and C is the number of components, that in a single-phase region the composition will be dependent on pressure for a given temperature, while in a two-phase region the composition will be independent of pressure. Hence the phase boundaries can be deduced from fig. 2.5 since the curved parts of the graph must represent single-phase regions.

The phase diagram, as assessed from the work of various authors by San Martin & Manchester[43] is given in fig. 2.6. The phase boundaries represented by solid lines were determined by the phase rule method; at lower temperatures the gas-metal reaction becomes too slow to attain equilibrium in a reasonable time, and the dotted boundaries have been inferred by linear extrapolation of the temperature-concentration-pressure data. The $\alpha/\alpha+\delta$ phase boundary has been determined from metallographic studies.

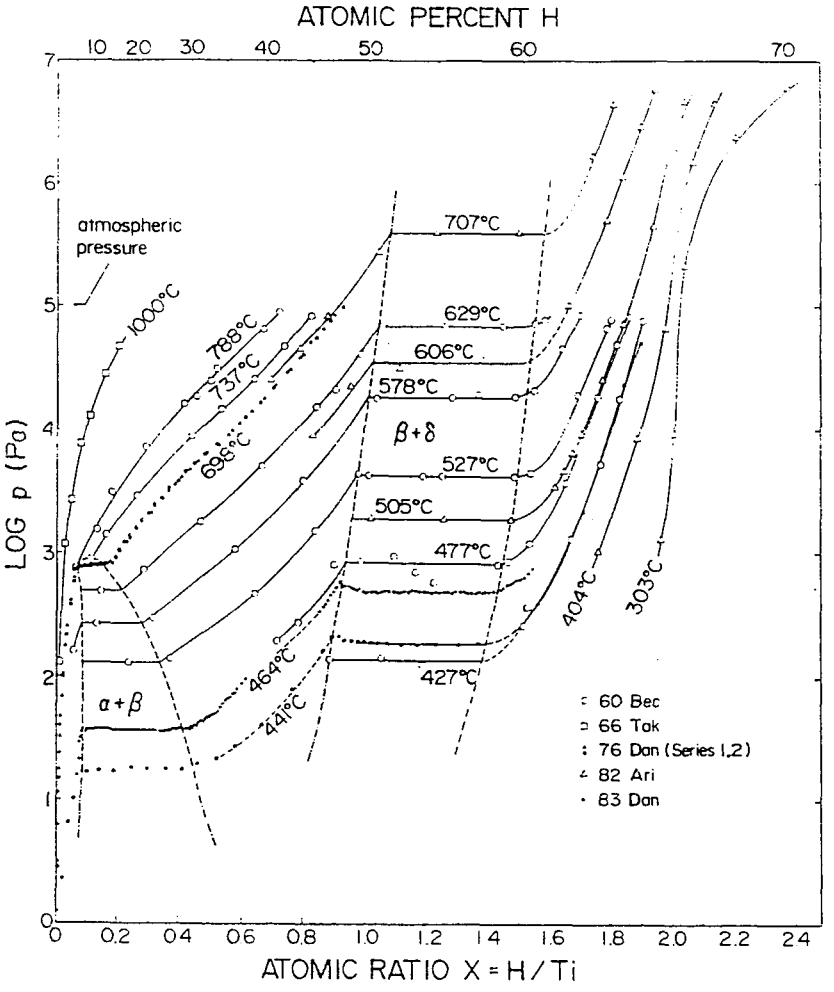

Fig. 2.5 Isothermal pressure/concentration curves for the hydrogen-titanium system, compiled from the results of various workers by San-Martin & Manchester[43]

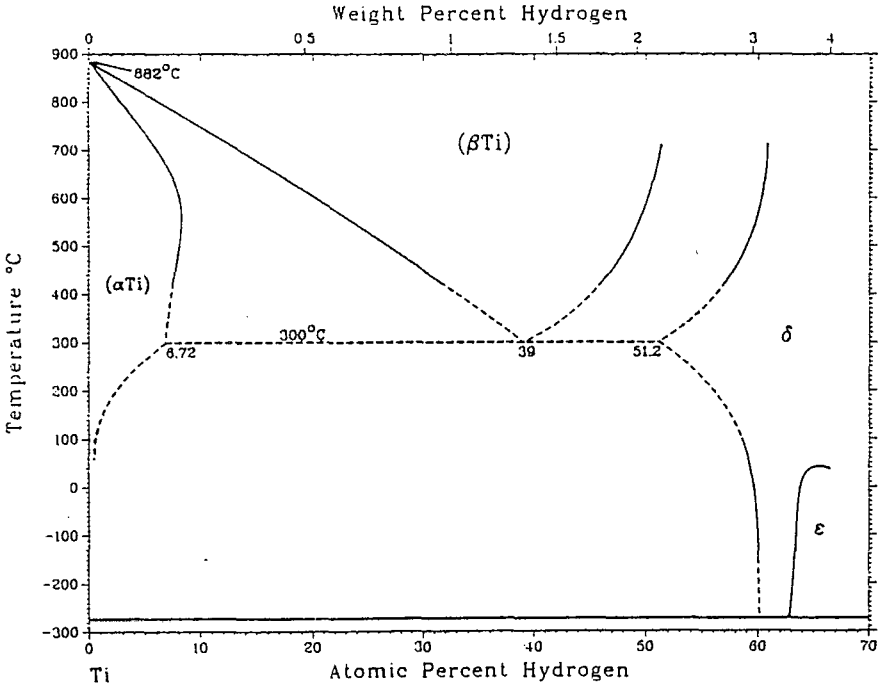

Fig. 2.6 Titanium-hydrogen phase diagram, compiled from the results of various workers by San-Martin & Manchester[43]

The phase diagram[is] of the eutectoid type. The equilibrium hydride phase δ^* is an ordered compound which is stable over the composition range $TiH_{1.53}$ to $TiH_{1.99}$. For the purposes of this study the most important feature is the location of the $\alpha/\alpha+\delta$ phase boundary. This gives the equilibrium solubility of hydrogen in α titanium. It can be seen that this decreases markedly at temperatures below the eutectoid, and at 125 °C it lies between 0.05 and 0.14 at.% (500 and 1400 ppm).

The stabilisation of the β phase by dissolved hydrogen has been explained in terms of the size of the interstitial sites in α and β titanium[37]. The interstitial sites in the α structure are of two types: tetrahedral, having a radius of 0.034 nm, and octahedral, having a radius of 0.062 nm. Those in the β structure are all tetrahedral, and have a radius of 0.044 nm (fig. 2.7). The hydrogen atom, of radius 0.041 nm, probably does not occupy the tetrahedral positions in the α structure, since that would lead to considerable distortion of the lattice and to a large change in the hardness, which is not seen. Therefore it occupies the octahedral sites, in which it will have a higher free energy than in the β phase tetrahedral sites, owing to the greater freedom of vibration, and this causes the transformation to the β phase at lower temperatures than would otherwise occur.

The solubility of hydrogen in α titanium is quite low, of the order of 20-200 ppm at room temperature[46]. This concentration, however, causes a measurable dilation of the lattice as seen by X-ray diffraction. The solubility of hydrogen in β titanium is much greater[47]. The greater hydrogen solubility reduces the tendency for hydrides to

* The nomenclature for the titanium-hydrogen phase diagram varies between different sources. In older work the designation γ is generally used for the whole hydride field, but some authors[44,45] have adopted the letter δ to indicate the tetragonal modification of the cubic structure (see below). San-Martin & Manchester have used γ for the metastable TiH phase and δ and ε for the cubic and tetragonal equilibrium hydride phases respectively. These changes have been in order to bring the nomenclature for the titanium-hydrogen system into line with that for the isostructural zirconium-hydrogen system.

α Titanium (HCP)

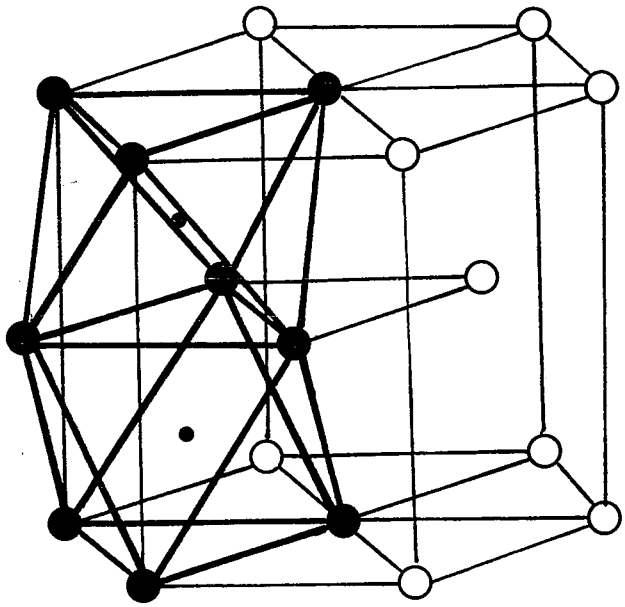

β Titanium (BCC)

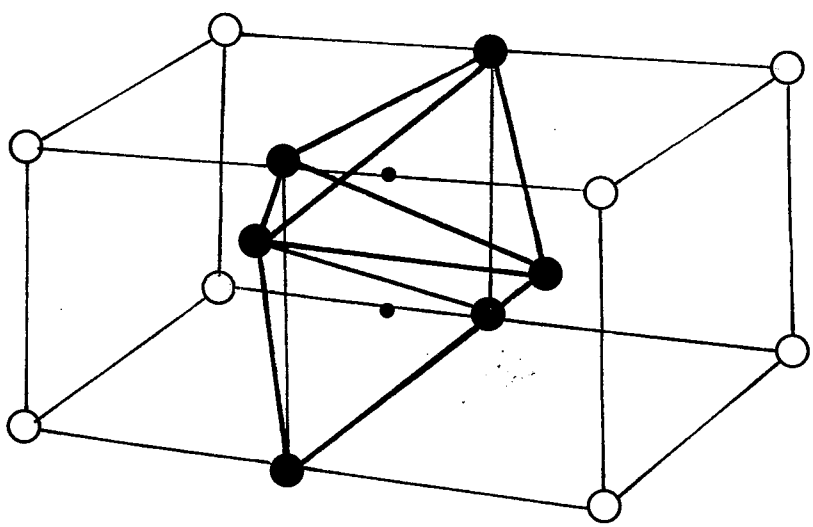

Fig. 2.7 Interstitial sites in α and β titanium lattices

precipitate in β-stabilised alloys such as Ti-V and Ti-Mo[48, 49]. These alloys have been observed to be better at resisting embrittlement than pure titanium. This is preliminary evidence that the embrittlement may be due to hydrides.

More than 4000 ppm hydrogen are soluble in a Ti-18Mo alloy at room temperature[47]. There is an increase in the lattice parameter but no measurable change in the strength or ductility. This is strong evidence that hydrogen dissolved in the β titanium lattice has no effect on mechanical properties. At extremely high hydrogen concentrations (>10000 ppm), catastrophic embrittlement occurs without the preciptation of hydrides. This may be due to electronic effects leading to a weakening of the metallic bond. The solubility of hydrogen in the β phase cannot be exactly specified because the alloys disintegrate before hydride formation is observed.

2.11 Titanium Hydride

Titanium hydride has the fluorite structure, consisting of an FCC arrangement of titanium atoms with hydrogen atoms at the tetrahedral interstices[50]. At higher hydrogen concentrations or lower temperatures this becomes modified to a structure which can be regarded either as face-centred tetragonal with c/a ≈ 0.95 or body-centered tetragonal with c/a ≈ 1.3, the exact ratio depending on the composition[51, 52]. The transformation temperature has a maximum of 40°C at compositions close to TiH_2, but descends rapidly for compositions below $TiH_{1.8}$, so that hydrides of these compositions are effectively always cubic[53, 54].

There is some evidence for the existence of a metastable phase of composition TiH, which has been reported as having an FCT structure with c/a about 0.88, and which may form in β alloys under some circumstances[28,55]. This phase is probably isostructural with γ zirconium hydride.

The equilibrium titanium hydride is typical of the "pseudo-metallic hydrides" formed by group IIIA, IVA and VA transition metals[56]. In general they are non-stoichiometric, and their bonding is thought to be partially ionic and partially metallic in nature. The maximum hydrogen to metal ratio is two, and non-stoichiometry is accommodated by hydrogen vacancies.

The mechanical properties of titanium hydride have been tested by Irving & Beevers[57] at various stoichiometries and temperatures. They found that the yield stress increased with decreasing temperature and with increasing hydrogen vacancy content. The temperature dependence of the yield stress became greater at higher vacancy contents. The slip plane was found to be {111} in cubic hydrides. The yield stress was found to be rather strain-rate dependent, increasing with increasing strain rate to maximum at a strain rate of 10^{-1}/s. At higher strain rates fracture occured without a yield point being reached, and the fracture stress fell with increasing strain rate. The plasticity was found to be about 3% for $TiH_{1.75}$ at room temperature. The authors attributed all the effects of temperature, vacancy concentration and strain rate to the effect of these factors on hydrogen ion mobility. These facts may or may not be relevant to the failure of hydrogen-embrittled titanium, since it is not certain in that system whether the cracks proceed through the hydride or through the metal, though the cracking is certainly closely linked to the presence of hydrides, as will be discussed.

2.12 Hydrides in Titanium

Hydrides in titanum take the form of plate-like precipitates on particular habit planes in the matrix, though viewed metallographically or in thin foils the precipitates usually appear as needles. The habit planes were determined by Liu & Steinberg[58] as $\{10\bar{1}0\}$ and $\{10\bar{1}1\}$ for both pure titanium and Ti-2V alloy. More recently, a near-basal habit plane has also been reported, which has been variously indexed between $\{10\bar{1}5\}$ and $\{10\bar{1}9\}$[59]. The two habit planes found by Liu & Steinberg fall on two of the three possible slip planes for titanium at room temperature. They suggested that this might give rise to a

shortened nucleation period for the slip process, which would not affect the static or slow strain rate properties of the material, but which would be noticeable in short duration tests such as impact tests. The near-basal habit plane is also near a matrix slip plane, but the reason for the small deviation from {0001} is not clear. Willams[60] suggests that fine hydrides sometimes occur in "sheafs" which are resolvable using transmission electron microscopy, but which in optical analysis appear as a single large hydride on an irrational lattice plane, though the individual hydrides actually lie on rational lattice planes.

Sanderson & Scully[61] have examined FCC hydrides formed in Ti-5Al-2.5Sn and four binary Ti-Al alloys using transmission electron microscopy and electron diffraction and have obtained the following orientation relationships:

$\{0001\}_{metal}\|\{010\}_{hydride}$, $\quad <1\bar{2}10>_{metal}\|<110>_{hydride}$

and

$\{0001\}_{metal}\|\{112\}_{hydride}$, $\quad <1\bar{2}10>_{metal}\|<110>_{hydride}$.

Boyd[62] has added a third from observations of precipitation in Ti-8Al-1Mo-1V:

$\{0001\}_{metal}\|\{110\}_{hydride}$, $\quad <1\bar{2}10>_{metal}\|<110>_{hydride}$.

Hall[63], however, only reported one, different, orientation relationship in Ti-6Al-4V:

$\{0001\}_{metal}\|\{001\}_{hydride}$, $\quad <01\bar{1}0>_{metal}\|<110>_{hydride}$

Boyd only reported the $\{10\bar{1}0\}$ type of habit plane, but Hall reported $\{10\bar{1}0\}$ and $\{10\bar{1}1\}$ in differently heat-treated materials, and also precipitates on a near-basal habit that were found to consist of sub-platelets of the $\{10\bar{1}1\}$ type. The different orientation relationship found by Hall may be explained by his alloy being the most β-stabilised. There is some evidence that the orientation relationships found depend on the hydrogen-charging conditions, a greater range of orientations being observed at higher charging temperatures, although whether charging is done from the gas phase or electrochemically does not seem to affect the results[62].

The misfit between the lattice parameters of the metal and the hydride results in non-coherent precipitation. This has been shown by transmission electron microscopy, which reveals misfit dislocations along the broad interface between the metal and the hydride needles or plates[46]. These dislocations are of opposite signs on opposite sides of the plates. There are also loops of dislocations punched out into the matrix at the ends of the hydrides. If the foil is heated, the hydride partially re-dissolves. Its volume then diminishes and the loops collapse back into the hydride. This process is reversible under conditions of heating and cooling.

Paton et al.[64] have suggested that the greater hydrogen solubility in titanium-aluminium alloys as compared with pure titanium is due to the increase in matrix strength due to solid solution strengthening. This increases both the elastic stresses associated with hydride growth and the plastic work done in loop-punching.

2.13 Effects of Hydrogen on Mechanical Properties

2.13.1 Tensile Properties

Investigators in this field have generally concluded that embrittlement in titanium and its alloys is greatest at the fast and slow extremes of strain rate employed in mechanical tests. Embrittlement has been reported as being more severe in pure α titanium than in two phase $\alpha+\beta$ alloys.

Beevers & Edmonds[65] have shown that increasing the grain size or decreasing the temperature increases the degree of embrittlement in α titanium. From careful metallographic observations of the hydride precipitates they concluded that the reasons for these facts were: 1) that larger metal grains allow the growth of longer hydride platelets leading to more continuous brittle paths through the material, increasing the area subject to brittle fracture, and, 2) that at higher temperatures plastic deformation of the platelets occurs rather than fracture. They thus associated brittle fracture of the material

always with the nucleation of cracks in the hydride platelets, the connection with temperature and grain size being indirect and due to the influence of these parameters on the platelets.

The samples in these experiments were charged from the gas phase to a range of hydrogen concentrations using a modified Sievert's apparatus. Particularly convincing are the optical micrographs of secondary cracks (etched) near the fracture surface taken at -200°C. They can be seen to run along paths connecting up large numbers of platelets, though on this scale it cannot be seen whether the actual hydrides crack, as the authors assert, or whether the crack is at the interface between metal and hydride.

Also given are scanning electron micrographs of fracture surfaces formed at 150°C and above in which the platelets can be seen to be severely deformed, the matrix failing by void growth leaving the platelets protruding from the fracture surface. This is evidence that the temperature dependence of embrittlement may be linked to the deformation properties of the hydride.

It has been suggested by Paton and Williams[47] that the detrimental effect of high strain rates is due to the fracture stress of titanium hydride being lower at higher strain rates. At low strain rates hydride cracking would be lessened, hence they make the suggestion that during low strain rate embrittlement the stress-induced diffusion of hydrogen to form new hydrides at crack tips is taking place. This theory will be discussed in more detail later. The consequence is that at sufficiently low strain rates the cracking process becomes diffusion controlled, and since the test time is long, the growth in the number of hydrides is able to outweigh the effect of their increased fracture stress.

Evidence adduced by Paton & Willams in support of these ideas is the results of mechanical testing of bulk titanium hydride by Beevers & Edmonds[65]. However, the results of these workers, which appear to be the only ones avaliable on the subject, do not

really support Paton & Williams' conclusions because 1) the change in the yield stress with strain rate is not in the same direction over the entire range of strain rate, 2) the fracture stress of the hydride, which is likely to be the most important parameter if the hydrides are to be considered as crack nuclei, has not been reported except for cases in which fracture occurred without yield, so the general relationship between fracture and yield stresses is unknown, and 3) it is in any case doubtful whether the results of tests on bulk samples of the hydride can be simply applied to the much more complex situation in which hydrides are present as precipitates in the metal, with perhaps stress-induced diffusion, precipitation and cracking of hydrides occurring simultaneously.

Williams[66] has made tensile tests on the α-β alloy Ti-2Mo-2Fe-2Cr at a range of strain rates and at temperatures from 100K to 400K (fig. 2.8). At the fastest stain rate there is no embrittlement, but at lower strain rates there is a sharp minimum in the ductility at 250K. Lower strain rates still broaden the temperature range of the embrittlement.

The lack of embrittlement above about 300K has been attributed by Williams to the increasing solubility of hydrogen in the alloy and hence lesser tendency of hydrides to nucleate, but in the light of the observation of Beevers and Edmonds that the hydrides are noticably more plastic at room temperature than at lower temperatures, this alternative or additional explanation also suggests itself. The reduced embrittlement at very low temperatures (<150K) presumably points to the kinetics for hydride growth being slow, though the driving force for nucleation is high. The lower the strain rate, the less important the growth kinetics will become and the greater should be the embrittlement at low temperatures, which is what is observed.

These explanations require that the material be supersaturated with respect to hydrogen before embrittlement occurs. The basic discrepancy has been pointed out by Paton and Williams[47] that the published solubility data for various alloys give higher hydrogen concentrations than some which have been shown to result in slow strain rate

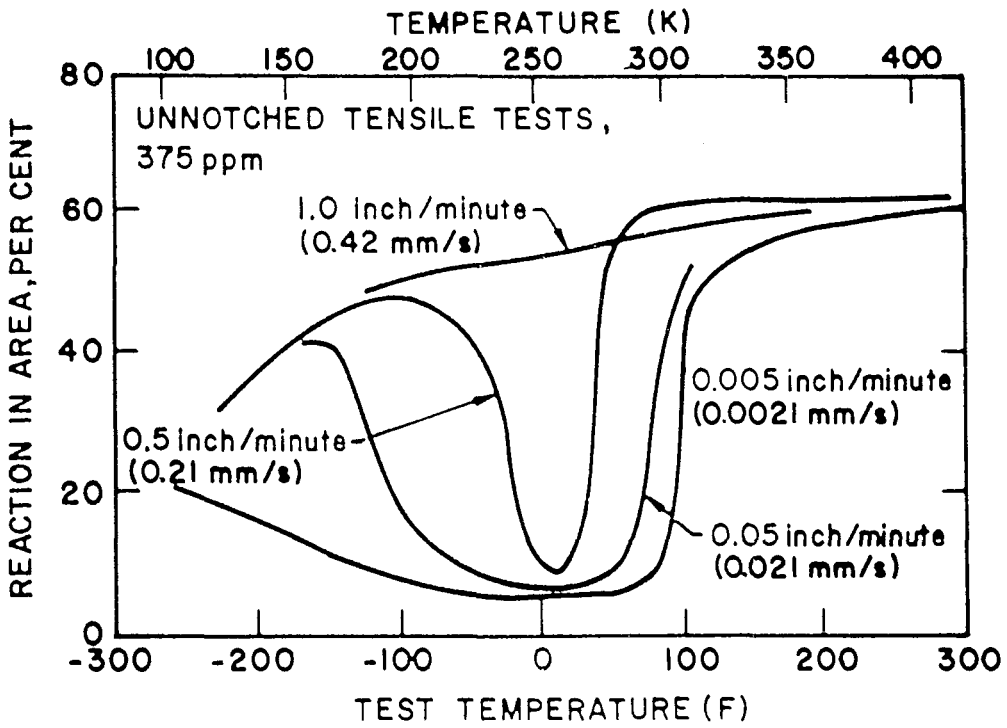

Fig 2.8 Reduction in area against temperature for various strain rates in tensile tests on Ti-2Mo-2Fe-2Cr, after Williams[66]

embrittlement, with precipitation of hydrides. This has led them to the conclusion that it is necessary to consider the effects of stress on the solubility of hydrogen in the microscopic crack-tip region. These effects are linked to the diffusion-controlled precipitation of hydrides in slow strain rate tests, and will be described in detail later.

The lesser embrittlement observed in two-phase $\alpha+\beta$ alloys is probably due to the higher hydrogen solubility in the β phase leading to less embrittlement of this phase. Ti-6Al-4V has been tested by Williams[66] at various strain rates and with up to 800ppm hydrogen. There was found to be no embrittlement up to at least 600 ppm in finer-grained samples. However, coarser grained acicular samples showed embrittlement at 300ppm. No explanation was advanced for this microstructural dependence; however, it would seem likely that the larger grain size in the acicular material allowed longer hydride crack paths, in line with the observations of Beevers and Edmonds.

The effect of the orientation of the hydrides on the tensile properties of samples has been studied by Nishigaki et al.[67]. They used commercial purity titanium which was hydrided electrochemically in a dilute sulphuric acid solution and then homogenised by heating at 400°C for an hour in air. Some of the samples were furnace cooled from 400°C which created a random hydride orientation. The rest had a stress of 6.6 MPa, equivalent to 80% of the yield stress at 300°C, applied in tension when the samples had cooled to that temperature. This resulted in most of the hydrides being precipitated perpendicular to the loading direction. This was to be expected in view of the size misfit between the metal and hydride (the hydride being some 18% greater in volume) and the tendency of a tensile stress to relieve the back stresses that otherwise inhibit hydride growth.

It was found that the tensile and yield strengths were little affected by any of the treatments, but that the ductility was seriously reduced by the formation of the hydrides and was worst in the the samples with oriented hydrides. This is consistent with the view that cracks proceed along hydrides, since clearly a preferred crack direction

perpendicular to the tensile axis will cause failure sooner than a selection of randomly-oriented preferred cracking directions. This result is important since this type of hydride precipitation could well arise in practice when a component is subjected to a tensile stress, albeit in a much less extreme form.

2.13.2 Sustained Load Tolerance

Various titanium alloys have been reported to suffer from sustained load cracking. This phenomenon is probably in essence the same as slow strain rate embrittlement at the limiting case of zero strain rate. The experiments have usually been conducted by loading samples for long periods in corrosive media, so that hydriding occurs under loaded conditions, and are thus rather similar to stress corrosion cracking experiments, which will be discussed later.

Williams[68] has studied the cracking of the α-β alloys Ti-4Al-1.5Mo-0.5V and Ti-4Al-3Mo-1V using cantilever bend samples which were fatigue cracked and then statically loaded for up to 10,000 minutes in a 3.5% NaCl solution. Meyn & Sandoz[69] have performed similar experiments using Ti-6Al-1Mo-1V, Ti-5Al-2.5Sn, Ti-7Al-1Mo-1V and pure titanium in a wide variety of environments including alcohols, hydrocarbon gases and carbon tetrachloride as well as aqueous solutions.

The media in which the critical stress intensities for crack propagation were reported to be lowest were salt water, methanol and ethylene glycol. The critical stress intensities were not found to be much dependent on the grain size of the samples. It was observed that cleavage was the dominant mode of fracture, and that flat, sharply defined cleavage surfaces were more commonly observed on samples that had been cracked in those environments that gave low values for the critical stress intensity. The proportion of cleavage became less, and became mixed with a higher proportion of ductile fracture modes (dimples and so on), as the applied stress intensity was increased.

In two phase alloys, cleavage was always in the α phase, the β phase failing by ductile tearing, and correspondingly alloys containing a continuous network of β phase seemed to be better at resisting cracking. Thus the β phase in the alloys seems to be a crack arrester. Since the evidence is that the β phase does not itself become embrittled, cracks moving into this phase from the α are likely to become blunted because of the increased propensity for slip.

Meyn & Sandoz reported that the cleavage plane in the α phase was invariably oriented at 15° from the (0001) plane, but their data was not good enough to assign indices. The 15° cleavage plane may correspond with the near-basal habit plane that has sometimes been reported for titanium hydride.

The varied media in which sustained load cracking has been observed seem to support the proposition that hydrogen is the responsible species, since it is the only common factor. The largest effect reported[70] has been in the α-β alloy Ti-6Al-4V where very small amounts of hydrogen (<50 ppm) have been said to result in a 20% reduction in fracture toughness. This is surprising in view of the high tolerance to hydrogen that was reported by Williams for slow strain rate tests on this alloy, and perhaps indicates that in circumstances in which a slow but continuous supply of hydrogen is available at the surface, alloys containing higher proportions of the β phase will be at a disadvantage because the enhanced diffusion in the β phase will allow a more even distribution of hydrogen in the bulk. This rule would only apply up to a certain point, since a largely β alloy would not be able to precipitate enough hydride for continuous or near-continuous crack paths to occur, in line with the observations of Meyn & Sandoz.

Although most of the work in this area has been done on α-β alloys, the normal morphology of the α/β interfaces tends to mask the presence of hydrides, so that hydrides are easier to observe in single-phase alloys. Such observations have been reported by Paton & Williams[47] for the α phase alloy Ti-4Al. Compact tension specimens were

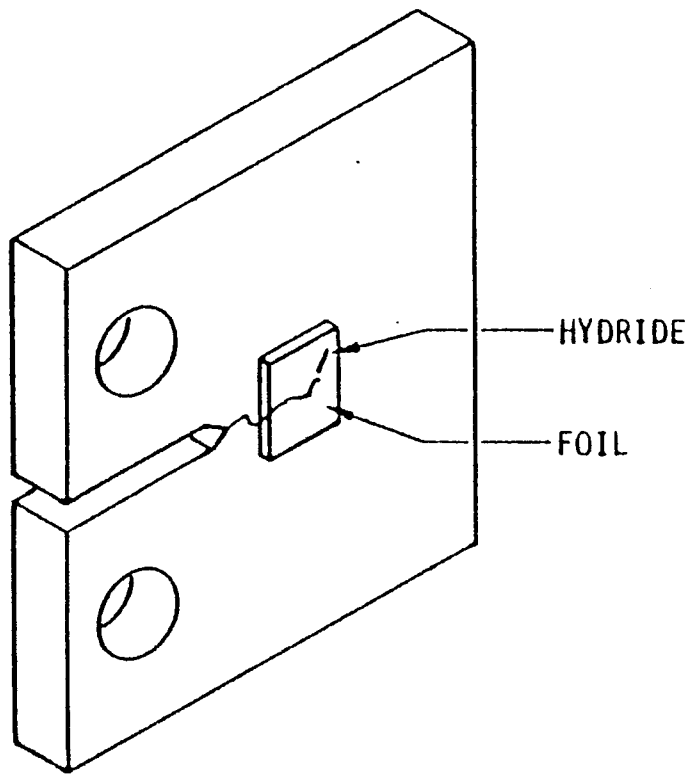

Fig. 2.9 Hydride formation ahead of crack front in compact tension specimen of Ti-4Al, after Paton & Williams[47]

employed as shown in fig. 2.9. They were cracked using a sustained load and then foils were prepared from the region of the crack tip. Precipitates were observed ahead of the crack front which were identified as hydrides by means of imaging with a hydride reflection. The overall hydrogen concentration in this alloy was only 100 ppm, far below solubility limits reported elsewhere for titanium-aluminium alloys[71]. Therefore these hydrides may have been the result of higher local hydrogen concentrations, or the reported hydrogen solubility in these alloys might, as Paton & Williams suggest, represent a non-equilibrium limit that is influenced by the matrix strength barrier that has to be overcome by precipitating hydrides. In the vicinity of a crack tip, hydrostatic tension may lessen this effect and reduce the solubility towards a lower equilibrium value, though the effects are probably more complicated than this owing to the fact that the equilibrium solubility itself is probably not independent of stress, as will be discussed later.

2.13.3 Enhanced Room-Temperature Creep

This has been reported by Paton and Williams[47] for the alloy Ti-5Al-2.5Sn. This was charged with hydrogen from the gas phase using Sievert's apparatus. It was found that samples with hydrogen contents greater than 200 ppm exhibited higher creep rates. The authors speculate that this is due to the stress-induced nucleation and growth of hydrides, the larger specific volume of the hydride relative to the metal accounting for the increased creep. In addition, the punched-out dislocation loops around growing hydrides might also contribute to the creep strain.

Transmission electron microscopy was performed on specimens containing varying quantities of hydrogen that had been subjected to comparable creep exposures. The specimens containing more than 200ppm hydrogen exhibited massive hydrides, whereas those containing less than 100 ppm were hydride-free.

Grimm & Nowak[72] have performed stress rupture tests on notched tensile spcimens of Ti-6Al-6V-2Sn. The material was rolled below the α-β transus to obtain a fine-grained $\alpha+\beta$

microstructure, and the specimens were hydrogen charged to contents ranging from 56 to 1039 ppm cathodically in a sulphuric acid solution. They were dead-weight loaded in a creep rupture testing machine to various load levels and the times to rupture were recorded. Macroscopic examination of the fracture surfaces indicated a ductile mode of failure for all specimens having hydrogen contents of 550 ppm or less and a brittle mode for those containing more hydrogen than this.

Similar stress rupture tests have been performed by Reisen & Kah[73] on unnotched samples of Ti-6Al-4V, with hydrogen contents from 110 to 300 ppm. Severe embrittlement was encountered above 240 ppm. It is noticable that the hydrogen tolerance levels quoted by the various authors for creep experiments on α–β alloys show a correlation with the proportion of the β stabiliser, vanadium, in the alloys. The highest tolerance has been reported for the most β-stabilised alloy, Ti-6Al-6V-2Sn, indicating probably the higher hydrogen solubility in the β phase, and the tendency of the β phase to arrest cracks.

2.13.4 Fatigue

There is limited data on the effect of hydrogen on the fatigue properties of titanium alloys. It has, however, been stated that unnotched fatigue life is not reduced by up to 140 ppm hydrogen in high purity α titanium[74]. This result was obtained using tension-compression tests and it might differ from that obtained using more conventional tests which employ tension-tension loading, since continuous tension would create a situation more akin to a creep test, in which the continuous stress-induced nucleation of hydrides would be possible so long as the material remains supersaturated with respect to hydrogen.

Data on Ti-6Al-4V indicate that moderate interstitial quantities of hydrogen are actually beneficial to unnotched fatigue strength[75]. There appears to be no information on the effects of hydrogen on crack growth rates in fatigue situations though this information

would be useful to designers. The component of this EURAM project carried out at VTT (Finland) has been attempting to rectify this situation.

2.13.5 Stress Corrosion Cracking

There is evidence that hydrogen is responsible for various cases of stress corrosion cracking, though the association between hydrogen and SCC is not invariable. The most extensively studied area is that of hot sodium chloride solutions. In these there is general agreement that hydrogen plays the major role in promoting cracking of titanium and its alloys.

Gray[76] has used ion and laser microprobes to show that the concentration of hydrogen is greater at the surface of a hot salt SCC fracture than elsewhere in the specimen: up to 10,000 ppm. On cooling to room temperature a loss of ductility remains, indicating the formation of a reaction product while hot. If the specimens are then vacuum annealed at 500°C their ductility is restored. This reversibility is, as has been already noted, characteristic of the presence of hydrogen in titanium, though whether in the form of hydride or dissolved hydrogen was not, in this case, proved. There was found to be a threshold for hot salt stress corrosion cracking which was very dependent on microstructure, alloy composition and surface condition.

The cracking of titanium in various other liquids has also been studied. In methanolic chloride solutions and at low stress intensities an intergranular fracture mode has been observed in titanium and titanium alloys[47]. There was no well defined threshold stress for this fracture mode. A hydride layer was observed along the grain boundaries in partially failed specimens. The crack propagation velocity was low, suggesting a hydrogen transport rate-controlled hydride mechanism.

At higher stress intensities, cleavage fracture has been found to occur in both aqueous and non-aqueous environments[77]. This fracture mode shows two stages with respect to K, the

stress intensity. Initially there is a linear crack velocity to K relationship, but later the velocity becomes independent of K. This dependence of the crack velocity is similar to that observed by Williams & Nelson[78] in gaseous hydrogen. However, experiments by Blackburn & Smyrl[79] on Ti-8Al-1Mo-1V in anhydrous molten salts have shown the same two stages of cracking. In this environment there is no external hydrogen available to react at the crack tip. Consequently it can still be disputed whether or not hydrogen plays the crucial role in all cases of stress corrosion cracking of titanium alloys in aqueous solutions.

2.13.6 Impact Ductility

The results of impact testing would be expected to be in a different class to the results of the other mechanical tests described, because in tests of very short duration hydrogen transport will be impossible and consequently, on the basis of the evidence already presented, no embrittlement would be expected unless hydrides are present in the sample before the test.

Most of the work in this area is Russian, and is reviewed in English by Kolachev[80]. Indeed Kolachev reports that there is a sharp reduction in the impact ductility of titanium and titanium alloys which corresponds to the hydrogen concentration at which the first massive precipitates are formed. However, he also states that some $\alpha+\beta$ alloys exhibit two concentration ranges in which their impact ductility reduces sharply. The reason for the reduction of impact ductility in the low concentration region is not clear. The effect in the high concentration range has been linked by Paton & Williams[47] to the supposed particular brittleness of titanium hydride at high strain rates. However, as noted earlier, the avaliable results on the mechanical properties of the hydride do not support such a conclusion; in particular, they have not been taken to the very high strain rates that would correspond to impact tests.

Oxygen-strengthened titanium is of widespread use in the aerospace industry, and the combined effect of hydrogen on the properties of oxygen-strengthened titanium has recently been investigated by Wasz et. al.[81]. They have reported that although oxygen does not exacerbate the loss of ductility caused by hydrogen in slow strain rate tests, it does worsen the loss of impact resistance. Oxygen is known to increase the solubility of hydrogen in titanium[82,83], but it cannot be said that enough work has been done to understand how these two elements might interact in solution.

2.14 Paton & Williams' Theory of Hydrogen Embrittlement

Having described the evidence for hydrogen embrittlement in titanium and its alloys, the leading theory that attempts to explain most of these facts will now be discussed. Paton & Williams[20, 47, 60] take it as axiomatic that hydrogen embrittlement does not occur if the hydrogen concentration is maintained below the solubility limit. An alternative view to this will be given later. Paton & Williams are interested in the circumstances in which local concentrations might rise above this level, specifically, the conditions of high triaxial stress encountered at a crack tip.

When a hydrostatic tensile stress is applied to a sample, the equilibrium solubility of hydrogen will increase, whereas when a compressive stress is applied it will decrease. This is because hydrogen in solution produces an increase in the lattice parameter, and the energetic barrier to this occuring is reduced by the application of a tensile stress. If V_H is the volume increase due to a mole of hydrogen atoms in solution and P is the hydrostatic stress, then the equilibrium hydrogen solubility is related to the unstressed equilibrium solubility by

$$C_H = C_H^0 \exp (PV_H/RT).$$

The thermodynamic consequence of this is that hydrogen will diffuse up a tensile stress gradient to regions where the solubility is higher, i.e. the energetic barrier to lattice expansion is lower. Such a stress gradient will exist in the zone of dilation behind a crack tip when a sample is strained, and hence hydrogen atoms will diffuse up the concentration

gradient to the tip (fig. 2.10). This can mean that at a crack tip the hydrogen concentration can easily pass a 150 ppm solubility limit even though the concentration in the bulk may be only 50 ppm.

However, the practical solubility limit, as opposed to the equilibrium limit, is in general affected by stress in a different manner. When α titanium containing hydrogen in solid solution is converted to the hydride there is a volume increase of about 18%. This misfit must be accommodated either by elastic strains or by plastic deformation of the matrix. In either case mechanical work must be done by the chemical energy of the phase transformation. If ΔG is the standard free energy change for the formation of the hydride from hydrogen in solid solution and W_e and W_p are respectively the elastic and plastic work done by the transformation, then the effective hydrogen solubility for the case of zero applied stress is given by

$$C_{eff}^{0} = \exp[(\Delta G + W_e + W_p)/RT],$$

where

$$\Delta G = RT \ln C_H^{0}.$$

Hence W_e and W_p both act to increase the apparent solubility. A tensile stress will assist hydride precipitation by reducing the amount of work to be done by the hydride, and this will lower the apparent solubility limit, whereas a compressive stress will increase it.

Under conditions of zero applied stress, self-stresses around a growing hydride will eventually produce a barrier to further hydride growth and a considerable degree of supersaturation of hydrogen in solid solution will be necessary for any hydrides to grow to a significant size. This is particularly true when the matrix is strengthened by alloying with elements such as aluminium. Introducing a tensile stress externally can then relieve the self-stresses permitting the hydride to grow and reducing the solubility towards the equlibrium value. Hence the tendency of slow strain rate tests to generate hydrides which then act as crack nuclei. Of course, these cracks can then attract their own hydrogen "clouds" and thus create further hydrides. Thus the cracking process can be concieved of

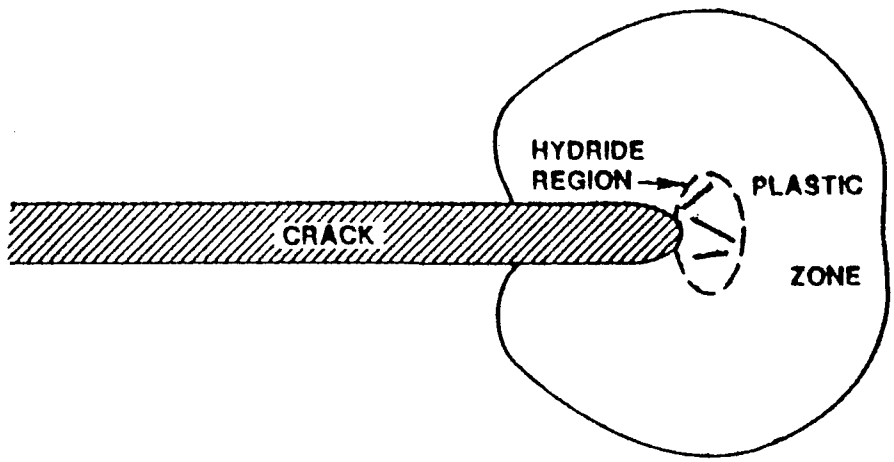

Fig. 2.10 Hydrogen cloud due to triaxial stress in crack tip region during slow crack growth

as being self-regenerating under the correct circumstances. There is direct evidence that such a cycle occurs in the cracking of some other hydride-forming metals, as will be seen later.

This theory has found experimental support in the work of Boyd[49], who has tested samples of thermally hydrogen-charged Ti-8Al-1Mo-1V and produced TEM foils which show that samples containing 400 ppm hydrogen were hydride-free before straining, but after 2-3% deformation at room temperature hydrides 8-10 nm thick were present in the foils on the $\{10\bar{1}0\}$ titanium slip planes. The conclusion from this is that the 400 ppm is a level of supersaturation which was below the practical solubility limit before the strain was imposed, but above it afterwards, and in this sense the hydrides were strain induced. It does not prove that the equilibrium solubility was altered, and an experiment that would test this part of the theory explicitly is hard to concieve of. Evidence for this effect is to be found in the observations of discontinous crack growth in non hydride-forming metals (section 2.16.2), thought to be caused by the diffusion of hydrogen up the stress gradient leading to a concentration that gives rise to atomic decohesion of the metal, and in which there are no precipitates present to complicate the situation by changing the apparent solubility limit. In the β-phase alloy Ti-8Mo-8V-3Al-2Fe, Adler and Schulte[84] have fairly convincingly demonstrated the stress-induced redistribution of solute hydrogen by concentration measurements using a lithium atomic resonance microprobe.

2.15 Embrittlement Without the Precipitation of Hydrides

The idea that this type of embrittlement exists has been promoted particularly by Russian authors. Livanov et al.[85] have drawn up a complex classification of different types of embrittlement on the basis of proposed mechanisms. This will not be reproduced as most of them can be reduced to the hydride mechanism already discussed.

However, Livanov et al. also propose that embrittlement can occur in certain alloys at hydrogen levels below the solubility limit, for example the β alloy Ti-3Al-11Cr-7Mo,

which it is claimed suffers embrittlement at 2500 ppm hydrogen, though the first precipitates are seen at 5000 ppm hydrogen.

It is conceivable that the measured dilation of the titanium lattice caused by hydrogen in solution may lead to a weakening of the metallic bond. Livanov et al., however, proffer an explanation involving interstitial hydrogen atoms interfering with the progress of dislocations through the metal. This seems to go against the commonly accepted view that there is little effect of solid solution strengthening by hydrogen atoms in titanium alloys. It might be, though, more likely in β alloys than in α alloys, on which most of the work on impurity effects has been done, because although the interstitial space in the β lattice is greater, the interstitial holes occupied by the hydrogen atoms are smaller (section 2.10), and so the interference to slip by hydrogen atoms locked at these sites may be greater, paralleling, perhaps, the influence of carbon in BCC iron. There seems to be insufficient work on this subject to decide.

Another mechanism that has been proposed to deal with some cases of embrittlement (Livanov et al., Cox & Gudas[86]) is the initiation of cracks by molecular hydrogen in voids and cavities in the material under high pressure. Cox & Gudas have put this theory forward for some cases of embrittlement of α-β alloys, pointing out that in these cases no hydrides have been observed on the fracture surfaces after the test, despite evidence of cleavage fracture. Against this it may be noted that microstructural observations of the cracking process in zirconium (to be described in the next section), another hydride-forming metal, have shown that the hydride nuclei of cracks can re-dissolve back into the matrix after complete fracture and consequent release of the tensile stress. The hydrogen bubble theory has not achieved much popularity.

2.16 Hydrogen Embrittlement in Other Metals

2.16.1 Hydride-Forming Metals

It is necessary in an account of the hydrogen embrittlement of titanium to mention some of the work that has been done on the embrittlement of other hydride-forming metals, particularly niobium, vanadium and zirconium, since study of the processes operating in these metals may well have a strong relevance to the understanding of the embrittlement of titanium.

There is reasonably good fractographic evidence that embrittlement in these metals can occur by the formation and fracture of brittle hydrides at crack tips. Metallography of specimens containing initially only solute hydrogen has revealed hydride phases at and ahead of crack tips, and hydrides are often observed on both halves of cleavage-like fracture faces[87].

In niobium it has been found that bulk specimens of the hydride cleave along {110} planes, and this is the same fracture plane as is observed in specimens containing initially only solute hydrogen[88]. Brittle fracture of hydrogen-charged niobium only occurs at slow strain rates and temperatures above about 250°C, which allow for the hydrogen to diffuse to crack tips. Embrittlement is observed at temperatures above those at which the niobium hydride would normally be expected to be stable. However, this may be explained by the hydride being stable at higher temperatures when a hydrostatic stress field exists in the material than would otherwise be the case. In cases where the hydrogen is still only present as a solute at the end of the test, embrittlement has not been observed.

In-situ studies have been made in a high voltage electron microscope of crack growth in foils of vanadium, by Koike & Suzuki[89], and zirconium, by Cann & Sexton[90]. The experiments on vanadium were performed at 170K, those on zirconium, at room

temperature. The micrographs produced by these workers show clearly that such crack growth occurs by repeated formation and fracture of hydrides at crack tips.

The method used by Cann & Sexton was a gaseous hydrogenation process followed by homogenisation of the samples at high temperature. After preparation of the foils, the perimeter of the perforation in the specimen was examined in the microscope for small cracks. A number of these cracks were then observed while the specimen was slowly strained until growth by ductile fracture of at least one of the cracks occurred due to the stress build-up. Straining was then stopped and all the crack tips were observed over a period of days for the growth of hydrides. Successive photographs taken over these days show the gradual growth of a hydride at the tip of one crack, then the fracture of this hydride, followed by the growth of a new hydride at the new crack tip at the head of the previous hydride. Thus the crack advances. The resolution is sufficiently good to indicate that cleavage definitely occurs within the hydride rather than at the metal-hydride interface.

The experiments of Koike & Suzuki relied on hydrogen introduced into the foils as a by-product of electropolishing. In contrast to the slower procedure of Cann & Sexton, micrographs were taken at 10 second intervals over a period of a few minutes while the specimen was being strained. The observations of hydride precipitation and cleavage at crack tips were very similar. A plot of the extension of a crack against time made from the photographs showed not steady growth, but a series of abrupt steps. This type of discontinuous crack growth may explain the striations found on the fracture surfaces of various hydride-forming metals, though it is true that some non hydride-forming metals, discussed below, also show this feature[87]. Koike & Suzuki also showed by electron diffraction that the cleavage plane in the hydride was always parallel to (110), which is the plane in the hydride most densely packed with hydrogen atoms. Some of the micrographs also showed that when a crack has propagated beyond a particular hydride, the hydride will sometimes redissolve into the matrix, presumably due to relaxation of the

hydrostatic stress. This seems to confirm the dependence of hydrogen solubility on localised stress conditions in these metals.

The conclusion from these various results is that in these materials brittle fracture almost certainly occurs through repeated sequences of: 1) hydrogen diffusion to crack tips under the influence of a stress gradient, 2) nucleation and growth of a hydride at crack tips, 3) cleavage of a hydride when it reaches a critical size and 4) crack arrest at the hydride-metal interface. Of course, ductile tearing is always likely to occur as well between the hydrides when the hydride phase is not continuous.

2.16.3 Non Hydride-Forming Metals

The hydrogen embrittlement of metals that do not form stable hydrides is perhaps an even greater economic problem than the embrittlement of those that do, since this category includes such widely-used structural metals as iron, steels, nickel alloys and aluminium. Considerable research effort has been devoted to this subject, but there is still disagreement as to what are the most important mechanisms. In view of the opinions of some workers that the hydrogen embrittlement of titanium does not necessarily involve the precipitation of hydrides, it is worth briefly reviewing the theories of solute hydrogen embrittlement in metals.

In the most common model, usually known as the decohesion model, the role of hydrogen has been seen as reducing the stress necessary for a crack to propagate by reducing the surface energy of the metal atoms at the crack tip[91]. Chen and Gerberich[92] have developed this model to account for the hydrogen-assisted cracking of Fe-3Si single crystals. Fig. 2.11 illustrates their proposed mechanism, in which the interaction between a crack tip under applied stress and a dislocation array is said to produce a maximum stress in a region slightly ahead of the crack tip into which hydrogen is driven by the stress field. When the hydrogen concentration reaches a critical value a microcrack is nucleated either because of a reduction in the local cohesive strength, or because dislocation motion

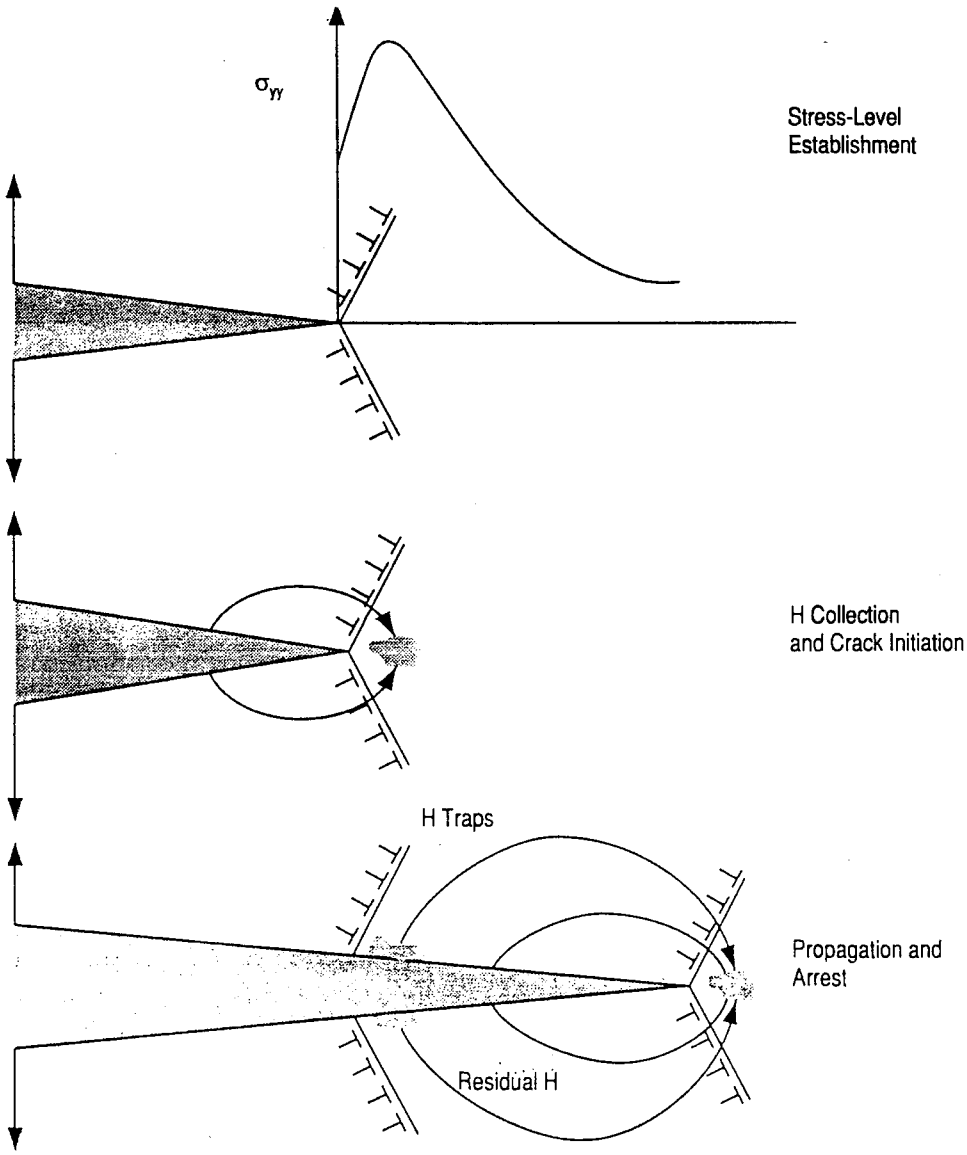

Fig 2.11 Proposed hydrogen embrittlement mechanism in Fe-3Si, after Chen & Gerberich[92]

is blocked in the hydrogen-enriched zone. The microcrack arrests slightly ahead of the tip, and the process then repeats itself giving rise to discontinuous crack growth accompanying plastic deformation. There is a close analogy here with the theory of discontinuous crack growth by the stress-induced nucleation of hydrides.

Other workers such as Birnbaum[93] have stated that hydrogen causes a localised decrease in the resistance to dislocation motion at a crack tip, and hence a reduction in the threshold stress for plastic instability. This view has been supported by in-situ TEM experiments on nickel alloys in which dislocation sources were found to be activated by the addition of hydrogen gas, and de-activated again by its removal. Oriani[94] has argued that the decohesion model and the localised slip model are both descriptions of essentially the same phenomenon, the first emphasising the colinear mode of separation and the second the shear mode, but both depending on the bond-weakening action of the hydrogen atom. That the role of stress gradients is significant in causing localised hydrogen concentrations is indicated in the low fatigue resistances often encountered in steels in corroding environments, where hydrogen evolved in the corrosion reaction is believed to become trapped at specific sites in the metal by dislocation cells[95]. For some cases of hydrogen embrittlement, for example of aluminium alloys, the trapping of hydrogen at grain boundaries leading to intergranular decohesion has been suggested[96]. Alternatively, as in the case of titanium, some have talked of the build up of a hydrogen gas pressure in microcracks, interstitial hydrogen having been driven to these surfaces by stress gradients, leading to cleavage-type fracture[97]. Most authors, however, have preferred some variant on the decohesion model.

One possibility that seems to have been generally ignored by writers on the hydrogen embrittlement of titanium is that the embrittlement mechanism could in fact be essentially the same as in non hydride-forming metals, the presence of the hydrides being a symptom rather than the chief cause of the embrittlement. It seems feasable that the particularly low hydrogen solubility in the α phase could go along with a particularly low

tolerance to the decohesive effect of solute hydrogen, in which case the presence of hydrides would be merely an indication of a level of solute hydrogen sufficient to cause brittle fracture. It is notable that the progress of cracks in titanium via hydrides has only been convincingly demonstrated at very low temperatures (~75K), in the region in which the hydride is known to be particularly brittle, and the metal particularly ductile. It does seem to be the case that β titanium, which comes in the category of a non hydride-forming metal, suffers less from the presence of hydrogen, but the common assumption that β alloys do not become embrittled needs to be questioned in the light of the work of Livanov et al. Despite the general opinion to the contrary, the present writer would not be at all surprised if it became clear eventually that hydride mechanisms are not the dominant cause of the hydrogen embrittlement of titanium under most conditions.

3. EXPERIMENTAL METHODS

3.1 Preparation of Tensile Specimens

3.1.1 Materials

The supplied materials used for making tensile specimens were IMI 120 titanium (a British equivalent of ASTM grade 2 commercially-pure titanium), in 1 mm thick sheet form, and grade 12 titanium supplied by Timet in 5 mm thick sheet form. The manufacturer's analysis of the grade 12 is given in table 3.1. These were all cold-rolled to 0.5 mm thickness. In the case of the 5 mm material it was necessary to do this in two stages, with an anneal at 850°C for 24 hours under argon after 50% reduction to undo the work-hardening. Nevertheless the grade 12 showed a considerable amount of cracking at the edges after rolling, thus reducing the usable material. Its hardness was measured at 280 (Vickers hardness test, 10 kg load) after the processing, compared to a value of 135 for the grade 2.

3.1.2 Annealing

Tensile specimens of the dimensions shown in fig. 3.1 were stamped and drilled from the sheets. The specimens were then put into batches and variously annealed under argon. The specimens were first separated from each other using molybdenum foil to prevent diffusion bonding, and the batches were then wrapped in more foil to prevent contact with the silica tube. The batches were sealed in silica ampoules containing argon at 1/3 atmosphere pressure, and placed in the furnace.

Some of the batches of grade 12 titanium were directionally annealed in a travelling furnace. This consisted of a tube furnace, of size 20 cm cubed, on rails, and powered via a variac transformer. The tube holding the samples in their molybdenum packages was fixed, and the furnace was drawn along it by an electric motor at an approximate speed of 1 mm/minute. A gentle flow of argon was passed through the tube. The furnace was wound with more turns at the ends than in the middle, so there would be created a plateau

N	C	H	Fe	O	Mo	Ni	Ti
0.0170	0.0100	0.0021	0.1100	0.1500	0.2600	0.6600	Bal.

Table 3.1 Analysis of the grade 12 titanium used in this work (values in atomic %)

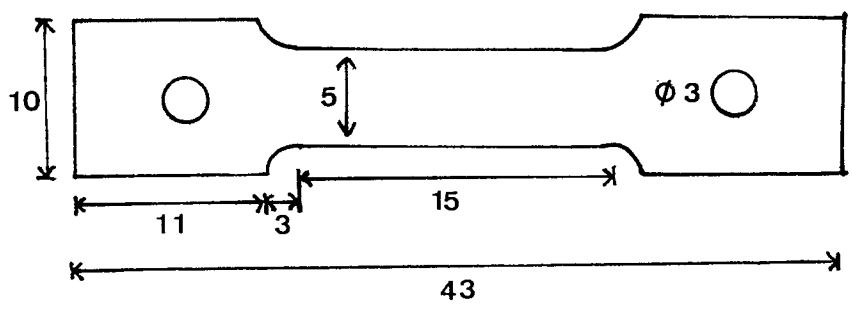

Fig. 3.1 Pattern for tensile specimens (dimensions in mm)

of constant temperature in the body of the furnace, with as steep a gradient as possible at the ends. Thus there should be no "hot zone" as in an evenly wound furnace, and the sample, with the furnace travelling over it, should experience about 3 hours of constant temperature in which to equilibrate, followed by a rapid fall to ambient temperature, progressing along the long axis of the tensile specimens. This was part of the investigation of the effect of grade 12 microstructure on hydrogen absorption, and was intended to cause the growth of elongated grains of α and β phases parallel to the tensile axis by directional recrystallisation above the α/β transus.

Several attempts were made to idealise the winding of this furnace, the temperature profile being measured by means of a chromel-alumel thermocouple, stationary in the sample tube, connected to a digital thermometer. The furnace was run along the tube and the temperature recorded at 10 minute intervals. One such graph is shown in fig. 3.2. Since the furnace speed was 1 mm/minute, the horizontal axis can be read as minutes or mm. The pattern of the windings was modified several times to try and obtain the best temperature profile.

3.1.3 Arc-Melting

Further to the investigations on grade 12 titanium it was decided to make up a new alloy whose bulk composition would be equal to that determined by electron-probe microanalysis for the β phase in the grade 12. This was made from Aldrich Chemicals sponge titanium (99.5% pure) and carbonyl nickel in ball form. An electric arc-melting furnace containing 1/3 atmospheric pressure argon was used to consolidate the sponge and subsequently melt together the titanium and nickel (3.5 atomic % Ni). The apparatus was first filled with argon and evacuated 3 times, and a titanium getter was melted prior to melting the components in order to minimise oxygen contamination. The alloy was produced as ingots about 1 cm wide $\times$ 5 cm long which were then hot rolled. The hot rolling took the form of heating the ingots in an air furnace at 500°C for 1 hour, removing and rolling down by 10%, reheating for 10 minutes and re-rolling in stages

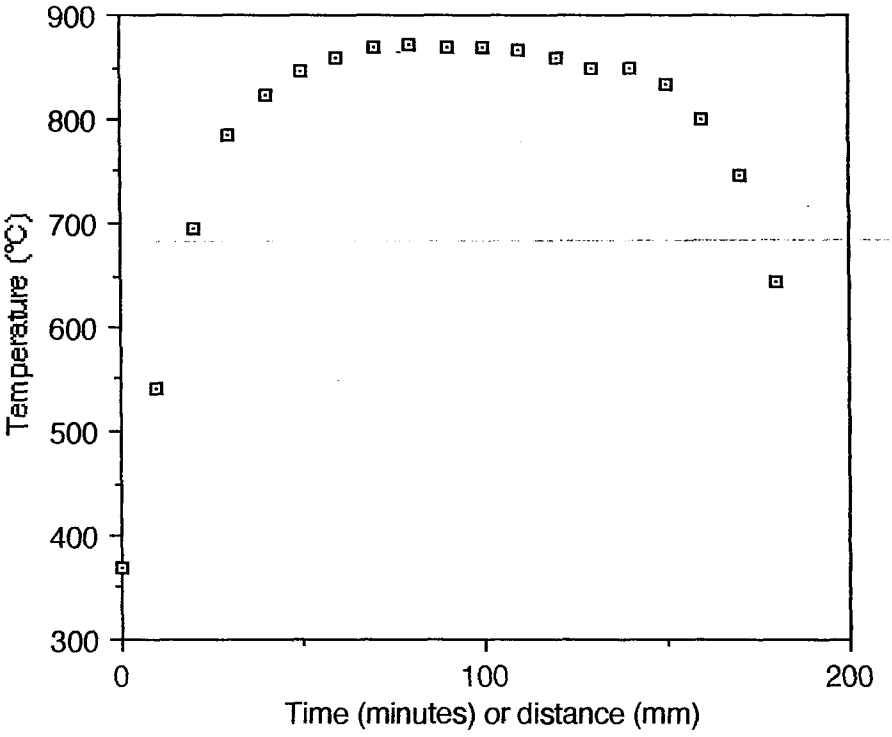

Fig. 3.2 Temperature profile of directional annealing furnace

until a 90% reduction was achieved. A final reduction to the 0.5 mm standard thickness was accomplished by cold-rolling for a better surface finish.

3.1.4 Surface Preparation

All tensile samples were given a standard surface treatment prior to hydrogen charging consisting of an electropolish for 3 minutes in a solution of 10% sulphuric acid in methanol at a temperature of -30 to -40°C. This was performed in a stainless steel beaker with the sample at +30 v with respect to the beaker. The grip sections of the tensile samples were first coated in Lacomit varnish in order only to electropolish the gauge sections. After polishing, a representative sample from each batch was etched in Kroll's reagent (3% HF, 10% HNO_3 in water) for 90 seconds for the purposes of optical metallography.

3.2 Hydriding Treatment

The hydriding method used in this work was electrochemical, in order to simulate the offshore situation in which absorption of hydrogen from an aqueous solution occurs when a negative potential is applied to the material. The electrolyte used was 0.1M sulphuric acid. The European partners used simulated seawaters of various pH in longer-term experiments to try and create realistic simulations of offshore conditions. In this work 0.1M sulphuric acid was used to obtain similar results in terms of the condition of the material in a shorter time.

The solution was contained in a stainless steel beaker and kept slowly stirred by a magnetic stirrer. It was found that without stirring, a brown deposit, presumably rust originating from the beaker, was deposited on the titanium sample after an exposure of several days. This layer did not adhere to the titanium, and constant stirring prevented its formation.

The titanium tensile specimens, again with the grip sections masked off, were made negative with respect to the beaker and connected to a power supply in series with a 450Ω, 1 W resistor. The power supply delivered a constant voltage. This was adjusted initially to give a current density on the samples of 10^{-6} A/m^2 of surface area, i.e. 15 mA per sample taking into account both sides but neglecting the edges. The samples were hydrided in batches of 3. They were held by stainless steel tweezers inserted through holes in a brass cover made for the beaker, but insulated from it. The brass cover served to connect the samples in parallel, and also to limit evaporation. The total current for a batch was 45 mA, and this was kept constant for all experiments. As time went on the solution was found to increase its conductivity as it took on the green colour associated with Ti^{4+} ions. After about 4 days the conductivity of the cell was observed to fall and the solution went brown. For the charging periods longer than this the solution was changed every 4 days.

The European partners allowed the current in their experiments to change during the course of the exposure. It seemed to be better to the present writer, however, to fix the current so that the quantity of charge passed was known. The series 450Ω resistor achieved this purpose. It was found typically that the initial voltage across the cell necessary to produce a current of 45 mA was about 2.3 V. This gave a cell resistance of 51Ω. The load resistor, chosen as about 9 times this value, would then ensure that 90% of the applied voltage was across the load rather than the cell, and it was not possible for the current to vary by more than 10%. The voltage from the power supply was then about 22.5 V, and the power dissipated in the load resistor was about 0.9 W. A 1 W resistor was used. In practice the current was maintained to within 2%. Later in the series of experiments, two cells were operated in series with one another, and the current was still maintained within the same limits. The arrangement was then as shown in fig. 3.3.

The length of the hydriding treatment varied from 1 to 20 days. Figure 3.4 gives the analysed hydrogen concentrations obtained from grade 2 and grade 12 titanium samples

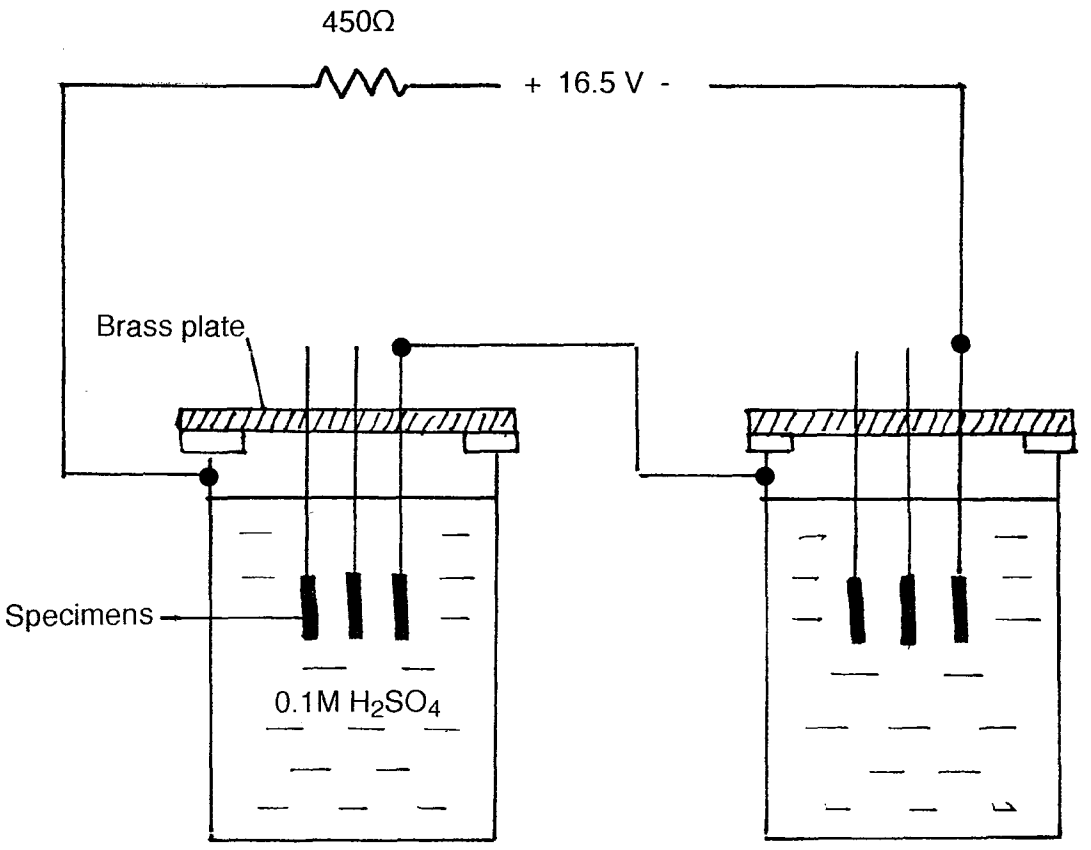

Fig. 3.3 Set-up for hydrogen charging of specimens

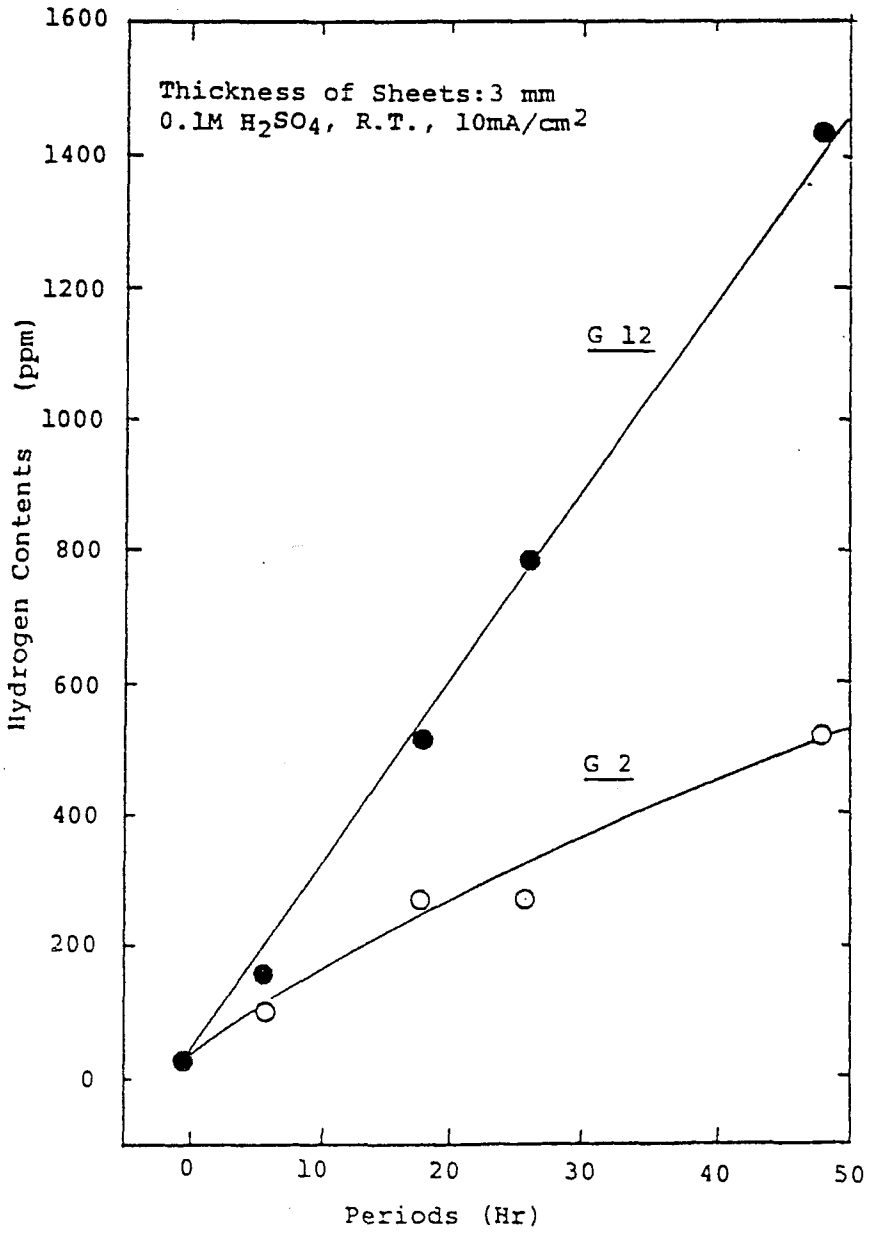

Fig. 3.4 Hydrogen contents of samples cathodically charged by Finnish (VTT) project partners at fixed potential of 1.5 V

subjected to hydriding under similar conditions for periods up to 2 days by the Finnish partners in the project. In their experiments, however, the voltage was fixed at 1.5 V and the current was allowed to vary according to the type of curves shown in fig. 3.5. For periods less than about 10 days the total charge passed can be seen to be somewhat greater than it would be in a constant-current experiment. Thus the hydrogen concentrations obtained in this work for a given time are expected to be lower than those in fig. 3.4, but of the same order. It was unfortunately not possible to analyse the actual hydrogen contents of the hydrided specimens as part of this work. It is noted from fig. 3.4 the more rapid hydrogen absorption in the grade 12, and the fact that the rate shows no sign of reducing after 2 days, although the grade 2 curve by that stage shows signs of levelling off.

In one experiment it was decided to perform hydriding at different voltages, but keeping the quantity of charge passed the same in order to determine, from microstructural observation, whether Faraday's law was obeyed, or whether there was a separate effect of voltage (in breaking down the initial resistance of an oxide layer, for example). This was achieved using beakers of two different sizes. The larger beaker required a potential of 2.3 V across the cell to achieve a current of 45 mA, the smaller a potential of 0.8 V.

3.3 Post-charging Annealing Treatment

Some of the hydrogen-charged samples were subsequently re-annealed at temperatures up to 450°C for 24 hours and furnace cooled. This was done in a tube furnace under flowing argon with a chromel-alumel thermocouple placed at the samples, which were again wrapped in molybdenum foil.

3.4 Tensile Testing

Tensile tests were carried out on a Nene Instruments tensometer with an analytical programme which produced a graph of stress versus engineering strain and also automatic measurements of peak stress, Young's modulus, yield point and proof stresses.

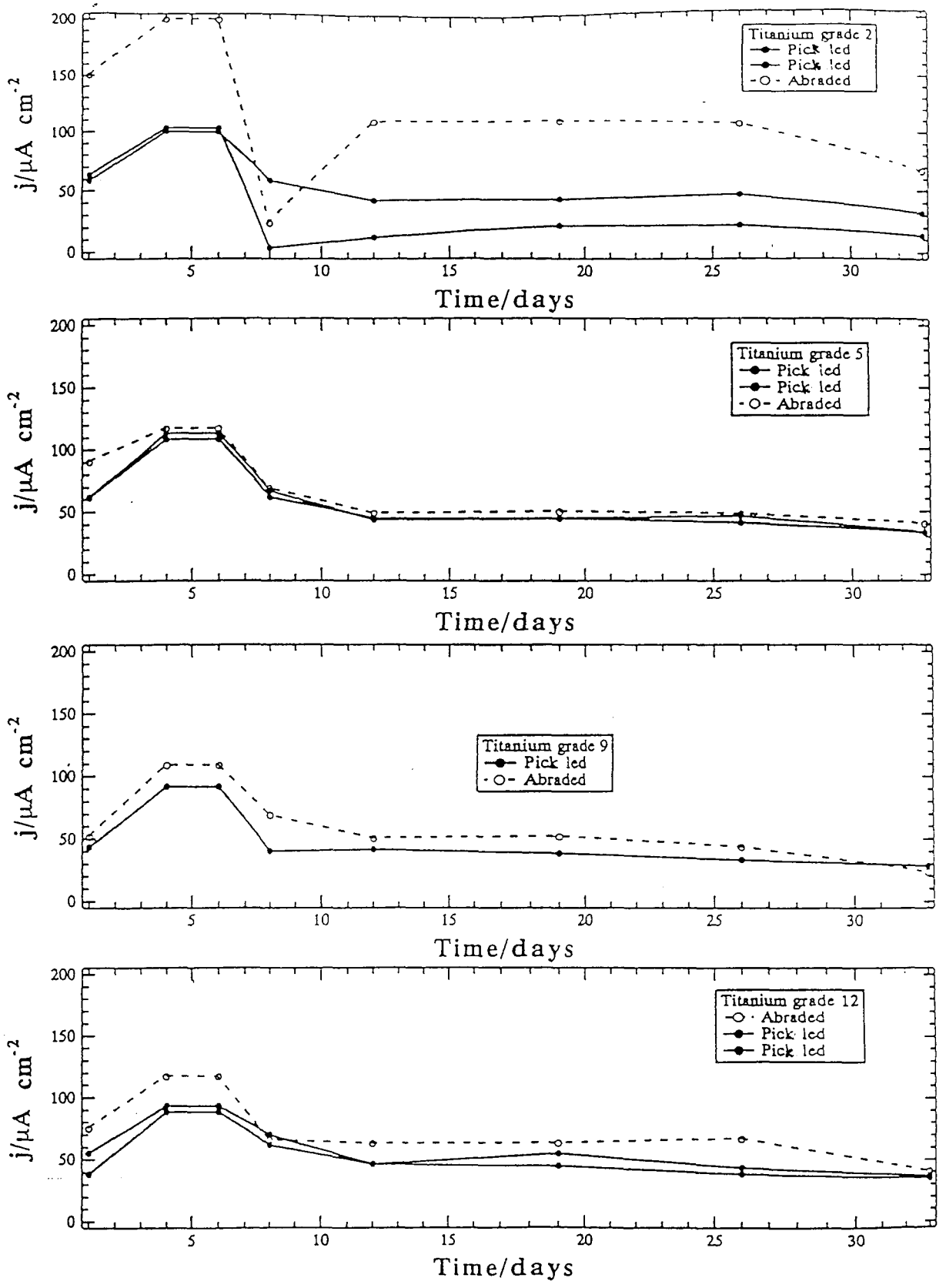

Fig. 3.5 Typical current against time curves for cathodic hydrogen charging at fixed voltage, obtained by Norwegian (IFE) project partners

The machine's estimate of ductility was not used since it failed to take into account slip of the sample between the grips and other effects, and ductility was found to be better estimated by drawing construction lines on the graph as in fig 3.6, extrapolating the linear section to a baseline. The titanium alloys showed no clearly defined yield point, and a 0.1% proof stress measurement was used as the parameter with which to define the onset of plastic deformation. A nominal crosshead speed of 0.2 mm/minute was used, the lowest possible, which corresponded for the 15 mm gauge length to a strain rate of 2×10^{-4}/s. However, measurement of the time taken from the start for the machine to register a 1 mm displacement indicated that the speed was in reality slower than this, and that the strain rate was about 8×10^{-5}/s.

The machine elasticity, estimated by obtaining the stress-strain curve resulting from driving the empty crossheads together for a brief period, was negligible in comparison to the elasticity of the samples. However, the results obtained for the Young's moduli were generally of the order of 5000 MPa, a factor of 20 less than the accepted value for bulk commercial-purity titanium. This is thought to be due to the small size of the specimens, their non-ideal shape, with some extension of the grip sections occurring, and the elasticity of the various grip components which would have been difficult to measure. The results for Young's modulus were not used in the analysis of the data. All values used in the analysis are the means of the values for 3 samples having the same treatment. In cases in which the results were very inconsistent more than 3 tests were done and the 3 central values used. Error bars given are the standard deviations for a particular type of measurement determined from many tests.

3.5 Fractography

Fractured specimens were cut from their grip sections and mounted on aluminium stubs at an angle of about 30° , electrical connection being made with silver paint. Scanning electron microscopy using secondary electron imaging was performed using a JEOL T220A instrument. The 30° angle allowed an oblique view of both the fracture

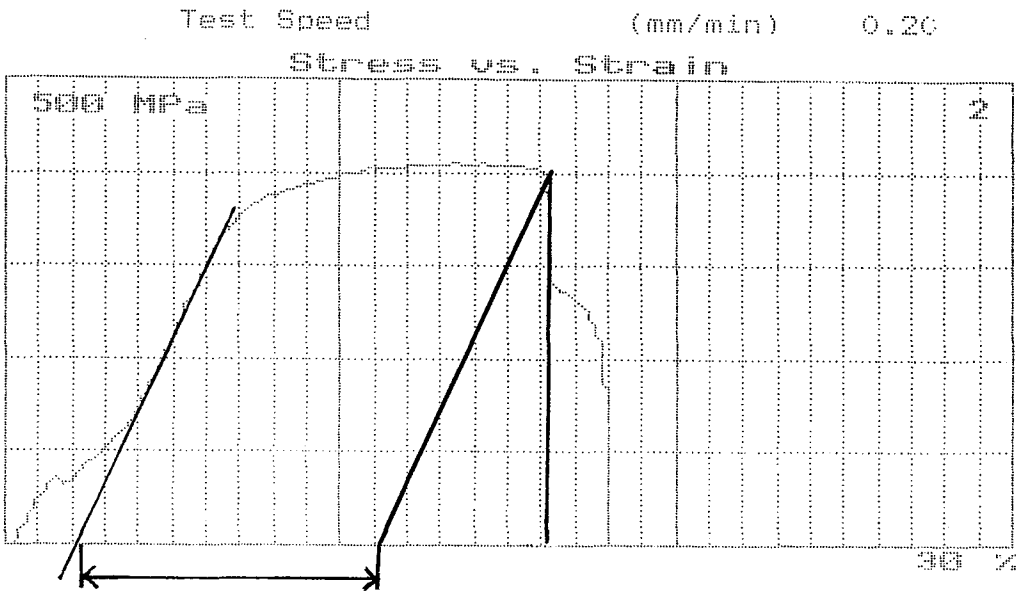

Fig. 3.6 Determination of ductility from machine stress-strain curve

surface and the specimen side. This was found to produce more informative images than a direct view of the fracture surface.

3.6 Metallography

Fractured samples were mounted in bakelite, sandwiched between two other pieces of titanium in order to obtain more even polishing across the surface of the sample. If this was not done the rather thin samples tended to slope sharply away at the edges after polishing, making examination of the near-surface area difficult. The bakelite cylinders were mechanically ground down to obtain a surface some way back from the fracture, and then polished using alumina down to 0.1 μm grade. Unetched surfaces were used for backscattered electron imaging, which was performed on a JEOL T200 scanning microscope, with a Link Systems semi-quantitative energy-dispersive X-ray analysis system. For optical microscopy and secondary electron viewing the samples were etched in Kroll's reagent for 90 seconds.

Backscattered electron imaging using polished specimens was used in the examination of α-β alloys in order to distinguish between the phases through the contrast arising from the differing average atomic numbers between the phases due to the partitioning of α and β stabilisers to the α and β phases respectively. Backscattered imaging also allowed the hydride phase to be distinguished as darker than both the α and β phases because of its substantially lower atomic number density. Secondary electron imaging and optical metallography of etched specimens were used primarily to study microstructures, hydrides and cracks in α titanium.

3.7 Transmission Electron Microscopy

Thin foils were prepared from the broken tensile samples by grinding them to 0.25 mm thickness. In some cases the samples were ground equally on both sides, and in some cases care was taken to grind the same surface all the time so as to reduce the sample as close as possible to one surface. 3 mm disks were spark-cut from these foils, so as to

impose no extra distortion on the material, and then the "surface" disks were given a very light grinding on the hydrided side in order to remove the oxide layer, prior to twin-jet electropolishing. The oxide layer that builds up during electrochemical hydriding seems to be quite thick, and if not removed it was found that electropolishing did not occur properly on that side of the foils, and a detached oxide layer remained around the electropolished window.

Electropolishing of the foils was performed using a Struers twin-jet electropolisher with a 10% solution of sulphuric acid in methanol cooled to between -30 and -35°C, a medium flow rate, and voltages from 20 to 40 V. It was found in the process of the preparation of the thin foils that the same voltage was not suitable for electropolishing all the materials. While satisfactory results were obtained at 40 V for grade 2, use of this voltage, with the same solution and temperature, on grade 12 samples resulted in the extensive oxidation of the foils, TEM examination showing only oxide layers at the edge of the perforation between which the metal had been completely dissolved. Correct polishing was obtained by reducing the voltage to 30 V. However, with Ti-3.5Ni and Ti-5Ni samples, 30 V again resulted in oxidation, and it was found necessary to reduce the voltage to 20 V. These observations suggest some influence of the nickel content of the alloys on the activation energy of the oxidation reaction.

The foils were examined using a Philips EM 301 microscope operating at 100 kV, and analysis in transmission mode was performed on a JEOL 100CX "TEMSCAN" microscope, also operating at 100 kV, with a Link Systems quantitative energy-dispersive X-ray analyser.

3.8 In-situ Straining of Hydrided Specimens

Thin foils were also prepared from near-surface regions of hydrided grade 2 titanium for the purposes of in-situ straining experiments carried out in the AEI high voltage transmission microscope which was situated in the Materials Department, Imperial College

until June 1991. The purpose of these experiments was to observe directly the effect of strain on the hydrided material and to look for the stress-induced nucleation and growth of hydrides predicted by the Paton and Williams theory of hydrogen embrittlement as had been previously done by Cann & Sexton[90] with zirconium.

The foils for this experiment were made according to the pattern in fig. 3.7 by grinding down one surface of a hydrided specimen, cutting to shape with scissors, taking care not to bend, and drilling the holes with a 0.5 mm drill. The thickness of the foil was determined by the geometry and by the fact that the maximum force that could be exerted by the straining stage was 20 N, which had to be sufficient to strain the sample into the plastic region of deformation. The yield stress for bulk grade 2 titanium is 420 MPa. Thus for the stage to be able to break the specimen the cross-sectional area must be no greater than 0.045 mm^2. Fig. 3.8 shows an estimate of the geometry of the electrothinned specimen sectioned perpendicular to the tensile axis. By this model the cross-sectional area is equal to 1.75 times the thickness, hence the thickness required is 0.025 mm. This is a factor of 10 thinner than normally employed for TEM foils, but it was found possible to achieve it by very careful grinding. In the Struers electrothinning apparatus a polyethylene spacer with a 1 mm window had to be inserted with the sample to prevent the solution flowing round the foil. Electrothinning conditions were as before.

The Gatan straining stage for the high voltage microscope was employed, in which the force was applied by two pins placed through the 0.5 mm holes, the ends of the thin foil being clamped by small plates screwed down over the pins. The strain was controlled by a variable current delivered to a heater which altered the tension in a spring which applied the force to the pins. The microscope was used at 400 kV, 40% of its maximum voltage, to reduce the chance of radiation damage effects. (This voltage is the approximate threshold for displacement damage in titanium). The foil was initially observed at zero strain and the hydrides located. The strain was then gradually increased, micrographs being taken of hydrides and of the development of cracks. The slowness with which this

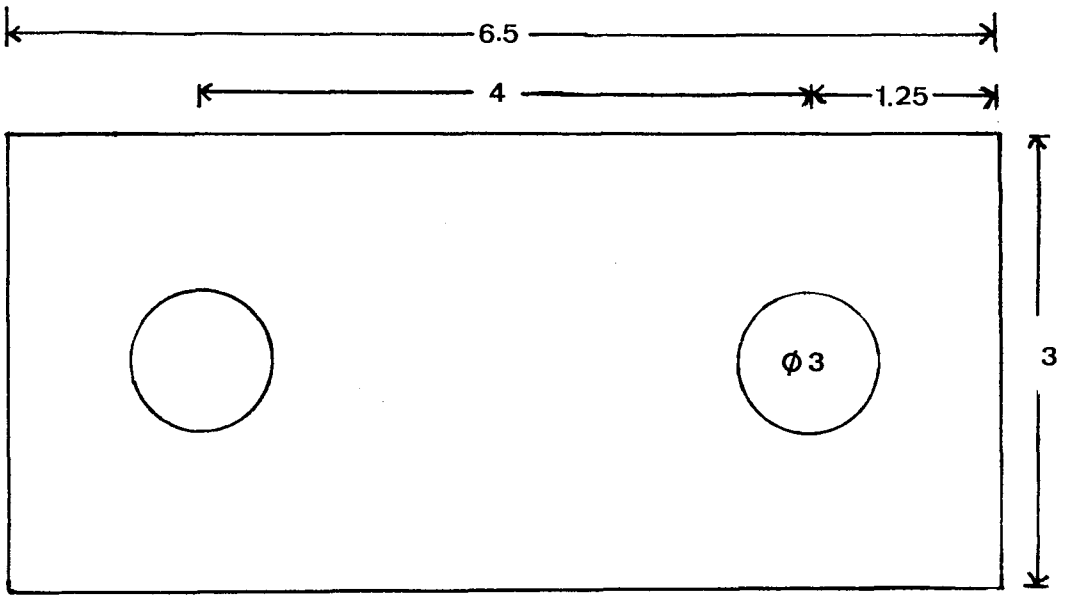

Fig. 3.7 Pattern for tensile specimens for HVEM in-situ straining experiment (dimensions in mm)

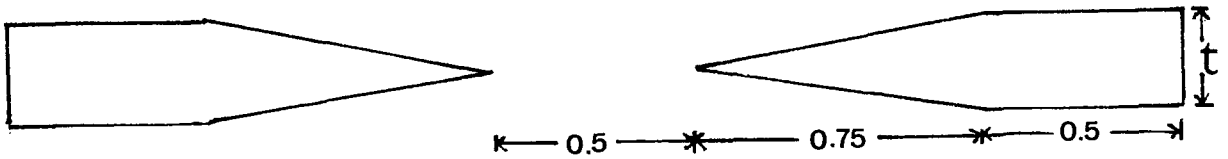

Area = 1.75t mm^2

Fig. 3.8 Hypothetical cross-sectional geometry of electropolished thin foil (dimensions in mm)

could be done was limited by the fact that the filament of the high voltage microscope was electrically isolated from the rest of the instrument (to prevent discharge) and powered by batteries which gave a maximum period of use of about 4 hours. Hence the averaged strain rate had to be at least 3×10^{-5} (taking a value obtained from the macroscopic tensile tests for the ductility of equiaxed grade 2 titanium of 40%) to achieve failure within this time.

3.9 X-ray Diffraction

X-ray diffraction of alloys was performed on a Philips PW 1710-based diffractometer with PC APD software using 0.5 mm thick samples polished flat on one surface to 1 μm.

4 RESULTS

4.1 Materials: Composition and Microstructure

4.1.1 Grade 2 Titanium

The commercial-purity titanium was subjected to 2 heat treatments:

(1) An anneal for 1/2 hour under argon in the α phase field at 800°C followed by air cooling,

(2) An anneal for 1/2 hour under argon in the β phase field at 950°C followed by air cooling.

Treatment (1) resulted in an equiaxed microstructure, mean grain size 50 μm (fig. 4.1). Treatment (2) resulted in a transformed β microstructure, with the formation of lamellar α grains by diffusional transformation within the prior β grain boundaries. The lamellae were typically 20 μm × 200 μm and the transformed β grains 200 μm across (fig. 4.2).

Transmission electron microscopy revealed the presence of an electron-optically dense second phase on the grain boundaries of the transformed β samples (fig. 4.3). X-ray microanalysis of the foils (fig. 4.4) showed this to be an iron-rich phase, though the precipitates were too narrow to allow the concentration to be assessed. Iron is the major impurity allowed in grade 2 titanium, up to a maximum of 0.3 atomic % (ASTM specifications). Clearly the iron must partition to the β phase during cooling through the α/β transus (iron is a β stabiliser), and thus concentrate on the grain boundaries in the transformed microstructure. Reference to the titanium-iron phase diagram (fig. 4.5) shows that the iron could be present as a solute in retained metastable β or in the form of the Ti Fe equilibrium intermetallic compound. The former is more likely since the intermetallic is slow to nucleate.

Fig. 4.1 Grade 2 annealed 800°C, equiaxed microstructure (optical)

Fig. 4.2 Grade 2 annealed 950°C, transformed ß microstructure (optical)

Fig. 4.3 Dark grain boundary phase in transformed ß grade 2 thin foil (TEM)

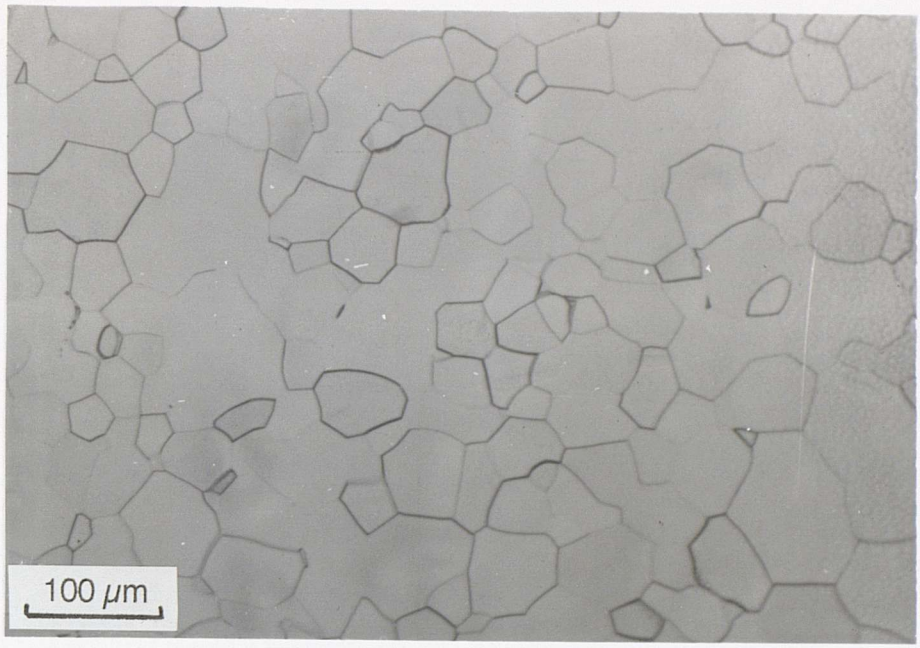
100 μm

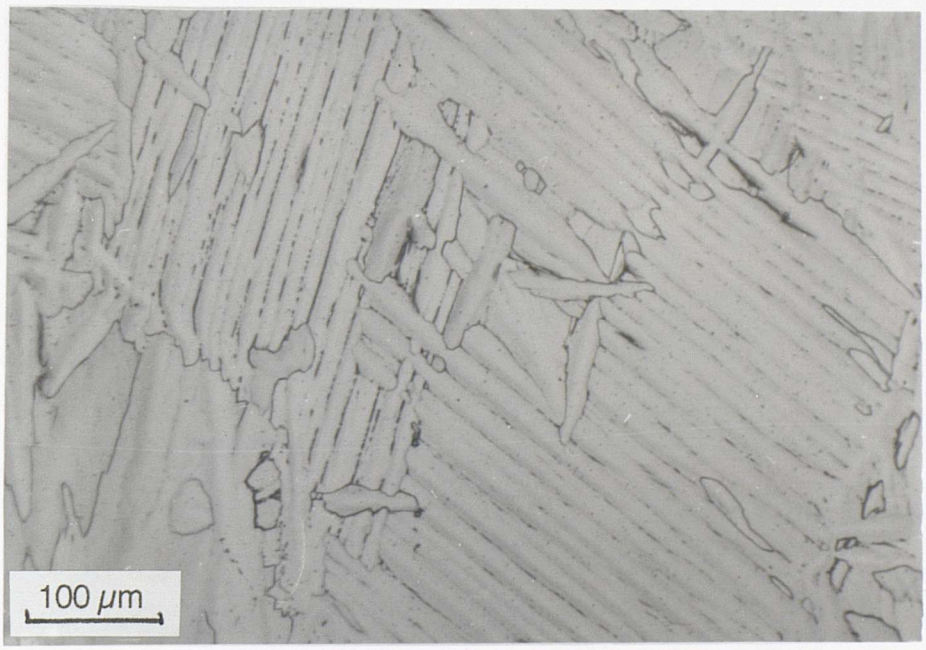
100 μm

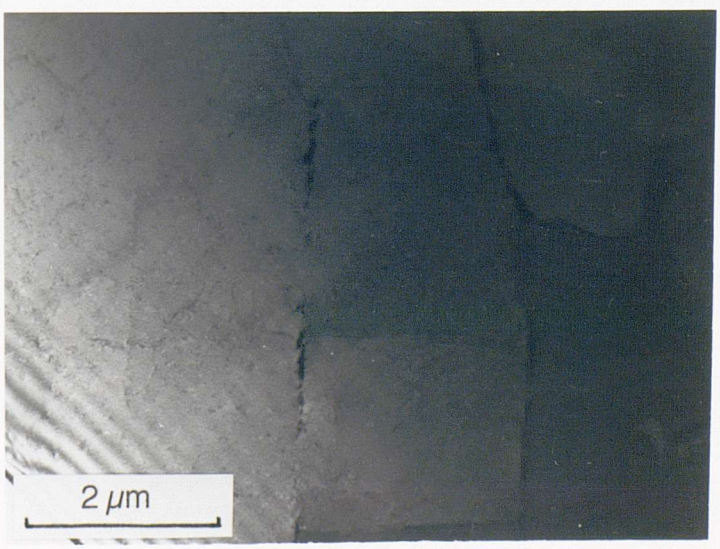
2 μm

Matrix

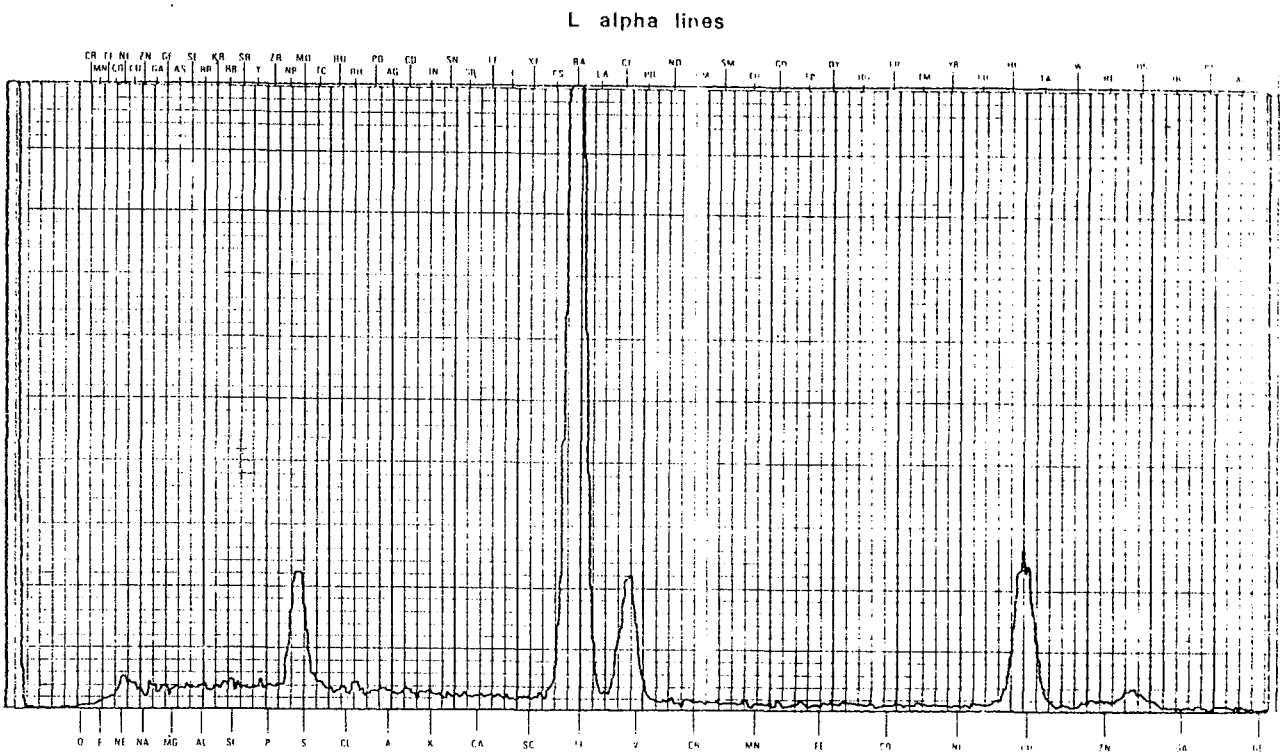

Grain boundary phase

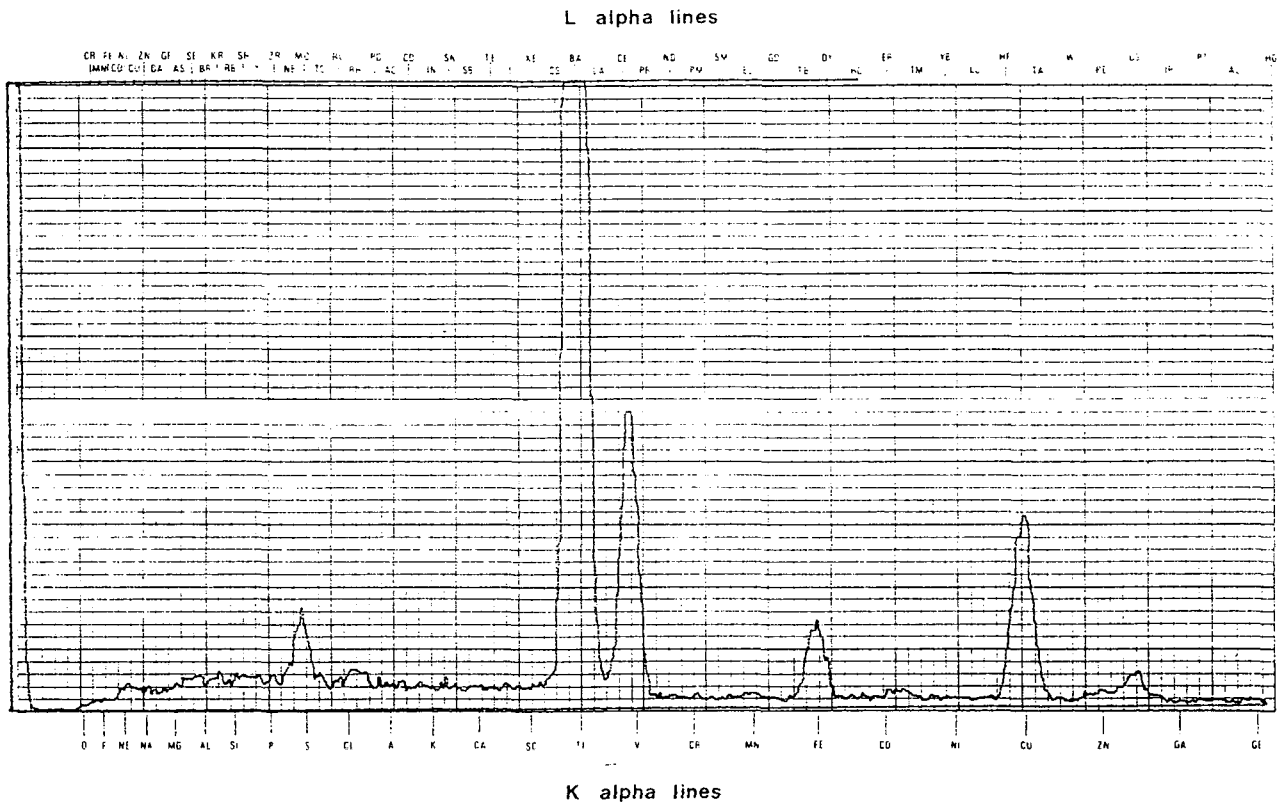

Fig. 4.4 X-ray microanalysis in transmission of transformed β grade 2

(Cu peaks are due to sample holder; S peaks are due to electropolishing film.)

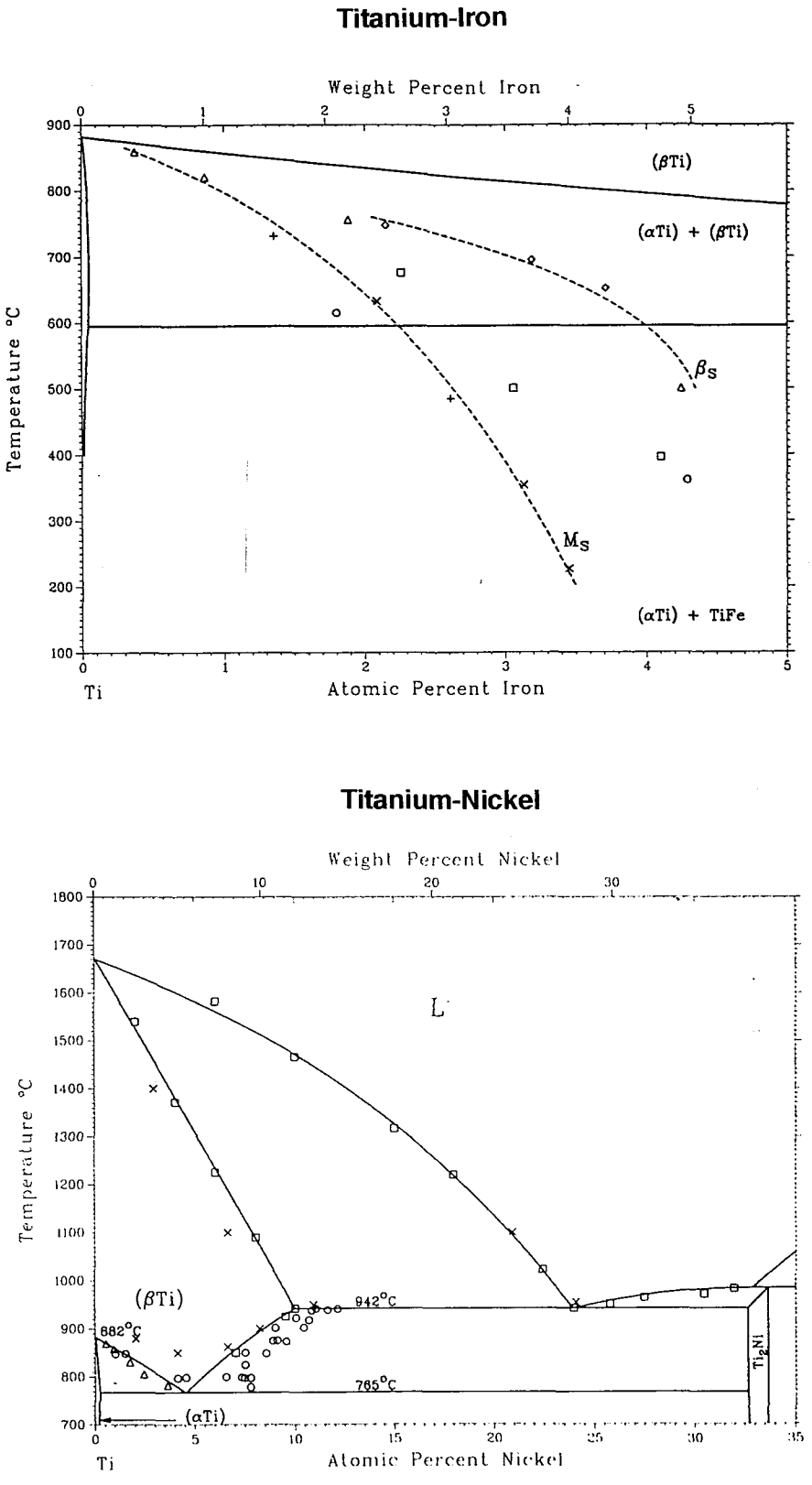

Fig. 4.5 Titanium-rich regions of the titanium-iron and titanum-nickel phase diagrams, after Murray[98]

4.1.2 Grade 12 Titanium

The alloying elements present in the grade 12 are nickel (0.6 %) and molybdenum (0.2%), both of which are β stabilisers. The microstructure of the as-received material is shown in fig. 4.6. There is a second phase present which in places forms bands, presumably the result of inadequate annealing after rolling. X-ray microanalysis of thin foils (fig. 4.7) gave a detectable concentration of nickel only in the second phase, which appeared electron-optically denser than the primary phase (fig. 4.8), of the order of 3-4%. The grains, however, were about the minimum size of the beam, so the true concentration may be higher. There was no detectable concentration of molybdenum.

Electron diffraction in the TEM (fig. 4.9) confirmed that the second phase was nickel-stabilised β titanium, rather than an intermetallic compound, the measured lattice parameter being 0.335±0.005 nm, compared to the established value for pure titanium in the β phase (extrapolated to room temperature) of 0.330 nm[99]. Reference to the titanium-nickel phase diagram (fig. 4.5) shows that this β must be metastable, the result of the slow nucleation of the Ti_2Ni intermetallic compound, similar to the titanium-iron case, except that in this case the volume fraction of retained β is much greater. The fact that the measured lattice parameter is in agreement with the theoretical value for pure BCC titanium at room temperature within the error of measurement indicates that the effect of this level of supersaturation of the structure by nickel on the lattice parameter is small. There is no data available on the effect of nickel on the lattice parameter of β titanium because, according to Murray[98], phase separation during quenching always occurs in all but the most dilute alloys.

Annealing of the as-received material at 850°C for 2 hours (under argon) was found to be adequate to obtain a completely equiaxed microstructure with a grain size of 20 μm (fig. 4.10). This annealing temperature is in the α + β phase field assuming that the material behaves according to the titanium-nickel phase diagram, i.e. assuming that the 0.2%

Matrix

L alpha lines

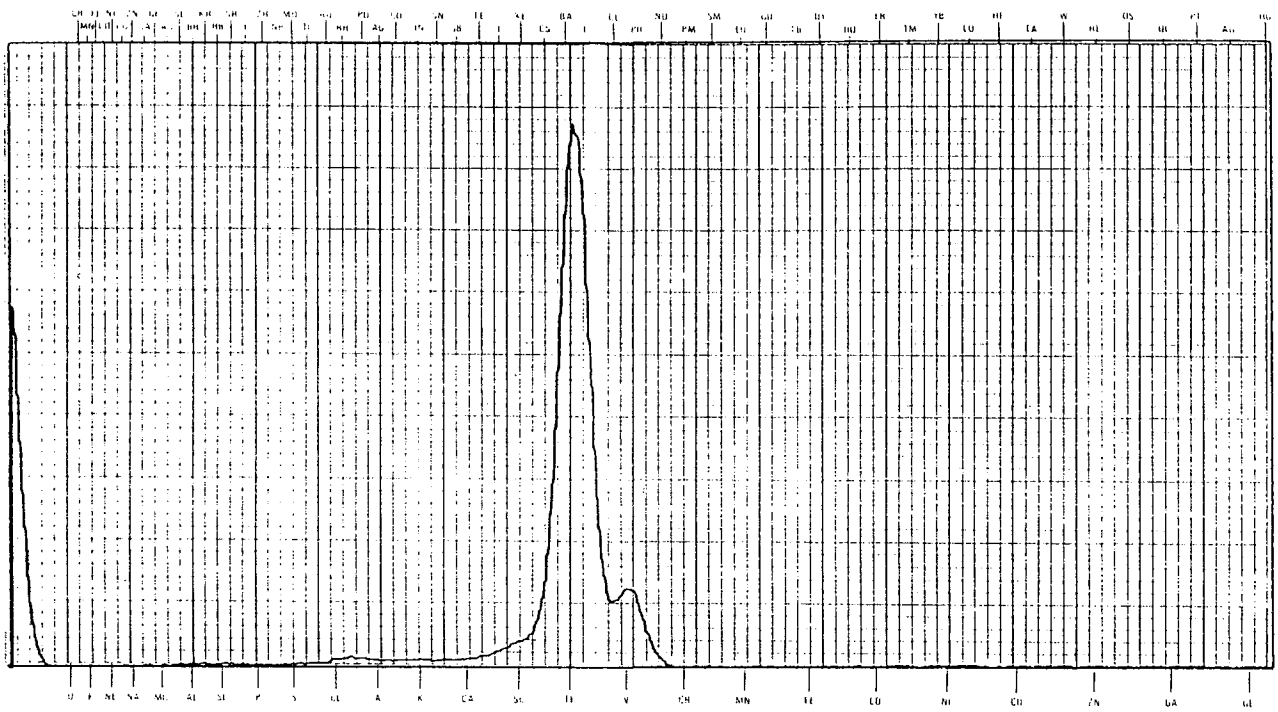

K alpha lines

Grain boundary phase

L alpha lines

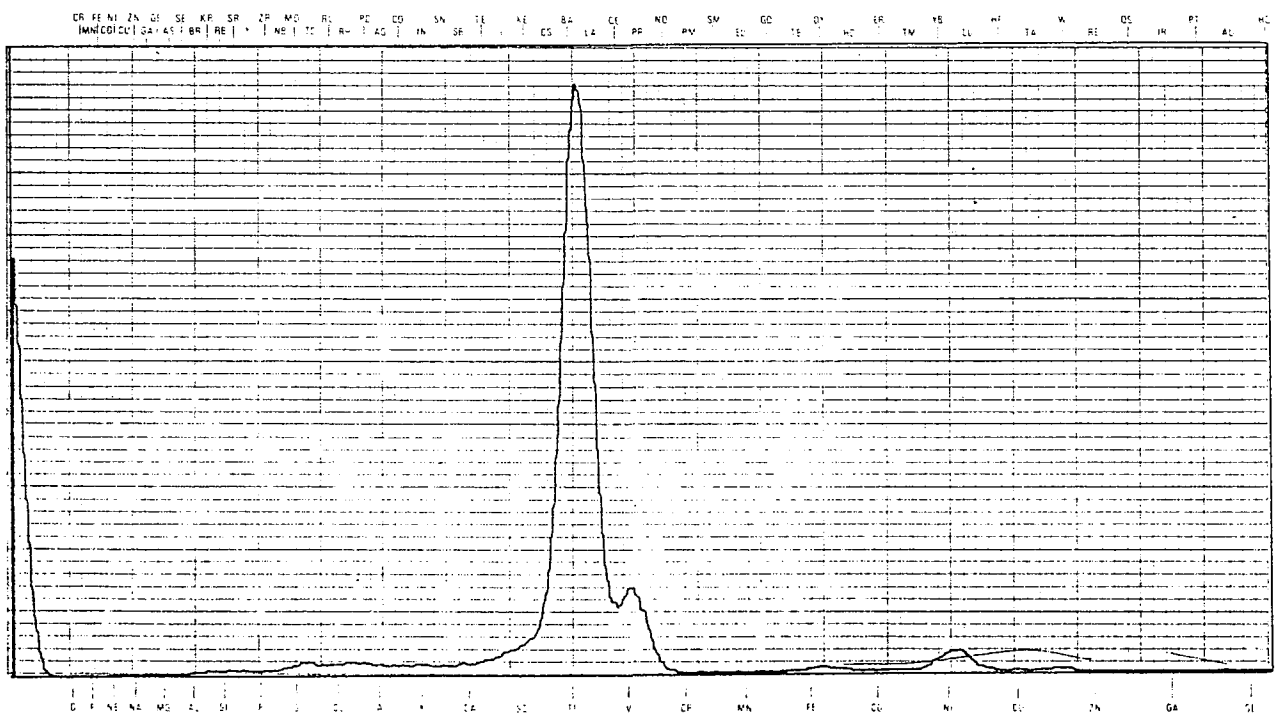

K alpha lines

Fig. 4.7 X-ray microanalysis in transmission of as-received grade 12

molybdenum makes little difference to the equilibrium state, though there is evidence that it affects kinetics. When the material was reduced by cold rolling by 90% for the purpose of making tensile samples, an anneal of 24 hours at 850°C was found necessary to obtain a completely equiaxed microstructure. Annealing in the β field at 950°C for 1 hour, followed by furnace cooling, lead to a basketweave microstructure, typical α plate size 100 × 10 μm (fig. 4.11).

Results on the formation of hydrides in the grade 12 α/β microstructures suggested the desirability of making, by means of directional annealing with the travelling furnace, a deliberately highly banded microstructure, in order to discover what effect this would have on the hydride distribution and mechanical properties. Experiments were done on this at various temperatures and with a travelling rate of 1 mm/minute. It was found that the equiaxed structure was unaltered at temperatures up to 850°C, and higher temperatures produced microstructures of the type shown in fig 4.12, which shows packets of lamellar diffusionally transformed α/β grains in two preferred orientations, one with the lamellae almost perpendicular to the surface, and the other with the lamellae almost parallel to the surface. The lamellae were not aligned in the direction of furnace travel as had been hoped, but at a variety of angles to it. Possibly the speed of the furnace was wrong, or the temperature gradient on entering was not steep enough. From these experiments it was concluded that the (α + β) ↔ β transformation temperature for the grade 12 titanium lay between 850 and 875°C. This agrees with the value of 870°C read off the titanium-nickel phase diagram at 0.6 % nickel.

4.1.3 Grade 5 Titanium

Grade 5 is the alloy Ti-6Al-4V. Only a small quantity of this material was available, in the form of a 3 mm diameter bar supplied by the Spanish (INASMET) partner in the project, and tensile specimens were not prepared, but hydriding was carried out under the same conditions as for the other alloys. The material was used in the as-received condition.

Fig. 4.6 Grade 12 as received, showing deformation microstructure (optical)

Fig. 4.8 Grade 12 as received (TEM)

Fig. 4.9 SADP of dark phase in as-received grade 12

[Fig.4.9]

[Two types of spot and two slightly different spacings are apparent in this pattern. The horizontally aligned, bright, sharp pair of spots give a spacing of 0.238 nm which is identifiable with the ß titanium {101} spacing 0.233 nm[99]. The other two pairs of inner spots both give a spacing of 0.247 nm, which could be identified with the TiO_2 {101} spacing 0.249 nm[40]. These spots are fainter, and show arcing, possibly due to the presence of a variety of crystallite orientations.]

Fig. 4.10 Grade 12 annealed 850°C, equiaxed microstructure (SEI)

Fig. 4.11 Grade 12 annealed 950°C, basketweave microstructure (SEI)

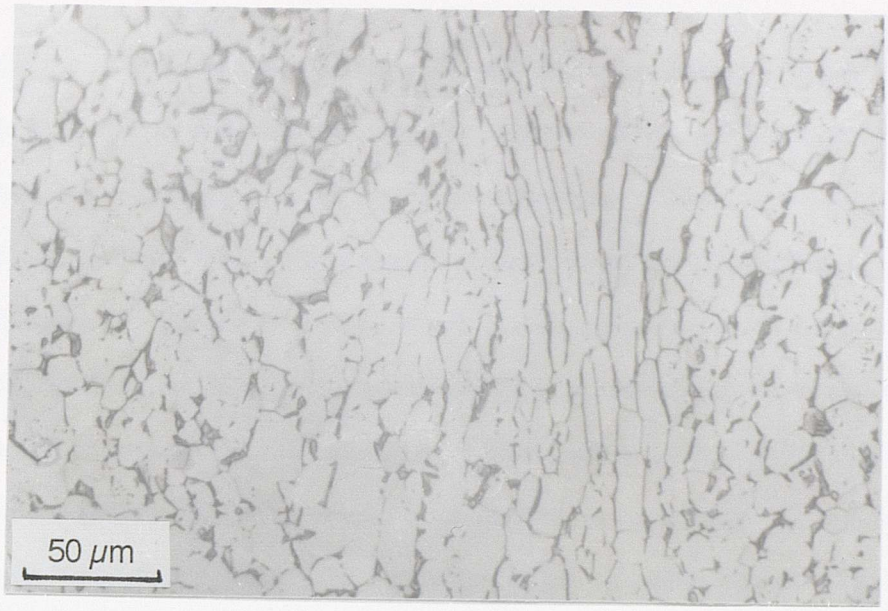
50 μm

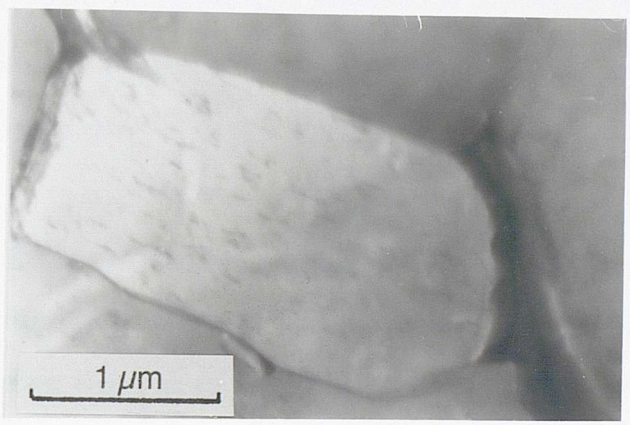
1 μm

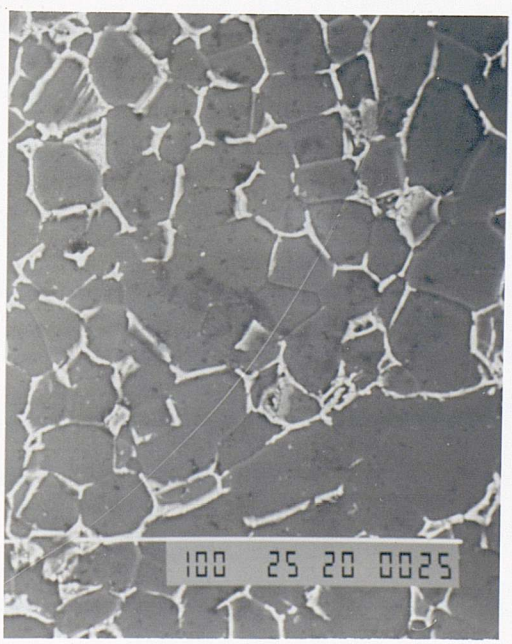
100 25 20 0025

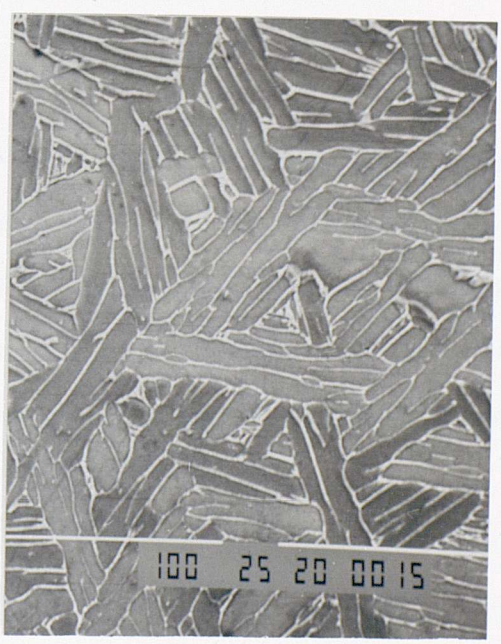
100 25 20 0015

The microstructure, shown in fig. 4.13, is again two-phase, equiaxed with some shear banding. The grain size is rather smaller than in the grade 12, typically 10 μm, and the phase distribution can best be seen by means of backscattered electron imaging in the SEM (fig. 4.14). The secondary phase appears bright, suggesting partitioning of the higher atomic number element vanadium, which is a β stabiliser, to this phase. This is confirmed by qualitative X-ray microanalysis (fig. 4.15) which shows a higher concentration of vanadium in the secondary phase, and a higher concentration of aluminium in the primary phase, as would be expected for equilibrium in an α/β alloy containing both kinds of stabilisers. (The vanadium k_α line coincides with the titanium k_β line, hence the height ratio between the 2 titanium lines is shown in the figure for both phases.) The β phase is more disconnected than in the grade 12, forming strips about 1 × 10 μm in size.

4.1.4 Titanium-Nickel Alloys

Further to the work on the mainly nickel-stabilised α/β alloy grade 12, three simple titanium-nickel alloys were cast: Ti-3.5Ni, Ti-5Ni and Ti-10Ni. The Ti-Ni phase diagram (fig. 4.5) shows that these will as solidify as β phase and transform entirely to a mixture of α titanium and the intermetallic compound Ti_2Ni below the eutectoid temperature 765°C assuming equilibrium conditions.

It was found that the Ti-10Ni alloy was too brittle to be rolled from the cast ingots at the rolling temperature of 500°C, and had to be abandoned. The Ti-5Ni alloy cracked to a certain extent during rolling but could be reduced to 1 mm thickness. The Ti-3.5Ni alloy rolled well down to 0.75 mm. The Vickers hardnesses of the as-cast alloys and of the pure titanium used in their preparation are shown in fig. 4.16 as a function of nickel content. A linear increase in hardness with nickel content is observed.

The optical microstructures of the as-cast Ti-3.5Ni and Ti-5Ni are shown in fig. 4.17. The former shows a fine lamellar pattern, the lamellae about 2 × 50 μm in size, and probably

Fig. 4.12 Grade 12 directionally annealed at 900°C (optical)

Fig. 4.13 Grade 5 as received, showing deformation microstructure (optical)

Fig. 4.14 Grade 5 as received (BEI)

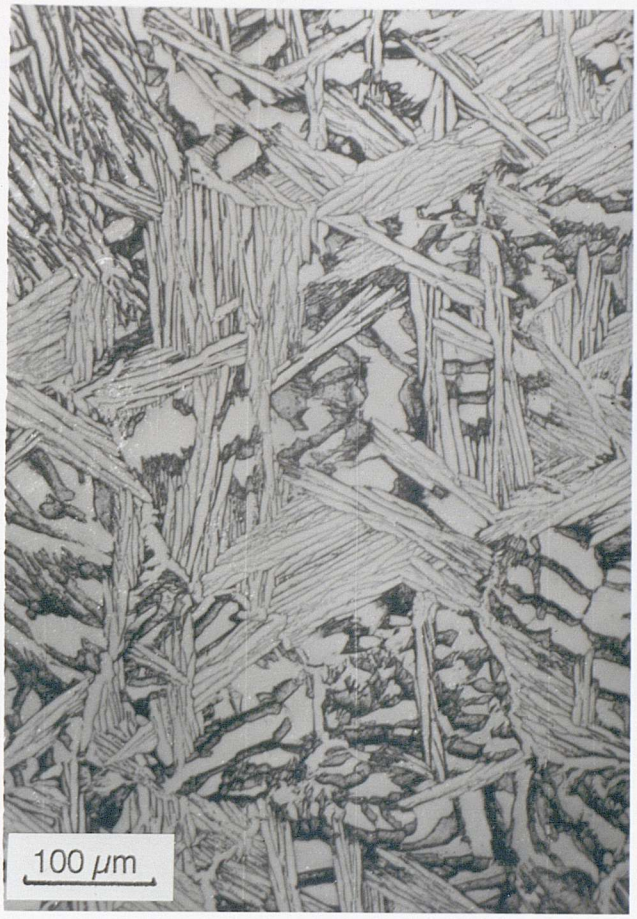
100 μm


25 μm

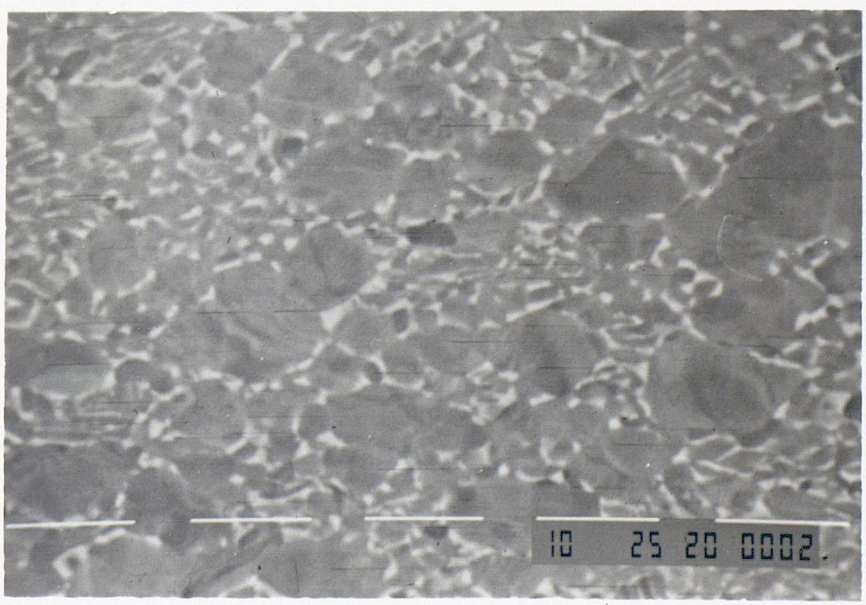
10 25 20 0002.

Matrix

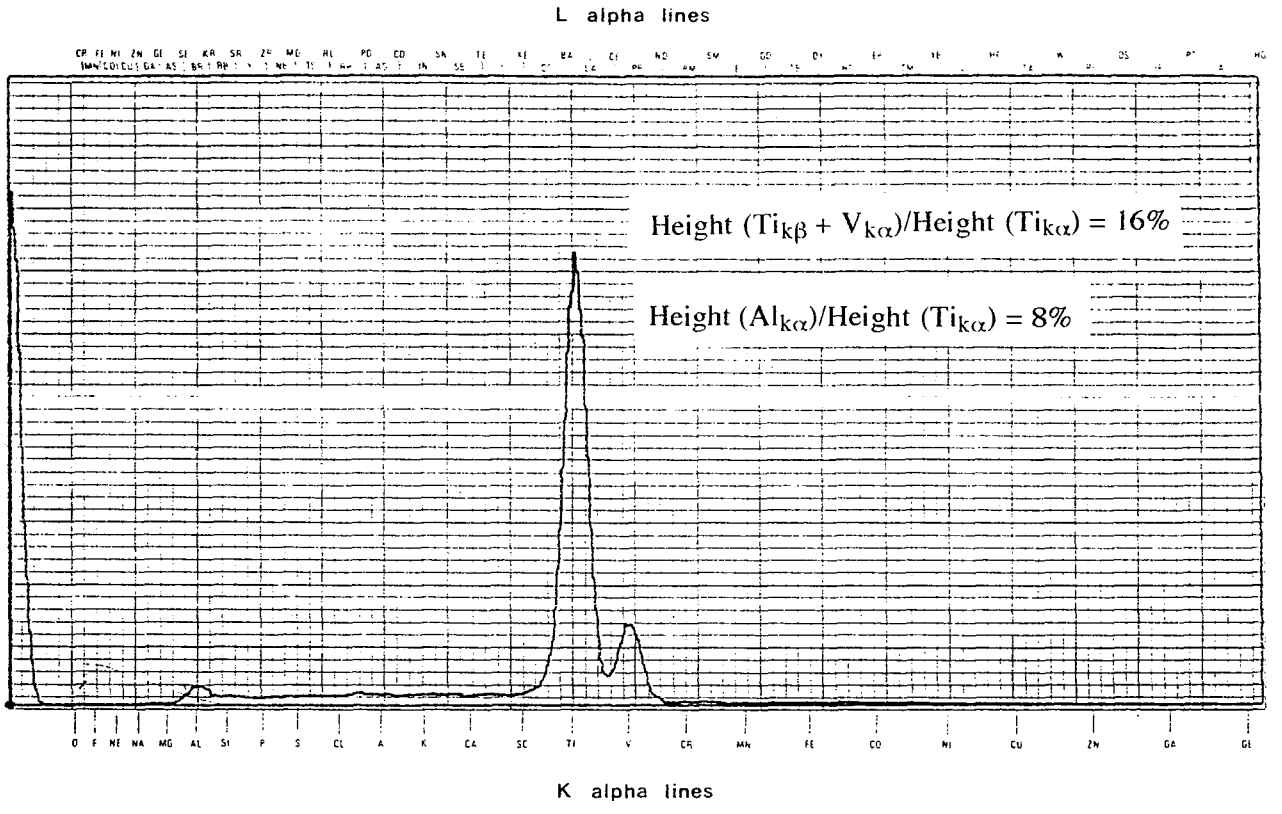

Grain boundary phase

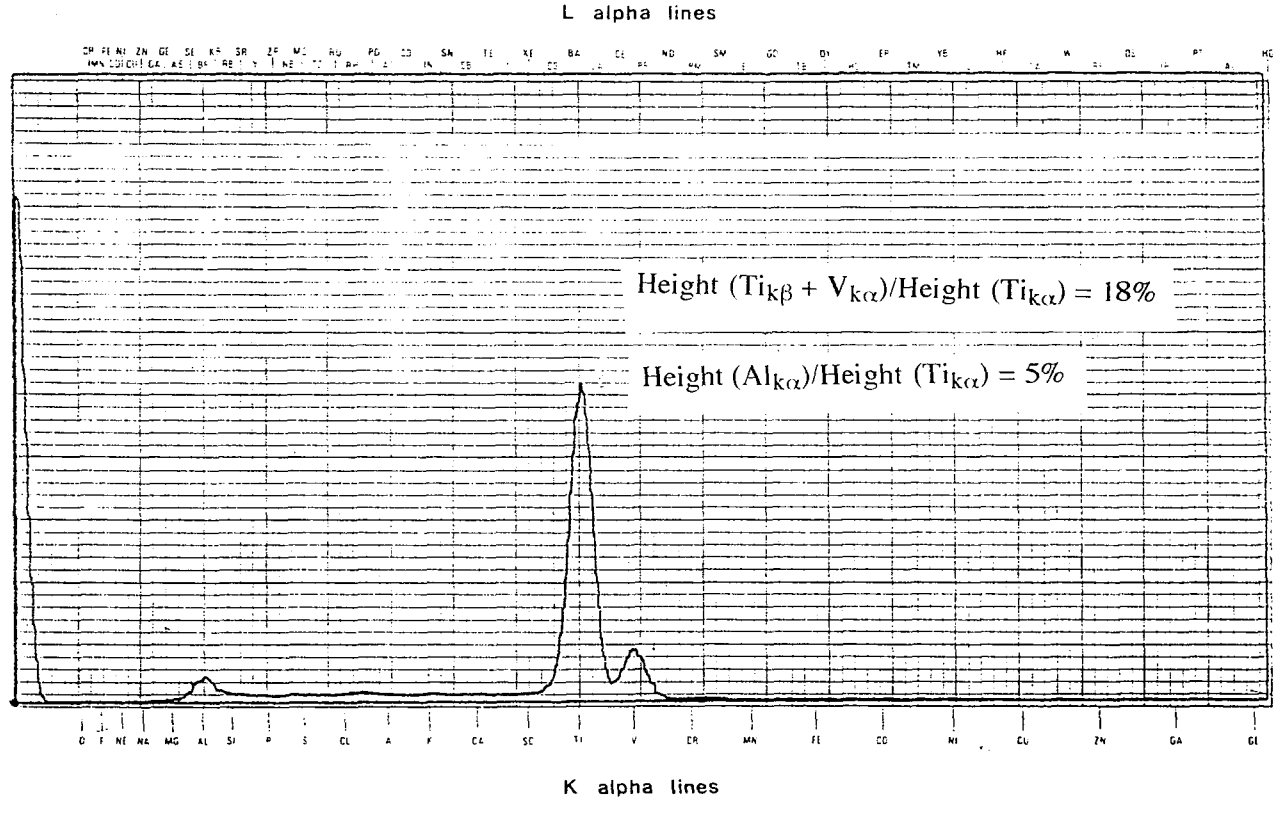

Fig. 4.15 X-ray microanalysis in scanning mode of as-received grade 5

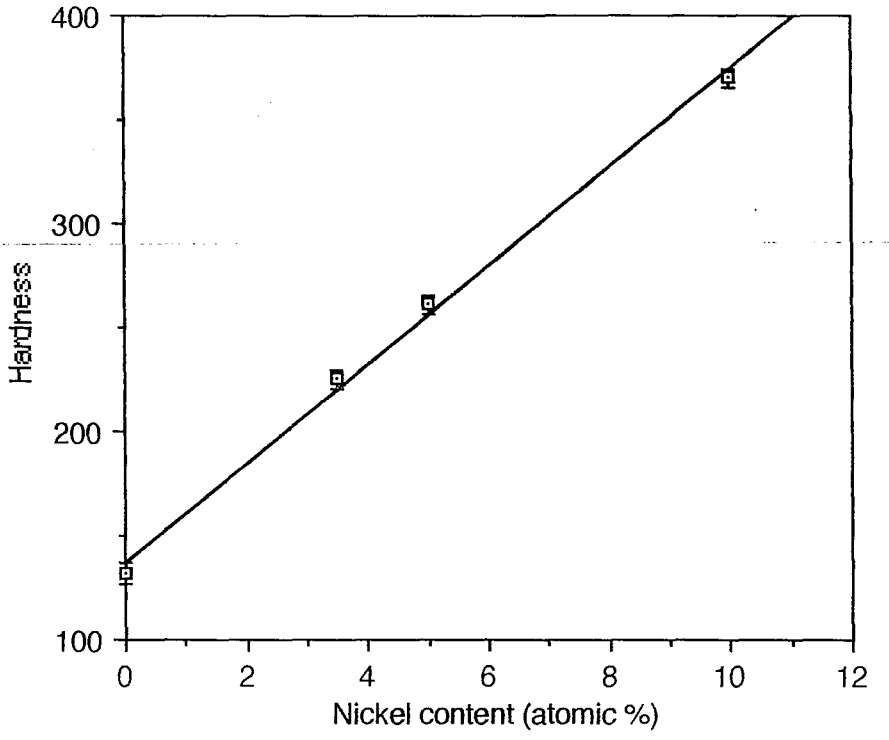

Fig. 4.16 Hardness as a function of nickel content for titanium-nickel alloys (Vickers hardness test, load 10 kg, results ±5)

represents a mixture of transformed α and retained β. The latter shows an even finer acicular pattern, the needles less than 5 μm long. This closely resembles a microstructure published by Polonis and Parr[100] for Ti-6Ni quenched from 1000°C, described by them as a 100% retained β structure. However, Margolin & Bunshah[101] believed this microstructure to represent a fine dispersion of ω phase particles in retained β. These structures can be considered a consequence of the relatively rapid cooling rate in the arc-melting furnace.

After hot rolling at 500°C and annealing at 725°C for 2 hours to relieve stresses (this temperature being chosen as being safely below the eutectoid temperature), no microstructures were visible optically. Using backscattered electron imaging, a very fine microstructure was revealed in both alloys consisting of islands of a brighter (therefore nickel-rich) phase about 1-2 μm across, the islands being slightly more densely distributed in the Ti-5Ni case (fig. 4.18). The α grains were only observed by transmission electron microscopy (see below) which showed them to be about 4 μm in size.

X-ray diffraction performed on these alloys gave the results shown in figs. 4.19-4.20 and tables 4.1-4.2. The significant peaks can all be identified as belonging to the α titanium or Ti_2Ni patterns, with the exception of two, at 0.244 and 0.155 nm, present in both patterns. The Ti_2Ni phase is more prominent in the Ti-5Ni pattern than in the Ti-3.5Ni pattern. The third phase, which is also stronger in the Ti-5Ni pattern, cannot be identified. Retained β phase is ruled out since the two peaks are not consistent with a BCC pattern with a lattice parameter in the region of 0.33 nm. The absence of retained β in these alloys is surprising in view of the stabilisation of the β phase by only 3-4% nickel in the grade 12, and indicates presumably an effect of the 0.2% molybdenum content in the grade 12. Molybdenum is a slow-diffusing species in titanium and so probably retards

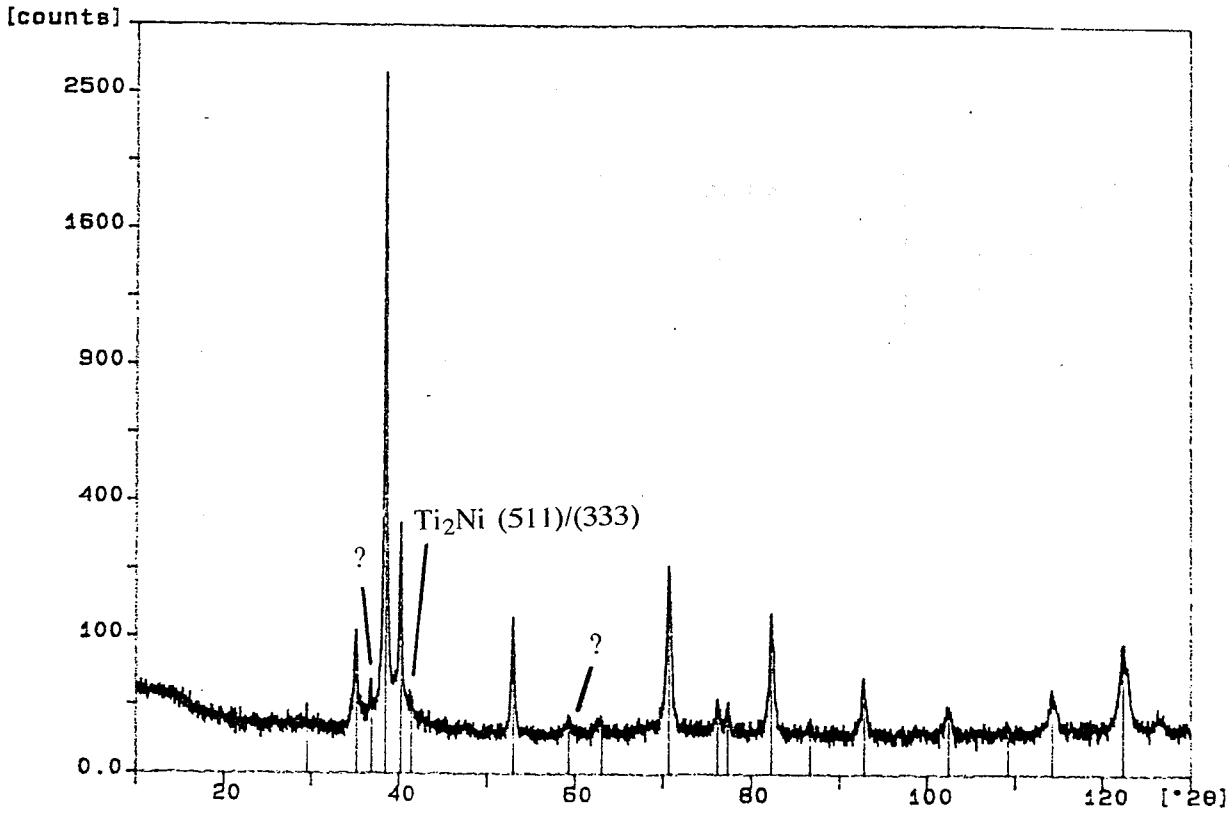

Fig. 4.19 Ti-3.5Ni: X-ray diffraction trace

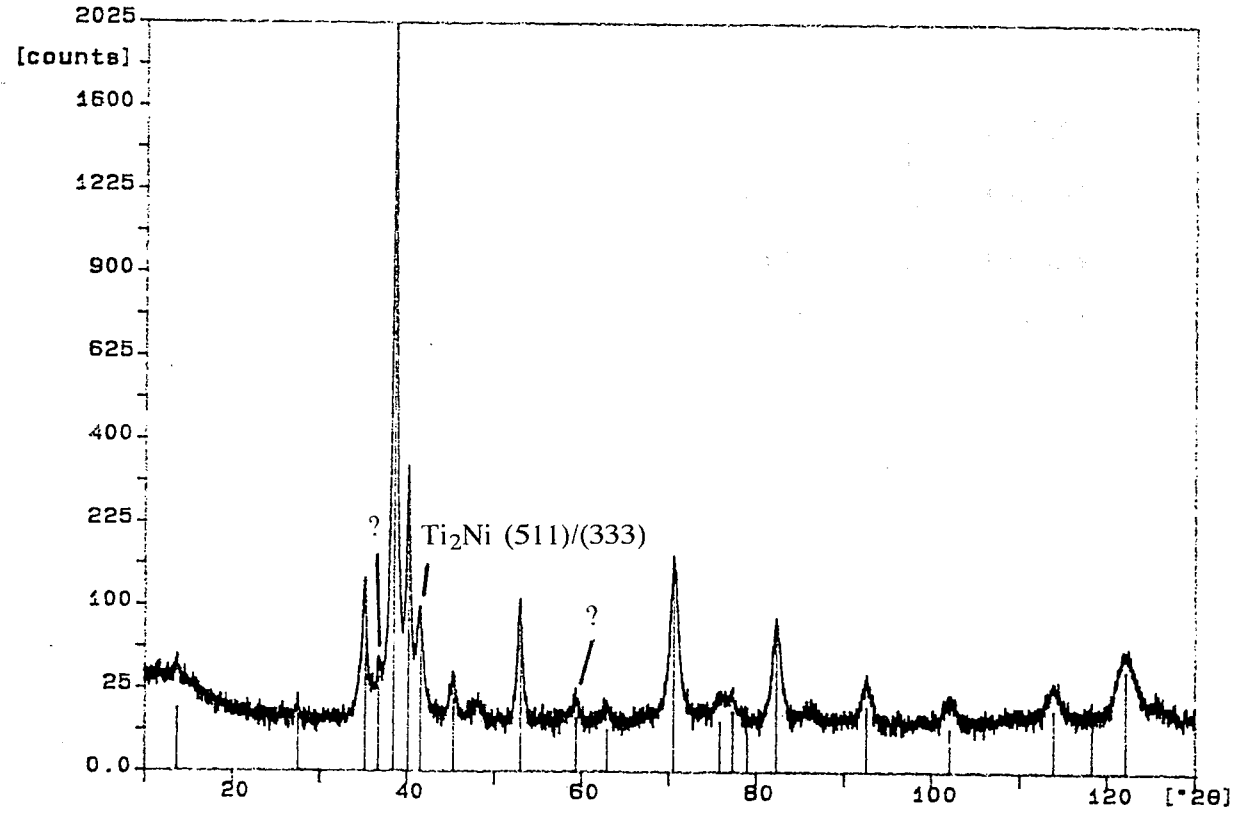

Fig. 4.20 Ti-5Ni: X-ray diffraction trace

Angle (°2θ)	d-value α_1 (nm)	Rel. intensity (%)	Identification	d-value* (nm)
29.510	0.30245	0.5	low significance	-
35.220	0.25461	3.8	α $(10\bar{1}0)$	0.2557
36.870	0.24359	1.2	?	-
38.445	0.23396	100.0	α (0002)	0.2342
40.210	0.22409	12.5	α $(10\bar{1}1)$	0.2244
41.445	0.21770	0.7	Ti_2Ni (511)/(333)	0.2171
53.045	0.17250	4.7	α $(10\bar{1}2)$	0.1726
59.270	0.15578	0.2	?	-
63.060	0.14730	0.3	α $(11\bar{2}0)$	0.1475
70.645	0.13323	8.4	α $(10\bar{1}3)$	0.1332
76.240	0.12478	0.8	α $(11\bar{2}2)$	0.1247
77.375	0.12323	0.5	α $(20\bar{2}1)$	0.1233
82.275	0.11709	5.0	α (0004)	0.11708
86.705	0.11221	0.2	α $(20\bar{2}0)$	0.11220
92.805	0.10637	1.5	α $(10\bar{1}4)$	0.10653
102.410	0.09883	0.5	α $(20\bar{2}3)$	0.09895
109.165	0.09452	0.2	α $(21\bar{3}1)$	0.09458
114.205	0.09174	1.0	α $(11\bar{2}4)$	0.09175
122.260	0.08796	2.9	α $(10\bar{1}5)$	0.08796

Table 4.1 Ti-3.5Ni: Diffraction peaks (Cu k_α radiation)

*d-values from JCPDS 5-0682 (α titanium) and JCPDS 18-899 (Ti_2Ni)

Angle (°2θ)	d-value α_1 (nm)	Rel. intensity (%)	Identification	d-value* (nm)
13.525	0.65416	0.7	Ti_2Ni (111)	0.651
27.390	0.32536	0.6	Ti_2Ni (222)	0.326
35.275	0.25423	5.9	α $(10\bar{1}0)$	0.2557
36.745	0.24439	1.6	?	-
38.395	0.23426	100.0	α (0002)	0.2342
40.095	0.22471	16.5	α $(10\bar{1}1)$	0.2244
41.555	0.21715	4.9	Ti_2Ni (511)/(333)	0.2171
45.425	0.19950	0.9	Ti_2Ni (440)	0.1994
53.000	0.17264	5.1	α $(10\bar{1}2)$	0.1726
59.315	0.15567	0.5	?	-
62.900	0.14764	0.3	α $(11\bar{2}0)$	0.1475
70.485	0.13349	7.7	α $(10\bar{1}3)$	0.1332
75.855	0.12532	0.5	α $(11\bar{2}2)$	0.1247
77.325	0.12330	0.7	α $(20\bar{2}1)$	0.1233
78.965	0.12115	0.3	low significance	-
82.245	0.11713	3.5	α (0004)	0.11708
92.540	0.10660	0.8	α $(10\bar{1}4)$	0.10653
102.035	0.09909	0.3	α $(20\bar{2}3)$	0.09895
113.825	0.09194	0.7	α $(11\bar{2}4)$	0.09175
118.270	0.08974	0.3	α $(21\bar{3}2)$	0.08927
122.065	0.08804	1.9	α $(10\bar{1}5)$	0.08796

Table 4.2 Ti-5Ni: Diffraction peaks (Cu k_α radiation)

*d-values from JCPDS 5-0682 (α titanium) and JCPDS 18-899 (Ti_2Ni)

phase separation.* It also probably would not partition to the Ti_2Ni phase, since there is no stable phase of the same structure in the titanium-molybdenum system, and so would hinder its nucleation. Huang et al.[103] have reported that in binary titanium alloys, increasing additions of molybdenum decrease the critical cooling rate necessary for retention of the β phase, whereas increasing additions of nickel increase it.

The microstructures of these alloys were also observed by transmission electron microscopy (fig. 4.21). The second phase particles are electron-optically dense and appear more angular and elongated than in the backscattered images, doubtless because of the higher resolution. They occur at triple points on the α grain boundaries. The high electron-optical density made it impossible to obtain selected area diffraction patterns of the particles.

4.2 Surface Effects of Hydriding

4.2.1 Grade 2 Titanium

The surfaces of the grade 2 tensile specimens were examined by light microscopy after 1, 3 and 7 days of the hydriding treatment. In the case of the equiaxed specimens, the 1 day exposure merely caused etching of the grain boundaries and the appearance of different coloured grains owing to the varying thickness of the oxide layer developed on grains of different crystallographic orientation. After 3 days exposure, however, patterns of small needles within the grains on a scale of about 5 μm began to show themselves, similar to those reported by other workers as being characteristic of surface hydrides in titanium alloys (fig. 4.22). By 7 days, these fine patterns had disappeared, to be replaced by a smaller number of much longer needles apparently extending over several grains (fig. 4.23). Close examination showed that these hydrides actually always change direction slightly at the grain boundaries, and occasionally divide in two directions separated by a

* The diffusion coefficients at 300K for nickel and molybdenum in titanium, calculated from radioactive tracer impurity diffusion data[38], are 18×10^{-6} m^2/s and 3.2×10^{-6} m^2/s respectively.

Fig. 4.17 As-cast microstructures of Ti-3.5Ni (A) and Ti-5Ni (B) (optical)

Fig. 4.18 Microstructures after annealing at 725°C of Ti-3.5Ni (A) and Ti-5Ni (B) (BEI)

Fig. 4.21 Ti-3.5Ni 725°C annealed (TEM bright field)

Fig. 4.22 Surface hydrides on equiaxed grade 2 hydrogen charged for 3 days (optical)

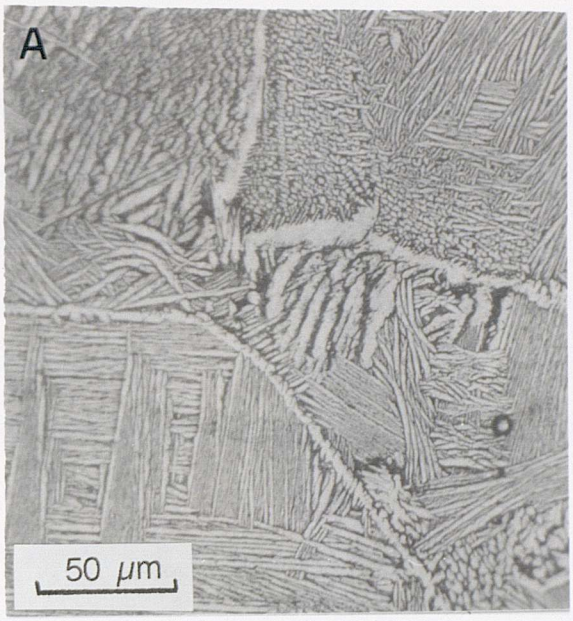
A
50 μm

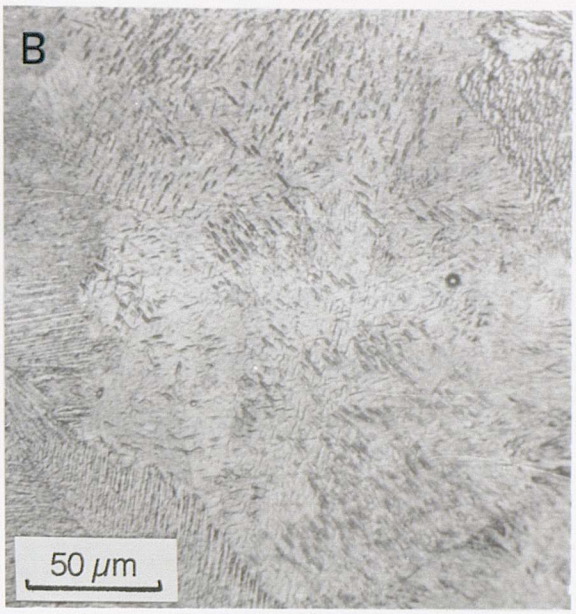
B
50 μm

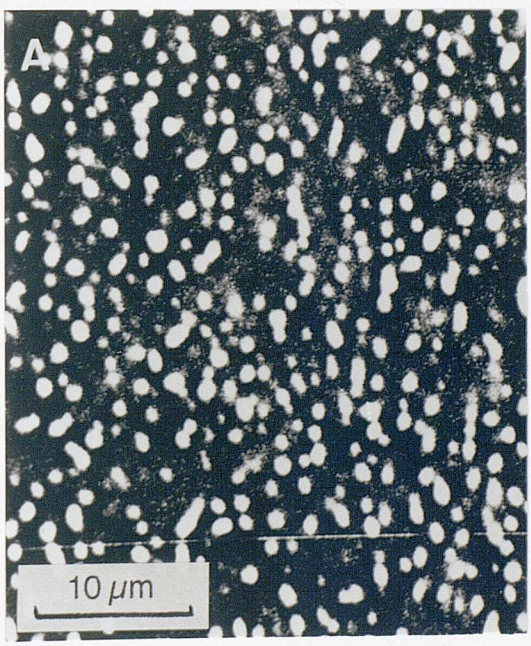
A
10 μm

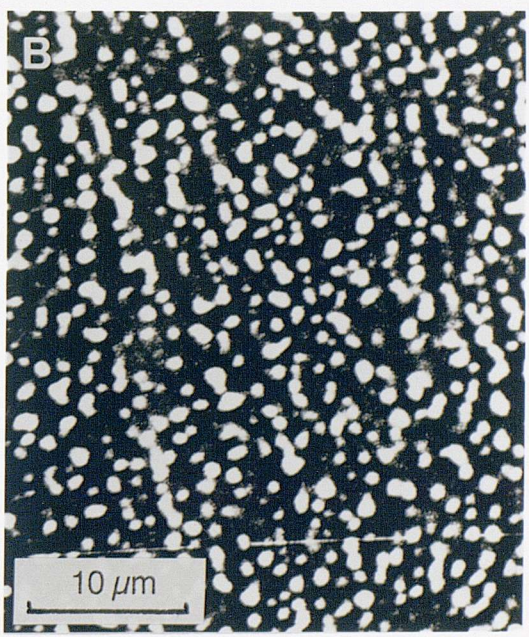
B
10 μm

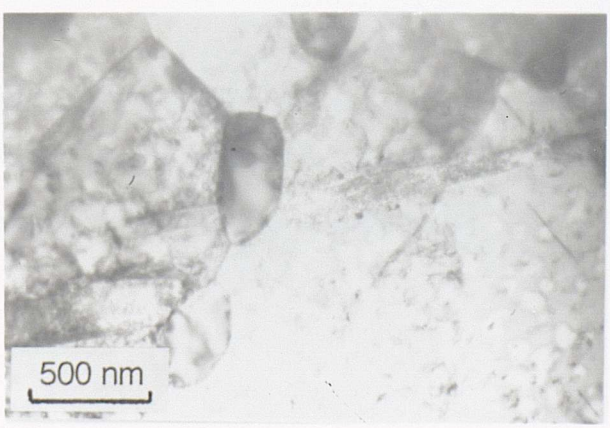
500 nm

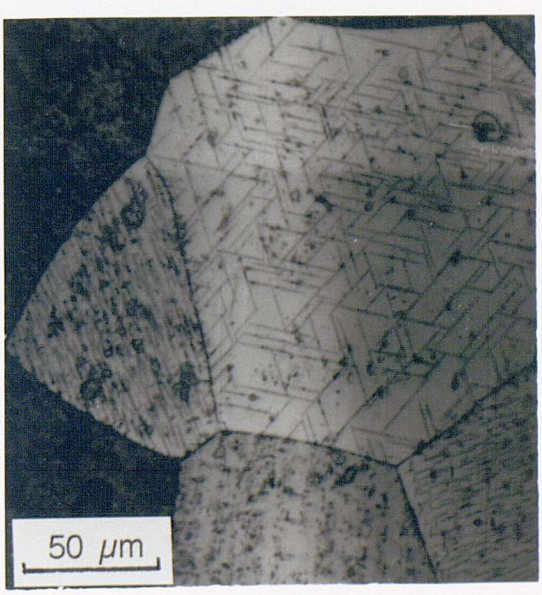
50 μm

small angle. Thus they provide an example of auto-catalytic nucleation, the hydride at the edge of one grain causing nucleation of another hydride in an adjacent grain on a plane or symmetrical pair planes as close as possible to the original direction in the new lattice. Previous work suggests that these needles are actually laths in 3 dimensions on particular habit planes in the titanium lattice. The change in the surface appearance between 3 and 7 days exposure suggests the effect of diffusional particle coarsening.

The transformed β specimens examined by light microscopy showed no such needles, suggesting that the hydrides, if present, must form in the boundaries between the fine lamellar grains (fig. 4.24). After 7 days exposure for both microstructures the surface oxide layer became too dark to permit optical examination of the surface.

4.2.2 Grade 12 Titanium

The hydrided grade 12 material did not show the formation of needles similar to those seen in the equiaxed grade 2 when the surfaces were examined optically, but a phase of intermediate darkness became visible between the α and β grains (fig. 4.25). This phase is much more clearly shown in the cross-sections examined by backscattered electron imaging in the SEM, to be described.

4.2.3 Grade 5 Titanum

Optical and SEM examination of the surface indicated no change in the microstructure of the grade 5 after hydriding.

4.2.4 Titanium-Nickel Alloys

Again, optical and SEM examination of the surfaces of these alloys revealed no microstructural changes on hydriding.

Fig. 4.23 Surface hydrides on equiaxed grade 2 hydrogen charged for 7 days (optical)

Fig. 4.25 Surface of equiaxed grade 12 hydrogen charged for 7 days (optical)

Fig. 4.24 Surface of transformed ß grade 2 hydrogen charged for 7 days (optical)

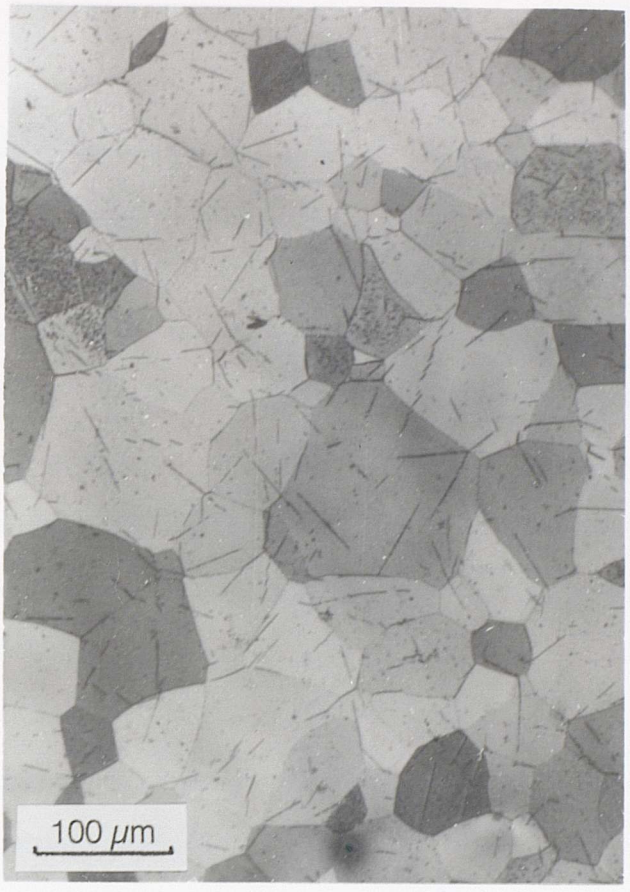
100 μm

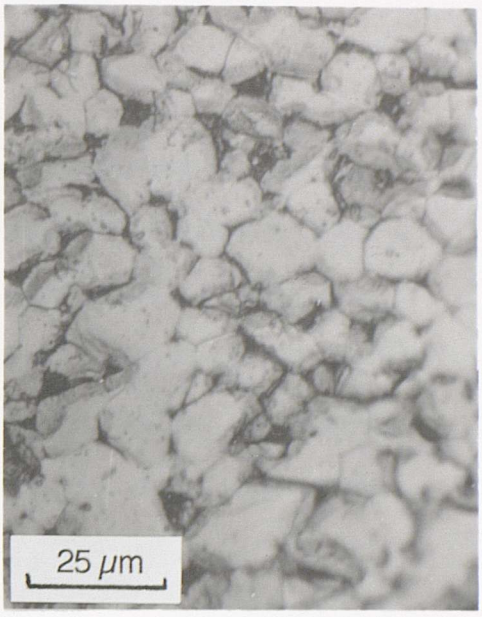
25 μm


100 μm

4.3 Tensile Properties

4.3.1 Grade 2 Titanium

Tensile tests were performed on both equiaxed and transformed β grade 2 samples after 0, 3, 7 and 20 days hydriding treatment. The results are shown in figs. 4.26-4.28. There is evidence of a small increase in ductility of both microstructures (of about 5%) up to 14 days hydriding, but this is removed by 20 days hydriding. There is no evidence of embrittlement. The peak stresses and 0.1% proof stresses show no changes. It is noted that the ductility of the equiaxed specimens is about twice that of the transformed β specimens.

Tensile tests were also performed on samples of both microstructures which had had a hydriding treatment of 7 days and a subsequent anneal under argon for 24 hours at temperatures of 250, 300 and 450°C in order to diffuse the hydride layer into the bulk. The results, given in figs. 4.29-4.31, show no evidence of any changes caused by these treatments.

4.3.2 Grade 12 Titanium

Tests were performed on samples having the equiaxed microstructure hydrided for 0, 7 and 20 days and on samples having the basketweave microstructure hydrided for 0 and 20 days. The results are shown in figs. 4.32-4.34. (The absence of data for the intermediate hydriding time for the basketweave material is due to a shortage of material.) It can be seen that there is a major degradation in the properties of both types of material when subjected to these treatments (table 4.3). The two microstructures suffer an equal percentage reduction in ductility, but the reductions in the peak and 0.1% proof stresses are greater for the basketweave. For the equiaxed material, tested for the intermediate hydriding time, it is seen that most of the reduction in ductility takes place by 7 days, but the peak and 0.1% proof stresses are not much affected until 20 days hydriding.

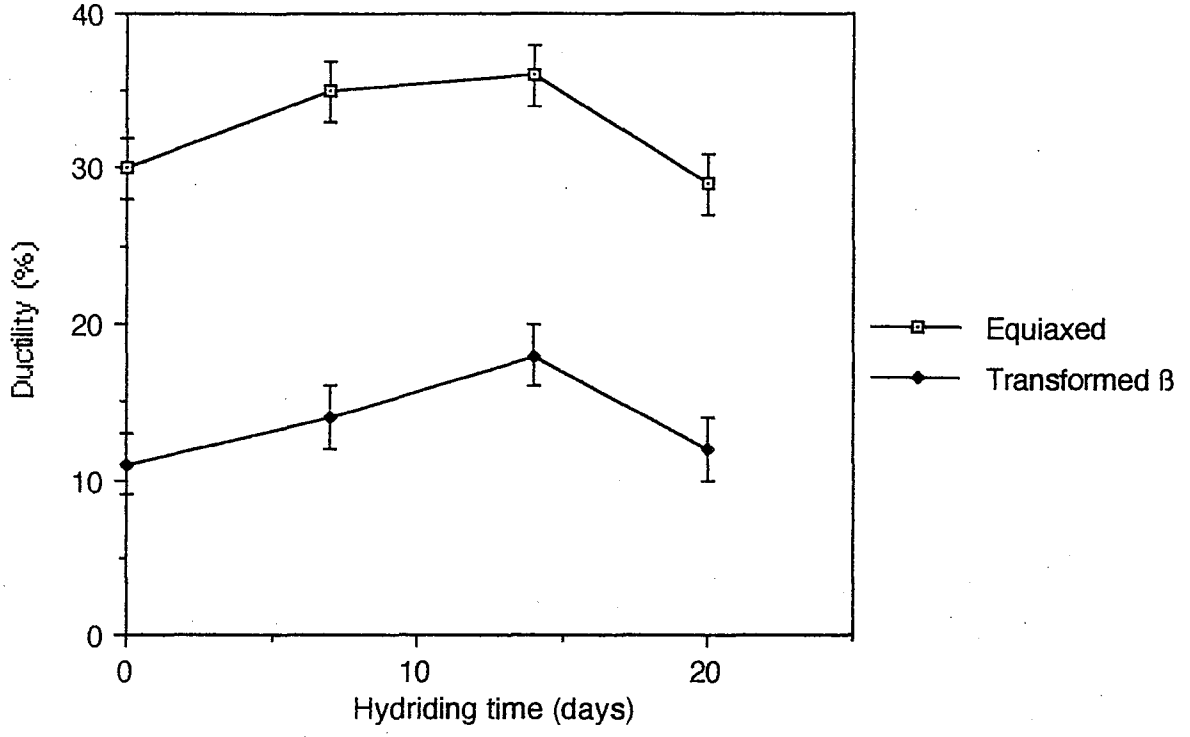

Fig. 4.26 Ductility of grade 2

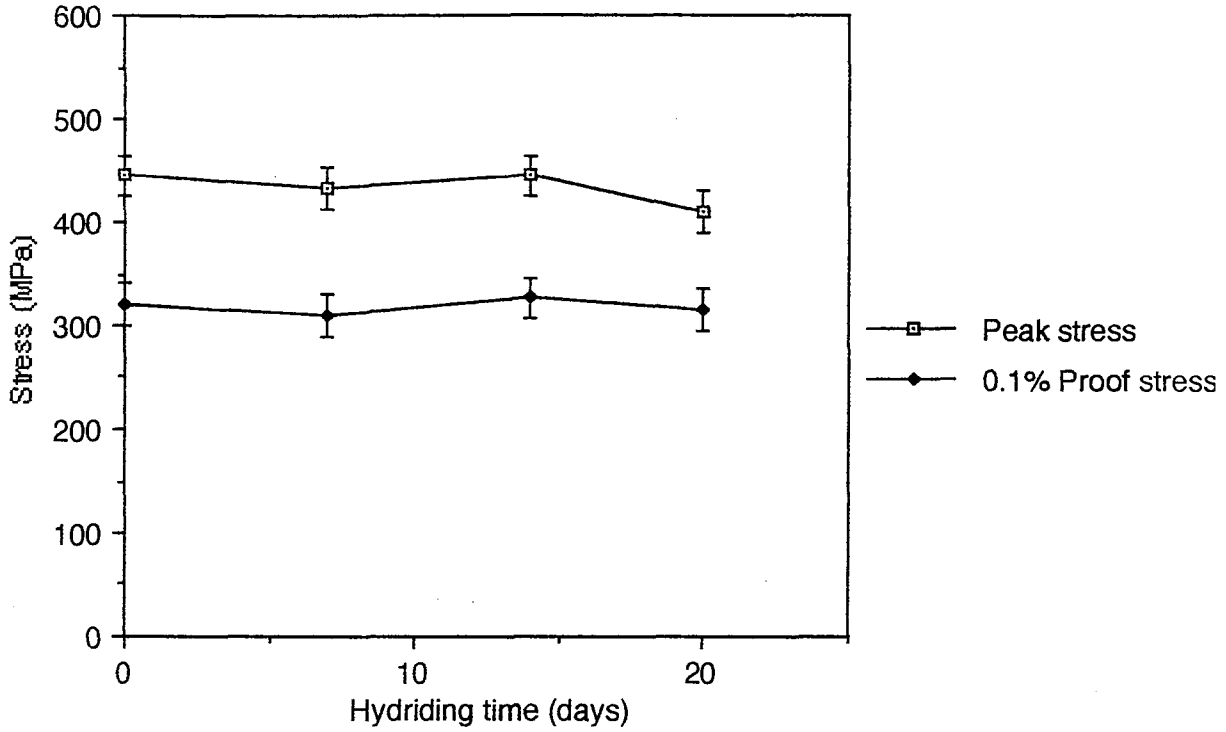

Fig 4.27 Peak stress and 0.1% proof stress for equiaxed grade 2

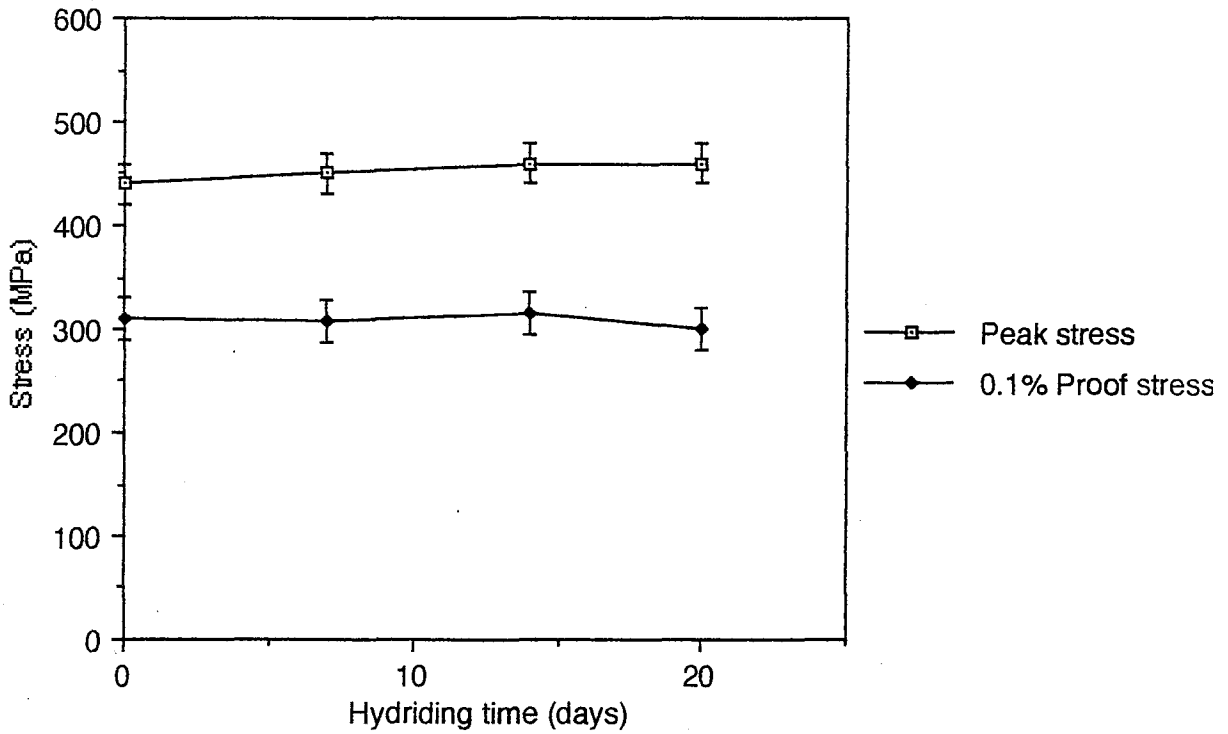

Fig. 4.28 Peak stress and 0.1% proof stress for transformed ß grade 2

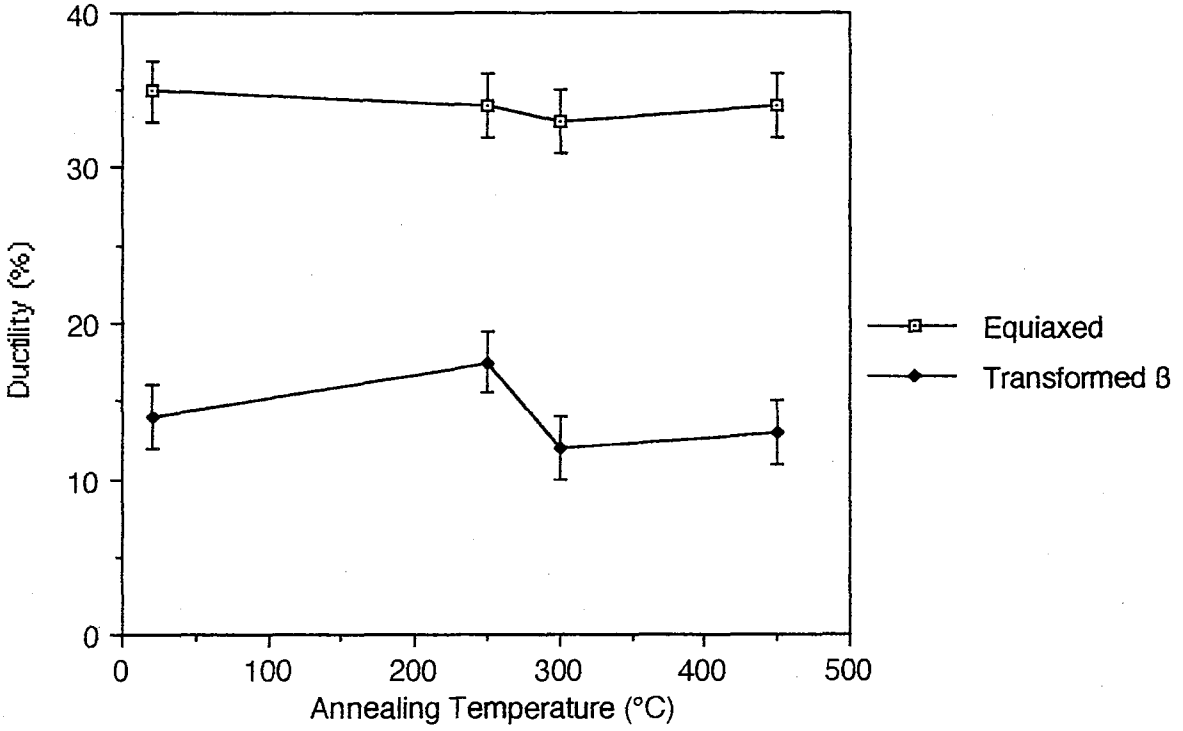

Fig. 4.29 Ductility against annealing temperature for 7 day hydrided grade 2

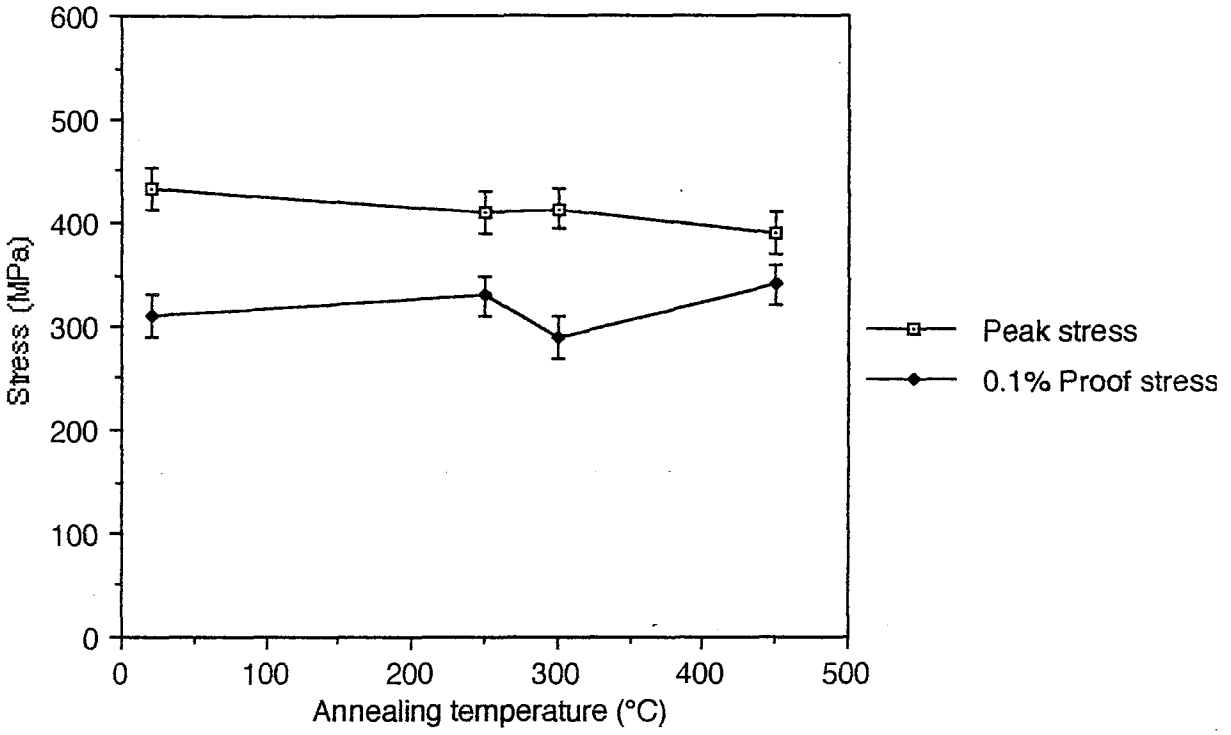

Fig. 4.30 Peak stress and 0.1% proof stress against annealing temperature for 7 day hydrided equiaxed grade 2

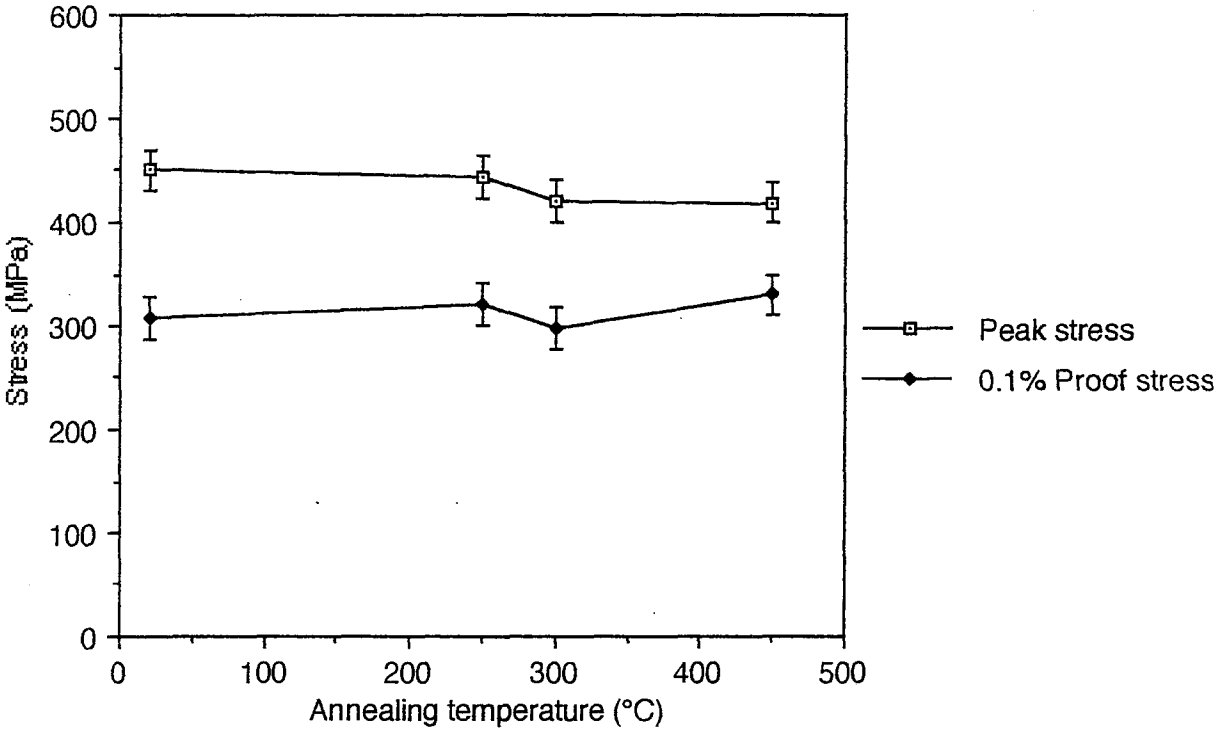

Fig. 4.31 Peak stress and 0.1% proof stress against annealing temperature for 7 day hydrided transformed ß grade 2

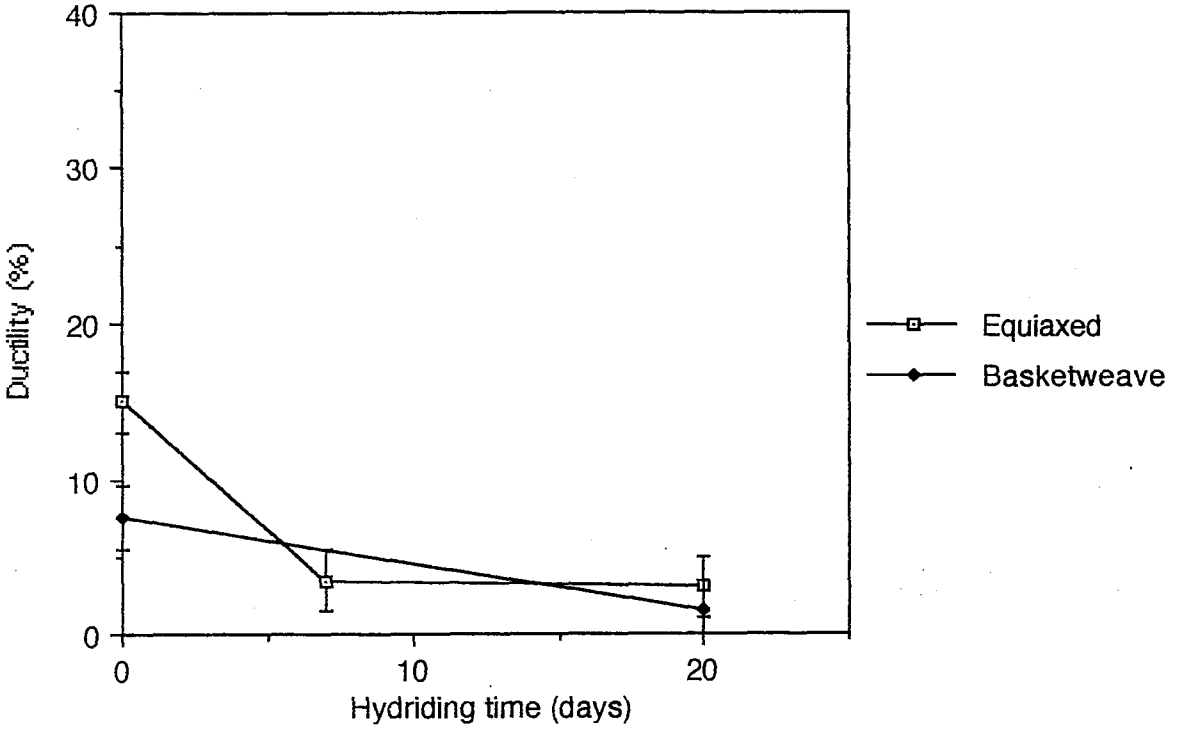

Fig. 4.32 Ductility of grade 12

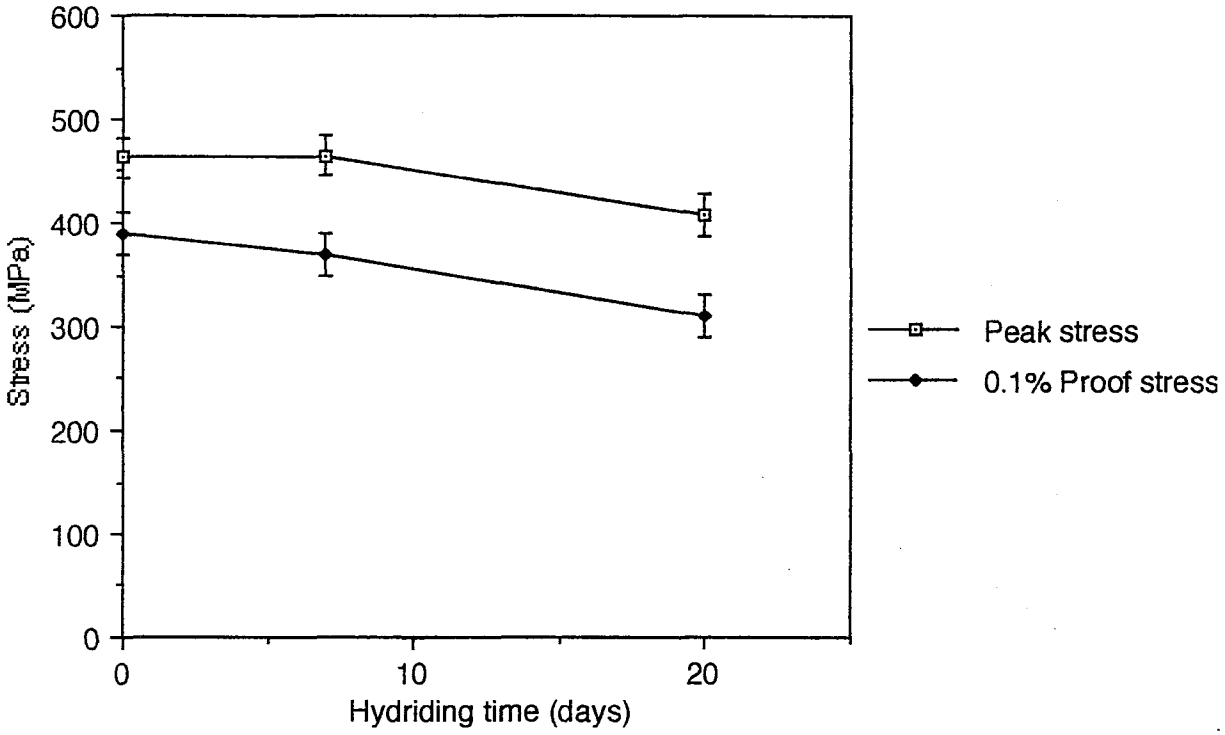

Fig. 4.33 Peak stress and 0.1% proof stress for equiaxed grade 12

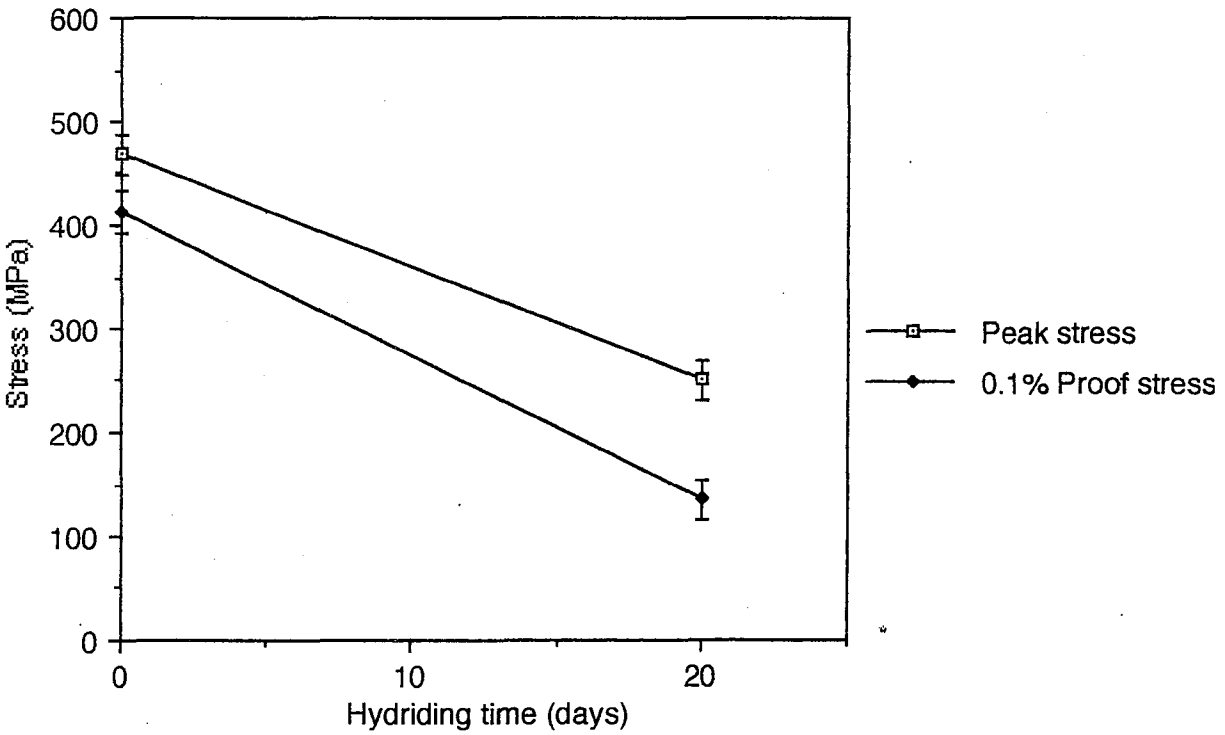

Fig. 4.34 Peak stress and 0.1% proof stress for basketweave grade 12

Tests were also performed on equiaxed samples hydrided for 7 days and then annealed for 24 hours at temperatures of 250, 300, and 450°C. The results, given in figs. 4.35-4.36, show a partial recovery of the lost ductlity between 250 and 300°C, but no effects on the peak and 0.1% proof stresses.

4.3.3 Titanium-Nickel Alloys

Samples of Ti-3.5Ni and Ti-5Ni were tested after 0 and 7 days hydrogen exposure, the results being given in tables 4.4-4.5. All properties show degradation in these alloys except from the peak and 0.1% proof stresses for the Ti-3.5Ni, which are little changed.

Tests were done on 7 day exposed Ti-3.5Ni samples subsequently annealed for 24 hours at 250, 300 and 450°C. The results are given in figs. 4.37-4.38. They show a further degradation of properties with increasing annealing temperature beyond that seen in the unannealed hydrided specimens. As before, most change in the ductilty seems to occur in the range 250-300°C, though the change here is in the opposite direction to that in the grade 12. This further degradation of properties may be the result of the diffusion of solute hydrogen from near-surface regions into the bulk during annealing, but the presence of the step in the ductility measurements between 250 and 300°C suggests the dissolution of hydrides in this range with subsequent redistribution of hydrogen through the material and reprecipitation of hydrides. Observations were made using backscattered electron imaging of cross-sections of annealed samples in order to test this (section 4.5).

4.4 Fracture Characteristics

4.4.1 Grade 2 Titanium

The general characters of the normal, unhydrided fractures of equiaxed and transformed β are shown in figs. 4.39-4.40. Both microstructures give rise to typical ductile fracture characteristics, with dimpled fracture surfaces and slip bands on the sample surfaces adjacent to the fractures indicative of extensive plastic deformation, though these are less prevalent on the transformed β surface, consistent with the lower ductility recorded for

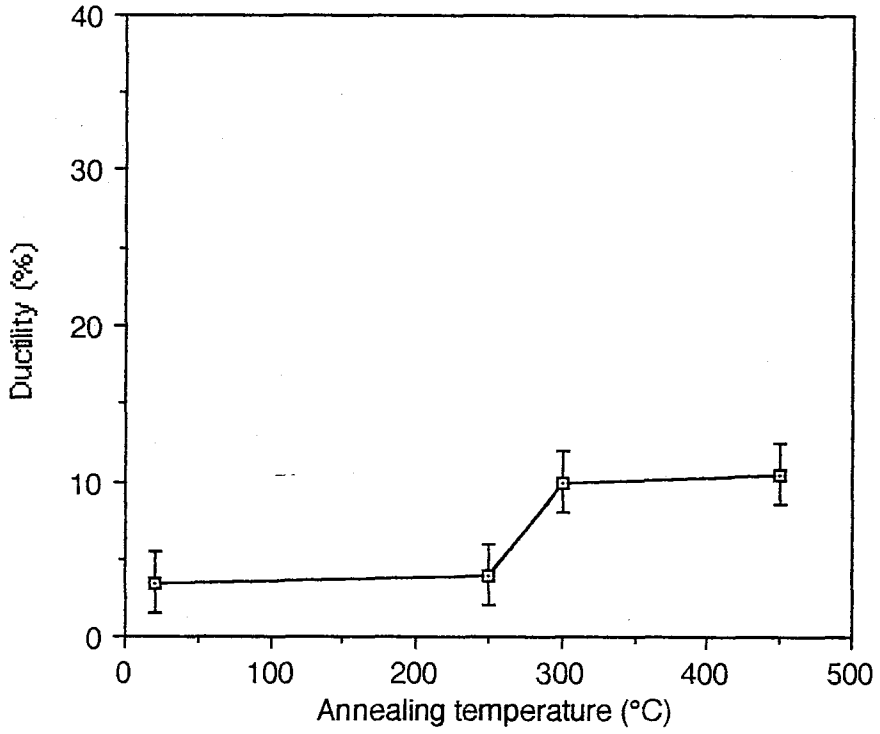

Fig. 4.35 Ductility against annealing temperature for 7 day hydrided equiaxed grade 12

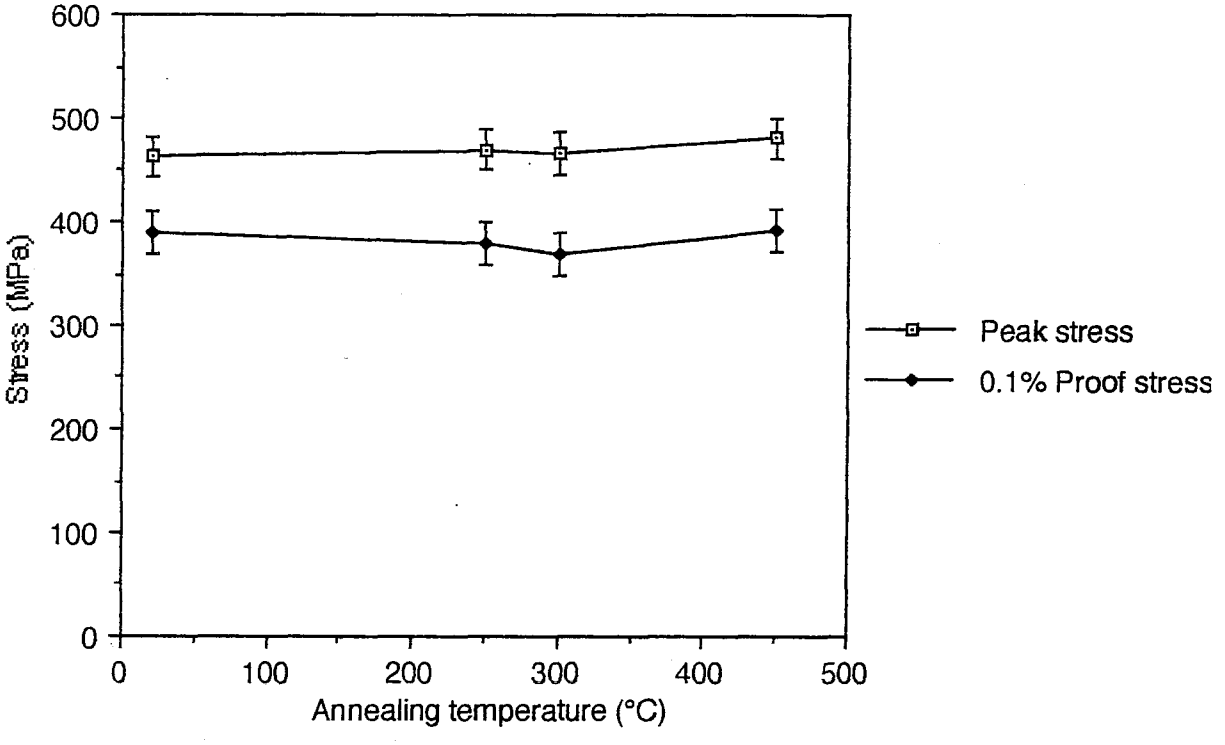

Fig. 4.36 Peak stress and 0.1% proof stress against annealing temperature for 7 day hydrided equiaxed grade 12

	Ductility	Peak Stress	0.1% Proof Stress
Equiaxed (7 days)	77	0	5
Equiaxed (20 days)	80	12	21
B/weave (20 days)	80	47	67

Table 4.3 Percentage reductions in tensile parameters of grade 12 microstructures after hydriding

	Ductility	Peak Stress	0.1% Proof Stress
Unhydrided	23.5±2%	504±20 MPa	370±20 MPa
Hydrided 7 days	11	486	370
% Reduction	53	4	0

Table 4.4 Ti-3.5Ni: tensile results

	Ductility	Peak Stress	0.1% Proof Stress
Unhydrided	13.5±2%	597±20 MPa	440±20 MPa
Hydrided 7 days	7	509	370
% Reduction	48	15	16

Table 4.5 Ti-5Ni: tensile results

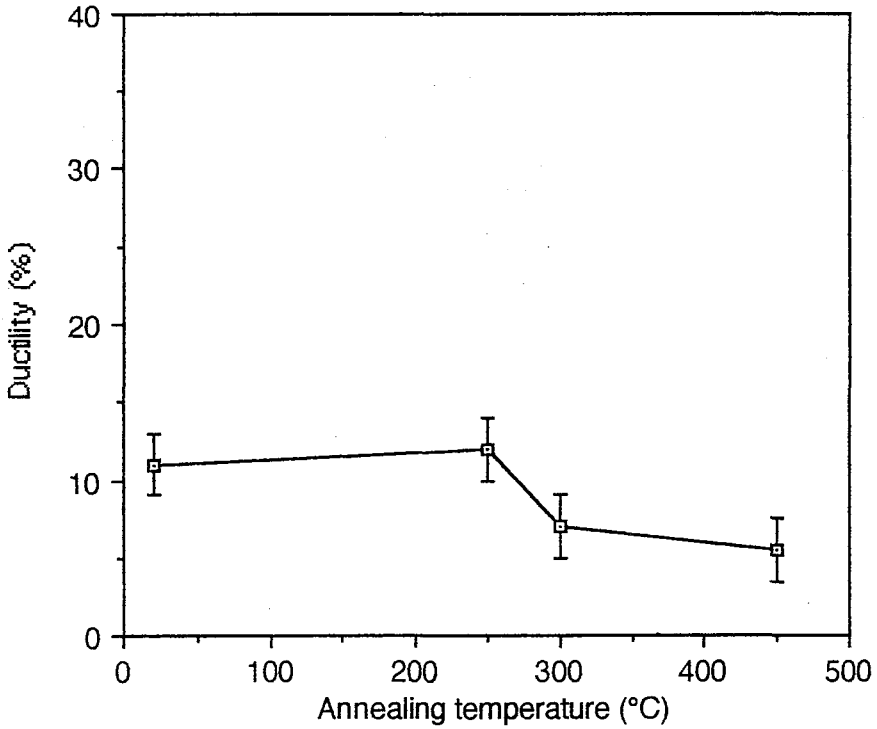

Fig. 4.37 Ductility against annealing temperature for 7 day hydrided Ti-3.5Ni

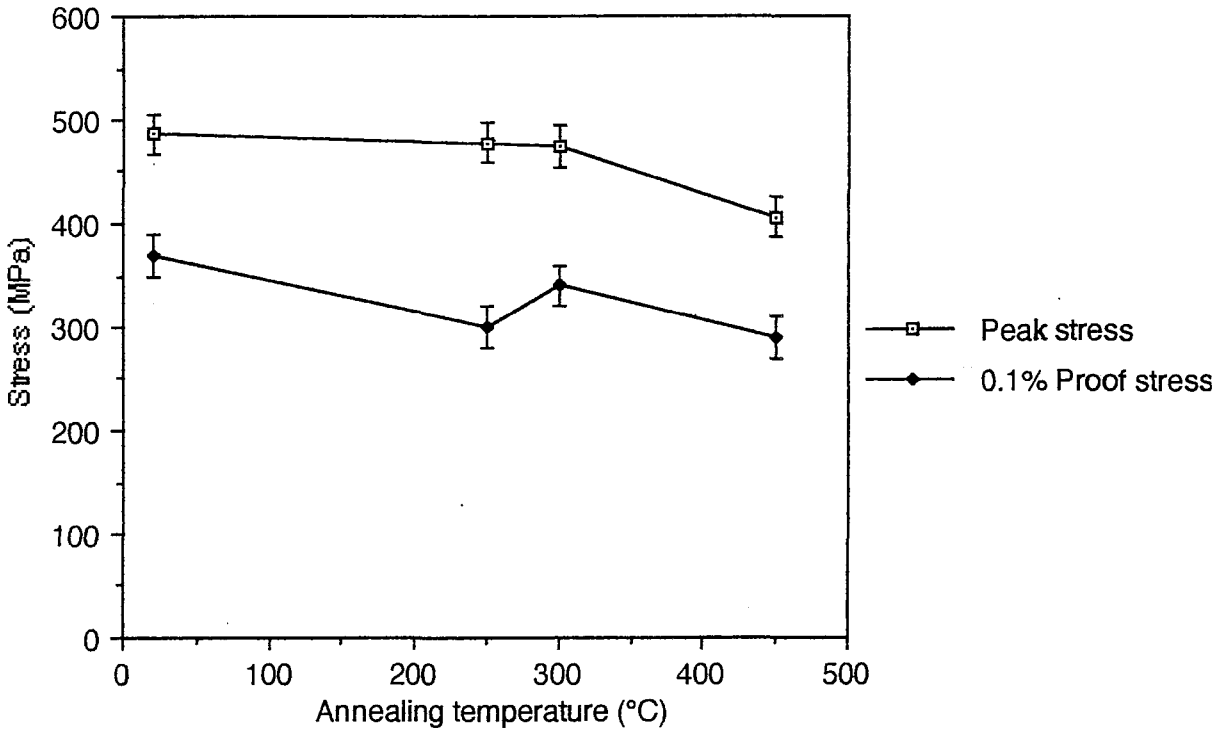

Fig. 4.38 Peak stress and 0.1% proof stress against annealing temperature for 7 day hydrided Ti-3.5Ni

that microstructure. The corresponding fractures after 20 days hydriding are shown in figs. 4.41-4.42. There are no marked changes, the fractures still being ductile, agreeing with the lack of any changes in the measured tensile properties. It is concluded that any embrittlement due to hydrides in the grade 2 must be restricted to a very narrow surface layer, and that up to 20 days the treatment resulted in no embrittlement of the bulk of the specimens.

4.4.2 Grade 12 Titanium

Changes were observed in the bulk fracture characteristics of the grade 12 samples consistent with the substantial measured degradation of their mechanical properties. The equiaxed material showed a change from a typical ductile fracture appearance (fig. 4.43) to a type of ridged fracture surface after 20 days hydriding (fig. 4.44). The basketweave material showed a change from a ductile (fig. 4.45) to a flat cleavage fracture appearance (fig. 4.46) after the same period. The fracture morphologies are probably related to the microstructures. The spacing of the ridges in the equiaxed case indicates that they may represent the greater plastic deformation of the less embrittled β grain boundary areas. The flat facets in the basketweave case probably represent the plate morphology in that case, in which embrittlement has occurred on the faces of the α plates.

The fractures of the 7 day hydrided equiaxed samples subsequently annealed at various temperatures were also studied. The unannealed and 250°C annealed samples (fig. 4.47), show a fairly ductile fracture appearance, in contrast to those annealed above 250°C (fig. 4.48), which show a jagged, cleavage-type fracture. On the other hand, the unannealed and 250°C annealed samples show more cracking at the surface than the higher temperature samples. The latter also show, in some cases (fig. 4.49), rectangular holes in the fracture surface. These results seem to confirm the conclusion given in section 4.3.3 that property changes in these alloys occur mainly in the annealing temperature range 250-300°C, suggesting hydride dissolution in this range.

Fig. 4.40 Fracture surface of unhydrided transformed ß grade 2

Fig. 4.42 Fracture surface of 20 day hydrided transformed ß grade 2

Fig. 4.39 Fracture surface of unhydrided equiaxed grade 2

Fig. 4.41 Fracture surface of 20 day hydrided equiaxed grade 2

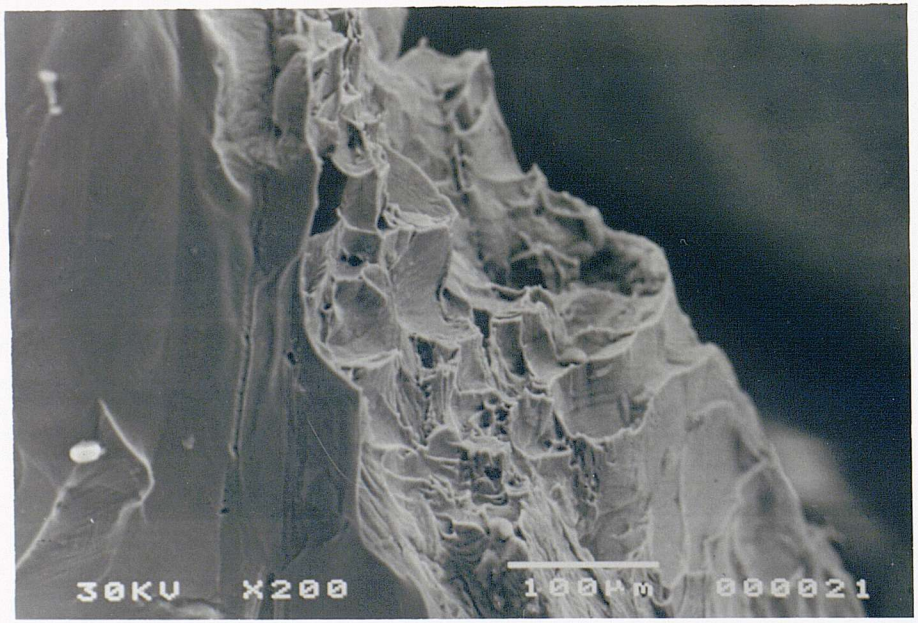
30KV X200
100µm 000021

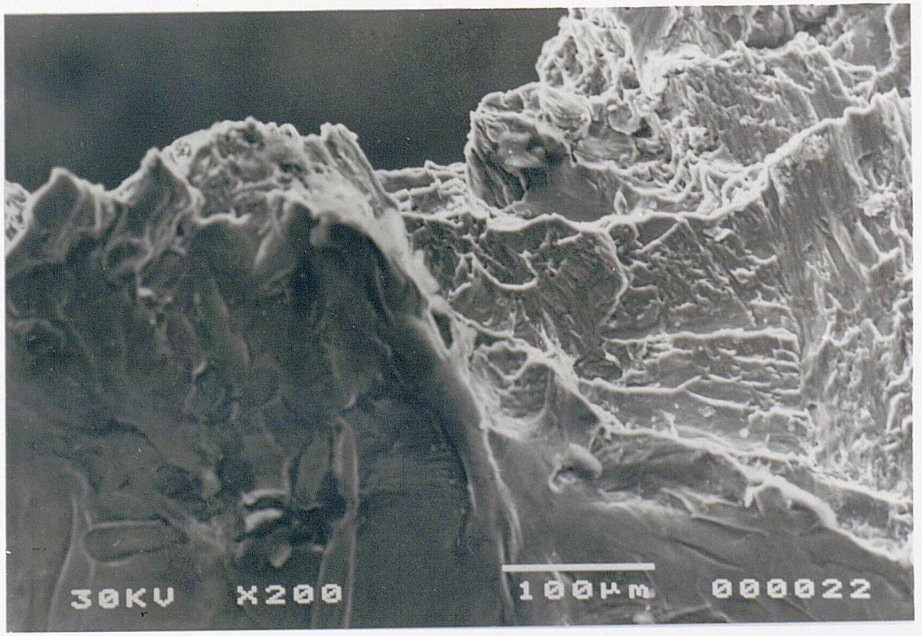
30KV X200
100µm 000022

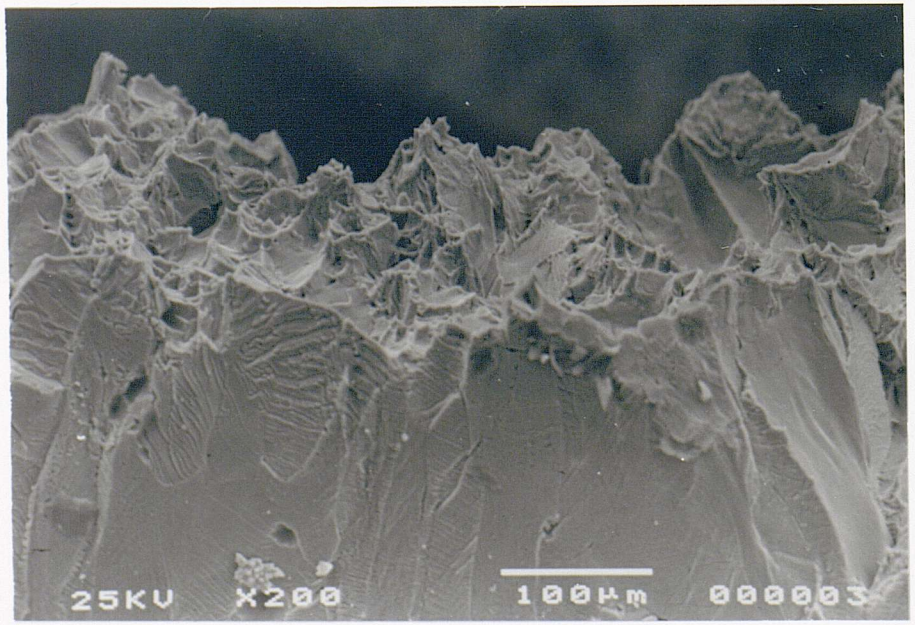
25KV X200
100µm 000003

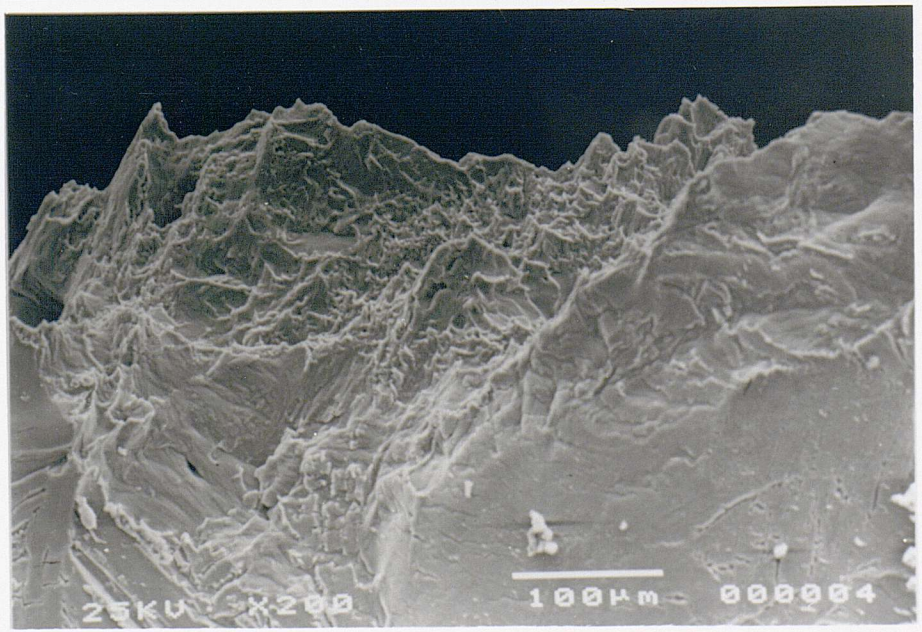
25KV X200
100µm 000004

Fig. 4.45 Fracture surface of unhydrided basketweave grade 12

Fig. 4.46 Fracture surface of 20 day hydrided basketweave grade 12

Fig. 4.43 Fracture surface of unhydrided equiaxed grade 12

Fig. 4.44 Fracture surface of 20 day hydrided equiaxed grade 12

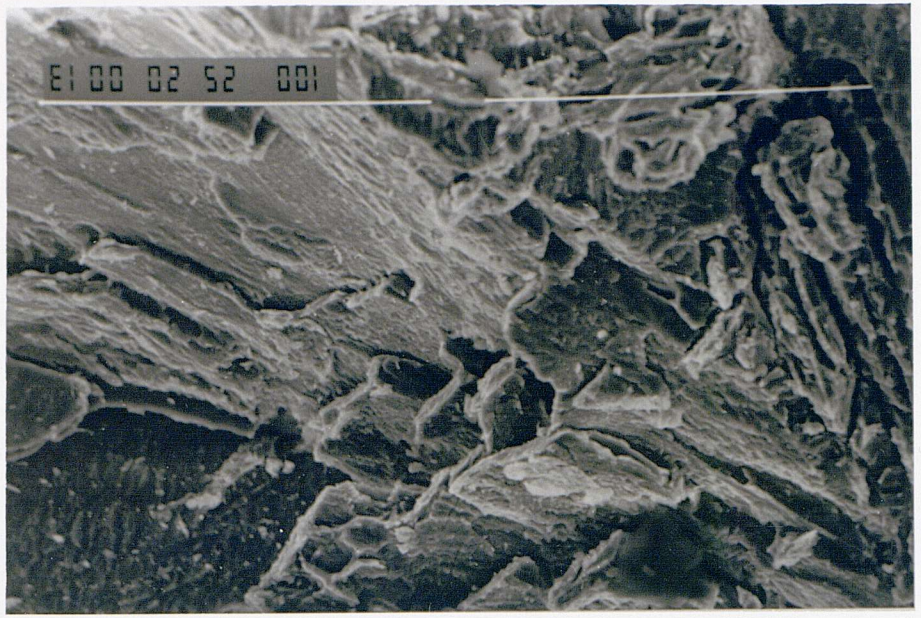
E1 00 02 52 001

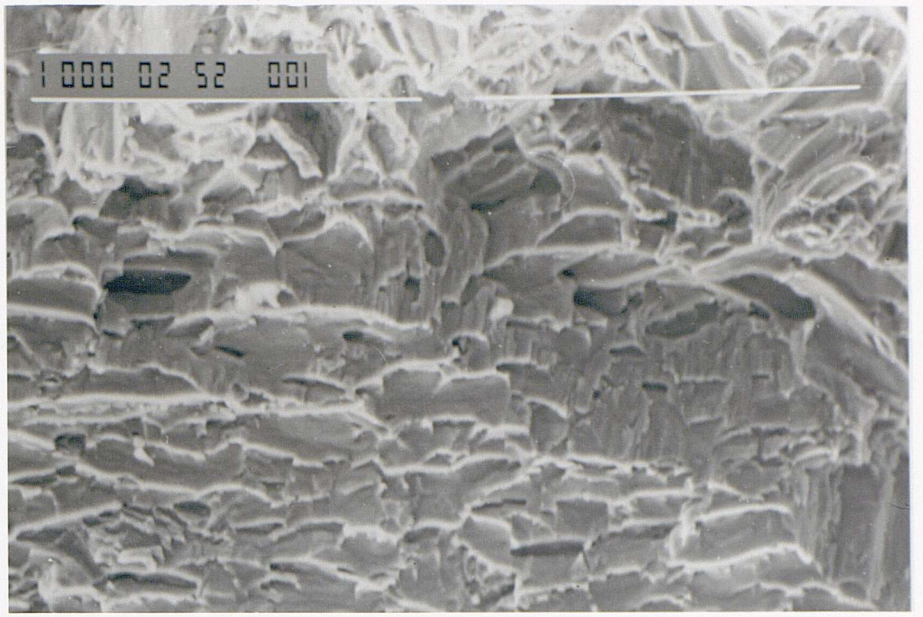
1 000 02 52 001

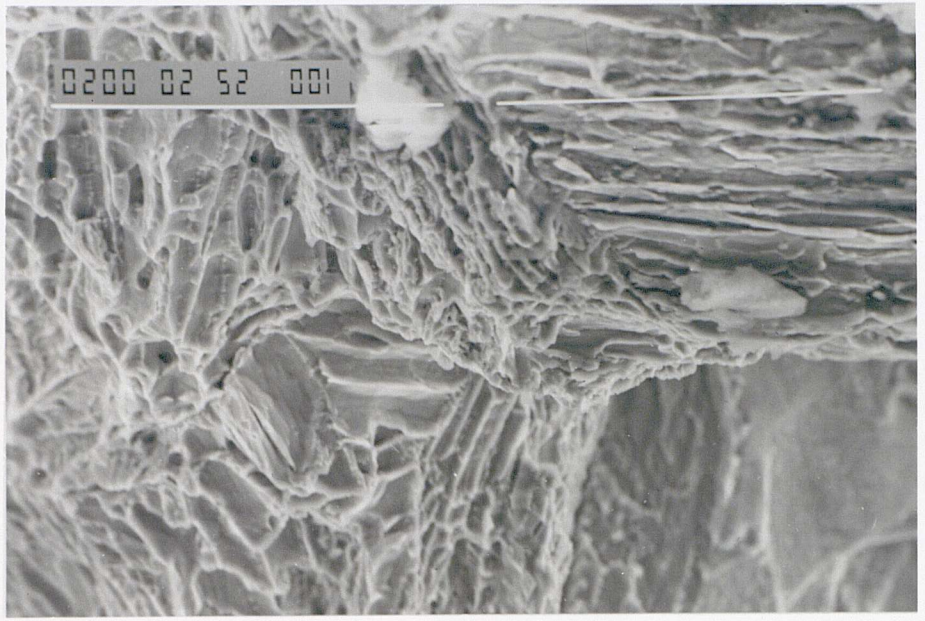
0200 02 52 001

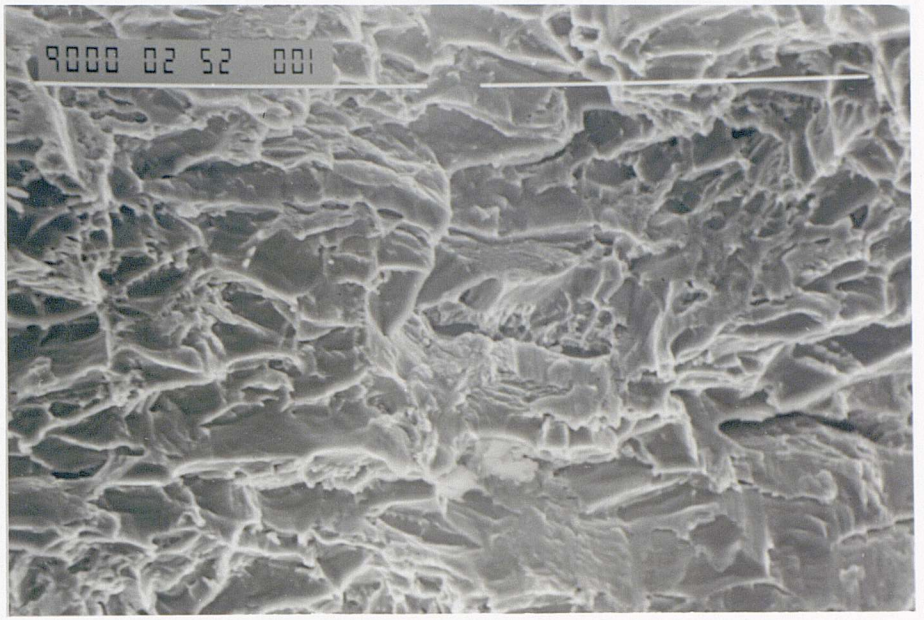
9000 02 52 001

Fig. 4.47 Fracture surface of unannealed 7 day hydrided equiaxed grade 12

Fig. 4.48 Fracture surface of 300°C annealed 7 day hydrided equiaxed grade 12

Fig. 4.49 Fracture surface of 450°C annealed 7 day hydrided equiaxed grade 12 showing rectangular holes

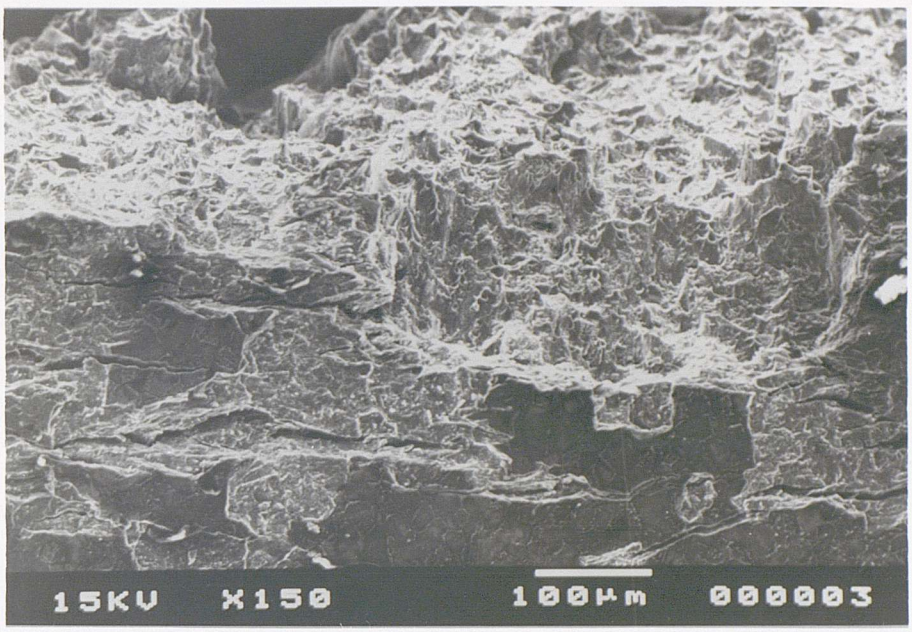
15KV X150 100µm 000003

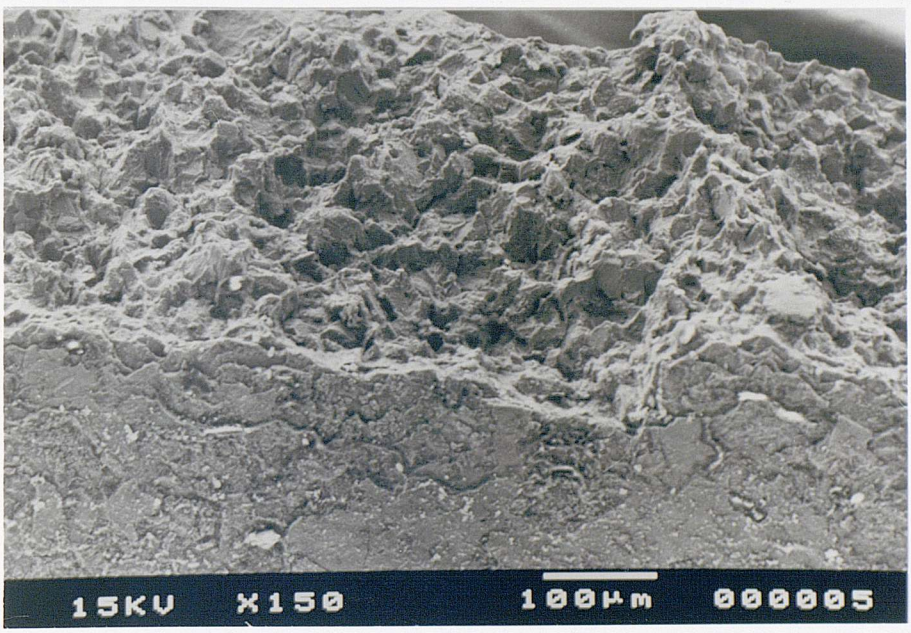
15KV X150 100µm 000005

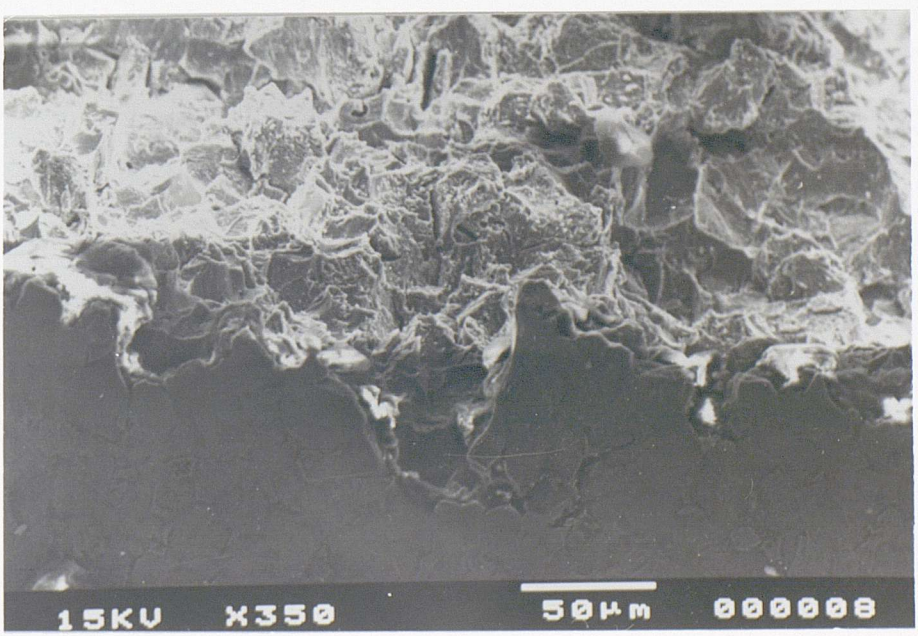
15KV X350 50µm 000008

4.4.3 Titanium-Nickel Alloys

The unhydrided fractures of Ti-3.5Ni and Ti-5Ni are shown in figs. 4.50-4.51. The detail on the fracture surfaces of these alloys is far finer than that on the fracture surfaces previously shown, and the dimpled structure is on a scale of about 2 μm, the same as the scale of the Ti_2Ni particles observed metallographically. The fracture surface detail in the Ti-5Ni seems slightly finer than that in the Ti-3.5Ni, corresponding with the slightly closer spacing of the particles in that alloy.

The equivalent images of the fracture surfaces of the 7 day hydrided specimens (figs. 4.52-4.53) show no changes. However, the lower magnification views of the samples (figs. 4.54-4.58) show, in both alloys, the development of a brittle surface layer estimated at 20-40 μm thick which has formed parallel cracks perpendicular to the strain axis and in some places at the edges has broken away.

The fractures of the 7 day hydrided Ti-3.5Ni specimens annealed at 250, 300 and 450°C all show this brittle layer (figs. 4.59-4.62), and show a progression from very parallel cracks in the layer on the unannealed specimen, through more irregular cracking, to a polygonal cracking pattern on the 450°C annealed specimen. Also, the tendency for the layer to break away from the underlying metal is lost in the 450°C specimen. At the same time, the high magnification views taken from near the centres of the fracture surfaces (figs. 4.63-4.66) show a gradual smoothing out of the dimpled surface to a cleavage-type fracture at the highest annealing temperature.

These results, and those of the mechanical testing, are clearly consistent with a model of hydrogen diffusion during annealing leading to a thicker embrittled layer and a progressively more uniformly embrittled material as the annealing temperature is raised. The cracks are parallel in the unannealed specimen because the surface layer has a much lower ductility than the material immediately underneath it and is thus stressed in only

Fig. 4.51 Fracture surface of unhydrided Ti-5Ni

Fig. 4.53 Fracture surface of 7 day hydrided Ti-5Ni

Fig. 4.50 Fracture surface of unhydrided Ti-3.5Ni

Fig. 4.52 Fracture surface of 7 day hydrided Ti-3.5Ni

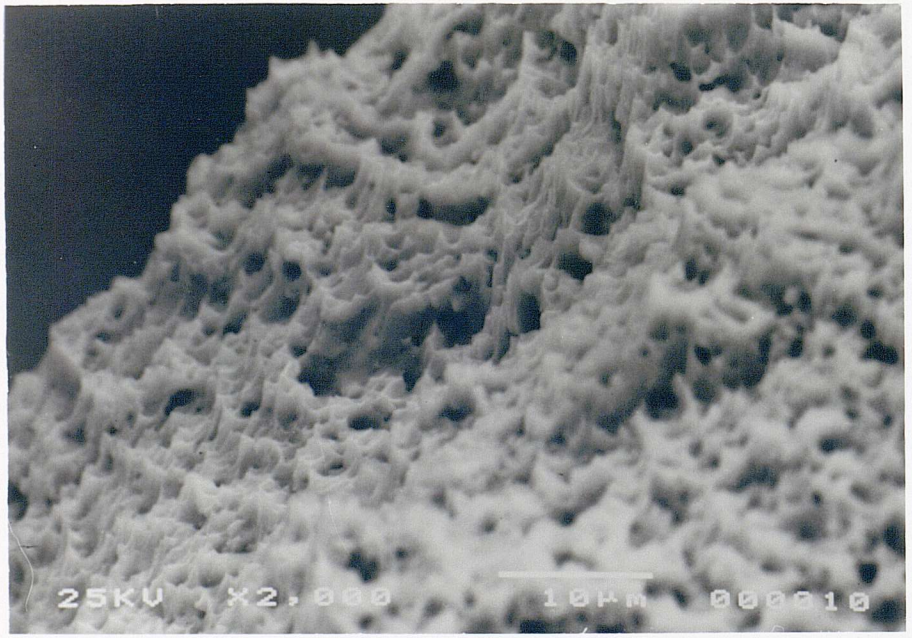
25KV X2,000 10µm 000010

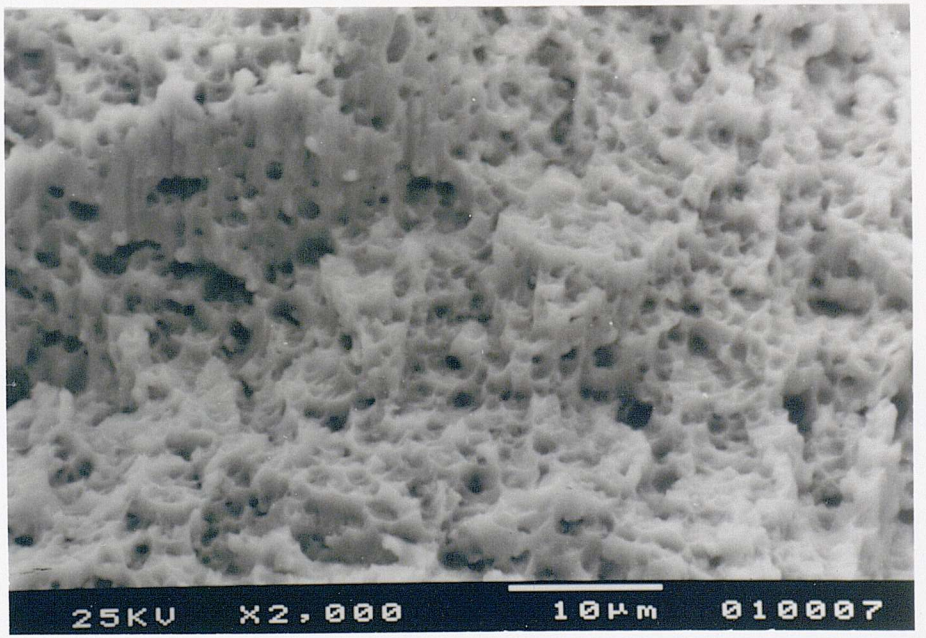
25KV X2,000 10µm 010007

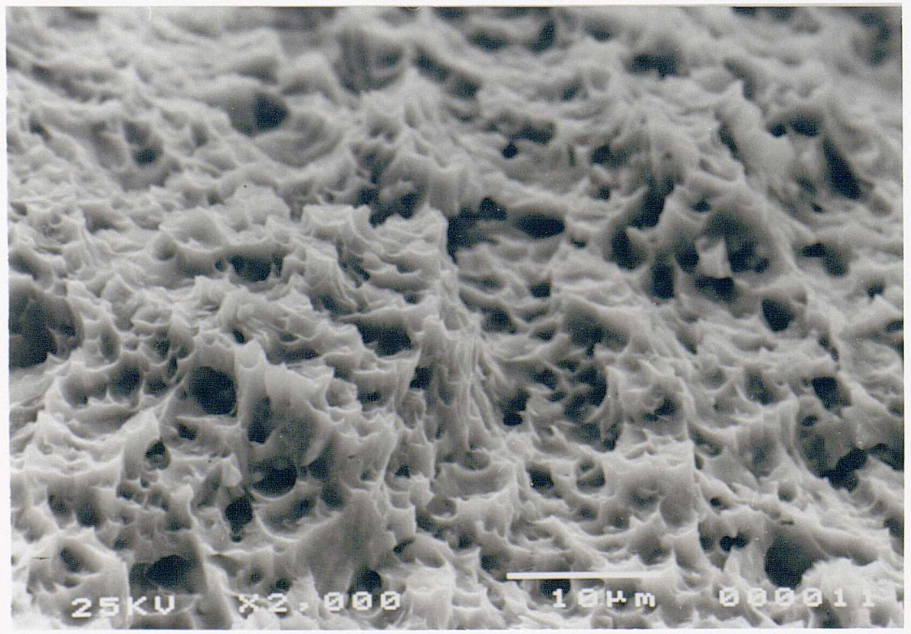
25KV X2,000 10µm 000011

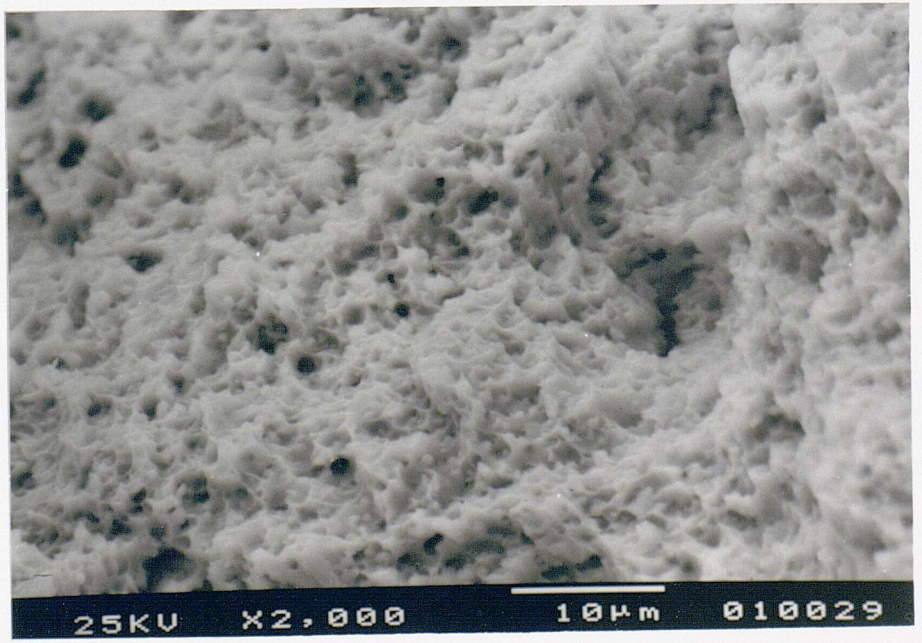
25KV X2,000 10µm 010029

Fig. 4.54 Fracture of unhydrided Ti-3.5Ni

Fig. 4.55 Fracture of 7 day hydrided Ti-3.5Ni

Fig. 4.56 Detail of above, showing breaking away of surface layer

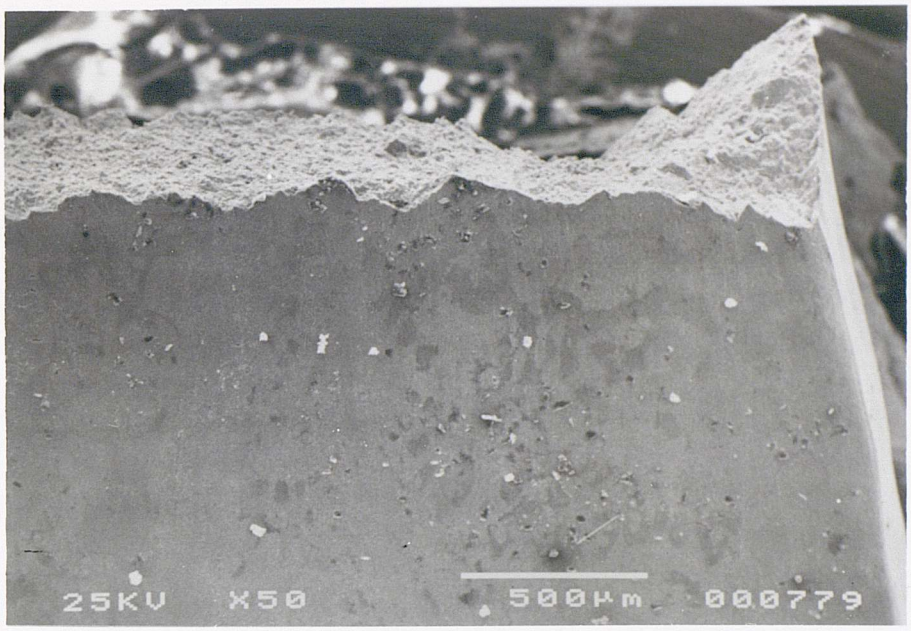
25KV X50 500µm 000779

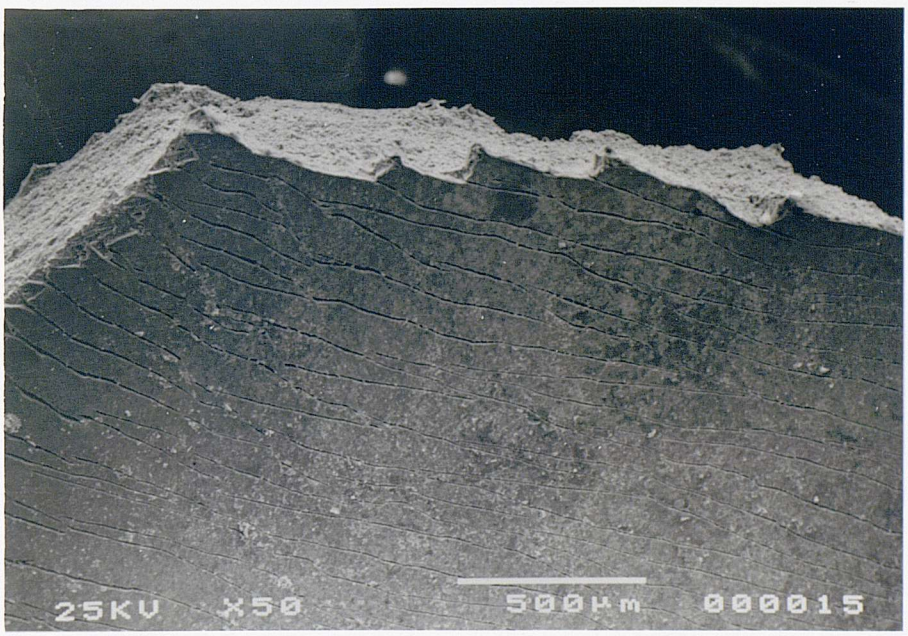
25KV X50 500µm 000015

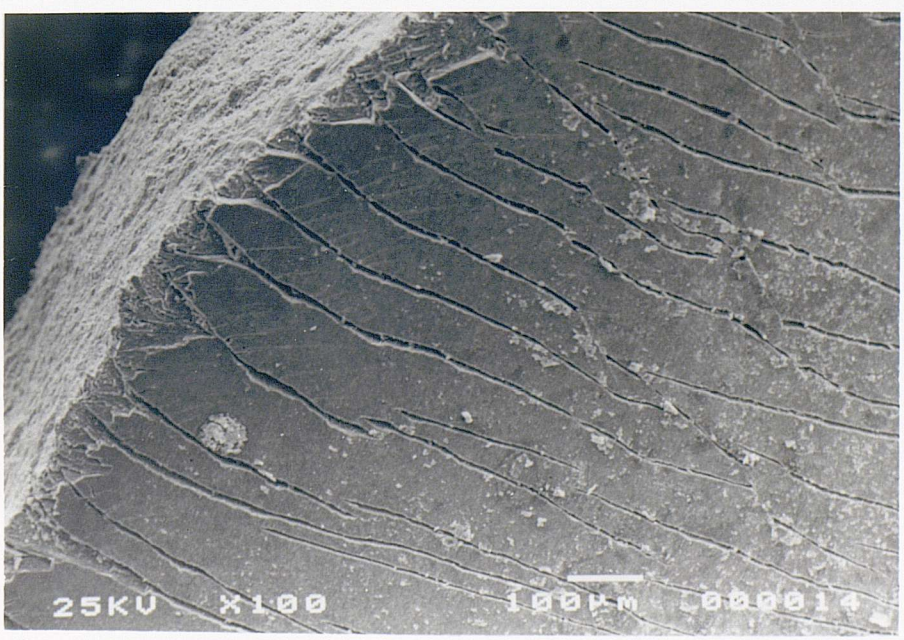
25KV X100 100µm 000014

Fig. 4.57 Fracture of unhydrided Ti-5Ni

Fig. 4.58 Fracture of 7 day hydrided Ti-5Ni

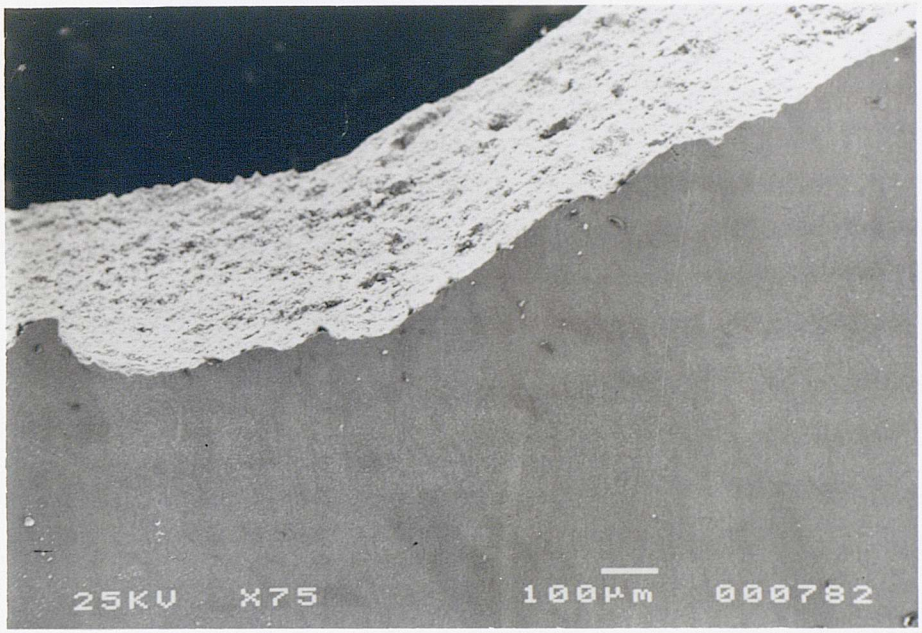
25KV X75 100µm 000782

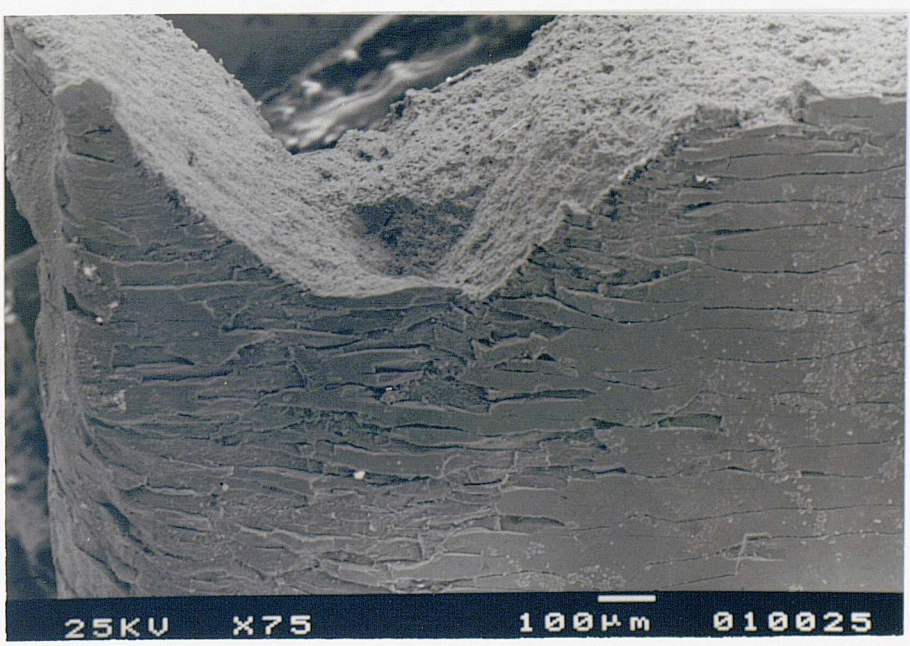
25KV X75 100µm 010025

Fig. 4.61 Fracture of 300°C annealed 7 day hydrided Ti-3.5Ni

Fig. 4.62 Fracture of 450°C annealed 7 day hydrided Ti-3.5Ni

Fig. 4.59 Fracture of unannealed 7 day hydrided Ti-3.5Ni

Fig. 4.60 Fracture of 250°C annealed 7 day hydrided Ti-3.5Ni

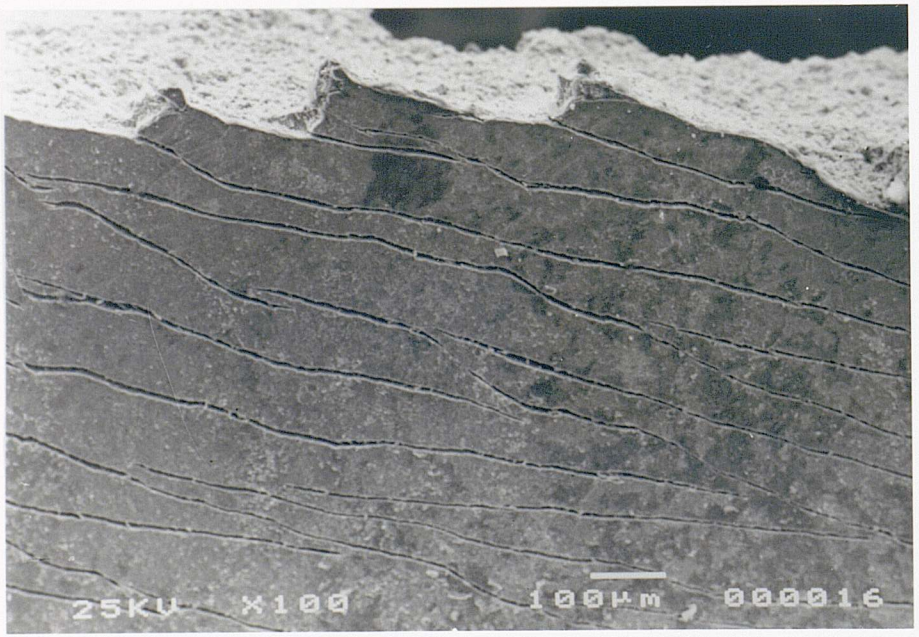
25KV X100 100µm 000016

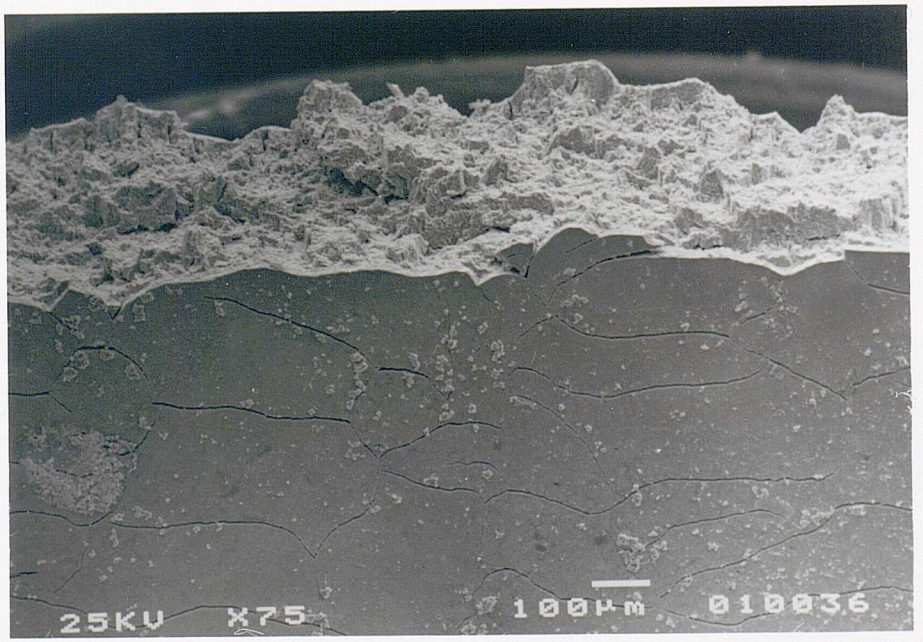
25KV X75 100µm 010036

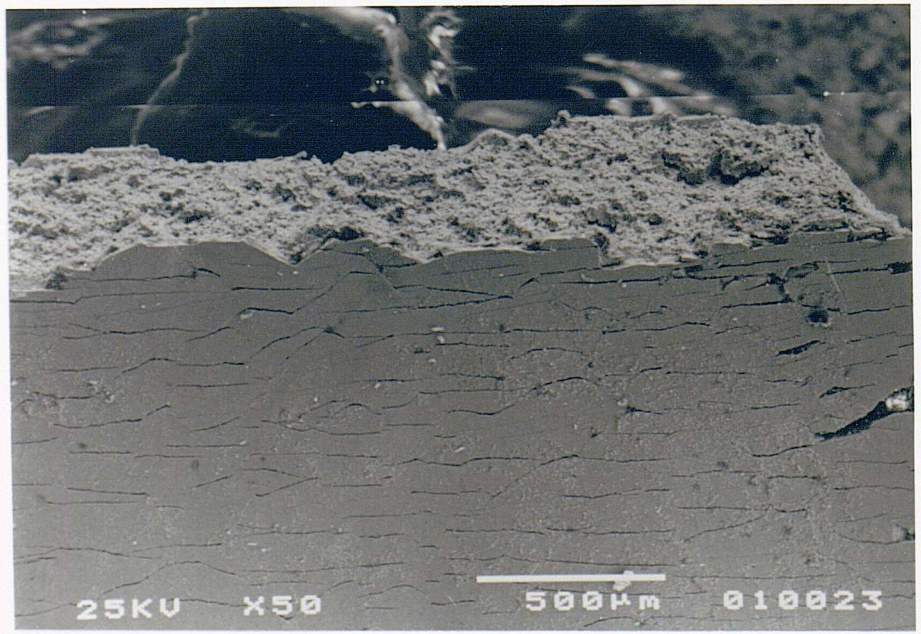
25KV X50 500µm 010023

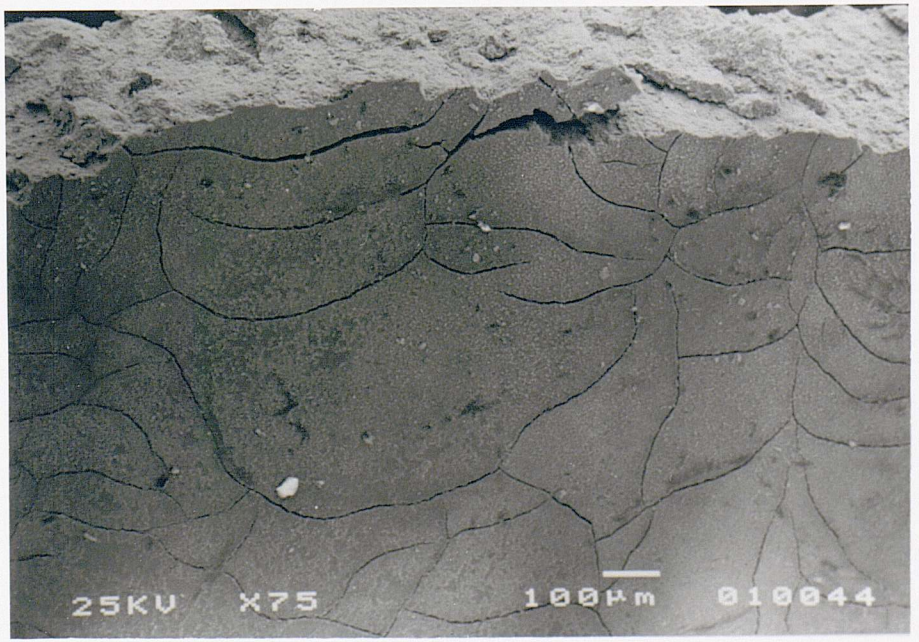
25KV X75 100µm 010044

Fig. 4.65 Fracture surface of 300°C annealed 7 day hydrided Ti-3.5Ni

Fig. 4.66 Fracture surface of 450°C annealed 7 day hydrided Ti-3.5Ni

Fig. 4.63 Fracture surface of unannealed 7 day hydrided Ti-3.5Ni

Fig. 4.64 Fracture surface of 250°C annealed 7 day hydrided Ti-3.5Ni

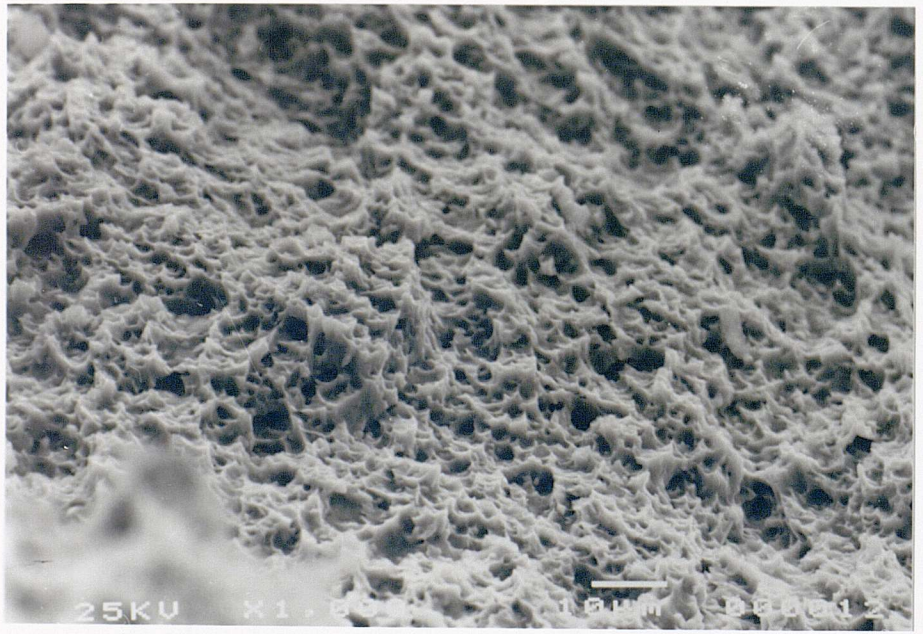
25KV


25KV X1,500

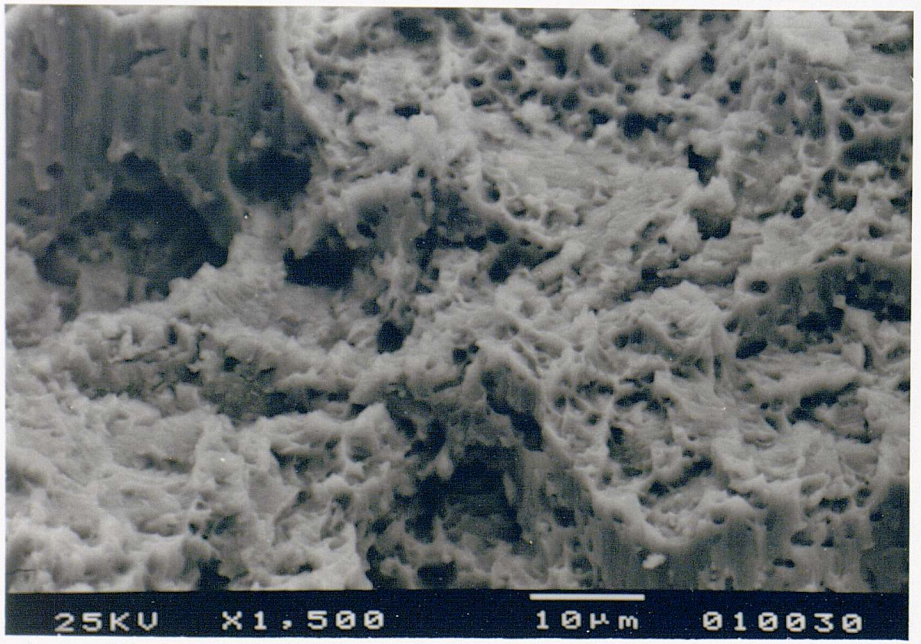
25KV X1,500 10µm 010030

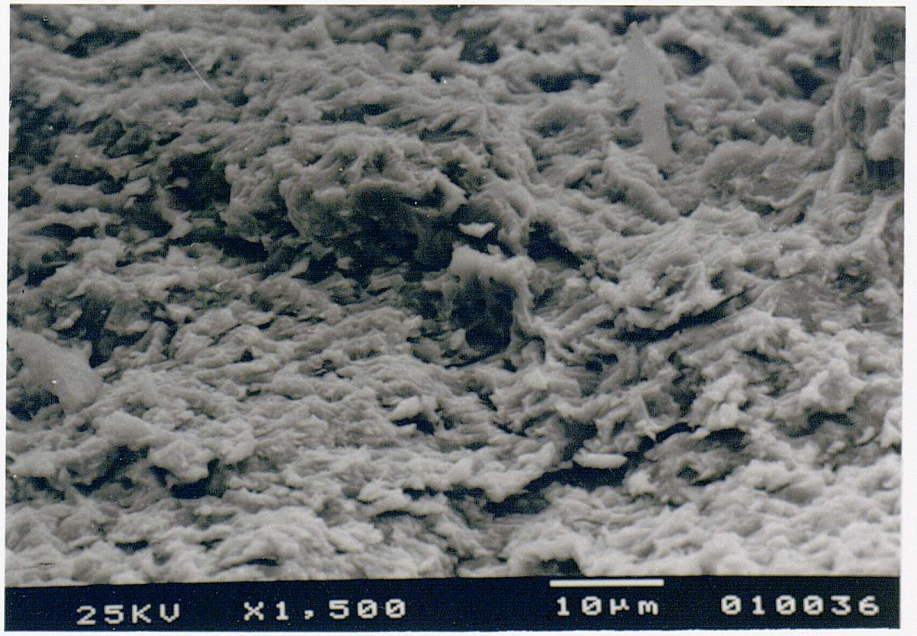
25KV X1,500 10µm 010036

one direction. As the material becomes more uniformly embrittled the difference in the ductility of the layers becomes smaller, the stress at the surface becomes less uniaxial, and the cracks are allowed to propagate in other directions.

4.5 Hydride Distribution and Penetration

4.5.1 Grade 2 Titanium

Hydride distribution and penetration in the alloys was studied by means of backscattered electron imaging of sections of the broken samples made perpendicular to the strain axis, some distance behind the fracture surface. Titanium hydride, having a lower atomic number density than titanium, is expected to show up in the backscattered images as darker than the matrix.

The grade 2 samples hydrided for up to 20 days showed no hydrides visible in this manner for either microstructure, neither did the 7 day exposed samples that had been annealed in order to encourage diffusion into the bulk.

4.5.2 Grade 12 Titanium

Figs. 4.67-4.69 show the appearance of the equiaxed samples after 5, 7 and 20 days hydriding. The nickel-rich β phase shows up brightly against the darker α matrix. The hydride is visible as the darkest phase. The mean hydride penetration for the 3 cases has been determined by measurement on the micrographs at a series of evenly spaced points along the sample edges.

The solution to the diffusion equation for the case of diffusion from a source of constant concentration into an infinite solid is

$$C_x/C_s = 1 - \text{erf}\,[x/2\sqrt{(Dt)}],$$

where C_x is the concentation at distance x from the surface, C_s is the surface concentration, t is time and D is the diffusion coefficient. If the limit of hydride

Fig. 4.67 Cross-section of equiaxed grade 12 hydrided for 5 days (BEI)

Fig. 4.68 Cross-section of equiaxed grade 12 hydrided for 7 days (BEI)

Fig. 4.69 Cross-section of equiaxed grade 12 hydrided for 20 days (BEI)

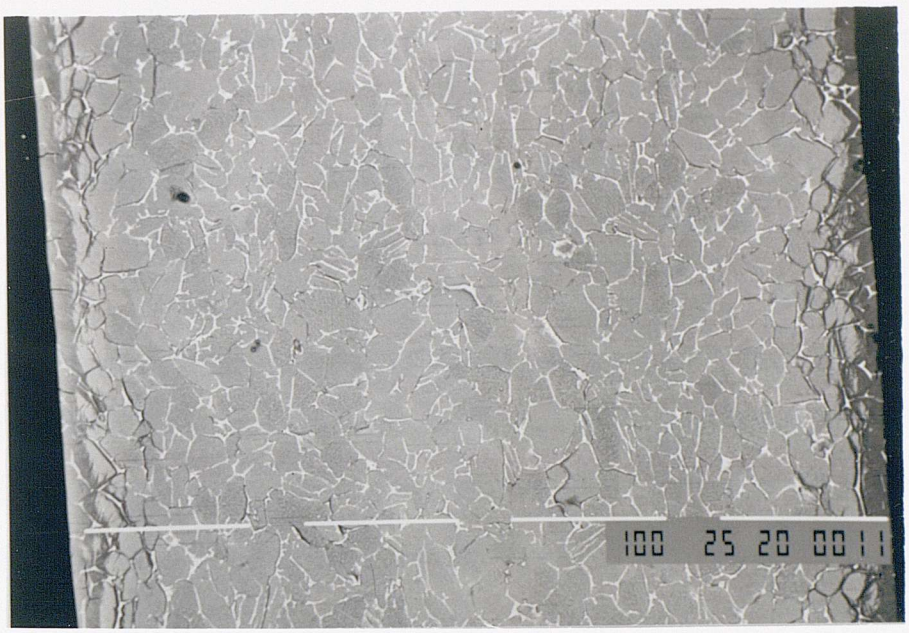
100 25 20 0011

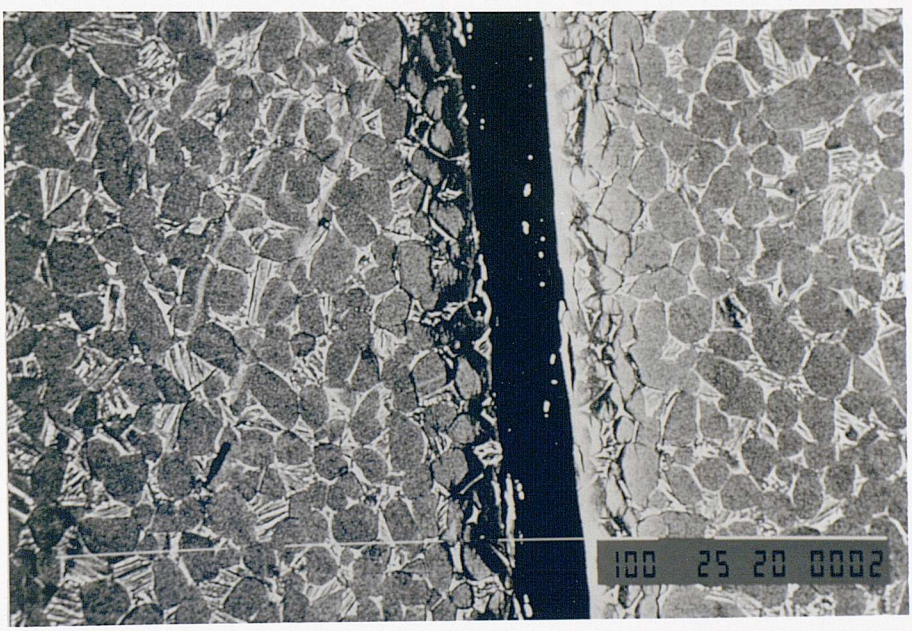
100 25 20 0002

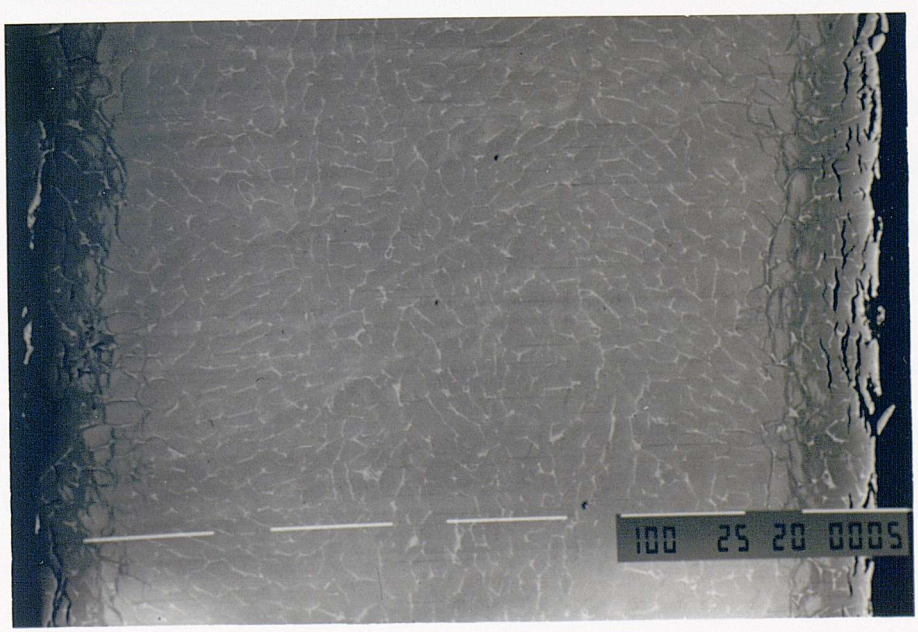
100 25 20 0005

penetration for different exposure times is measured, this corresponds to a constant value of C_x. Then

$$x/2\sqrt{(Dt)} = erf^{-1}(1 - C_x/C_s) = k = \text{a constant.}$$

Hence

$$x^2 = 4k^2Dt.$$

Thus if the hydrogen uptake is diffusion controlled, a plot of x^2 against t will be linear, though further conclusions cannot be drawn because C_x, C_s and D are all unknown. The graph of hydride penetration squared against exposure time (fig. 4.70) shows that this is the case. This indicates that the accumulation of the hydride layer does not affect the rate of absorption.

It may be noted that Mc.Kinskey et al.[23] have demonstrated a proportionality between the depth of the hydride layer and the analysed total hydrogen content of commercial-purity α titanium samples which had picked up hydrogen during acid pickling, for both round bars and sheet specimens, with hydride layers up to 1% the total thickness or diameter of the samples. There is thus some reason to believe that the penetration depth in these alloys should be a good guide to hydrogen contents.

The role of the β phase in the transport of hydrogen is clearly very significant in this alloy. The higher magnification view (fig. 4.71) makes clear that the hydride is not solid to the edge but crossed by bands of β phase. At the interior edge of the hydride layer the hydride is discontinuous, and borders bands of β phase, with needles extending from these borders into the α grains. It has been noted that the solubility of hydrogen in the β phase is much greater than that in the α phase, and also that the diffusion of hydrogen is 10^4 times faster in the β phase at room temperature. These images suggest strongly that the precipitation of the hydride in the grade 12 occurs in the α phase, and that the β phase network acts to conduct the hydrogen through the surface layer and into the bulk, allowing rapid growth of the hydride layer and the consequent embrittlement observed.

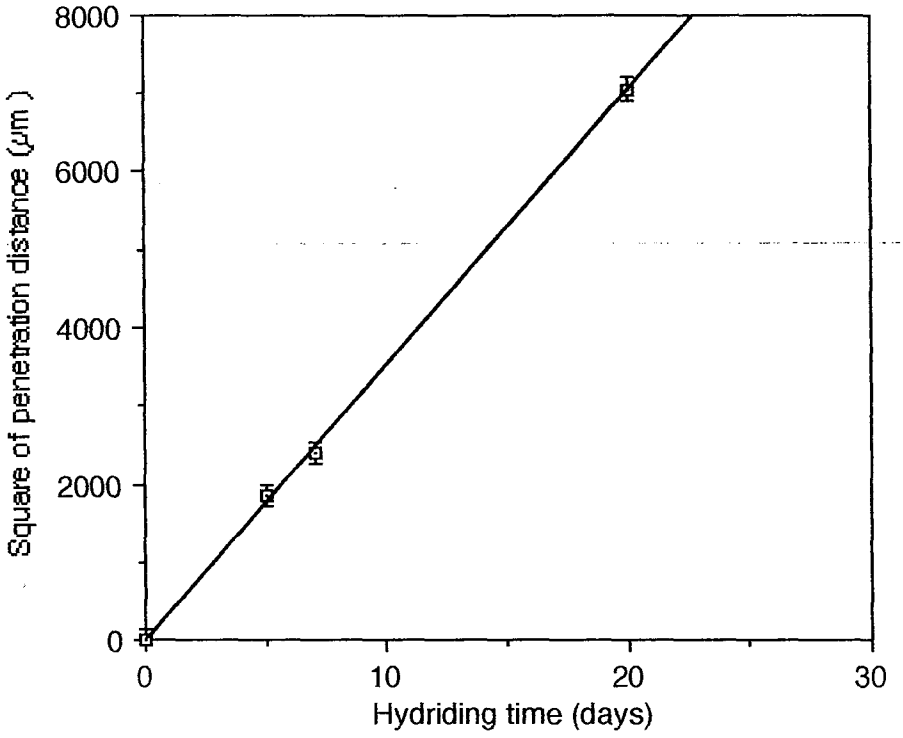

Fig. 4.70 Square of hydride penetration distance against time of exposure for equiaxed grade 12

This view is supported by the appearance of the 20 day hydrided basketweave sample (fig. 4.72). In this case the pattern of the β network has allowed the hydrides to penetrate the whole thickness of the sample, thus accounting for the measured 80% reduction in ductility. The hydride is much more dispersed than in the equiaxed structure and there is no solid layer in the α at the edge. The pattern of hydride needles growing into the α phase perpendicular to the hydride-lined β strips is even more clearly shown here at the edges (see the "herringbone" areas shown in fig. 4.73).

Of the 7 day hydrided equiaxed samples subsequently annealed for 24 hours, the sample annealed at 250°C (fig. 4.74) showed no detectable change, while those annealed at 300 and 450°C both showed a uniform distribution of hydride on the β boundaries throughout the material (figs. 4.75-4.76). This hydride redistribution between 250 and 300°C again suggests the dissolution of the hydrides in this range, the solute hydrogen then diffusing at the elevated temperatures and causing reprecipitation of hydrides on cooling.

In order to prove that the quantity of hydride formed in a particular microstructure really is dependent only on the total quantity of charge passed, and that there is no separate influence of voltage, another equiaxed sample was hydrided for 5 days using the standard current density of 1×10^{-6} A/m^2 through the standard solution, but using a cell constructed to have a lower resistance than the standard cell, so that the initial potential difference between the sample and the beaker was 0.8 V instead of 2.3 V. The resulting hydride distribution is compared with that resulting from 5 days exposure in the normal cell in fig. 4.77. The conclusion is that they are very similar, thus the hydride formation is dependent only on the quantity of charge passed. This vindicates the decision to perform the hydriding under constant current rather than constant voltage conditions.

Fig. 4.71 Cross-section of equiaxed grade 12 hydrided for 20 days (BEI)

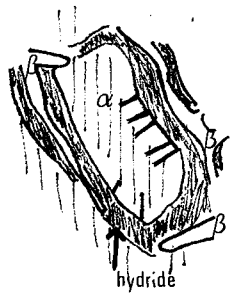

Fig. 4.72 Cross-section of basketweave grade 12 hydrided for 20 days (BEI)

Fig. 4.73 Detail of above

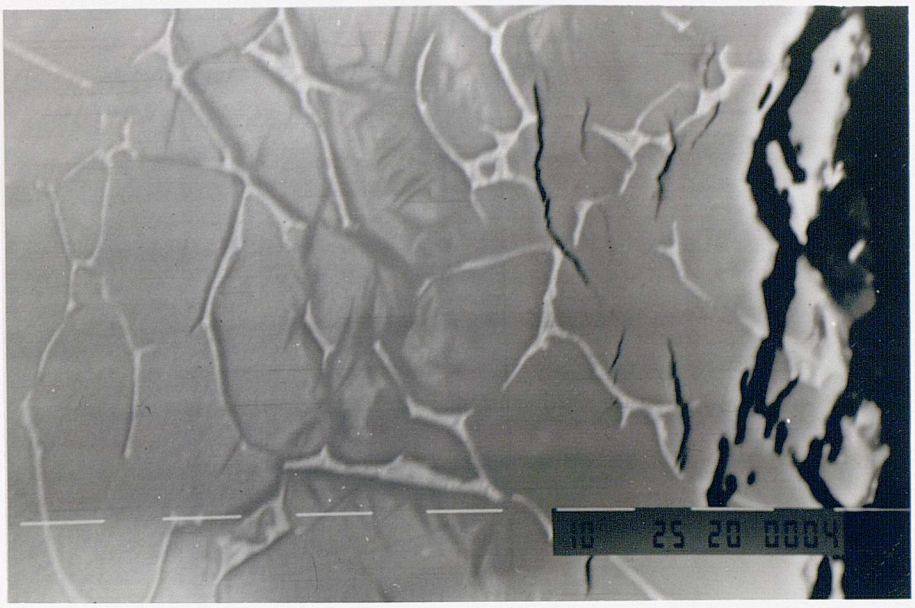
10 25 20 0004

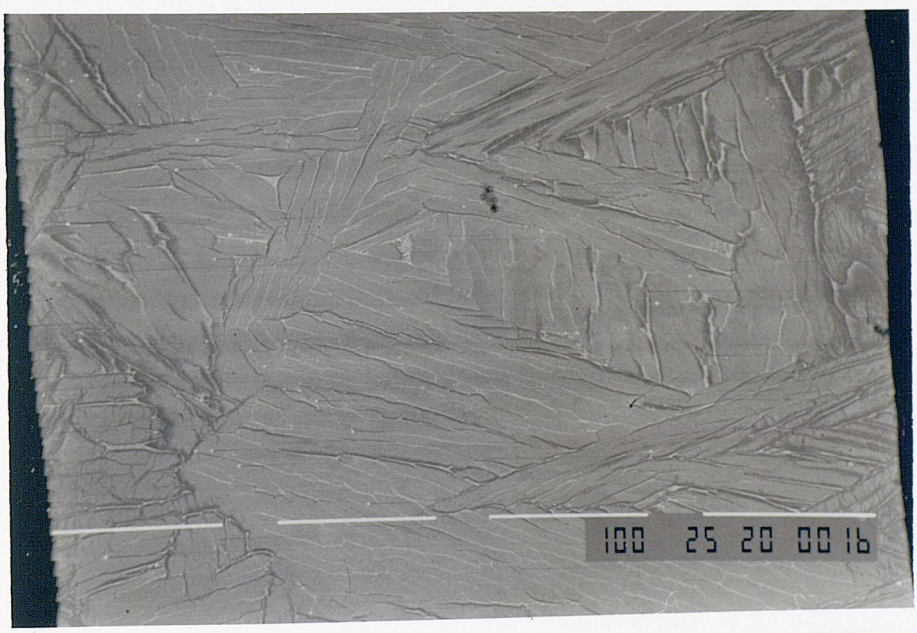
100 25 20 0016

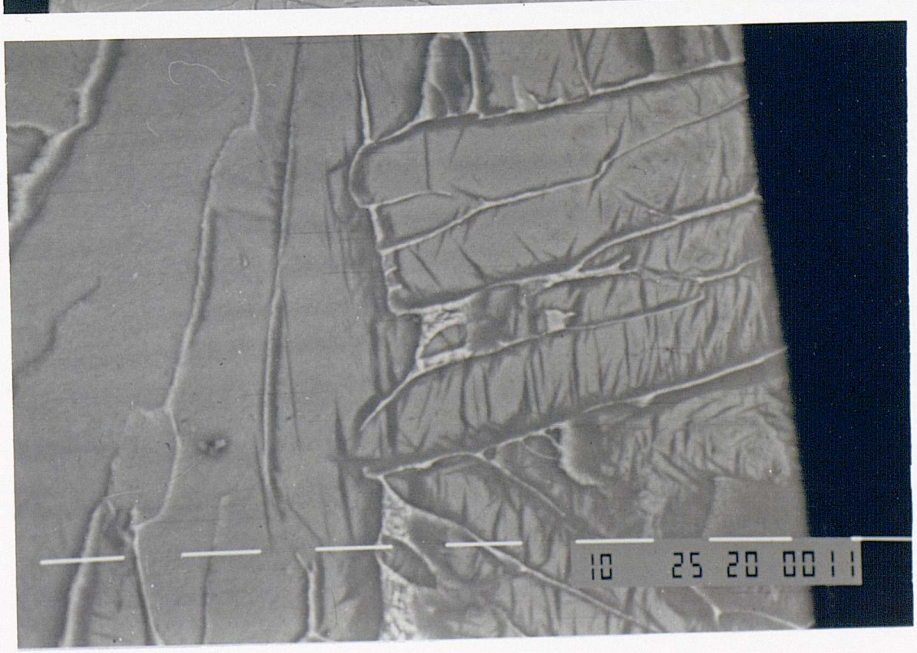
10 25 20 0011

Fig. 4.74 Cross-section of 7 day hydrided equiaxed grade 12 annealed at 250°C (BEI)

Fig.4.75 Cross-section of 7 day hydrided equiaxed grade 12 annealed at 300°C (BEI)

Fig. 4.76 Cross-section of 7 day hydrided equiaxed grade 12 annealed at 450°C (BEI)

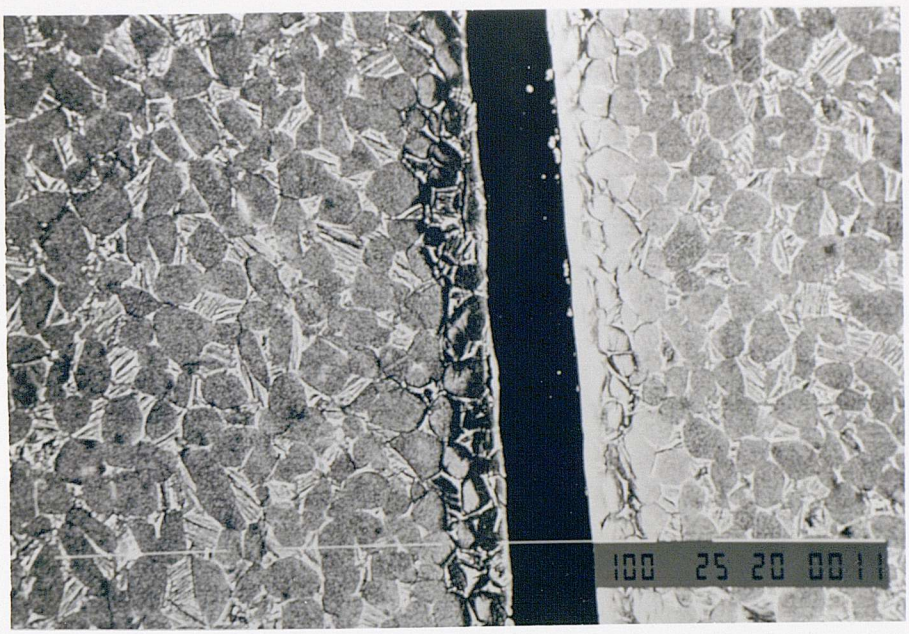
100 25 20 0011

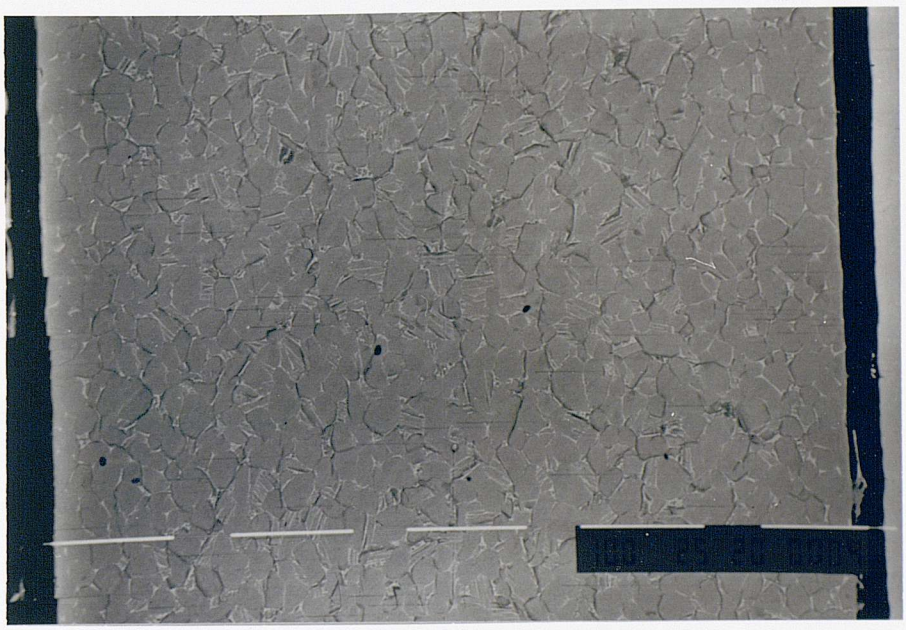

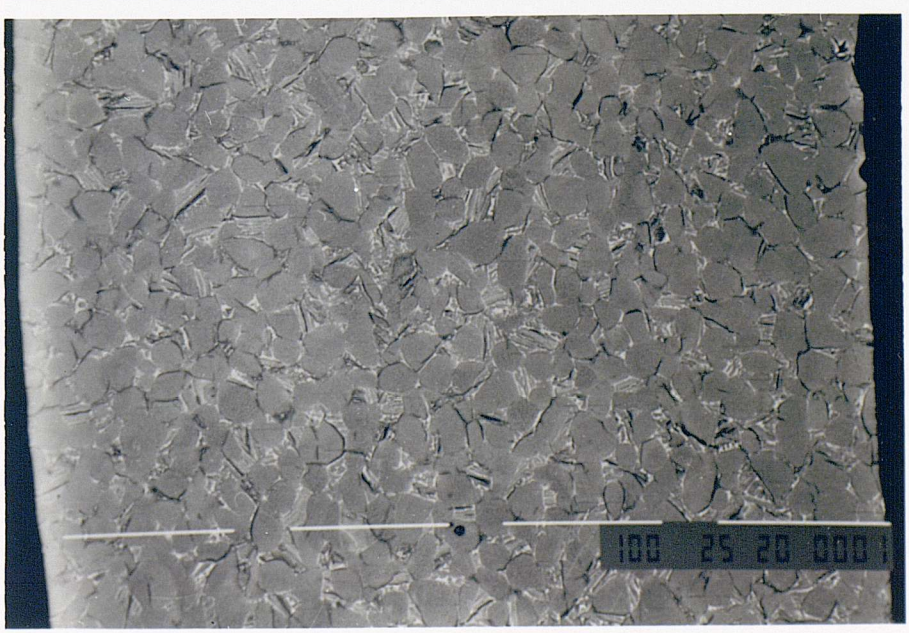
100 25 20 0001

Fig. 4.77 Cross-sections of 5 day hydrided equiaxed grade 12 samples hydrided at 10^{-6} A/m^2, -0.8 V (A), and 10^{-6} A/m^2, -2.3 V (B) (BEI)

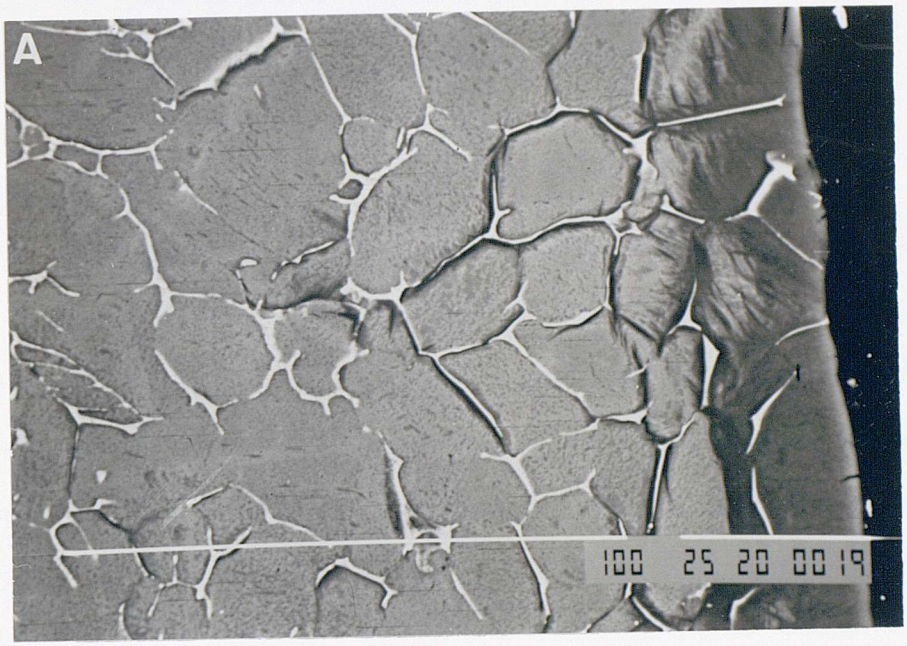
A
100 25 20 0019

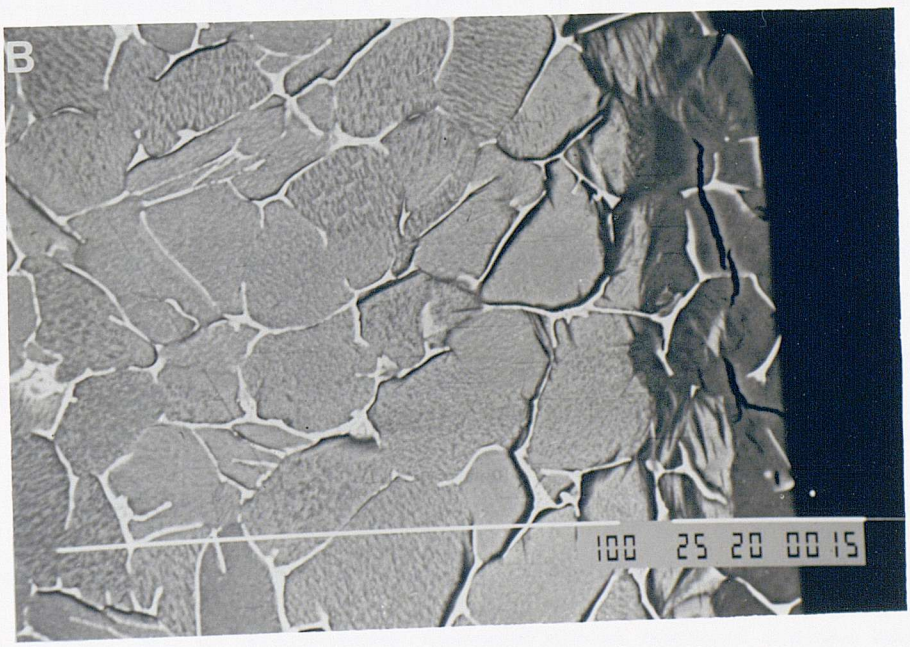
B
100 25 20 0015

4.5.3 Grade 5 Titanium

The grade 5 exposed for 7 days showed no hydride at all in the backscattered electron image, neither did the 7 day samples subsequently annealed at 250, 300 and 450°C.

4.5.4 Titanium-Nickel Alloys

Cross-sections of 7 day hydrided Ti-3.5Ni and Ti-5Ni, and also 7 day hydrided Ti-3.5Ni annealed at the 3 temperatures were examined using backscattered imaging; again no evidence of hydride precipitation was found in any of the specimens, and the unhydrided microstructures were apparently unchanged and continuous right to the sample surfaces. This is a surprising result in view of the embrittlement measured for these alloys, and indicates either that the hydrides are very small, or that a different embrittlement mechanism is operating.

4.6 Hydride Characteristics

In this section will be described the results of observation of hydrides by transmission electron microscopy. Hydrides were observed in all materials examined, which includes all those mentioned except for the grade 5 which was in the form of a cylindrical rod, difficult to grind down to a foil. Some hydrides were observed in unhydrided materials. It has been noted by other workers[27,28] that hydrides are sometimes formed in thin foils of titanium alloys by the electropolishing process used to produce the foils. Thus it is unfortunately impossible to be certain of the origin of any particular hydride observed.

Hydrides appear in the TEM as electron-transparent needles or rods which show up light or dark against the matrix depending on the diffraction conditions. They were observed as intergranular, intragranular or transgranular, isolated and in coherent masses, and varying in size from about 20 nm to 200 nm (figs. 4.78-4.81). In the grade 12 the same morphology as reported from the SEM backscattered studies was observed (fig. 4.80),

Fig. 4.78 Hydrides in equiaxed grade 2 thin foil (TEM), c.f. optical (surface) observation fig. 4.7 A

Fig. 4.79 Isolated lenticular hydride in grade 2. Punched-out dislocations are visible around ends. (TEM)

Fig. 4.80 Massive hydride in grade 12 bo rdering ß phase strip (dark). Small coherent hydrides lie adjacent to ß at bottom, and masses of dislocations surround large hydride. (TEM)

Fig. 4.81 Set of small coherent hydrides in grade 2: bright field (A), dark field (B) (TEM)


500 nm

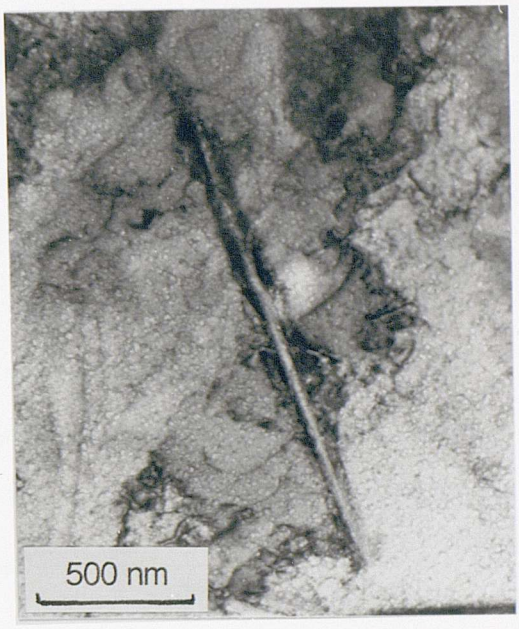
500 nm

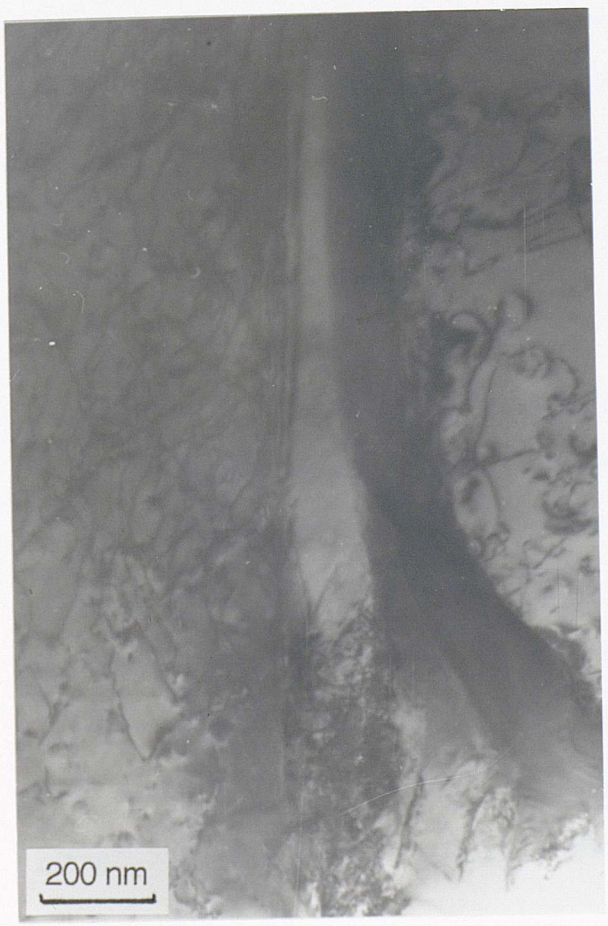
200 nm

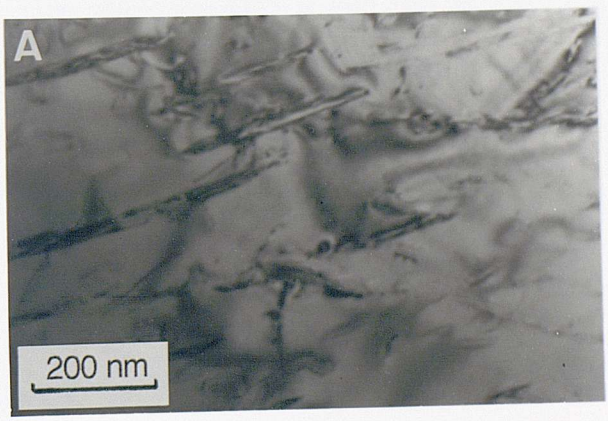
A
200 nm

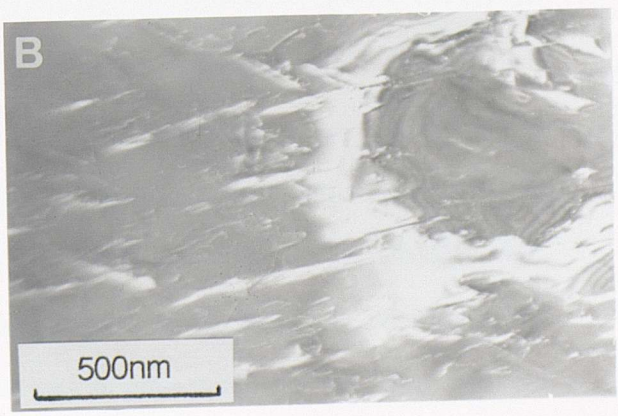
B
500nm

with massive hydrides formed on α-β grain boundaries and intragranular hydride needles extending from these into the α.

In general the hydrides were too small to allow a selected area diffraction pattern to be taken of only the hydride, and hence the general method adopted for analysing their diffraction patterns was to take two photographs, one of the diffraction pattern including the hydride or coherent set of hydrides, and one of the adjacent matrix, to trace all the spots from the first photograph onto tracing paper, and then to place the tracing paper over the second photograph to eliminate the spots appearing in the matrix pattern and thus isolate the hydride pattern. The measured hydride lattice parameter, averaged over a number of observations of different samples, is 0.441±0.005 nm. This agrees with the value given by Crane[52] for cubic $TiH_{1.924}$ of 0.445 nm.

The diffraction patterns of the hydride and matrix, once separated, can be used to establish the orientation relationship, since the two zone axes in the single diffraction pattern must be approximately parallel in the beam direction. Then if one spot in the hydride pattern lies in the same direction relative to the undiffracted beam as one spot in the matrix pattern, the corresponding planes in the lattices must be parallel, and a pair of parallel directions and a pair of parallel planes suffice to define an orientation relationship between the phases.

The orientation relationships observed are shown in fig. 4.82. The α titanium patterns have been identified by comparison with the calculated diffraction patterns for titanium by Fujishiro & Gegel[105] by means of the measurement of angles and spot distance ratios, and the hydride patterns have been similarly identified by comparison with the calculated FCC patterns by Edington[104]. These orientation relationships have been further reduced using stereographic projections generated using the "Diffract" computer program[106]. The program is capable of calculating simultaneously the projections of crystal planes and crystal directions for both a matrix crystal and a precipitate having any rational

Fig. 4.82 Determination of hydride orientation relationships: in each case, from left to right, micrograph, SADP matrix, SADP hydride + matrix

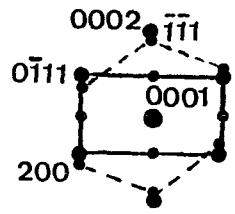

Conclusion: $\{0001\}\|\{\bar{1}11\}$

$<2\bar{1}\bar{1}0>\|<011>$

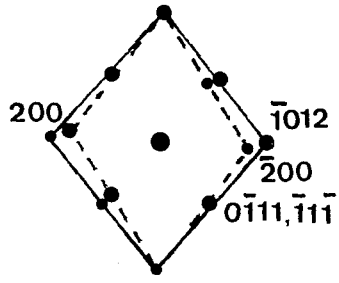

Conclusion: $\{0\bar{1}11\}\|$ 5° from $\{111\}$*

$<10\bar{1}1>\|<011>$

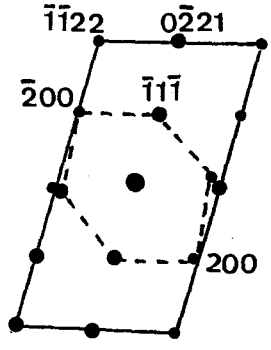

Conclusion: $\{0\bar{2}21\}\|\{\bar{1}11\}$

$<5\bar{1}\bar{4}6>\|<011>$

*Angles measured positively anticlockwise

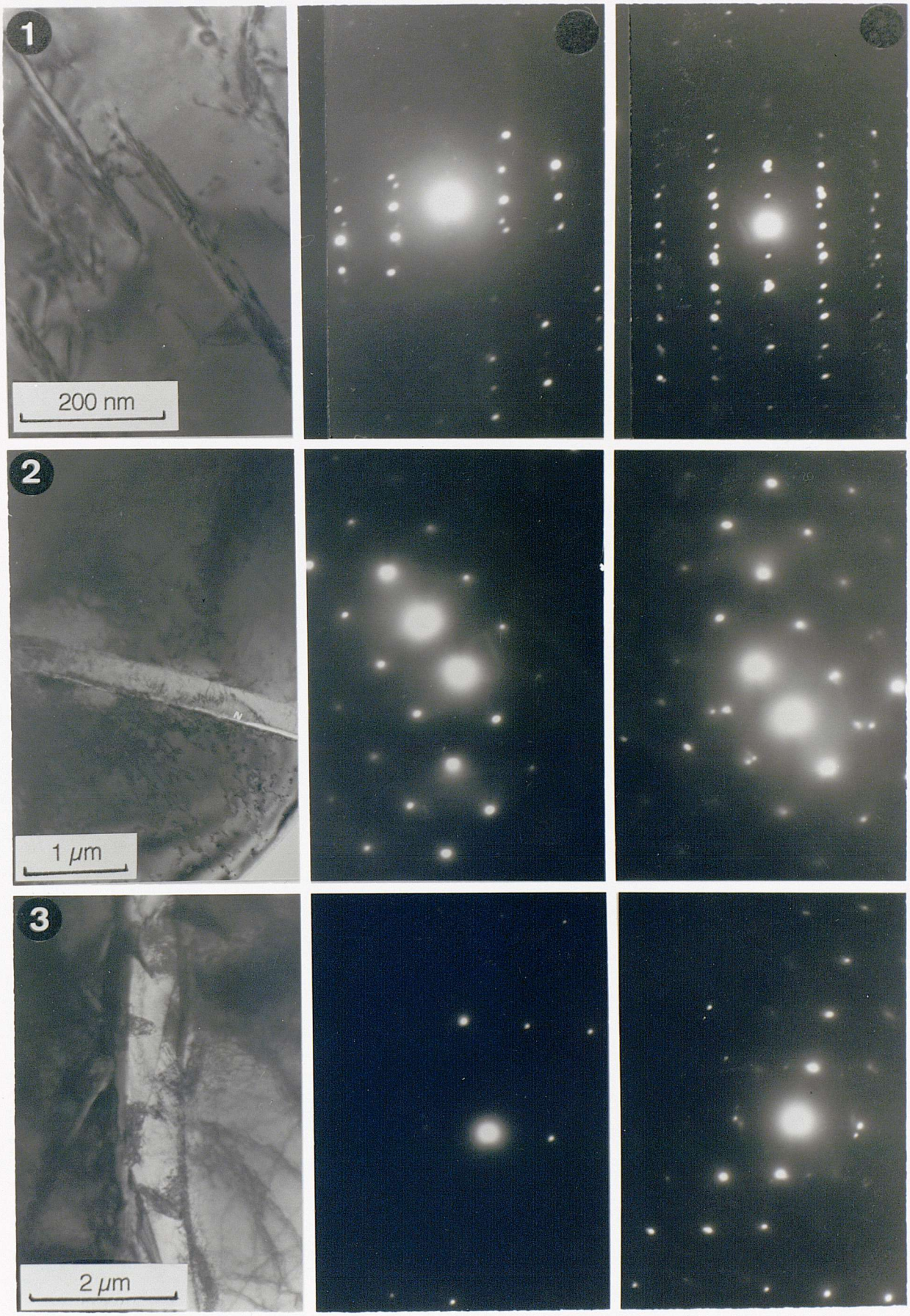
1
200 nm
2
1 μm
3
2 μm

Fig. 4.82 (continued)

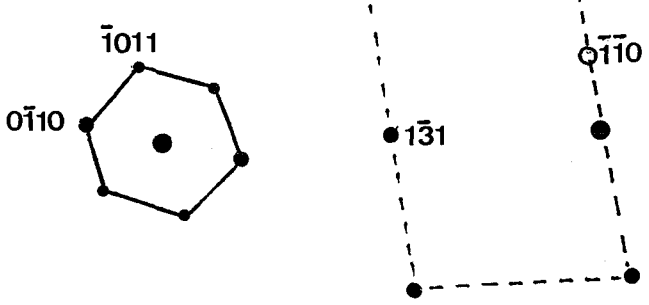

Conclusion: $\{\bar{1}011\}\|\{110\}$

$<2\bar{1}\bar{1}3>\|<\bar{1}14>$

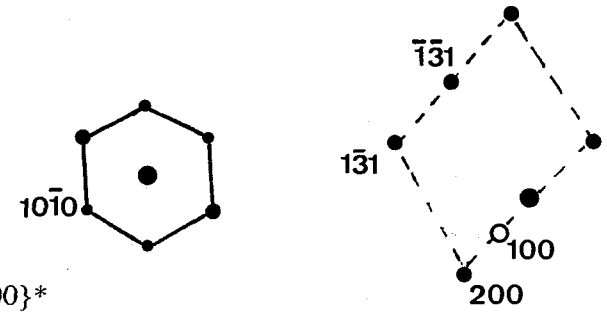

Conclusion: $\{10\bar{1}0\}\|$ -13° from $\{100\}$*

$<0001>\|<013>$

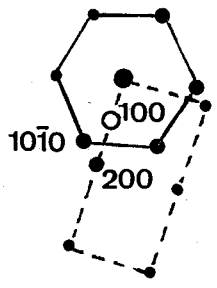

Conclusion: $\{10\bar{1}0\}\|$ -16° from $\{100\}$*

$<0001>\|<001>$

*Angles measured positively anticlockwise

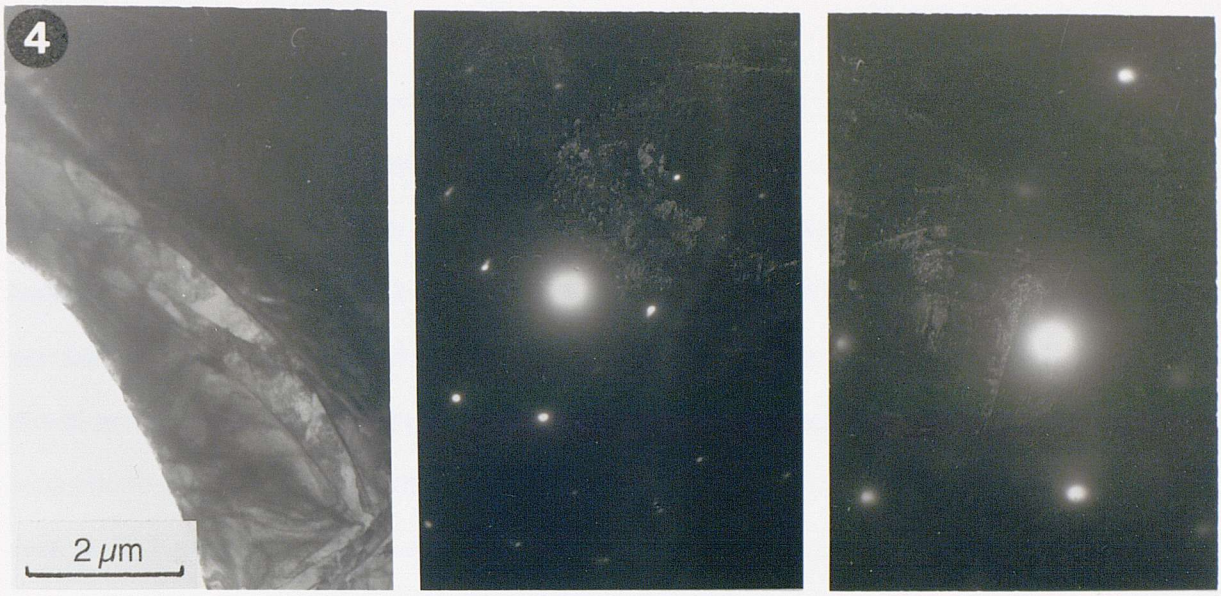
4
2 μm

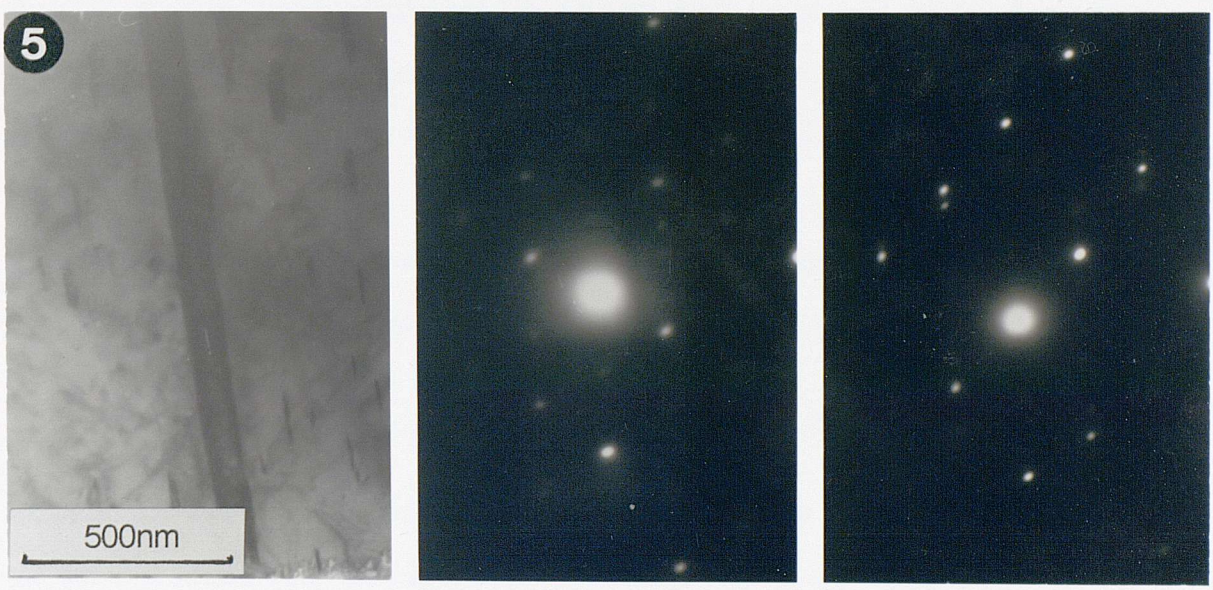
5
500nm

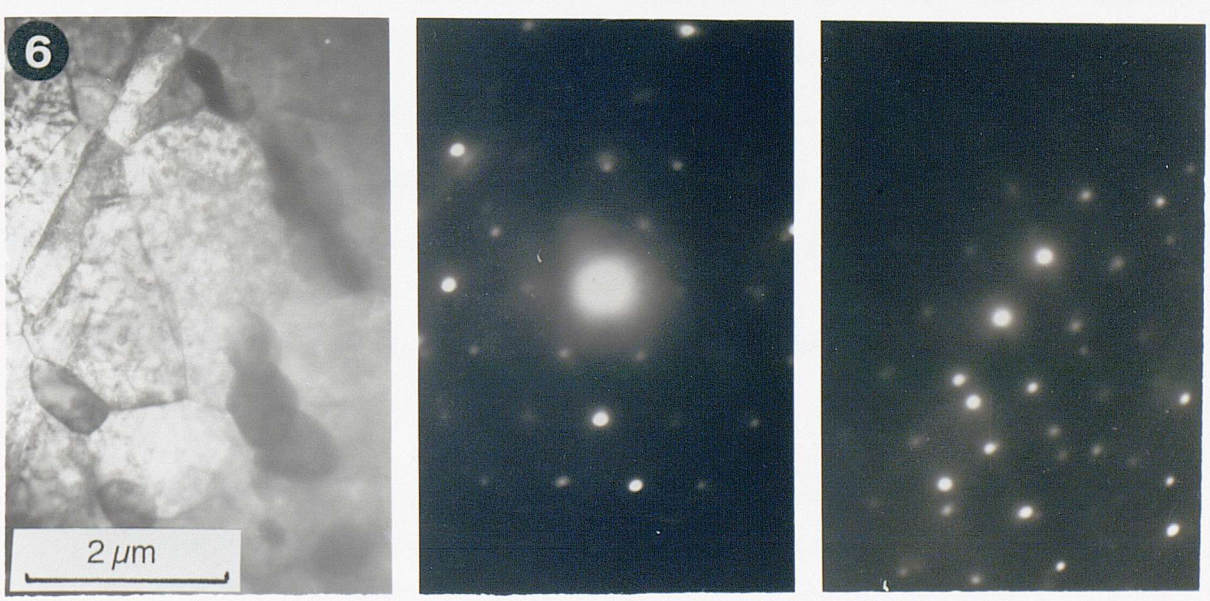
6
2 μm

orientation relationships between their planes and directions and also of taking into account any observed angular misorientation with respect to the given rational relationships. In this work only misorientation of the planes could be taken into account because of the method of making the observations. This was done by angular measurement on the diffraction patterns in cases in which an exact alignment of directions in the reciprocal lattices was not apparent.* For comparison the stereographic projections corresponding to the previously reported orientation relationships given in section 2.12 have been generated (figs. 4.83-4.86). The stereographic projections for the observed orientation relationships from fig. 4.82 are given in fig. 4.87. Matrix planes are shown as black and precipitate planes as white. Planes are shown having h, k, (i,) l values up to 2, and the projections are centred on the matrix (0001) pole.

The conclusions from this analysis are given in table 4.6. 3 of the 6 observed cases (nos. 3, 5 and 6) correspond reasonably well with the orientation relationship reported by Hall:[63]

$$\{0001\}_{metal}\|\{001\}_{hydride}, \qquad <01\bar{1}0>_{metal}\|<110>_{hydride} \qquad (I)$$

This can most easily be seen from the stereographic projections by observing the square (or distorted square when the alignment of the central poles is not exact) of poles in the hydride lattice surrounding {110}, as shown on the relevant projections. The bisecting line of this square running from {110} through {210} is at a angle of 16° from the direction of a {1010} matrix pole in the standard projection fig. 4.86. The projection of the first orientation relationship reported by Sanderson & Scully[61] and also Boyd[62]

$$\{0001\}_{metal}\|\{010\}_{hydride}, \qquad <1\bar{2}10>_{metal}\|<110>_{hydride} \qquad (II)$$

* In the "Diffract" program this type of misorientation is referred to, confusingly, as a rotation of directions, irrespective of whether it is applied to a projection of planes or a projection of directions, and is executed as a rotation of the precipitate pattern with respect to the matrix pattern about an axis in the direction of the centre of the projection, measured positively anticlockwise, points which are not explaned in the manual.

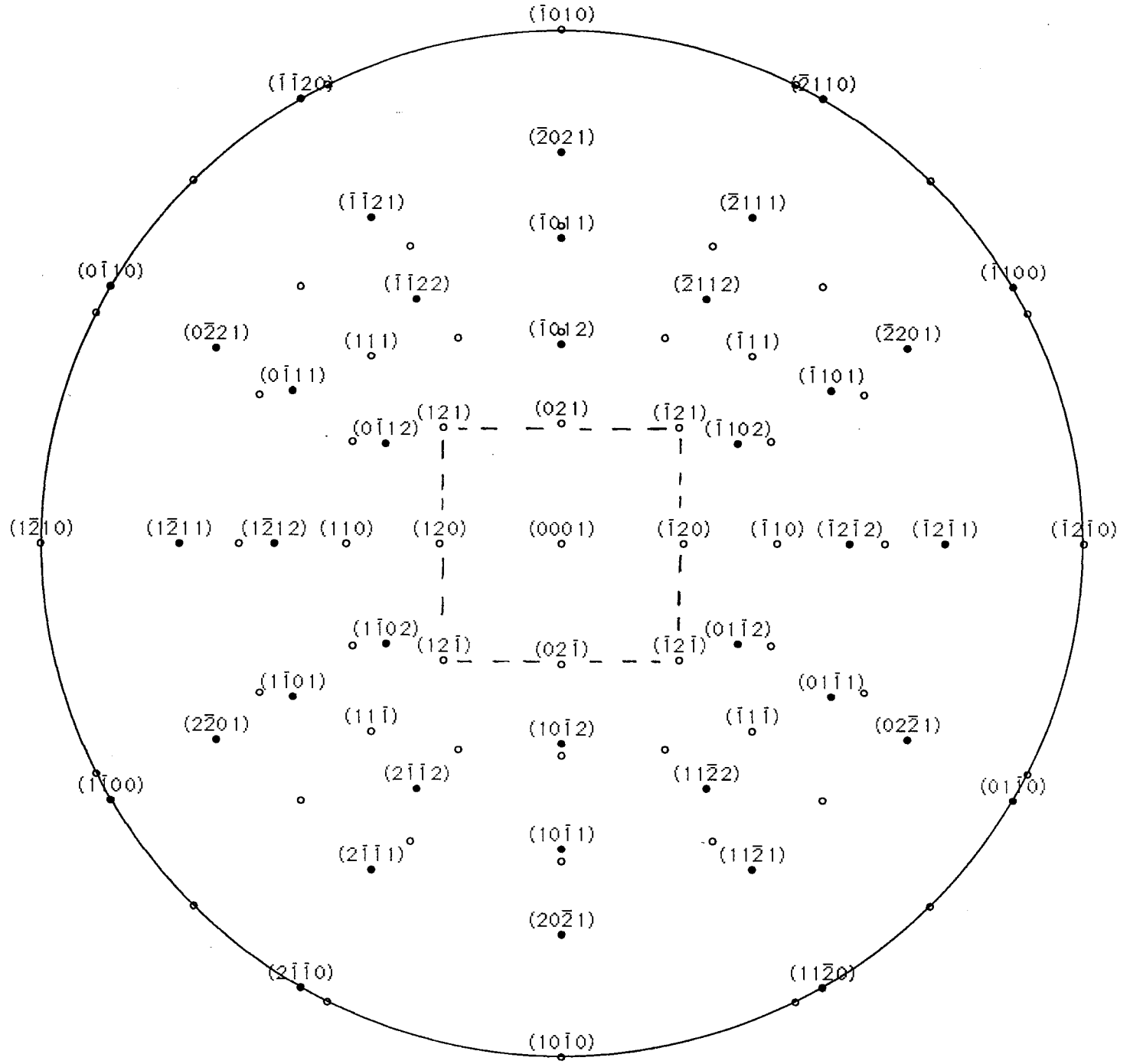

Fig. 4.83 Stereographic projection of orientation relationship

$\{0001\}\|\{010\}$, $\langle 1\bar{2}10\rangle\|\langle 110\rangle$

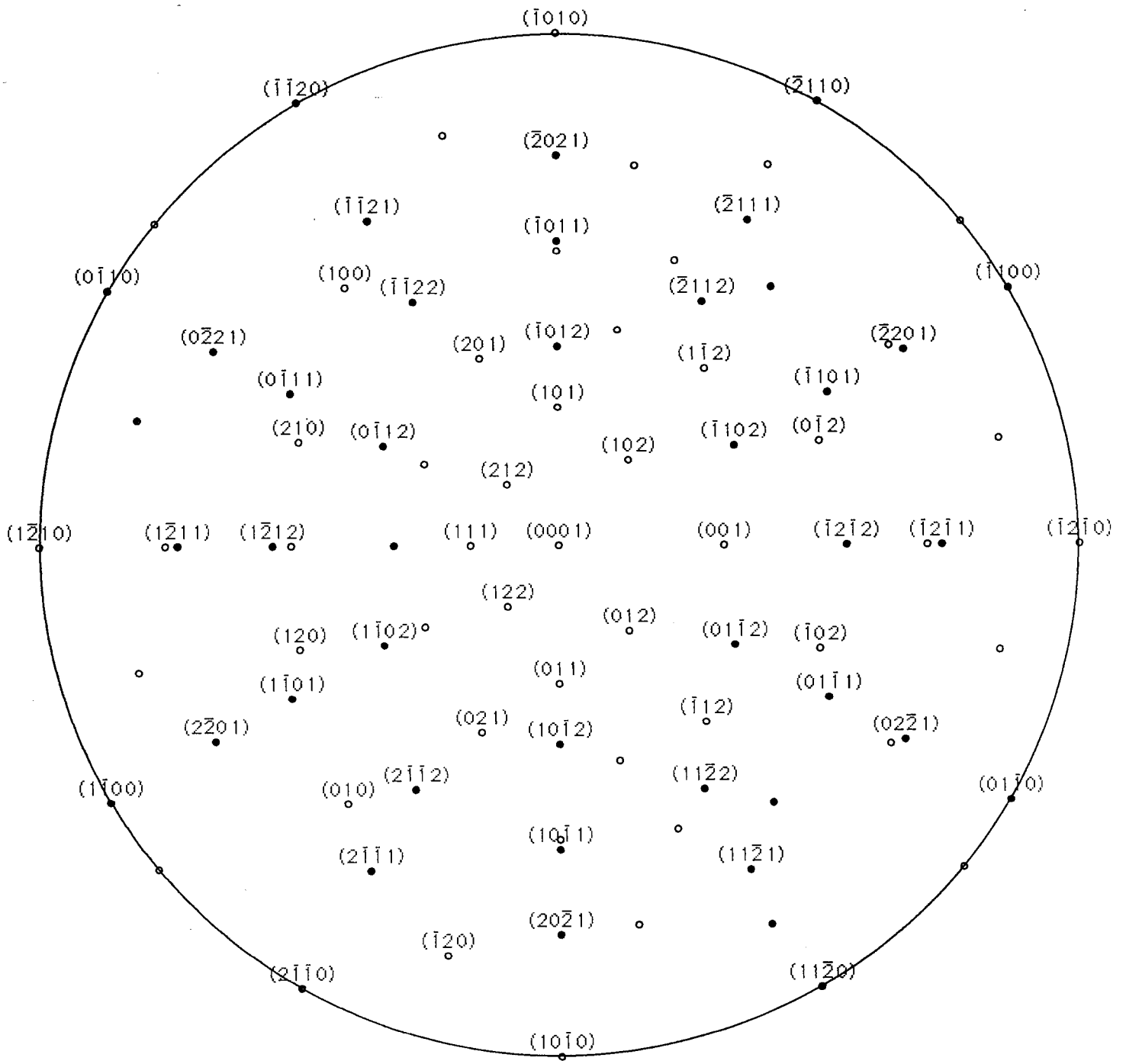

Fig. 4.84 Stereographic projection of orientation relationship

$\{0001\}\|\{112\}$, $<1\bar{2}10>\|<110>$

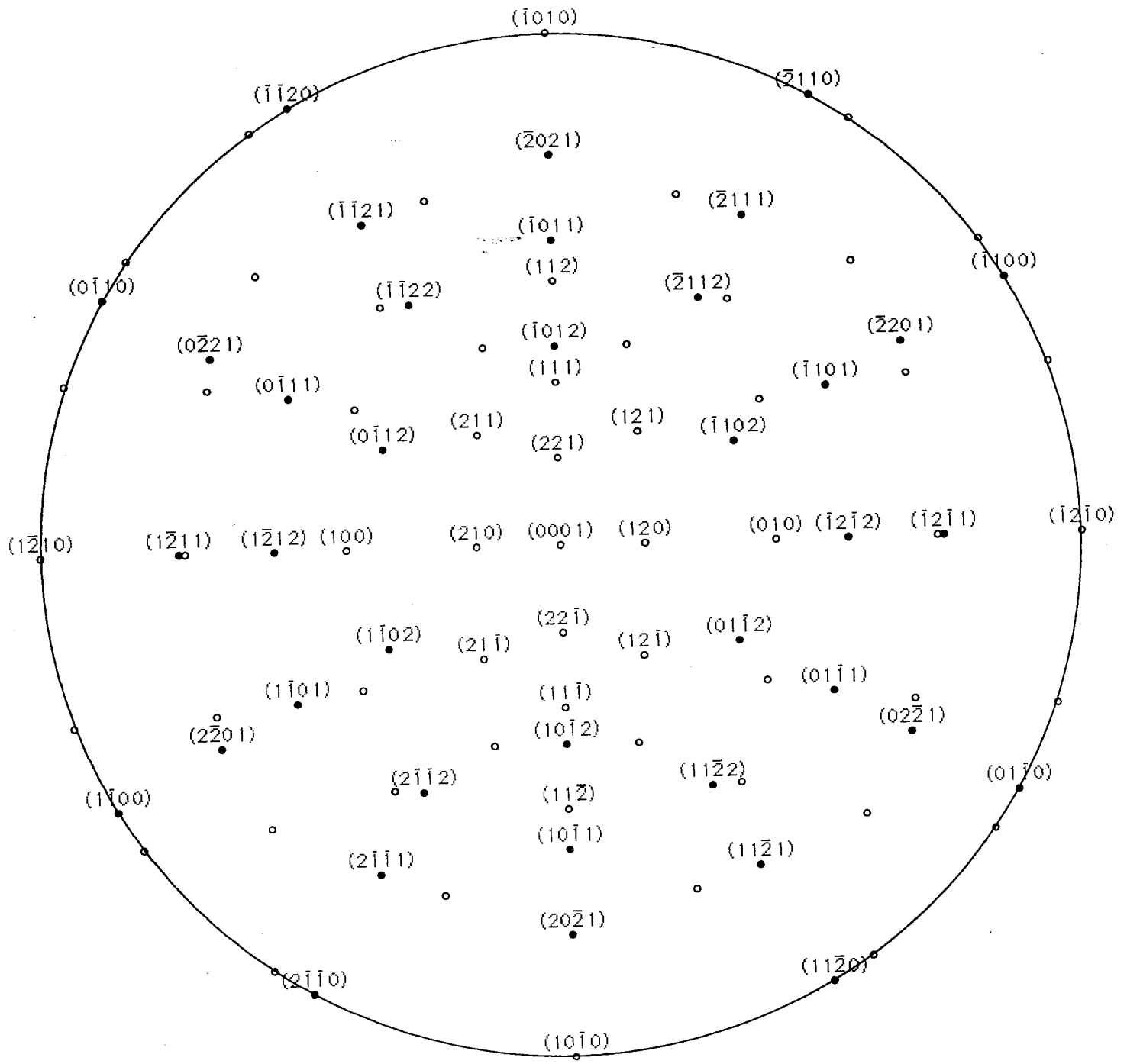

Fig. 4.85 Stereographic projection of orientation relationship

$\{0001\}\|\{110\}$, $\langle 1\bar{2}10\rangle\|\langle 110\rangle$

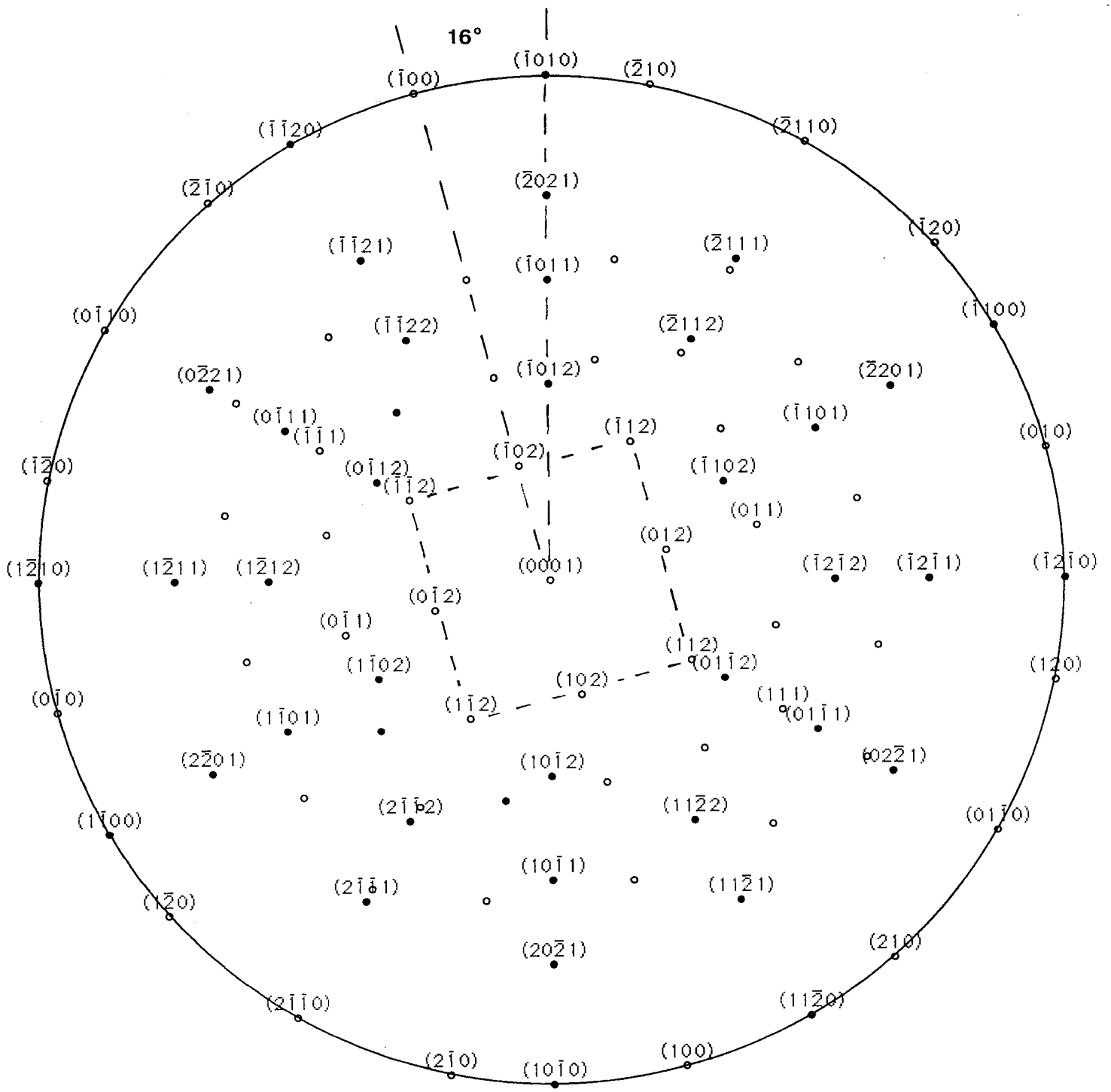

Fig. 4.86 Stereographic projection of orientation relationship

$\{0001\}\|\{001\}$, $<10\bar{1}0>\|<110>$

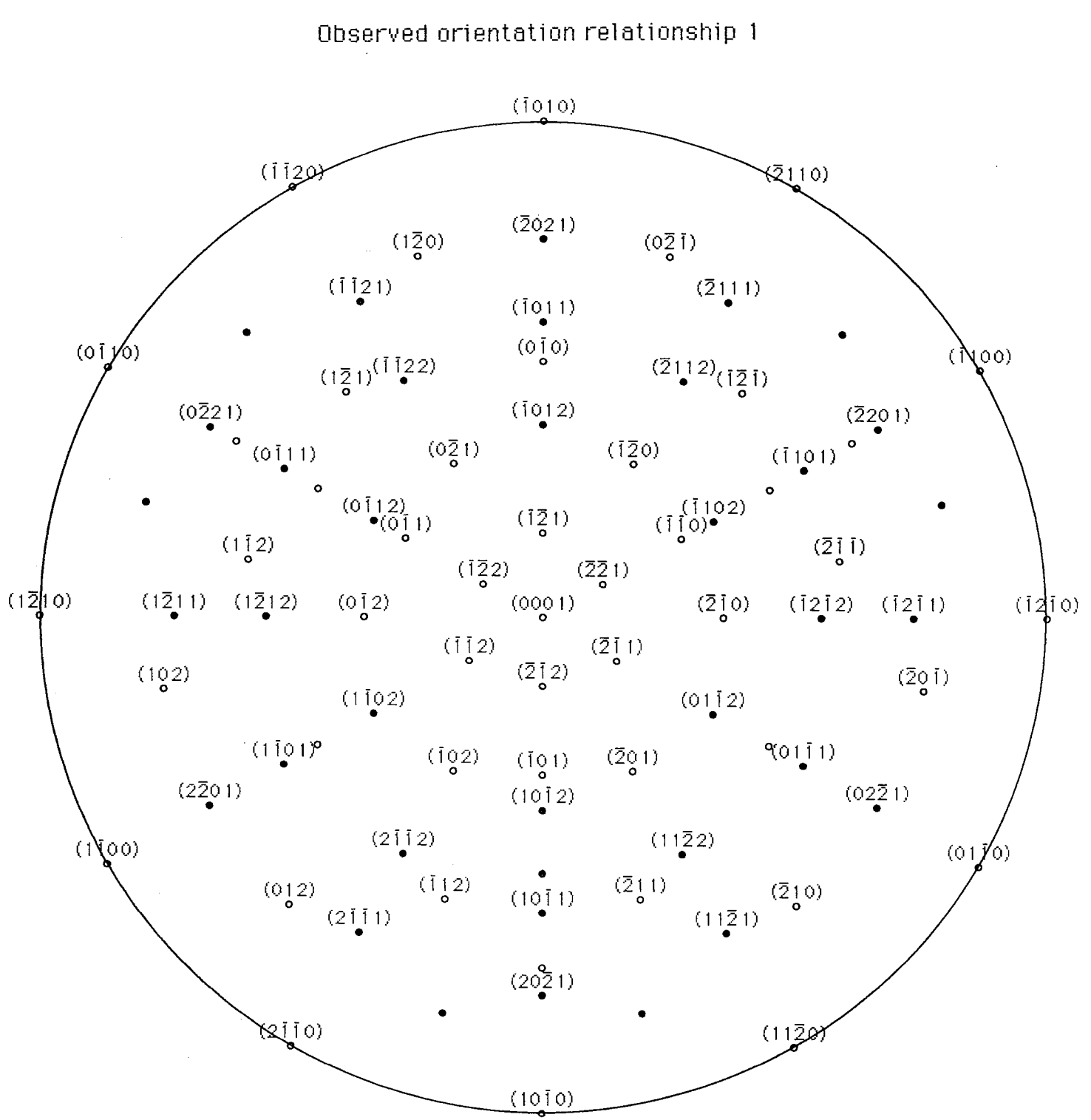

Fig. 4.87 Stereographic projections of the observed orientation relationships from fig. 4.82

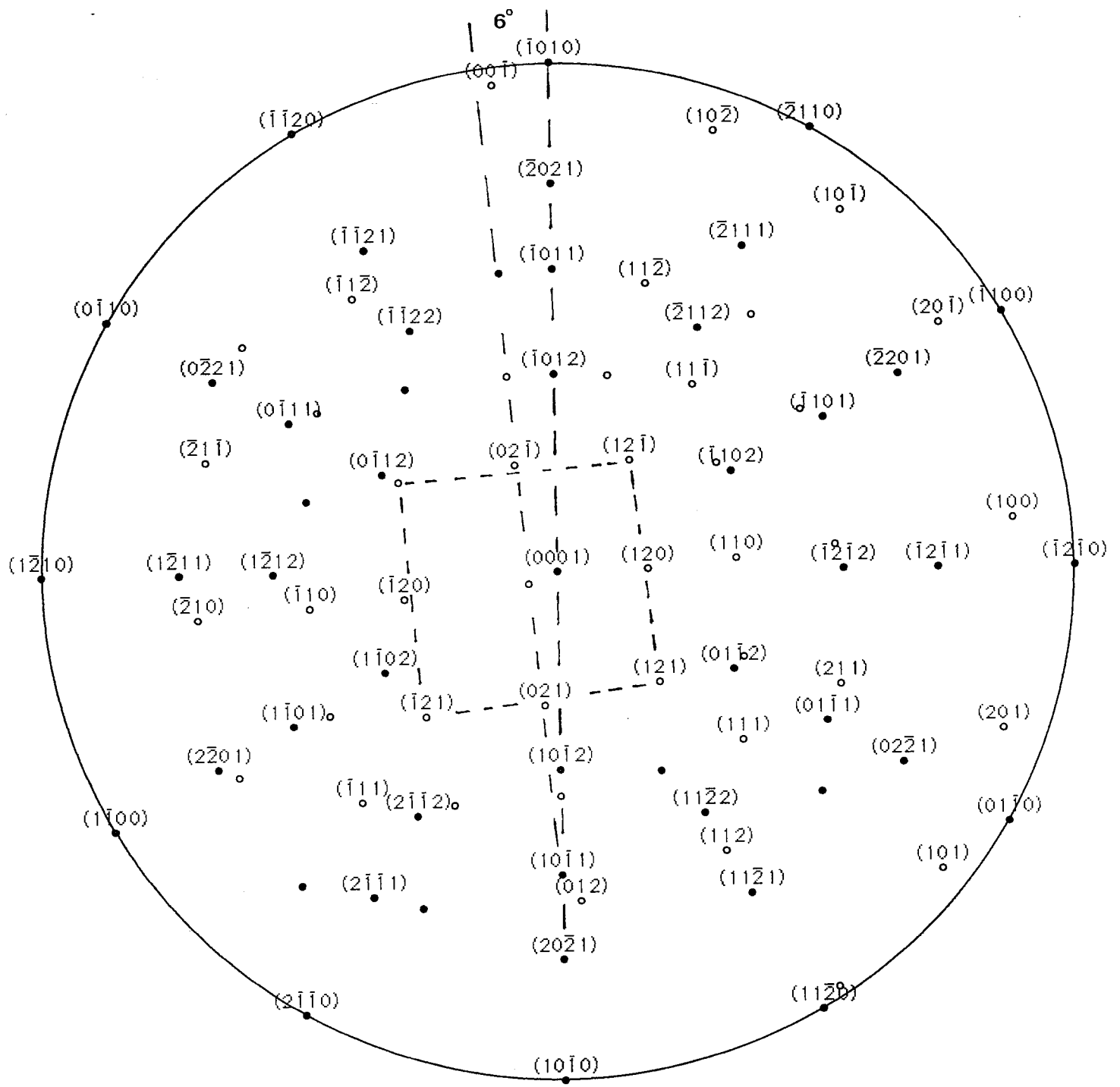

Fig. 4.87 (Continued)

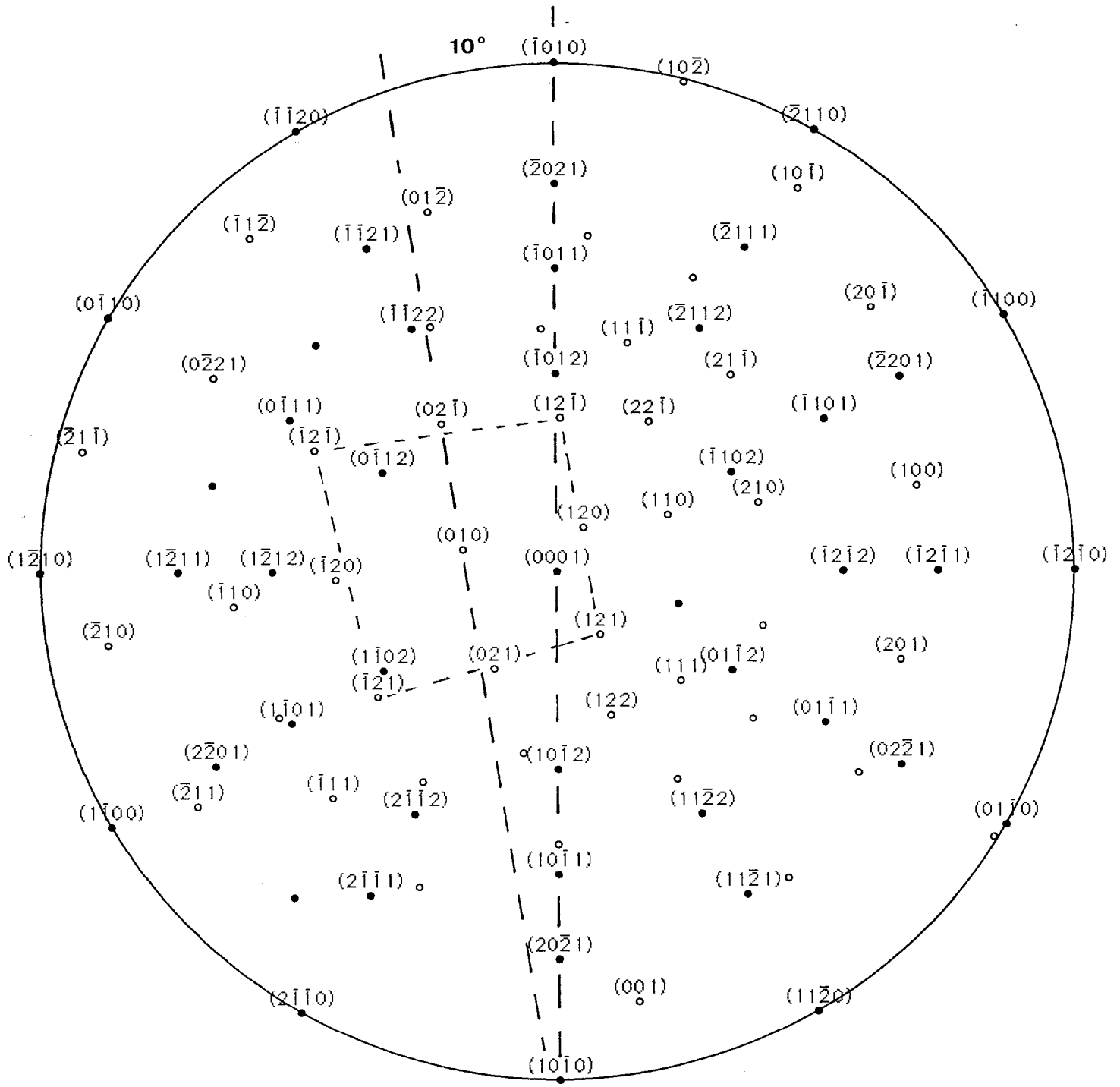

Fig. 4.87 (Continued)

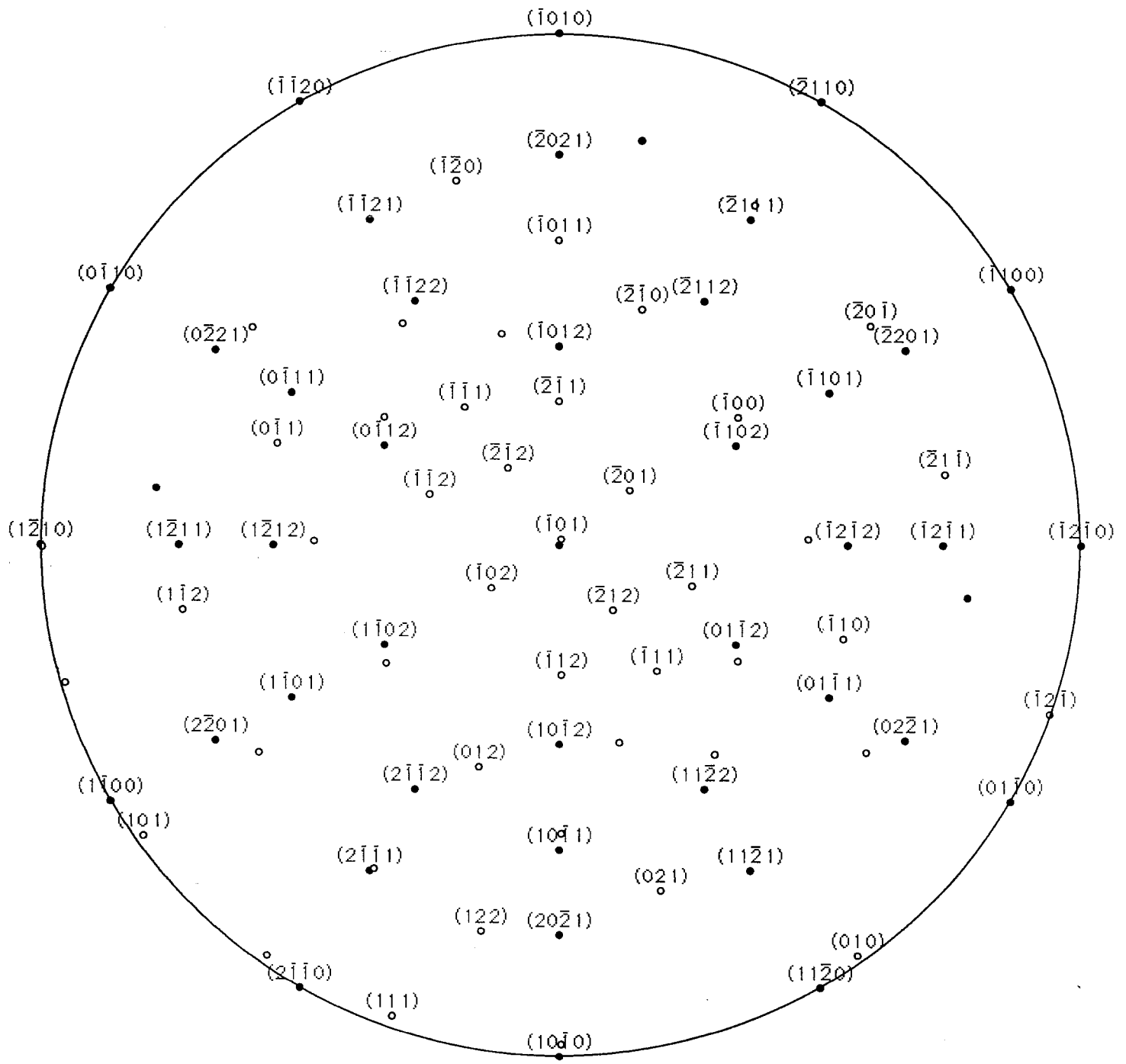

Fig. 4.87 (Continued)

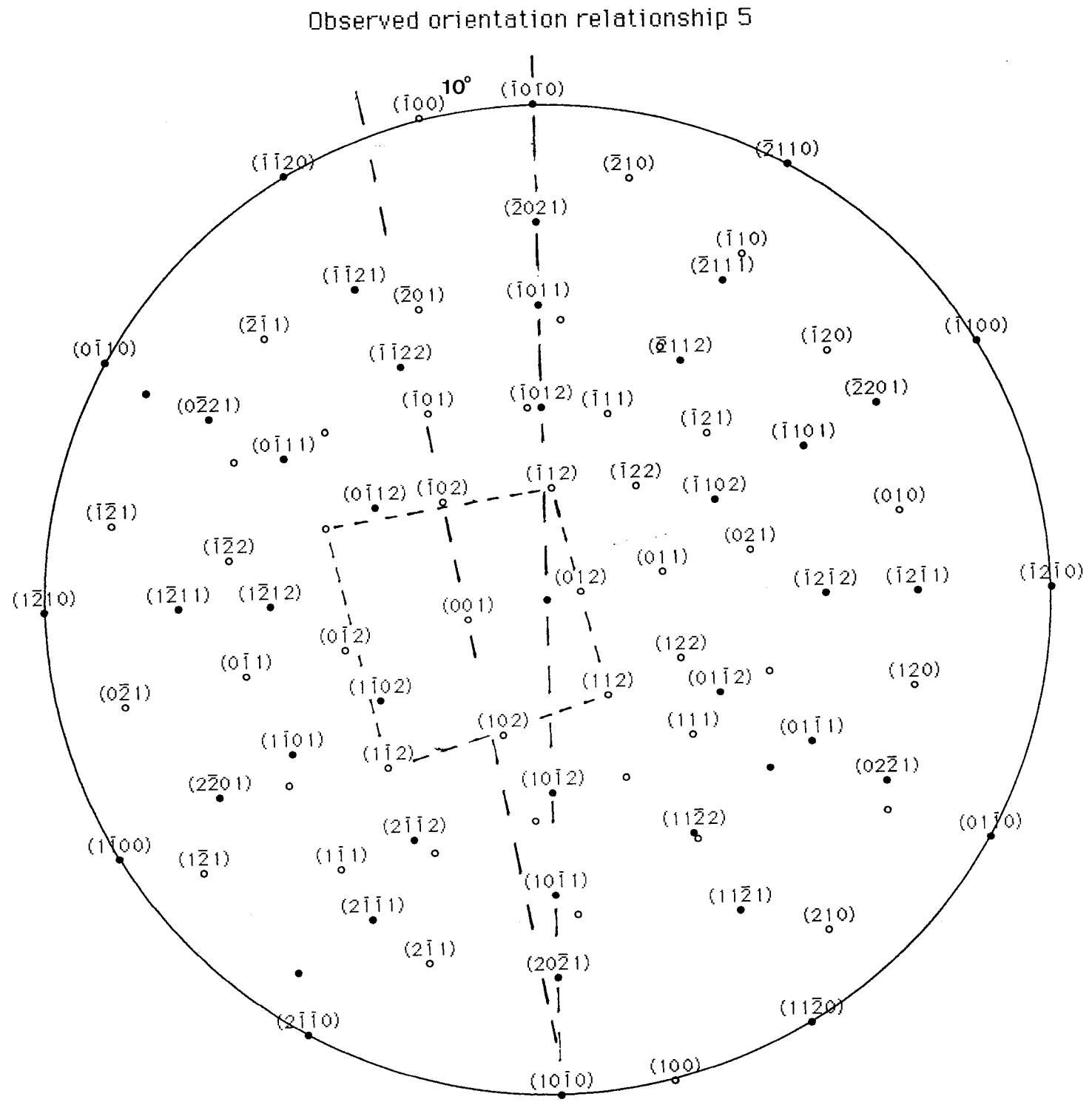

Fig. 4.87 (Continued)

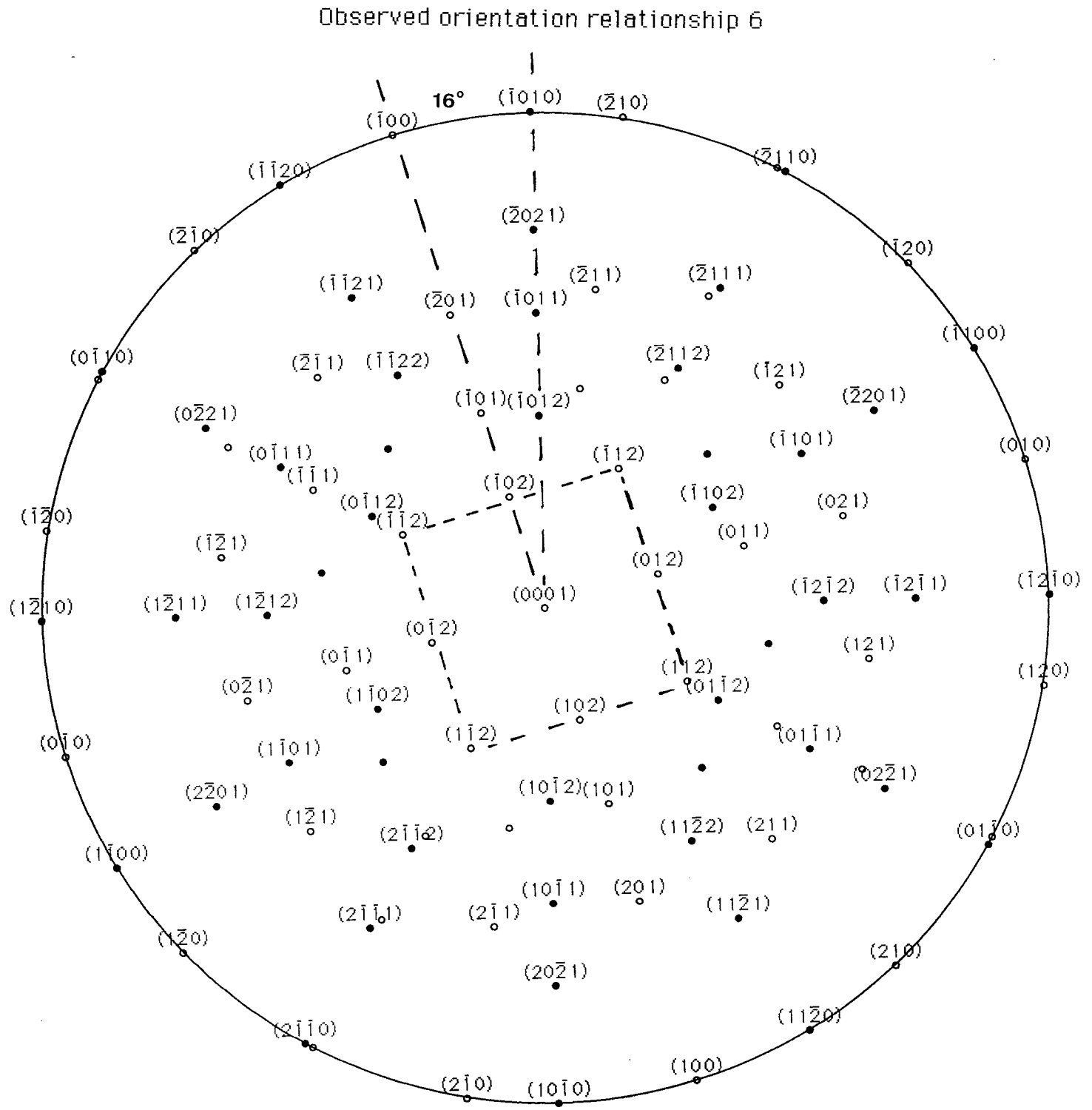

Fig. 4.87 (Concluded)

No.	Origin	Reduced O. R.	Type
1	Grade 2	{0001}‖{111} <$1\bar{2}10$>‖<101>	III
2	Grade 12	{0001}‖{010} <$1\bar{2}10$>‖<110>	II
3	Grade 12	{0001}‖{001} <$01\bar{1}0$>‖<110>	I
4	Grade 2	{0001}‖{101} <$1\bar{2}10$>‖<111>	IV
5	Grade 2 450°C annealed	{0001}‖{001} <$01\bar{1}0$>‖<110>	I
6	Ti-3.5Ni 450°C annealed	{0001}‖{001} <$01\bar{1}0$>‖<110>	I

Table 4.6 Results of stereographic analysis of observed orientation relationships

(fig. 4.83) is very similar to this, except that the bisecting line of the central square is at 0° from the direction of a {1010} matrix pole in this case. One of the observed orientation relationships (no. 2) is best identified with this pattern. The deviation of up to 6° in the orientation of the observed patterns with respect to the standards, and the displacements of the pattern centres, are to be expected from non-ideal diffracting conditions seen in some of the electron diffraction patterns, manifested in an asymmetrical brightness of the spots in both matrix and precipitate patterns.

Relationship (I) has previously only been reported in an α-β alloy (Ti-6Al-4V)[63], but here it has been observed in grade 2 (entirely or almost entirely α), grade 12 (α-β) and Ti-3.5Ni (α-intermetallic). Relationship (II) has previously been reported in both α and α-β alloys.[61,62] The two remaining observations (nos. 1 and 4) correspond accurately with two simple, previously unreported relationships:

$$\{0001\}_{metal} \| \{111\}_{hydride}, \qquad \langle 1\bar{2}10\rangle_{metal} \| \langle 101\rangle_{hydride} \qquad \text{(III)}$$

and

$$\{0001\}_{metal} \| \{101\}_{hydride}, \qquad \langle 1\bar{2}10\rangle_{metal} \| \langle 111\rangle_{hydride}. \qquad \text{(IV)}$$

These relationships, however, are both known in connection with titanium alloys, since (III) was also reported by Hall[107] as the orientation relationship between α titanium and the interface phase in Ti-6Al-4V. This interface phase was cubic with a lattice parameter 0.436 nm, rather close to the lattice parameter of the cubic hydride, and Hall speculated that consequently the interface phase encouraged grain boundary hydride nucleation in this alloy. It is therefore not surprising that the hydride itself can adopt this orientation with respect to the matrix.* Relationship (IV) is also the usual Burgers relationship between α and β titanium. The occurrence of this relationship between the hydride and α

* Recently there has been debate as to whether the interface phase observed in Ti-6Al-4V by Hall and others is in fact a hydride phase introduced by the electrothinning of thin foils, since ion beam-milled thin foils do not show it[108]. This work would seem to make this more likely, especially in view of the tendancy observed in grade 12 for hydrides to form at α-β interfaces.

is more difficult to explain since the lattice parameters of the hydride and β phase are quite different. Altogether it would seem that there are at least 6 orientation relationships that hydrides in titanium alloys can adopt.

The habit planes have also been determined for the hydrides in fig. 4.82 (except for nos. 3 and 4, which are examples of the massive form of hydride bordering the β phase in grade 12, where the habit of the hydride is determined by the grain boundary). This has been done for each case by angular measurement of the direction of the long axis of the precipitate on the micrograph, application of an angular correction due to the rotation of the image in the microscope with respect to the diffraction pattern, these corrections being different for every magnification, and construction of a normal to the resultant angle to find the direction expected for a spot in the matrix diffraction pattern that would be responsible for a habit plane in the observed direction. The results are shown in fig. 4.88. It is noted that this method assumes that the hydrides cut the foil perpendicularly, and that if a hydride platelet was at an angle to the plane of the foil its trace could be coincidentally colinear with that of a matix plane on the observed zone axis. However, the results were found to agree with previous reports of the hydride habit planes as determined from two surface analysis. This is probably a consequence of the selection of areas for observation as being those giving simple rational matrix zone axes, thus increasing the chances that the hydrides, occurring on or close to low index habit planes, would be parallel to the zone axis.

Both the habit planes reported by Liu & Steinberg,[58] $\{1\bar{1}00\}$ and $\{1\bar{1}01\}$, have been observed, also a habit plane inclined by 20° to the {0001} basal plane, eqivalent to a plane with indices $\{10\bar{1}5\}$. This agrees with previous reports of near-basal habit planes. The proposition of Williams,[60] that the less-rational habit planes sometimes observed could be due to "sheafs" of unresolved hydrides having a directional trend different to their true habit plane, is clearly inapplic able here, since the hydrides are individually resolved.

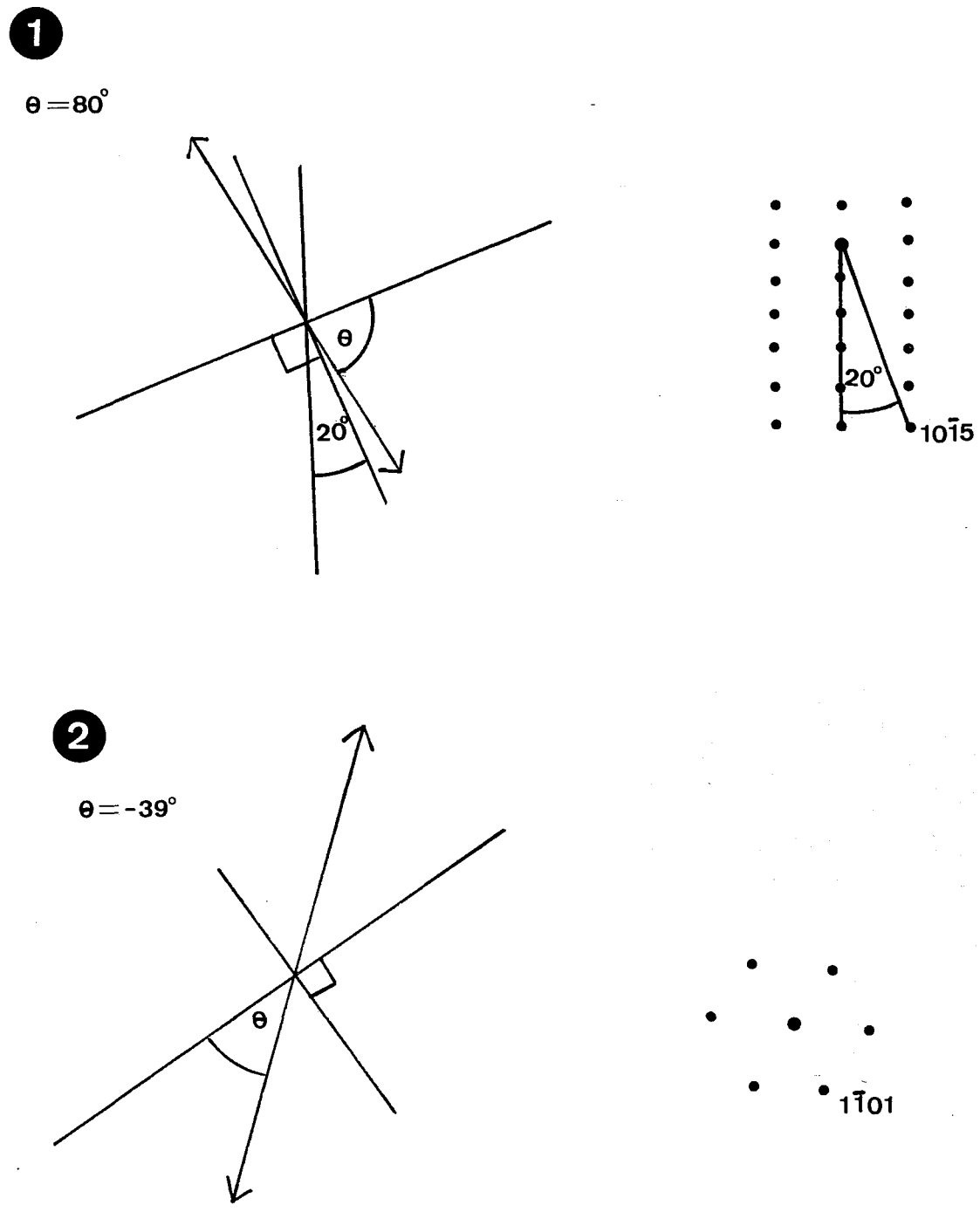

Fig. 4.88 Determination of habit planes for intragranular hydrides in fig. 4.82, assuming perpendicularity in all cases to the plane of the foil (Arrow indicates line of hydride(s), drawn to correspond with micrograph, θ is microscope image rotation for particular magnification. Diffraction spot corresponding to habit plane is indexed.)

5

θ = -83°

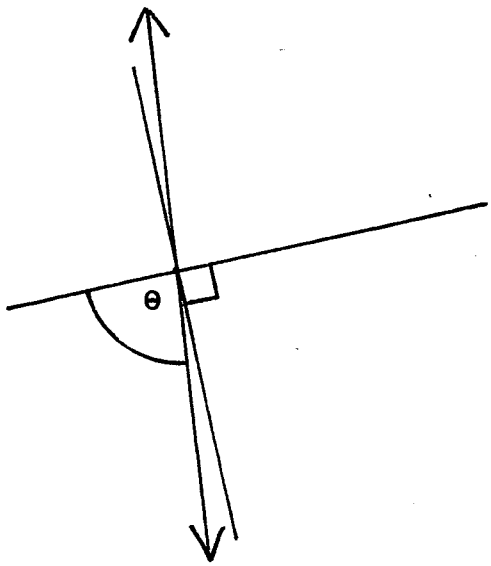

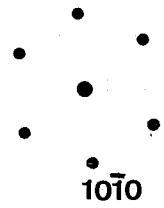

6

θ = -39°

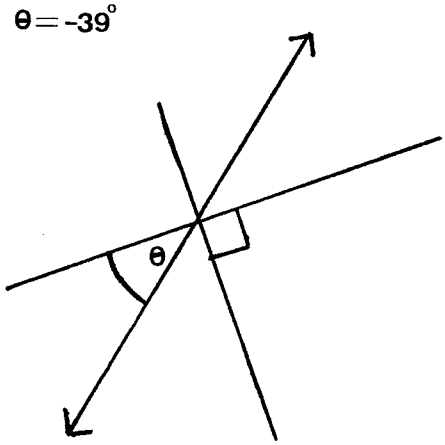

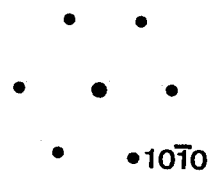

Fig. 4.88 (Concluded)

It was noted during the examination of the grade 12 foils that one zone axis, {111}, tended to predominate in the diffraction patterns of the β phase. This seems to reflect a strong anisotropy in the thinning properties of β titanium.

4.7 In-situ Straining

The principal objective behind the separate experiment on the in-situ straining of hydrided grade 2 titanium foils in the high voltage microscope was to observe directly the mechanism postulated by Paton and Williams[20,47,60] for the precipitation of hydrides at a crack tip in response to the applied stress gradient in a material supersaturated with hydrogen. However, no evidence for this mechanism was found. It may be that it can occur, but that in these tests either the concentration of hydrogen in the material was too low, or, more likely in view of the fact that the samples did actually contain hydrides, that the strain rate had to be too fast to allow time for diffusion to take effect because of the limitation of the filament battery life already mentioned.

Cracks were observed, and their gradual extension was followed as the applied stress was increased. Pre-existing hydrides were also observed, but the formation of new hydrides at crack tips was not. However, some cracks were observed to grow along large pre-existing hydrides, and the growth of such a crack through fracture of the hydride itself, rather than the matrix or interface, was observed. While matrix cracks (fig. 4.89) were observed to grow uniformly, maintaining a constant shape, the hydride crack (fig. 4.90) surprisingly seemed to grow in stages, with voids opening up ahead of the crack front, ligands forming and then failing in an apparently ductile manner. This pattern of hydride failure could be the cause of the fine ridge markings on the fracture surfaces of hydrided titanium alloys that have sometimes been reported[109]. It should be pointed out, however, that most of the cracks observed were not in hydrides.

In relation to the theory of stress-induced precipitation of hydrides, it may be mentioned that two other lines of enquiry produced null results. One was an experiment to

Fig. 4.89 Crack in grade 2 matrix photographed at successive times during straining in the HVEM (bright field): straining current = (A) 55 mA, (B) 70 mA

Fig. 4.90 Crack proceeding through hydride photographed at successive times during straining in the HVEM (dark field): straining current = (A) 160 mA, (B) 165 mA, (C) 170 mA

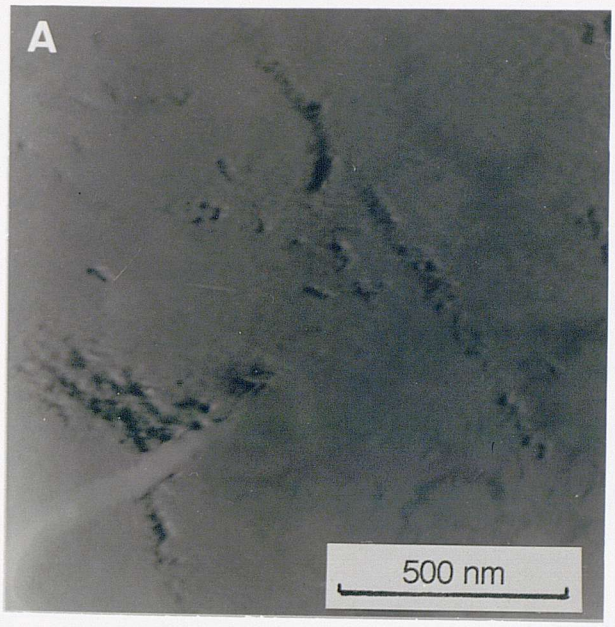
A
500 nm

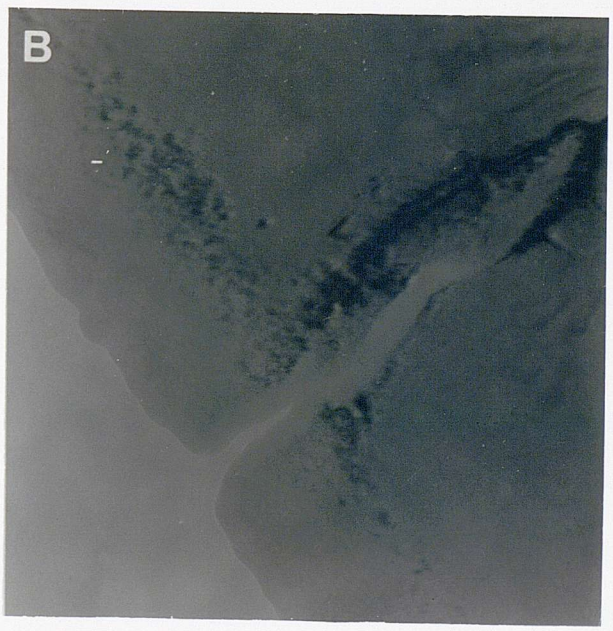
B

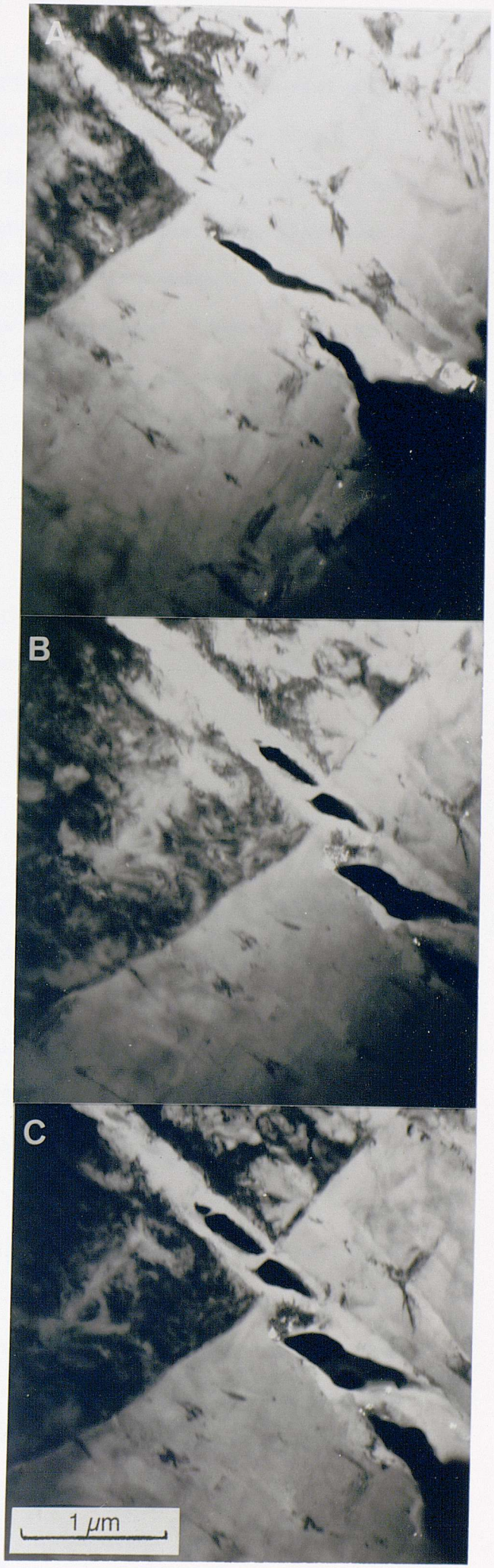
A
B
C
1 μm

photograph optically the hydrides on the surface of 7 day exposed equiaxed grade 2 before and after testing to fracture in order to look for a change in the density of the surface hydrides. This was made difficult by the irregularity of the surface after plastic deformation, but no change in the hydrides was detected. The other was the production of grade 12 metallographic sections from similar hydrided samples before and after straining to find out if there was any increase in the amount of hydride in the cross-sections viewed using backscattered electrons attributable to the deformation. Again no change was detected.

4.8 Other Observations

4.8.1 Stress-Hydriding Samples

In addition to the work on the samples hydrided as described, some microscopy was also performed on samples which had been hydrided while under tensile stress. These samples were supplied by the Spanish (INASMET) partners in the project.

The samples were 3 mm diameter cylindrical tensile specimens of grades 2, 5 and 12 which had been cathodically polarised at 1.5 v in synthetic seawater whilst undergoing a strain rate of 3×10^{-7}/s. This is a strain rate some 260 times slower than that in the work previously described. The conditions were designed to encourage the stress-induced absorption of hydrogen to take place. The hydriding solution and voltage represent slightly less aggressive conditions than in the work previously described. Unfortunately the samples did not all receive this treatment for the same period, the length of the tests being 10 days for the grade 2, 7 days for the grade 12 and 3 days for the grade 5.

Metallographic sections were made both perpendicular and parallel to the strain axes of the specimens and were examined optically and by means of secondary and backscattered electrons in the SEM. Hydride layers were seen in the grade 2 and grade 12, visible in all 3 types of image. Cracks in the hydride layers were observed in the sections parallel to the tensile stress. A rolling texture was visible in the grade 12 perpendicular to the tensile axis,

and it can be seen in the optical image (fig. 4.91) how the darkening of the grain boundaries, representing the hydride phase, penetrates further into the sample when the edge is perpendicular to the rolling direction than when it is parallel to it. Hence again the hydride distribution is determined by the distribution of the β phase, in this case caused by the rolling.

The hydride layers in the grades 2 and 12 are shown in figs. 4.92-4.93 (sections parallel to tensile direction). The layer in the grade 12 is about 30 μm in depth and quite solid and homogeneous. The layer in the grade 12 is about twice this depth but discontinuous, following the β phase paths as noted before. Referring to fig. 4.70, this is about twice the penetration observed for the same period with a similar microstructure in the unstressed hydriding experiments, and this indicates an influence of the stress in either encouraging diffusion or precipitation or both. Considering the volume increase that accompanies hydride formation, the latter seems more likely to be the major component, the tensile stress reducing the energetic barrier to hydride formation. Another explanation might be that deformation during hydriding breaks up the surface oxide layer allowing the hydrogen to reach the metal surface. The effect of the stress is apparently greater in the grade 2, since that material showed no hydride layer at all in the cross-sections when unstressed hydriding was employed for up to twice the hydriding period used here.

Because the grade 2 has been exposed for 43% longer than the grade 12 it could be said that the rate of growth of the hydride layer in the grade 12 is nearly 3 times that in the grade 2 under this treatment. This, however, ignores the different character of the layers in the two materials. A difference is also noticeable in the cracking behaviour of the surfaces. The cracks in the grade 12 are sharp and much deeper than those in the grade 2, often extending 2-3 times the depth of the hydride layer, while those in the grade 2 are blunt and shallow, never extending beyond the hydride layer. The cracks in the grade 2, however, are about twice as numerous as those in the grade 12. This accords with the lack of any measurable embrittlement in the grade 2. The cracking in this material merely

Fig. 4.91 Grade 12 cylindrical stress-hydriding specimen sectioned perpendicular to tensile axis, showing hydride penetration (optical): (A) edge perpendicular to direction of rolling texture, (B) edge parallel to direction of rolling texture

Fig. 4.92 Grade 2 cylindrical stress-hydriding specimen sectioned parallel to tensile axis, showing hydride layer and cracks (SEI)

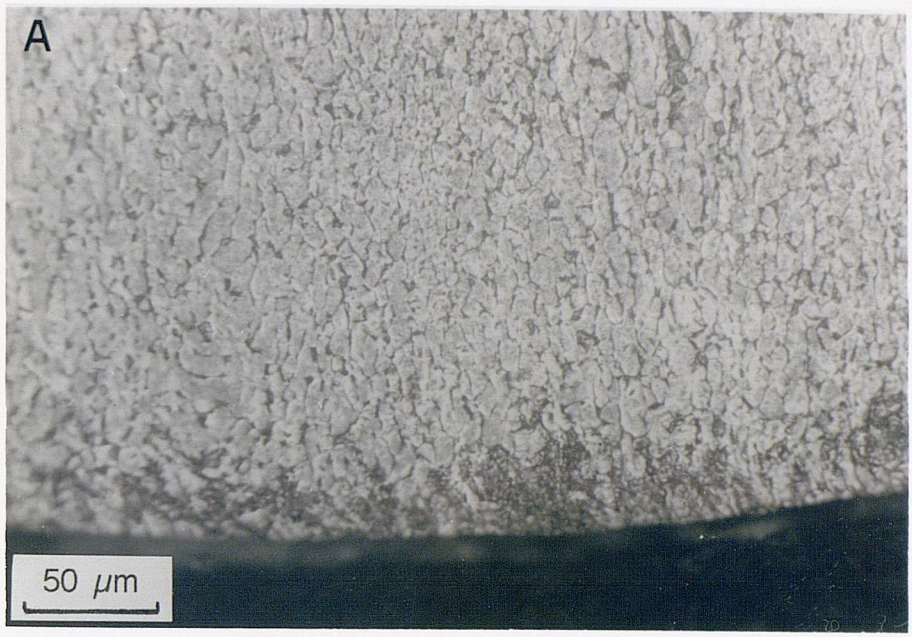
A
50 μm

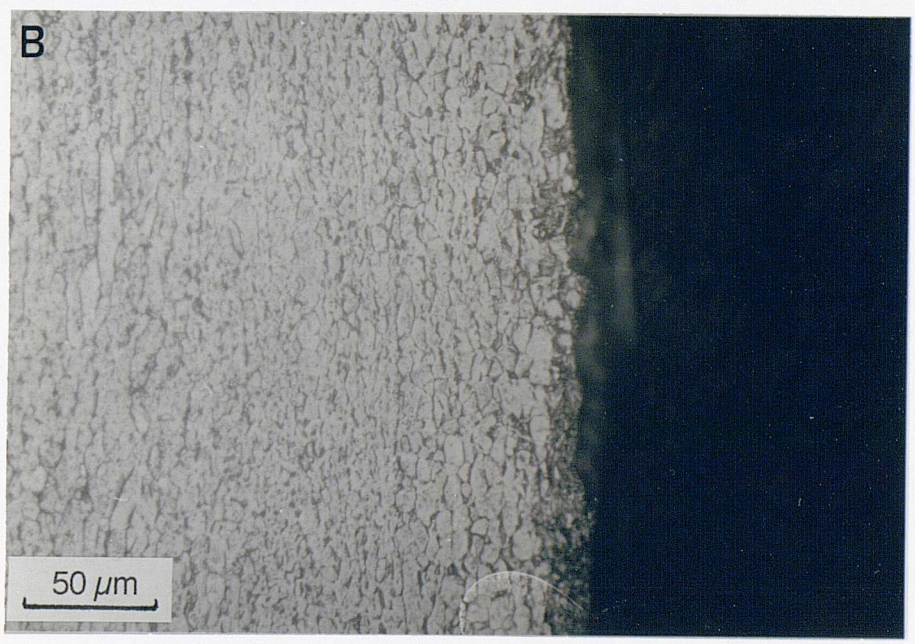
B
50 μm

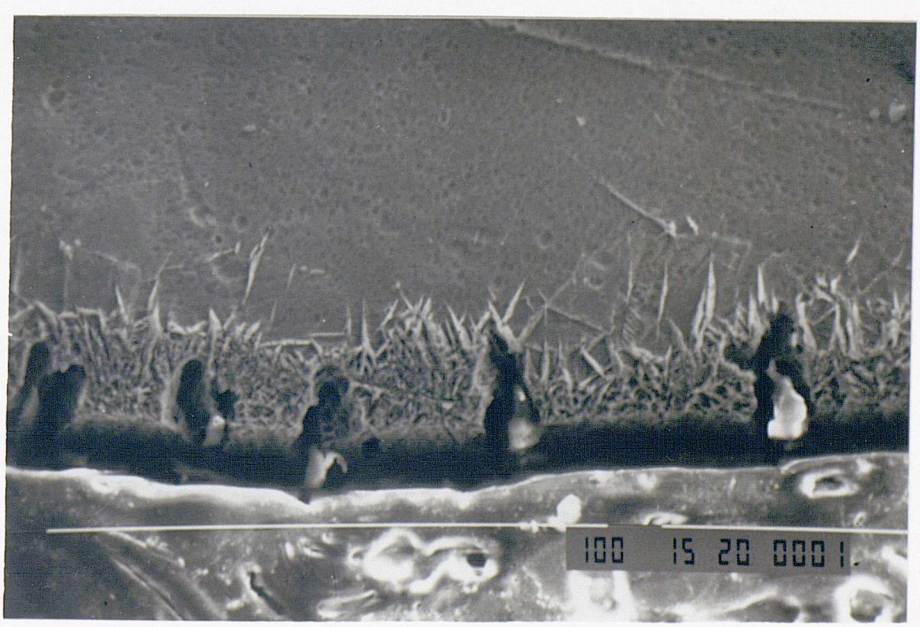
100 15 20 0001

represents the breaking up of a brittle surface layer as the metal underneath deforms, and thus the surface layer would have to grow to a much larger proportion of the total thickness of the sample (it is about 1% in the present case) to have a measurable effect on the properties. In the grade 12 however, there is internal embrittlement owing to the hydrides or solute hydrogen or both causing rapid crack growth. The fact that the cracks in the grade 12 do not in general seem to follow hydride paths or have hydrides at the tips supports the suggestion made by the author in section 2.16.2 that room temperature hydrogen embrittlement in titanium alloys could be primarily a matrix decohesion process, with crack growth due to a reduction in the surface energy of the metal caused by the interstitial hydrogen, as is believed to be the case in iron and steels, with the hydrides being only symptomatic of the high hydrogen concentration in the matrix.

The grade 5 showed no hydrides and no cracks in any type of image. It can thus be definitely stated that this alloy is the least susceptible to the effects of hydrogen.

4.8.2 Fatigue Sample

Finally, an examination was also made of a grade 2 fatigue sample supplied by INASMET. This was of the pattern shown in fig. 4.94, and had been tested for 18 days at 0.2 Hz in synthetic seawater with a polarisation of -1.5 V. A crack had propagated from the notch tip about 2 cm into the material. When separated, the sides of the crack showed evidence of hydriding, which the SEM showed to be in the form of large plates on the fracture surface. However, it seems likely that these formed following the crack, since examination of a polished and etched section of the crack tip (fig. 4.95) shows no apparent relation between the hydrides and the progress of the crack. There are many transgranular hydrides near the sample surface which the crack has cut across, but no evidence of particular hydriding at the crack tip. No effect of the hydrogen had been reported on the crack growth rate, so it seems that again the hydride effects in the grade 2 are superficial.

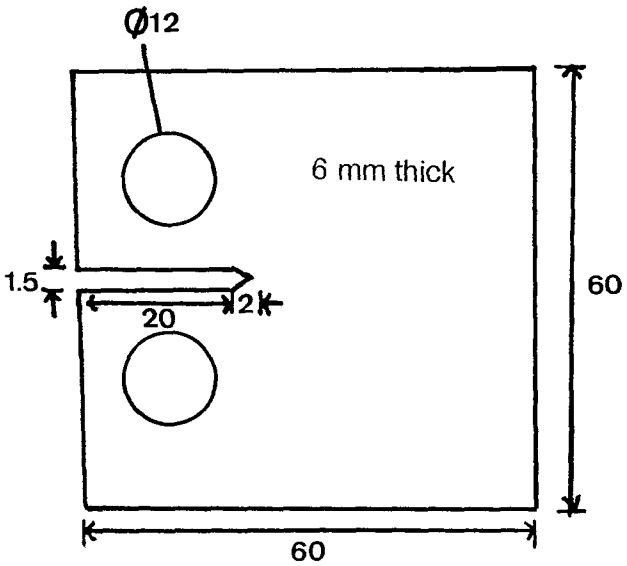

Fig. 4.94 Pattern for INASMET fatigue sample (dimensions in mm)

Fig. 4.93 (A & B) Grade 12 cylindrical stress-hydriding specimen sectioned parallel to tensile axis, showing hydride layer and cracks (BEI)

Fig. 4.95 Grade 2 fatigue specimen: section through crack tip region (BEI)

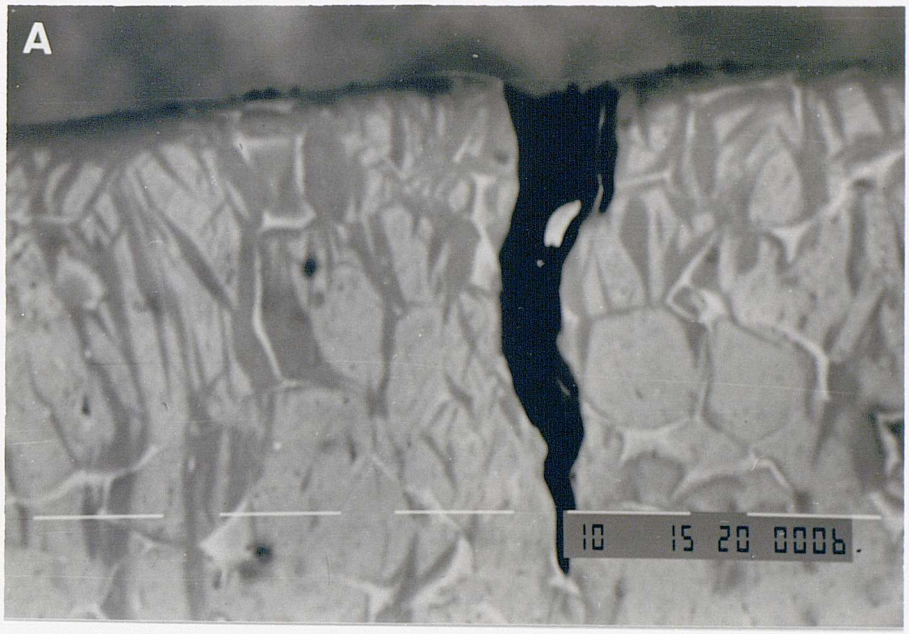
A
10 15 20 0006.

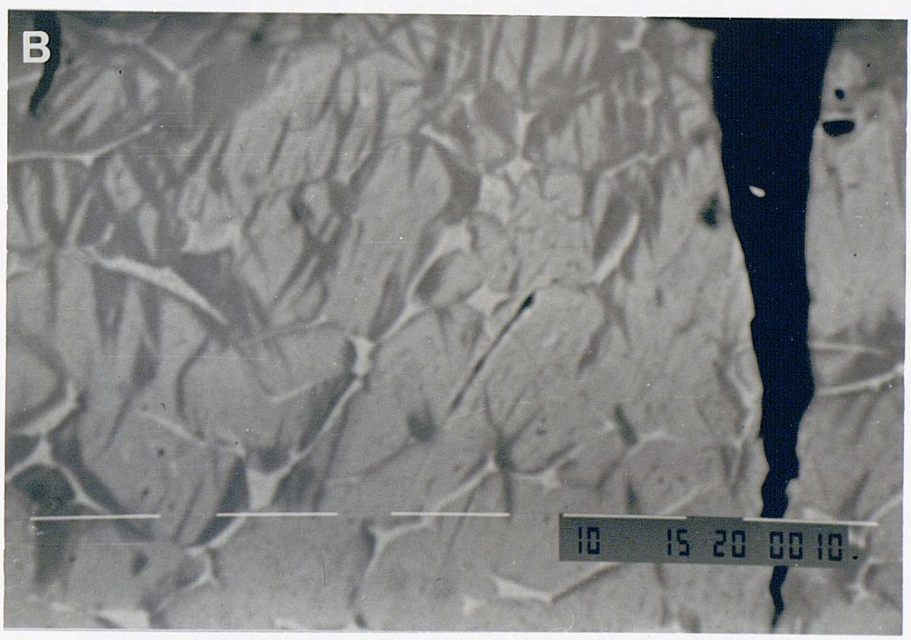
B
10 15 20 0010.


100 25 20 0407

5 DISCUSSION

The results of the present work on grade 2 (near-α titanium), for which ductility was observed actually to increase up to 14 days hydriding time, and thereafter to fall, may be compared to those of Haynes[110] on the α alloy Ti-5Al-2.5Sn, who also observed an increase in ductility in slow strain rate tests, up to a reported hydrogen content of 300 ppm, and thereafter a fall at higher hydrogen contents. Haynes identified the level of 300 ppm as the concentration at which the first hydrides were formed in his alloy. In the present work surface hydrides were seen in the equiaxed grade 2 for all hydriding times greater than 1 day, but no detectable hydride layer was visible in the cross-sections up to 20 days.

A means of relating hydride layer thickness to overall hydrogen concentration in commercially-pure titanium samples is provided by the work of Mc.Kinskey et al.[23], in which relationships have been derived and graphs drawn relating average hydrogen content to the ratio of hydride layer thickness to sample thickness for flat sheets, neglecting edge effects. These graphs were checked against measurements. Part of this work has been reproduced in fig. 5.1, which shows that a concentration of 300 ppm in a grade 2 sheet should correspond to a hydride thickness ratio of about 5×10^{-3}, giving for a 0.5 mm thick sample a layer thickness of 2.5 μm. If the grade 2 behaves similarly to the Ti-5Al-2.5Sn in terms of ductility changes with concentration, then this is the thickness expected in the grade 2 after 20 days hydriding, at which time the ductility has returned to its unhydrided level. It is feasible that this thickness might not be detected by backscattered imaging, given the problems of observing a polished surface at the very edge (c.f., for example, figs. 4.71 & 4.73). Hence these results seem to be consistent with earlier reported work, and had the hydriding been carried on much longer, some reduction in ductility of the grade 2 compared with the unhydrided value would have been expected.

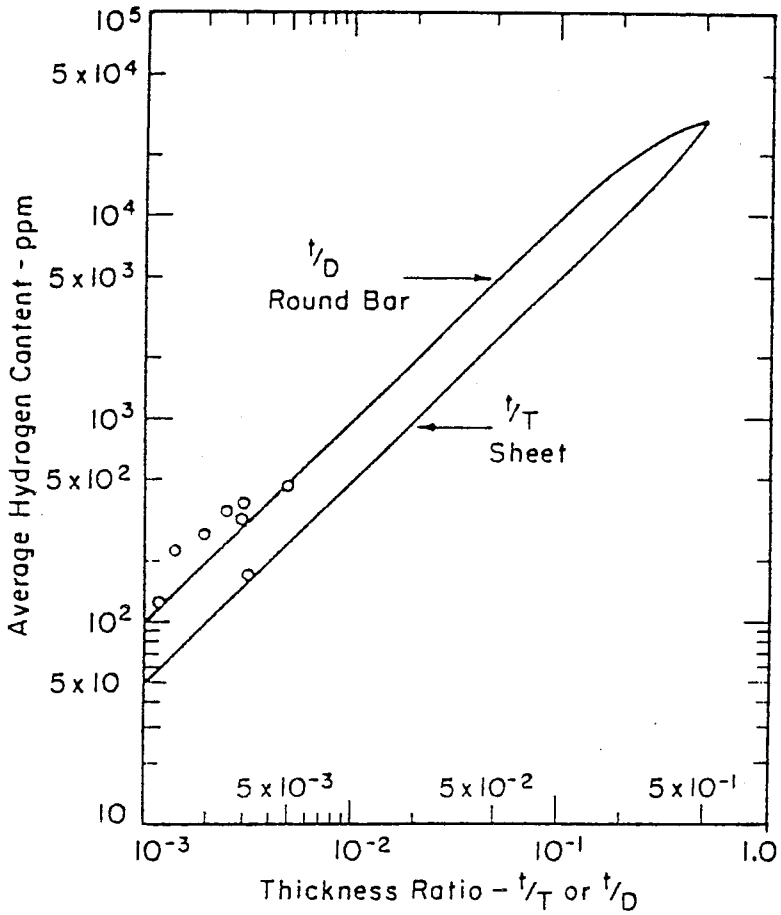

Fig. 5.1 Relationship between overall hydrogen concentration and hydride layer thickness ratio for commercially-pure titanium specimens as calculated by Mc.Kinskey et al.[23]

Haynes was not able to suggest any explanation for the increase in ductility at low hydrogen levels. The deformation modes of titanium might be altered by a change in axial ratio of the lattice, but there is no evidence that hydrogen in solid solution has this effect. The accumulation of hydrogen atmospheres around dislocations would be expected to have the opposite effect on ductility. Haynes also observed little effect of hydrogen up to 900 ppm on tensile strength and 0.1% proof stress.

Fig. 5.1 can probably not be applied to the results on the grade 12 material, in which hydride thicknesses were measured, except to provide a lower limit of hydrogen concentration, since the presence of the β phase in the grade 12 must increase the amount of hydrogen that can be stored in the material without precipitation. A further difficulty is that the hydride layer in the grade 12 is not homogeneous, but in the case of the equiaxed specimens (fig. 4.71, for example), the morphology is such that this is unlikely to affect the estimate of hydride volume by a factor of more than 2. The measured hydride depths in the 7 and 20 days hydrided equiaxed grade 12 specimens correspond by fig. 5.1 to average hydrogen contents of at least 2000 and 5000 ppm respectively. Some other work exists, by Sorensen and Ruppen[111], on the slow strain rate embrittlement of grade 12. They carried their tests to a maximum of 1000 ppm average hydrogen concentration, and found that at this level the ductility was reduced by a third of its unhydrided value. Since both the 7 day and 20 day samples in the present work gave ductility reductions much greater than this (77 and 80% respectively), this work is consistent with the minimum estimates of hydrogen concentrations given above. The fact that the large increase in hydride layer thickness between the 7 day and 20 day samples produced little further reduction in ductility suggests that the mechanism of ductility reduction is the initiation of cracks near the surface, which then spread rapidly through the bulk. The peak stress and 0.1% proof stress, on the other hand, are not seen to change significantly until 20 days hydriding, which is consistent with the view that the reductions in these parameters are due to the gradual reduction of the cross-sectional area of unaffected metal as hydriding proceeds. The percentage reductions in peak stress and 0.1% proof stress in the

equiaxed 20 days hydrided material, 12 and 21% respectively, are of the right order to be accounted for in this way, since the hydride penetration (taking into account both sides) is about 20% of the total thickness in that case. In the 20 days hydrided basketweave material, with its dispersed distribution of hydride, the percentage reduction in ductility is equal to that of the 20 day equiaxed material, but the percentage reductions in peak and 0.1% proof stress are 3-4 times higher. This suggests that the rate of absorption of hydrogen and the total volume of hydride produced in a given time are much greater in the basketweave microstructure.

Annealing of the 7 day equiaxed grade 12 at temperatures above 250°C resulted in a partial recovery of ductility accompanied by a reduction in surface cracking but an increase in the amount of cleavage in the bulk, a redistribution of hydride through the bulk of the material, and little change in the peak and 0.1% proof stresses. If the mechanism of ductility reduction is the initiation of cracks near the surface, the recovery of ductility may be attributed to the loss of hydride at the surface due to outgassing, and the more dispersed distribution of the same hydride volume may be seen as less favourable to the propagation of brittle cracks. The peak and 0.1% proof stresses, being dependent on the total volume of the hydride, are expected to be little changed.

The properties of the binary titanium-nickel alloys are more puzzling, since they showed substantial reductions in tensile parameters and changes in fracture characteristics without evidence of hydride precipitation. With increasing annealing temperature up to 450°C a continuous further degredation of properties is seen, though there is again evidence of a discontinuity in the ductility measurements between 250 and 300°C. This could imply the dissolution and redistribution of hydrides too small to be detected by backscattered imaging, say below 100 nm in width. Since the continuous phase in these alloys is α titanium as opposed to β in the grade 12, the slower thermal redistribution of solute hydrogen is to be expected, and explains why the tensile parameters continue to change, and the embrittled layer observed in the fractographs continues to extend, at temperatures

at which the grade 12 has attained equilibrium within the 1 hour annealing time. In the grade 12 but not in the binary alloys the dissolution temperature is already sufficient to diffuse the solute hydrogen uniformly through the sample thickness in this time. However, the reduction of ductility through annealing in the Ti-3.5Ni conflicts with what has been said before about the initiation of cracks by hydrides, and the reductions in the peak and 0.1% proof stresses cannot be explained by hydride redistribution. In this case all tensile parameters are adversely affected by a more uniform distribution of hydrogen, which suggests an atomic (interstitial) embrittlement effect.

The problems raised by the work overall are twofold. The first concerns the mechanism of embrittlement in the alloys: is it necessarily crack initiation by brittle hydrides, or is there an additional effect of matrix decohesion due to solute hydrogen, and do the two effects contribute differently to the embrittlement in different alloys? The second problem is to explain the large variation in the rate of hydrogen absorption between the alloys. If the estimates above are correct, the absorption rates under identical conditions of equiaxed samples of grades 2 and 12 differ by a factor of at least 16.

With respect to the first of these problems, the in-situ straining work in the high voltage microscope showed that cracks in grade 2 definitely can propagate through hydride failure along the long axis of the hydride. Such cracking would correspond to cleavage in one of the characteristic hydride habit planes. These have been re-examined in this work, all the observations on these alloys being consistent with the 3 habit planes previously reported, though not enough data was obtained to determine whether the proportions of the habit planes differ between the alloys. The most distinctive of these habit planes is $[10\bar{1}5]$, which is not a titanium slip plane, and this could well correspond with the near-basal cleavage that has been reported[69] in embrittled α alloys. In the observations that were made in this work on partially cracked stress-hydrided specimens, no cracking was seen except in the hydride layer in grade 2 specimens. In similar grade 12 specimens,

however, the cracks were generally in the matrix. These results suggest that both mechanisms occur, but definitive conclusions cannot be drawn from the present work.

On the question of absorption, the anomalously rapid uptake of grade 12 was noted by Sorensen and Ruppen[111], but no explanation seems to have been yet proposed. There can be little doubt on the basis of the present work of the important role played in the grade 12 by the nickel stabilised β phase paths in transporting the hydrogen through the surface layer of completely hydrided α titanium to allow new precipitation in the α below, and in generally accelerating the hydrogen diffusion. It has been shown in the present work that the more linear β network structure in the basketweave material transports the hydrogen still further into the material and increases the embrittlement.

If this is the complete explanation of the embrittlement in grade 12, however, it is difficult to account for the fact that grade 5, also an α–β alloy, shows no hydride precipitation and no embrittlement whatever. It is true that the β phase in the grade 5 is more broken up, but the gap between the β islands is typically less than 1 μm, a distance that in the grade 12 is regularly bridged by the hydrides, and some hydride formation at least at the edges would be expected. In fact the grade 5 is less susceptible to hydride precipitation than the purely α grade 2. On the other hand, severe embrittlement is encountered in the other titanium-nickel alloys although they contain no β phase and show no precipitation of hydrides.

It will now be proposed that the best explanation for these results can perhaps be found in the effect of the alloying elements on the electrical properties of the oxide layers on the alloys, with a consequent effect on oxide thickness and hence penetration of hydrogen ions.

As has already been briefly mentioned in section 2.7, the oxide layers on titanium and some other metals are believed to grow by a diffusional process in which electrons are

conducted from the metal, through the scale, to the surface where they combine with atmospheric oxygen to form O^{2-} ions which must then diffuse back through the scale in order to reach the metal surface, react with the positive metal ions, and add to the depth of the oxide layer. This is Wagner's theory of oxidation[112]. It is supported by experiments on many systems which show that the reaction rate constant for the oxidation process is directly proportional to the conductivity of the scale[113].

At low temperatures the scaling of metals generally obeys a logarithmic law and the scale reaches an ultimate thickness proportional to the oxidation reaction rate constant, and thus to the conductivity. In many systems the conductivity has been shown to be markedly sensitive to small alloying additions to the basic metal[113]. This mechanism seems worth considering with regard to the alloys in this work. There are various other effects that the alloying additions nickel, aluminium and vanadium (and the iron impurity in grade 2) may be causing, such as changes to the solid solubility of hydrogen, changes to the diffusion rate in the metal or the oxide, or changes to the lattice parameters of the metal and oxide and thus to the degree of coherence of the oxide scale, but all these effects are likely to be small for the fairly low alloying levels being considered, and do not seem likely to be able to explain the large differences between the hydriding behaviours of grades 2, 5 and 12. The conduction of oxide scales, however, has been shown to vary by 3-4 orders of magnitude for alloying additions of < 2% in systems such as ZnO (fig. 5.2, after Hauffe & Vierk[114]). Such a change in the conductivity of TiO_2 would cause a proportional change in the room temperature oxide thickness, and such a large change would be able to account for the difference in hydriding behaviours, along with the microstructural considerations already discussed. As yet, a behaviour similar to that of ZnO has not been convincingly demonstrated for TiO_2, but there is a certain amount of evidence to suggest it, as will be described.

The conduction in metal oxides is believed to be due to various defect mechanisms which can involve electrons, metal vacancies or oxygen vacancies[113]. Earle[115] has measured the

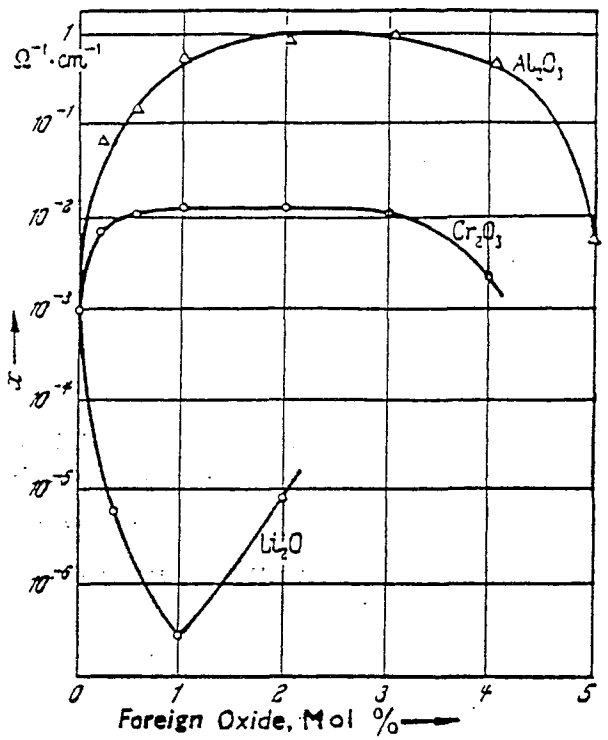

Fig. 5.2 Variation in conductivity in mixed oxides of zinc and other metals, after Hauffe & Vierk[114]

conductivity of titanium dioxide (rutile) as a function of the pressure of an oxygen atmosphere, and found that it decreases with pressure according to

$$\sigma = cp^{-1/4.3}$$

where c is a constant. From this he has concluded that rutile is an n-type semiconductor in which conduction is due to the presence of oxygen vacancies. Increasing the oxygen pressure eliminates these vacancies and causes the conduction to fall to an ultimate value c. The conduction of electrons is by means of the capture and release of the electrons by the oxygen vacancies, which create energy levels between the conduction and valence bands. This is confirmed by the work of Morton and Baldwin[116] who observed a blue colouration in the outer layers of titanium scales, thought to be due to the capture of electrons by O^{2-} vacancies (positively charged "holes") producing what are known as blue F centres.

Zinc oxide is also an n-type semiconductor, the difference being that in this case the conduction is thought to be by the exchange of electrons between positive metal ions on interstitial lattice sites. The changes in conductivity shown in fig. 5.2 are due to the introduction of oxides of metals having higher and lower valancies than that of zinc in ZnO. The addition of the lower valent lithium in LiO_2 causes effectively a freeing of some oxygen ions in the mixed oxide and a cancellation of the Zn^{2+} excess necessary for conduction. The conductivity thus falls to a minimum and then rises again on further additions of LiO_2 as an oxygen excess is created and the material goes over to become a p-type semiconductor. The addition of the higher valent metals chromium and aluminium in Cr_2O_3 and AI_2O_3 causes effectively a shortage of oxygen ions in the mixed oxide, amplifies the Zn^{2+} excess and thus causes the conduction to increase to a saturation point after which other processes take over.

The work of Hauffe and others[113] has shown that similar processes seem to take place in the homogeneous oxide layers formed on alloys as well as in the mixed oxides of different metals. In the case of the dilute titanium alloys we may put forward the model of

a uniform TiO_2 layer in which occasional titanium ions have been replaced by ions of another metal. The higher valence process would then consist of the foreign ion exerting a disproportionate oxygen affinity in the lattice, creating oxygen vacancies elsewhere in the lattice, and increasing the number of conduction sites (fig. 5.3). The lower valent process would consist of the foreign ions making some of the oxygen ions in the lattice redundant, thus decreasing the oxygen vacancy concentration and reducing the number of conduction sites (fig. 5.4). In the case of TiO_2, with a metal valence of 4, higher valence metals will be those forming stable oxides of the types M_2O_5 (valence 5) and MO_3 (valence 6). Lower valence metals will be those forming stable oxides of the types M_2O_3 (valence 3), MO (valence 2) and so on.

The existing data on whether titanium alloys obey these rules is inconclusive since no sufficiently systematic study of the oxidation rates of binary alloys seems to have been carried out. Most measurements of the oxidation rates of titanium alloys have been carried out at high temperatures, but Jenkins[117] has shown that the direction of the effect of alloying additions on the oxidation rate is often different between high and low temperatures. For example, 5% tungsten (valence 6) was shown to increase the oxidation rate of titanium at lower temperatures, in agreement with the theory outlined above, but the effect was reversed at 900°C. Since, in the work of Earle, the dependence of the conduction on the concentration of oxygen vacancies was found to decrease at higher temperatures, it seems likely that this mechanism is only the dominant one in determining oxidation rates at low temperatures, in the thin oxide layer, logarithmic rate law region that we are interested in.

Maynor et al.[119] showed that 4% vanadium (valence 5) increased the oxidation rate of titanium at a variety of temperatures, the increase being an order of magnitude at 750°C, the lowest temperature used. This is in accordance with the theory and of interest in connection with the behaviour of the grade 5 titanium (Ti-6Al-4V). No work has been found on the influence of nickel, (valence 2), which would be expected to decrease the

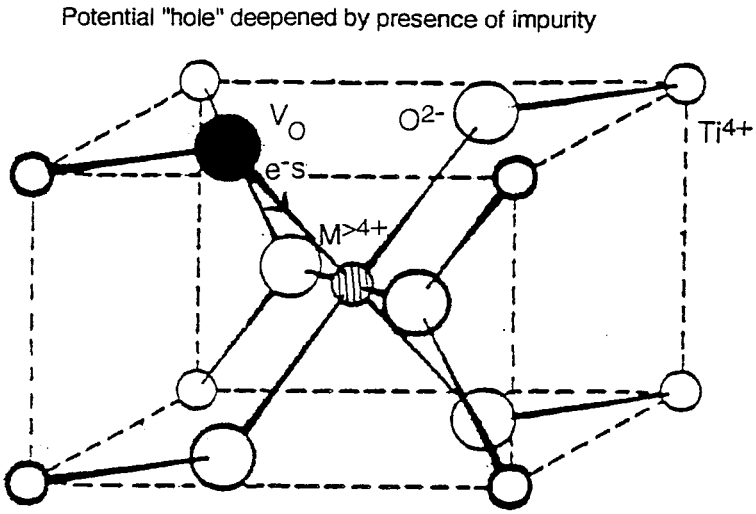

Fig. 5.3 Hypothetical effect of substitution of a higher valence ion for Ti^{4+} in TiO_2 lattice

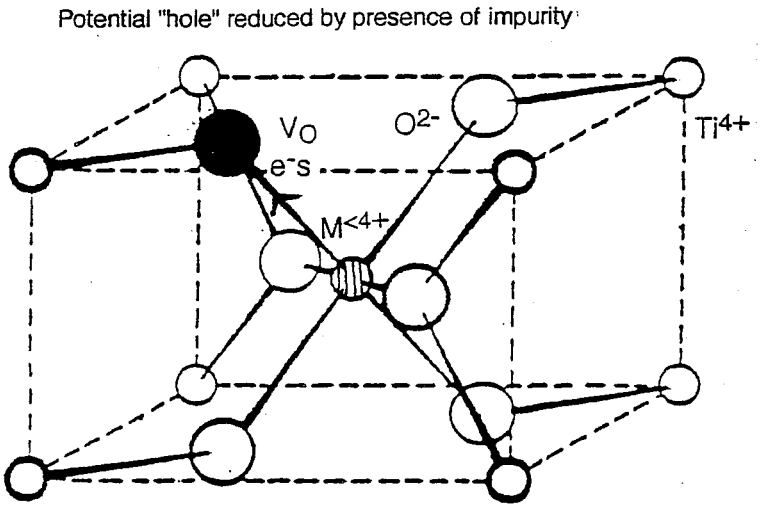

Fig. 5.4 Hypothetical effect of substitution of a lower valence ion for Ti^{4+} in TiO_2 lattice

(Structure of rutile after Wells[118])

oxidation rate. Jenkins also reported that 5% aluminium (valence 3) increased the rate of oxidation of titanium at 750°C. This may not be in conflict with the theory since, by analogy with the zinc case, 5% of a lower valence element may be sufficient to shift the oxide from being an n-type to a p-type semiconductor, and therefore an increased oxidation rate may be expected, or there may be some other reason for the increase at this temperature. What is required is data on the effect of the various alloying additions at a range of concentrations at lower temperatures.

Taking, however, the outlined mechanism as a hypothesis, we will impose a further assumption, that the oxide layer on the tensile samples is thin by comparison with the scale of the α/β microstructure, so that the situation is as in fig. 5.5. This assumption is justified by the fact that there is no obvious oxide layer visible in any of the SEM secondary electron micrographs of the cross sections. Then the concentration of the alloying elements in the oxide may vary according to what phase is adjacent to the oxide.

This theory accounts successfully for many features of the results. The fact that the nickel-containing alloys are always embrittled despite their containing different combinations of phases is explained because in the case of the grade 12 the partitioning of 3-4% nickel to the β strips ensures that the oxide layer is weakened at just the places at which the means for rapid hydrogen transport is present, and in the case of the Ti-3.5Ni and Ti-5Ni, the presence of small, frequently spaced islands of the very nickel-rich phase Ti_2Ni probably make the oxide layer uniformly thin because of the much smaller scale of these microstructures, and the higher overall nickel concentrations. In the grade 5, however, the higher valence element vanadium, which has been shown to have an oxidation-enhancing effect, is concentrated in the β phase, and so will have the effect of blocking those pathways at the surface. The aluminium concentration in the α can only have a limited effect on the hydrogen absorption of this relatively diffusion-resistant medium, though there is some evidence as mentioned that concentrations of about 5% aluminium increase the oxidation, so reinforcing the effect of the vanadium. The fact that

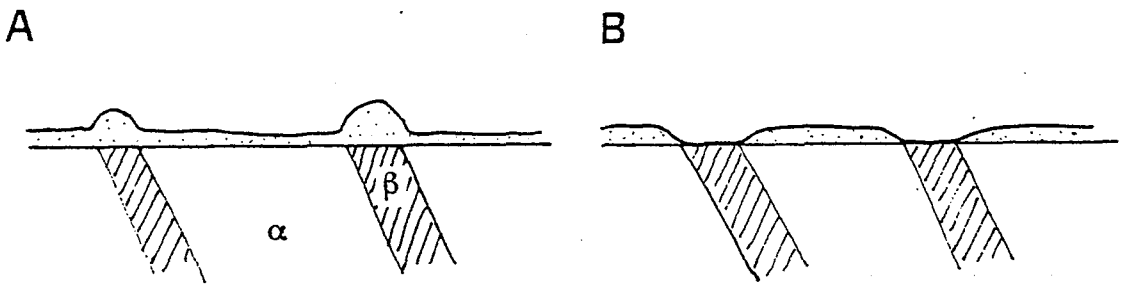

Fig. 5.5 Proposed effect of phases on room temperature oxide layer thickness in α–β alloys

a) β-stablising element of valence >4

b) β-stablising element of valence <4

the grade 2 is less resistant to hydriding than the grade 5 may be due to the iron content in the grade 2, iron having an oxidation valence of 3, putting it on the oxidation-limiting side, or it may just be due to the lack of oxidation-promoting elements. If the iron does have this effect it would explain the preference for high purity titanium in such applications as seawater-cooled heat exchangers and the like.*

Also explicable is the greater proportional effect on the hydride growth observed in grade 2 as compared with grade 12 when the samples were deformed during hydriding. Since the oxide on the grade 12 is weak anyway, oxide cracking under tension will have a less marked effect than in the grade 2 where the undisturbed oxide forms a more effective barrier. The fact that the percentage embrittlement in the nickel-containing alloys is greatest for the Ti-3.5Ni and diminishes slightly for the Ti-5Ni may indicate a reduction of the oxidation-limiting effect of the lower valence ion above a certain concentration as in the zinc alloys because of the complete cancellation of O^{2-} vacancies and a change to p-type conduction, but that is rather speculative.

Further in support of the theory, it may be mentioned that the Norwegian partners in the EURAM project performed some work on the alloy Ti-0.3Co-0.05Pd in which the hydrogen uptake by this alloy in cathodic experiments was found to be 2-3 times higher than that by grade 2 titanium. This alloy resembles grade 12 in being slightly β stabilised by an element of oxidation valence 2, in this case cobalt.

* There is some evidence for this in earlier work by the Finnish collaborators[120] on dilute titanium-iron alloys, in which it was found that increasing the iron concentration in the range 0.3 to 2.5 weight % increased the hydrogen absorption in cathodic charging experiments and also lowered (made more negative) the corrosion potential of the surface, indicating a reduction in the passivation effectiveness of the oxide film. The authors attributed these effects to the increasing volume fraction of β phase, but offered no explanation as to why this should reduce the corrosion potential.

It may be objected that this discussion has concentrated entirely on the entry of hydrogen into the material and not considered solubility effects, since what is observable is only the precipitation of hydrides. The solubility of hydrogen may be another variable factor, and as discussed in section 2.11, it has been suggested that solid solution strengthening by aluminium in titanium increases the level of supersaturation that is required for hydride precipitation owing to the expansion that accompanies precipitation. If this is so then a modified explanation of the different behaviours of the grade 2 and grade 5 might be that the aluminium content of the oxide covering on the grade 5 α phase is having its theoretically predicted weakening effect on the oxide, and the concentration of hydrogen in the near-surface areas of the α is as great or greater than that in the grade 2, but that the approximately 6% aluminium content of the α inhibits precipitation.

The main point that remains to be explained is the observed absence of hydrides in the Ti-3.5Ni and Ti-5Ni. If the equilibrium hydrogen solubility in the Ti_2Ni were particularly high then this might have the effect of preventing precipitation in the α through the provision of many small hydrogen "sinks", but this seems unlikely on the basis of the considerations shown in table 5.1, in which the atomic packing densities have been calculated for α and β titanium, nickel and Ti_2Ni. The atomic packing in the compound is shown to be even more efficient than a weighted average for α titanium and nickel, hence the interstitial space must be less than in α titanium. More probable, therefore, is an effect on the non-equilibrium solubility of hydrogen through strengthening of the metal. Since the nickel atom (in nickel metal) is significantly smaller than the titanium atom (in α titanium) (0.125 nm radius compared to 0.148 nm radius, a reduction of 15%), it is to be expected that there will be some strengthening effect in saturated or supersaturated solid solutions of nickel in α titanium. This would impede the precipitation of hydrides when the material is unstressed, but would allow the possibility of hydrides precipitating during testing due a reduction of the back-stress opposing hydride formation.

	Number of atoms in unit cell	Volume of unit cell (nm^3)	Volume per atom (nm^3)
α titanium	2	$ca^2 \sin 60 = 0.353$	0.176
β titanum	2	$a^3 = 0.359$	0.180
Nickel	4	$a^3 = 0.438$	0.110
Ti_2Ni	96	$a^3 = 14.42$	0.150

$$(2V_{\alpha Ti} + V_{Ni})/3 = 0.154 \text{ nm}^3$$

Table 5.1 Atomic volume calculations for various structures

The evidence is that Ti_2Ni is a brittle material, and therefore the scope for it to become further embrittled seems limited, implying that the embrittlement in these alloys must be due an effect on the α matrix, either intrinsic embrittlement due to interstitial hydrogen, or the stress-induced precipitation of hydrides during the test. The fractographs provide no particular evidence of hydride formation at the fracture surfaces, though massive hydrides are difficult to identify using secondary electron imaging, and there are certainly no hydrides in the cross-sections of the broken samples, unless they are smaller than the resolution limit of backscattered detection, therefore the evidence tends to support a theory of embrittlement of the metal by interstitial hydrogen.

6 CONCLUSIONS

• Alloys of titanium with nickel, including grade 12, are particularly susceptible to cathodic hydrogen embrittlement in an acidic environment. Commercially-pure titanium (grade 2) is much less susceptible, and Ti-6Al-2V (grade 5) is less susceptible still.

• The susceptibility to embrittlement of titanium alloys is influenced by microstructure, but it is more influenced by alloy chemistry.

• In α-β alloys the absorption of hydrogen is facilitated by continuous paths of β phase which allow hydrogen to diffuse into the bulk, bypassing the surface "passivating" hydride layer, which forms only in the α phase because of the much higher hydrogen solubility in the β. In grade 12 the basketweave microstructure, caused by annealing in the β field, and containing more direct diffusion paths through the β network, suffers 3-4 times more embrittlement in terms of the reduction in peak and 0.1% proof stresses compared with the equiaxed microstructure of the same alloy given the same treatment.

• Stress applied during cathodic hydriding accelerates the growth of the hydride layer, and the effect is greater on grade 2 than grade 12, though at a strain rate of 3×10^{-7}/s the rate of growth in the grade 12 is still 4 times that in the grade 2.

• Stress-influenced hydriding gives rise to internal embrittlement in grade 12, but only to a brittle surface hydride layer in grade 2.

• The progress of cracks in general in room temperature embrittlement experiments is not related to hydride pathways, indicating probably a level of internal embrittlement of the α titanium matrix by interstitial hydrogen.

• Embrittlement in Ti-3.5Ni and Ti-5Ni is not accompanied by the presence of hydrides detectable by SEM examination, nor by any other microstructural change.

• Hydrogen-charged Ti-3.5Ni and Ti-5Ni do, however, show the presence of a brittle surface layer which increases gradually in depth on annealing for 24 hours at temperatures between 250 and 450°C, the increasing depth corresponding to increased degradation of tensile properties.

• Hydrogen-charged grade 12 suffers a microstructural change at a threshold temperature between 250 and 300°C, indicating hydride dissolution at that temperature, but no further change occurs at higher annealing temperatures because the hydrogen is homogenised in 0.5 mm thick samples by diffusion through the β network at about the dissolution temperature. There is a partial recovery of ductility corresponding to this homogenisation, probably due to loss of hydrogen from the surface.

• The coincidence of the diffusion threshold temperature as determined from ductility measurements in Ti-3.5Ni with that in grade 12 may indicate that very small hydrides are involved in the embrittlement of the former alloy, and that the gradual extension of the embrittled layer is due to solute hydrogen diffusion through the α phase subsequent to hydride dissolution, but this point remains to be determined.

• Hydrides on the scale of TEM observation are found in all the alloys, though the effects of thin foil preparation have not been ruled out. 4 different orientation relationships between the hydride and the α phase have been observed, and 3 different habit planes for intragranular hydrides. In grade 12 the hydride occurs both in massive form on grain boundary habits, and in intragranular form.

• The presence of the β phase in the grade 12 is probably a result of the influence of the molybdenum addition on the kinetics of the (nickel-supersaturated β) → α + Ti_2Ni transformation.

• The influence of the β phase is not found to be crucial to hydrogen absorbtion since there is no detectable β present in the binary titanium-nickel alloys. It is suggested that some non-microstructural influence of alloying elements must be sought to explain the different susceptibilities to hydogen embrittlement, and that the oxidation properties of the alloys might be the crucial factor in cathodic hydrogen absorbtion. The results of the stress-hydriding experiments can be explained consistent with this idea as being due to oxide cracking.

7 SUGGESTIONS FOR FURTHER WORK

The theory of the effect of alloying elements of different oxidation valences concentrated in the different phases requires testing by means of a detailed study of the oxide layers on the alloys. This would probably involve holding the alloys at a slightly elevated temperature, say 200-300°C, in air, for a long period to try and obtain oxide layers observable in cross-sections by scanning electron microscopy, but not so thick as to obscure the proposed effect of the phases.

It would be desirable to discover the nature of the embrittled layer observed in the fractographs of the α-intermetallic titanium-nckel alloys; possibly this could be done by collecting sufficient of this material to perform X-ray powder diffraction on it.

A systematic study should be carried out of the behaviour of binary α–β alloys with various β stabilisers in order to test the proposition that resistance to embrittlement is conferred by using a β-stabilising element which exhibits a valence greater than 4 in its stable oxide. For really conclusive results to be obtained it would be necessary to adjust the compositions and heat treatments so as to obtain as closely as possible the same α/β microstructures in the alloys. Table 7.1 gives a list of the valences of the various β stabilisers.

The valence principle seems less applicable to α alloys because there are no α stabilisers with valences greater than 4, and only one with a lower valence, aluminium. It would be desirable to have systematic information on the hydrogen uptake of titanium-aluminium alloys at various compositions, since there is evidence of an oxidation-enhancing effect at concentrations around 5% which it has been proposed may be due to a reversal of the semiconducting type of the oxide. Whatever the reason, it may be beneficial to the hydriding resistance of the alloys. It has been seen that the combination of cathodic

β stabiliser	Valence
Tungsten	6
Vanadium	5
Niobum	5
Tantalum	5
Molybdenum	4
Manganese	4
Iron	3
Chromium	3
Nickel	2
Cobalt	2

Table 7.1 Valences of β-stabilising elements in their stable room temperature oxides

polarisation and tensile stress in a hydriding environment leads, probably due to the fracture of the oxide layer, to a bulk hydride growth in α titanium which, though relatively slow, would eventually render the material unserviceable. Therefore any alloying addition which accelerated the oxide growth and repair without, of course, excessively affecting the other desirable properties of the titanium would be an advantage.

8 REFERENCES

1. R. I. Jaffee, *Titanium 80* (Proc. Int. Conf.), AIME (1980), 51
2. E. A. Fisher & M. Dziekonski, *The Use of Titanium for Offshore/Subsea systems*, Titanium Engineers Inc. (1989)
3. *Metals Handbook*, ASM (1986), **2**, 814
4. H. Conrad, *Cryogenics*, **24** (1984), 293
5. W. G. Burgers, *Physica*, **1** (1934), 561
6. E. W. Collings, *Alloying*, ASM (1988), 257
7. P. Duwez, *Trans. AIME*, **45** (1953), 935
8. E. W. Collings, *The Physical Metallurgy of Titanium Alloys*, ASM (1984)
9. L. P. Luzhnkov, V. M. Novikova & A. P. Mareev, *Met. Sci. Heat. Treat.*, **2** (1963), 78
10. A. D. Mc.Quillan, *J. Inst. Met.*, **80** (1951), 363
11. F. R. Brotzen, E. L. Harmon & A. R. Troiano, *Trans. AIME*, **203** (1953), 413
12. Data sheet on IMI 318 Titanium, Imperial Metal Industries (1971)
13. J. M. Silcock, *Acta. Met.*, **6** (1958), 481
14. N. H. Polakowski & E. J. Ripling, *Strength and Structure of Engineering Materials*, Prentice-Hall (1968)
15. F. Ling, E. A. Starke & B. G. Lefevre, *Met. Trans.*, **5** (1974), 179
16. D. N. Williams & D. S. Eppelsheimer, *J. Inst. Met.*, **81** (1952-53), 553
17. P. Erlich, *Z. Anorg. Chem.*, **247** (1941), 53
18 Data sheet B256, ASTM
19. L. Lunde, *Offshore Use of Titanium-Benefits and Possible Limitations*, Norwegian Institute for Energy Technology, Report No. IFE/KR/E-95/004 (1985)
20. N. Paton, *Titanium 84* (Proc. Int. Conf.), AIME (1984), 2519
21. I. N. Kaganovich & T. V. Shikhaleeva, *Titanium and Titanium Alloys, Scientific and Technological Aspects*, AIME (1982), 1005

22. V. N. Modestova, V. V. Usova, N. D. Tomashov & T. I. Zhukova, *Ibid.*, 995

23. C. R. Mc.Kinskey, M. Stern & R. A. Perkins, *Trans. ASM*, **50** (1958), 438

24. J. C. Scully, *The Fundamentals of Corrosion*, Pergamon Press (1975)

25. A. R. Troiano, *Hydrogen in Metals* (Proc. Int. Conf.), ASM (1974), 3

26. A. H. Cottrell, *Introduction to Metallurgy*, Edward Arnold (1967), 460

27. M. J. Blackburn & J. C. Williams, *Trans. AIME*, **239** (1967), 287

28. G. M. Pennock, H. M. Flower & D. F. R. West, *Metallography*, **10** (1977), 43

29. K. Abe, H. Yoshinaga & S. Morozumi, *Trans. JIM*, **17** (1976), 551

30. R. I. Jaffee, *Designing with Titanium* (Proc. Int. Conf.), Inst. Met. (1986), 28

31. A. E. Jenkins, *J. Inst. Met.*, **82** (1953-54), 213

32. E. A. Gulbransen & K. F. Andrew, *Trans. AIME*, **185** (1949), 741

33. W. A. Alexander & L. M. Pidgeon, *Canad. J. Res.*, **B28** (1950), 60

34. T. T. Waber, G. E. Sturdy & E. N. Wise, *J. Amer. Chem. Soc.*, **75** (1953), 2269

35. N. Cabrera & N. F. Mott, *Rep. Prog. Phys.*, **12** (1948-49), 163

36. A. D. Mc.Quillan & M. K. Mc.Quillan, *Titanium*, Butterworths (1956)

37. R. J. Wasilewski & G. L. Kehl, *Metallurgia*, **50** (1954), 225

38. *Smithell's Metals Reference Book* (6th Ed.), Butterworths (1983), 13-58

39. G. R. Caskey, *Hydrogen in Metals* (Proc. Int. Conf.), ASM (1974), 465

40. M. E. Straumanis, T. Ejima & W. J. James, *Acta. Cryst.* **14** (1961), 493

41. T. Fukuzawa, K. Shimogri, H. Satoh & F. Kamikubo, *Titanium 80* (Proc. Int. Conf.), AIME (1980), 2685

42. A. D. Mc.Quillan, *Proc. Roy. Soc.*, **A204** (1950), 309

43. A. San-Martin & F. D. Manchester, *Phase Diagrams of Binary Titanium Alloys*, ASM (1988), 123

44. F. Ducastelle, R. Caudron & P. Costa, *La Journal de Physique*, **31** (1970), 57

45. H. Numakura & M. Koiwa, *Acta Met.*, **32** (1984), 1799

46. H. Margolin & H. Portisch, *Trans. AIME*, **242** (1968), 1901

47. N. E. Paton & J. C. Williams, *Hydrogen in Metals* (Proc. Int. Conf.), ASM (1974), 409

48. D. N. Williams, *Met. Trans.*, **4** (1973), 675

49. J. D. Boyd, *The Science, Technology and Application of Titanium*, Pergamon Press (1970), 545

50. A. Chretien, W. Freundlich & M. Bichara, *Comptes Rendus*, **238** (1954), 1423

51. L. D. Jaffee, *J. Metals*, **206** (1956), 861

52. R. L. Crane & S. C. Chattoraj, *J. Less-Common Metals*, **25** (1971), 225

53. H. L. Yakel, *Acta Cryst.*, **11** (1958), 46

54. Z. M. Azarkh & P. I. Gavrilov, *Soviet Physics-Crystallography*, **15-2** (1970), 231

55. S. S Sidhu, L. Heaton & D. D. Zauberis, *Acta Cryst.*, **9** (1956), 607

56. P. E. Irving & C. J. Beevers, *Met. Trans.* **2** (1971), 613

57. P. E. Irving & C. J. Beevers, *J. Mat. Sci.*, **7** (1972), 23

58. T. Liu & M. A. Steinberg, *Trans. ASM*, **50** (1958), 455

59. J. S. Bradbrook, G. W. Lorimer & N. Ridley, *J. Nuc. Mat.* **42** (1972), 142

60. J. C. Williams, *Effect of Hydrogen on the Behaviour of Materials* (Proc. Int. Conf.), AIME (1976), 367

61. G. Sanderson & S. C. Sculley, *Trans. AIME*, **239** (1967), 1883

62. J. D. Boyd, *Trans. ASM*, **62** (1969), 977

63. I. W. Hall, *Scand. J. Metall.*, **7** (1978), 227

64. N. E. Paton, B. S. Hickman & D. H. Leslie, *Met. Trans.*, **2** (1971), 2791

65. C. J. Beevers & D. V. Edmonds, *Trans. AIME*, **245** (1969), 2391

66. D. N. Williams, *Report on Hydrogen in Titanium and Titanium Alloys*, TML Report No. 100 (1968)

67. M. Nishigaki, A. Tanabe, Y. Ito & Y. Moriguchi, *Titanium 80* (Proc. Int. Conf.), ASM (1980), 1663

68. D. N. Williams, *Met. Trans.*, **4** (1973), 675

69. D. A. Meyn & G. Sandoz, *Trans. AIME*, **245** (1969), 1253

70. D. A. Meyn, NRL Memorandum Report 2461 (1972)

71. L. W. Berger, D. N. Williams & R. I. Jaffee, *Trans. AIME*, **212** (1958), 509

72. J. C. Grimm & W. J. Nowak, *Hydrogen in Metals* (Proc. Int. Conf.), ASM (1974), 433

73. A. E. Reisen & D. H. Kah, WADD Technical Report 60-275 (1960)

74. C. J. Beevers, *The Science, Technology and Application of Titanium*, Pergamon Press (1970), 535

75. TMCA Data Sheet *Room and Elevated Temperature Fatigue Characteristics of Ti-6Al-4V* (1957)

76. H. R. Gray, *Corrosion*, **28** (1972), 47

77. J. C. Williams, *Trans. ASM*, **60** (1967), 646

78. D. N. Wlliams & H. G. Nelson, *Met. Trans.*, **3** (1972), 207

79. M. J. Blackburn & W. H. Smyrl, *Int. J. Fract. Mech.*, **4** (1968), 171

80. B. A. Kolachev, *Titanium and Titanium Alloys, Scientific and Technological Aspects*, AIME (1982), 781

81. M. L. Wasz, C. C. Ko, F. R. Brotzen & R. B. Mc.Lellan, *Scipta Met.*, **23** (1989), 2039

82. A. Jostons & A. E. Jenkins, *Trans. AIME*, **239** (1967), 1318

83. M. T. Hepworth & R. Schuhmann, *Trans. AMIE*, **224** (1962), 928

84. P. N. Adler & R. L. Schulte, *Scripta Met.*, **12** (1978), 669

85. V. A. Livanov, B. A. Kolachev & A. A. Buhanova, *The Science, Technology and Application of Titanium*, Pergamon Press (1970), 561

86. T. B. Cox & J. P. Gudas, *Effect of Hydrogen on the Behaviour of Materals* (Proc. Int. Conf.), AIME (1976), 287

87. S. P. Lynch, *Metallography*, **23** (1989), 553

88. H. K. Birnbaum, *Atomistics of Fracture*, Plenum Press (1983), 733

89. S. Koike & T. Suzuki, *Acta Met.*, **29** (1981), 553

90. C. D. Cann & E. E. Sexton, *Acta Met.*, **28** (1980), 1215

91. N. J. Petch & P. Stables, *Nature*, **169** (1952), 842

92. X. Chen & W. W. Gerberich, *Met. Trans.*, **22A** (1991), 59

93. H. K. Birnbaum, *Environment-Induced Fracture of Metals*, NACE (1990), 21

94. R. A. Oriani, *Ibid.*, 439

95. W. W. Gerberich & X. Chen, *Ibid.*, 167

96. J. H. Watson, *Treatise on Materials Science and Technology,* **31**, Academic Press (1989), 501

97. A. S. Tetelman, *Hydrogen in Metals* (Proc. Int. Conf.), ASM (1974), 17

98. J. L. Murray, *Phase Dagrams of Binary Titanium Alloys*, ASM (1988)

99. *Pearson's Handbook of Crystallographic Data*, ASM (1985)

100. D. H. Polonis & J. G. Parr, *Trans. AIME*, **206** (1956), 531

101. H. Margolin & R. F. Bunshah, *Trans. AIME*, **209** (1957), 524

102. *Powder Diffraction File*, JCPDS

103. Y. C. Huang, S. Suzuki, H. Kaneko & T. Sato, *The Science, Technology and Application of Titanium*, Pergamon press (1970), 695

104. J. W. Edington, *Electron Diffraction in the Electron Microscope*, Philips Technical Library

105. S. Fujishiro & H. L. Gegel, *J. Less-Common Metals*, **14** (1968), 467

106. *Diffract v1.3*, Microdev Software

107. I. W. Hall, *Scand. J. Metall.*, **8** (1979), 17

108. D. Banerjee & J. C. Williams, *Scripta Met.*, **17** (1983), 1125

109. Discussion, EURAM Project Meeting (November 1990)

110. R. Haynes, *J. Inst. Metals*, **90** (1961-62), 80

111. N. R. Sorensen & J. A. Ruppen, *Corrosion*, **41** (1985), 561

112. C. Wagner, *Z. Phys. Chem.*, **B40** (1938), 455

113. K. Hauffe, *Oxidation of Metals*, Plenum Press (1965)

114. K. Hauffe & A. L.Vierk, *Z. Physik Chem.*, **196** (1950), 160

115. M. D. Earle, *Phys. Rev.*, **61** (1942), 56

116. P. H. Morton & W. M. Baldwin, *Trans. ASM*, **44** (1952), 1004

117. A. E. Jenkins, *J. Inst. Metals*, **84** (1955-56), 1

118. A. F. Wells, *Structural Inorganic Chemistry*, O. U. P. (1962)

119. H. W. Maynor, B. R. Barrett & R. E. Swft, WADC Technical Report 54-109 (1955)

120. K. Saarinen, I. Aho-Mantilla & J. Kivilahti, *Corrosion*, **45** (1989), 333